Measuring and Correcting the Effects of Scintillation in Astronomy

HARTLEY, KATHRYN,ELIZABETH

Measuring and Correcting the Effects of Scintillation in Astronomy

Kathryn E. Hartley

A thesis presented for the degree of

Doctor of Philosophy

Centre for Advanced Instrumentation

The University of Durham

United Kingdom

September 2023

Measuring and Correcting the Effects of Scintillation in Astronomy

Kathryn E Hartley

Abstract

High-precision ground-based time-resolved photometry is significantly limited by the effects of the Earth's atmosphere. Optical atmospheric turbulence, produced by the mixing of layers of air of different temperatures, results in layers of spatially and temporally varying refractive indices. These result in phase aberrations of the star light which have two effects: firstly the point spread function is broadened, thus limiting the resolution, and secondly the propagation of these aberrations results in spatio-temporal intensity fluctuations in the pupil-plane of the telescope known as scintillation. The first effect can be corrected with adaptive optics, however the scintillation noise remains.

In this thesis, the results from testing a scintillation correction technique that uses tomographic wavefront sensing are presented. The technique was explored extensively in simulation before being tested on-sky on the Isaac Newton Telescope in La Palma, Spain.

Scintillation noise also limits the signal-to-noise ratio that can be achieved for standard differential photometry as the random noise fluctuations in the comparison star and the target star light curves add in quadrature. A differential photometry technique that uses optimised temporal binning of the comparison star to minimise the addition of random noise fluctuations is presented and tested both in simulation and with on-sky data.

Finally, an investigation into the use of sparse arrays of small telescopes to reduce scintillation noise in photometry is presented. The impact of several parameters on the correlation of scintillation noise measured between sub-apertures in the array is explored.

Supervisors: Richard Wilson and James Osborn

Acknowledgements

Firstly, I would like to thank my amazing supervisors, Richard Wilson and James Osborn. Richard has been an incredible supervisor, guiding me throughout the PhD, despite global pandemics and volcanic eruptions. I would like to express my deepest gratitude for the many hours spent providing feedback and proofreading.

Special thanks to James for not only initially proposing the scintillation correction technique, the implementation of which has formed the majority of the work in this thesis, but for also funding most of the on-sky research - we quite literally couldn't have done it without you!

I would also like to thank Ollie for all of his help and support throughout my PhD. The many hours spent de-bugging code (and maths!) and proofreading all of my papers has been greatly appreciated.

I would also like to thank the staff and students I have met and worked with during my time at CfAI, old and new, for creating such a welcoming and friendly community. The many coffee breaks were invaluable. Additionally, many thanks to University College, which has been a second home to me over the last 9 years that I have been at Durham.

Finally, I could not have undertaken this journey without my friends, family and my partner Benedict, who all mean the world to me. Thank you for being there for me through thick and thin.

Contents

Declaration

The work in this thesis is based on research carried out at the Centre for Advanced Instrumentation, Department of Physics, University of Durham, England. No part of this thesis has been submitted elsewhere for any other degree or qualification, and it is the sole work of the author unless referenced to the contrary in the text.

Publications

Some of the work presented in this thesis has been published in journals and conference proceedings - the relevant publications are listed below.

Kathryn E. Hartley, Oliver J. D. Farley, Matthew J. Townson, James Osborn, and Richard W. Wilson "Correction of photometric scintillation noise via tomographic wavefront sensing: simulation and on-sky demonstration", Proc. SPIE 12185, Adaptive Optics Systems VIII, 121858J (29 August 2022); `https://doi-org.ezphost.dur.ac.uk/10.1117/12.2628703`

Kathryn E Hartley, Oliver J D Farley, Matthew J Townson, James Osborn, R W Wilson, "First on-sky demonstration of a scintillation correction technique using tomographic wavefront sensing", Monthly Notices of the Royal Astronomical Society, Volume 520, Issue 3, April 2023, Pages 4134–4146, `https://doi.org/10.1093/mnras/stad420`

Kathryn E Hartley, Oliver J D Farley, Matthew J Townson, James Osborn, Richard W Wilson, "Optical sparse telescope arrays and scintillation noise", Monthly Notices of the Royal Astronomical Society, Volume 526, Issue 1, November 2023, Pages 1235–1245, `https://doi.org/10.1093/mnras/stad2835`

Kathryn E Hartley, R W Wilson, "Optimized temporal binning of comparison star measurements for differential photometry", Monthly Notices of the Royal Astronomical Society, Volume 526, Issue 3, December 2023, Pages 3482–3494, https://doi.org/10.1093/mnras/stad2964

List of Figures

List of Tables

Chapter 1

Introduction

1.1 Motivation

"*It is unnatural in a large field to have only one shaft of wheat, and in the infinite Universe only one living world*" – Metrodorus of Chios, 4th century BC

Throughout history, philosophers and scientists have suspected the existence of extra-solar planets, planets around other stars. However, it wasn't until 1992 that the first exoplanet detection was confirmed around a pulsar star (Wolszczan and Frail, 1992). Since then, the hunt for exoplanets has been an ever-growing field in Astronomy, with more than 5,000 confirmed discoveries to date [†]. The discovery of exoplanets is an important step in answering one of life's biggest questions: are we alone in the universe? The ultimate goal of NASA's Exoplanet Program is to answer just that, and to find signs of life beyond Earth [‡].

Detecting exoplanets however is not easy since they do not emit visible light themselves and therefore cannot easily be observed directly. Hence, exoplanets are often detected by the effects they have on their parent star. There are multiple techniques used for detecting exoplanets including radial velocity spectroscopy, the transit method, pulsar timing, direct imaging and micro-lensing techniques. One of the most successful methods is the transit method, which has detected $\sim 75\%$

[†] https://exoplanets.nasa.gov/
[‡] https://exoplanets.nasa.gov/search-for-life/why-we-search/

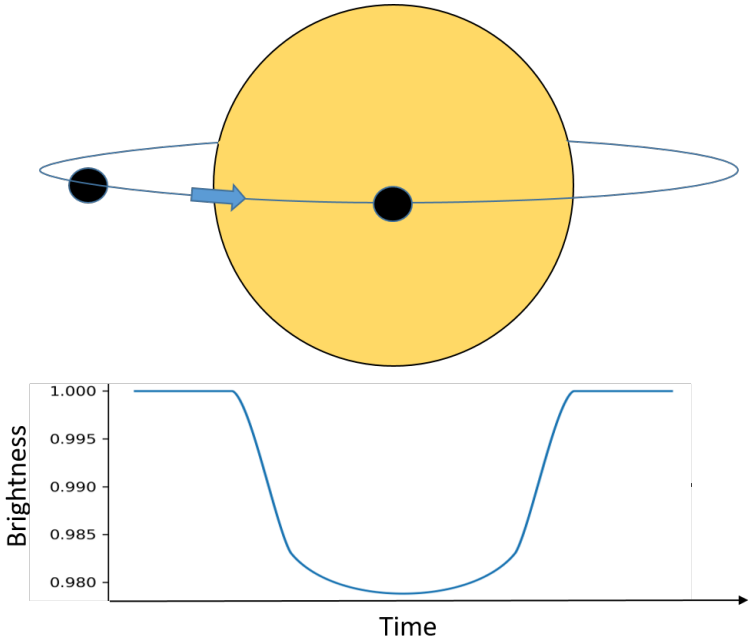

Figure 1.1: A schematic showing an exoplanet transit and its light curve. As the planet passes between the observer and its parent star, a dip in the measured intensity of the star is observed.

of exoplanets so far. This is where a dip in the measured brightness of a star is observed as a planet passes between the observer and the star, as demonstrated in Fig. 1.1.

One of the main benefits of the transit method is that a large number of parameters can be determined by the shape and duration of the transit dip. For example, in the simple case of a non limb darkened disk, the depth of the transit is directly proportional to the ratio of the radius of the planet to the radius of the star as given by:

$$\Delta F \propto \left(\frac{R_p}{R_*}\right)^2, \tag{1.1}$$

where ΔF is the change in the flux (i.e., brightness) of the star, R_p is the planet radius and R_* is the star radius.

The exoplanet transit parameters are measured by fitting a theoretical transit model to the observed transit light curve. However, the exoplanet parameters such as the planet radius, the orbital inclination and the semi major axis are all

degenerate. This is because a planet orbiting a larger star with a smaller orbital inclination can produce a similar transit light curve to a planet orbiting a smaller star with a larger inclination. Therefore, additional measurements including the star radius, radial velocity observations and the exoplanet transit period are required to constrain these parameters.

Assuming that stars behave as black bodies, measurements of the star's luminosity and effective temperature can be used with the Stefan-Boltzmann Law to estimate the stellar radius (Winn, 2010). Combining the stellar radius with measurements of the orbital period and transit duration can be used to constrain the inclination and semi major axis. Once the orbital inclination is known, then radial velocity measurements can be used to determine the exoplanet mass.

Additional properties such as the limb darkening coefficients and eccentricity are important parameters in fitting the exoplanet transit light curve as these affect the shape of the transit. However, having too many free variables during the fitting of the transit model can lead to inaccuracies. Therefore, some parameters, including the limb darkening coefficients, eccentricity and period, are often kept fixed.

A second dip in the measured flux, known as a secondary eclipse, can sometimes be measured as the planet passes behind the star, blocking the planet's flux. Observations of secondary eclipses can be used to study the composition of the exoplanet's atmosphere by comparing the measured spectra before and during the secondary eclipse. In addition, the secondary eclipse can be used to get a precise measurement of the planet orbital eccentricity (Alonso, 2018). However, these secondary eclipses are very small, on the order of 0.001 - 0.1 %, and are therefore very difficult to measure, especially from the ground.

Earth-like planets in the habitable zone - the zone in which liquid water can exist, and therefore where it is thought that extra-terrestrial life could survive (Kasting, 1997) - are of particular interest. However, such planets are very challenging to detect due to their relatively small size. To date, only 195 terrestrial (rocky) planets

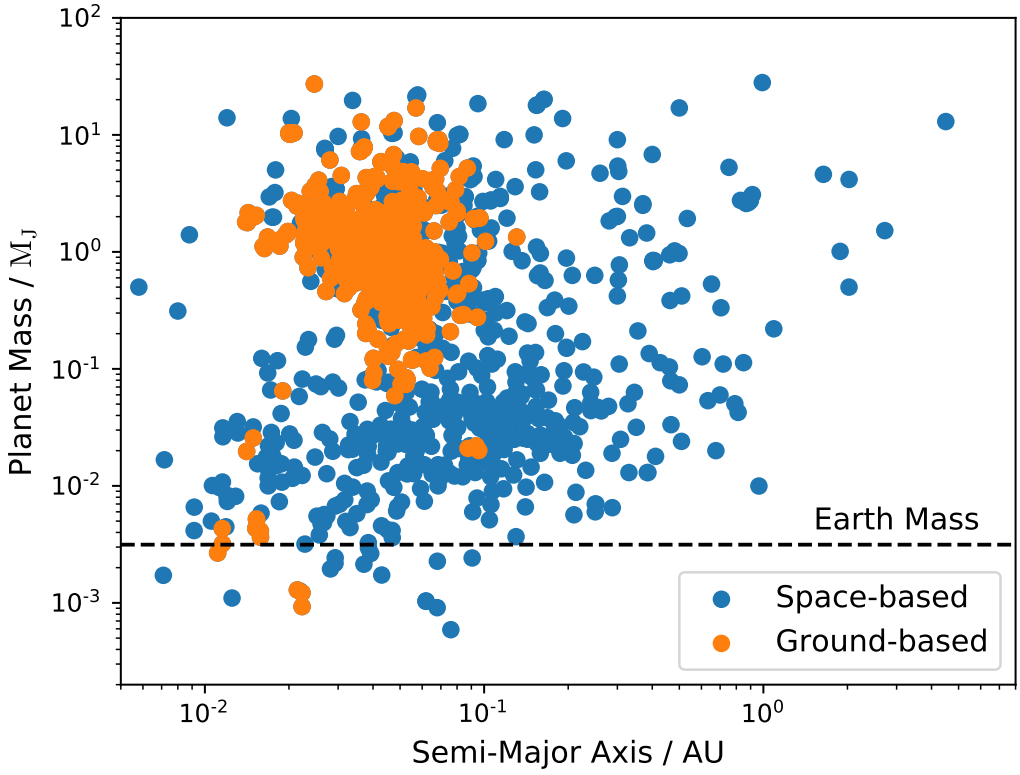

Figure 1.2: The exoplanet mass as a function of semi-major axis for exoplanets detected by the transit method for both space and ground based detection methods. The data for this plot was provided by NASA.

have been detected. Fig. 1.2 compares the exoplanet transit detection for space and ground based telescopes as a function of the exoplanet mass and semi-major axis *. As shown, the ground-based observatories primarily detect Hot Jupiter exoplanets, whereas space-based telescopes are able to detect a far greater variety of exoplanets.

Surveys such as the Transiting Exoplanet Survey Satellite (TESS) which was launched in April 2018 measure the brightness of thousands of stars and search for the characteristic periodic dips in the observed brightness of the star due to an exoplanet transit (Villanueva et al., 2019). These candidates then require follow-up observations to confirm their existence and to determine further details of the planetary system. These follow-up observations are usually carried out by ground-based

*https://exoplanetarchive.ipac.caltech.edu/

telescopes.

Whilst leaps and bounds have been made in the development of space-based telescopes such as JWST, ground-based telescopes are still favourable for multiple reasons. A significant advantage is the reduced cost. For example, the 6.5 m JWST cost £7.4 billion * whereas the cost of an 8.2 m VLT telescope was £300 million †. In addition, ground based telescopes have much easier access for maintenance. Space-based telescopes also have much higher risks, particularly during the space launch and once in orbit there are risks from impact with space debris.

However, despite all of these many advantages, ground-based telescopes have one major draw-back, which is having to observe through the Earth's atmosphere. The atmosphere is comprised of layers of air of differing temperatures, and poses lots of problems for astronomers (Serjeant et al., 2020). Firstly, a significant problem is atmospheric absorption, which makes observations in certain wavebands from the ground impossible. This effect is unavoidable and therefore space telescopes are necessary to observe in such spectral bands. Secondly, the atmosphere causes dispersion which changes the apparent position of stars and smears out broadband images. Additionally, the atmosphere scatters light such as light from the moon. Finally, another negative effect of the Earth's atmosphere is astronomical seeing which is defined as the blurring and distortion of an astronomical object due to atmospheric turbulence. This optical turbulence also produces intensity fluctuations known as scintillation which is seen by the naked eye as the twinkling of stars.

Optical atmospheric turbulence is caused by the mixing of layers of air of different temperatures, resulting in layers of spatially and temporally varying refractive indices. The effects of this turbulence are twofold. As the incoming wavefront passes through this turbulence, aberrations are introduced, thereby limiting the angular resolution. The second effect is that local regions within the turbulence either focus or de-focus the incoming light, resulting in spatial intensity fluctuations at the

*https://www.planetary.org/articles/cost-of-the-jwst
†Information@eso.org

ground. These fluctuations lead to photometric noise known as scintillation noise. This is seen by the naked eye as the twinkling of the stars.

The troposphere is the lowest and densest layer of the Earth's atmosphere up to a height of only $\sim$ 11 km and contains roughly 75% of all the atmosphere's air. It is this region where weather systems form and in which most optical turbulence occurs. Therefore, it is this layer of atmosphere that most interests ground-based astronomers. Interestingly, the height of the troposphere is lower at the Earth's poles and is higher at the equator. As such, above the surface layer, the astronomical seeing at the poles is extremely good (Lloyd, 2004).

The development of Adaptive Optics (AO) techniques that correct wavefront distortions in real-time have significantly improved ground-based imaging (Roddier, 1999). AO was first proposed by Babcock (1953) and is performed by measuring and correcting the phase aberrations produced by atmospheric turbulence in real time. A wavefront sensor (WFS) is used to measure the distorted wavefront. Based on these measurements, a command matrix is applied to a deformable mirror (DM) which mirrors the measured distortions, thereby flattening the incoming wavefront.

The first demonstration of AO was in 1989 with the COME-ON system at the Observatoire de Haute-Provence (Rousset et al., 1990). Since then, AO has become common place at most international observatories. Techniques that use the light from multiple stars to probe the atmosphere has enabled AO correction over large Fields of View (FOV) (Beckers, 1988). Furthermore, the limited sky coverage of these AO techniques have been overcome with the development of Laser Guide Stars (LGS), artificial stars that can be used to probe the atmosphere in any direction (Rigaut and Neichel, 2018).

These advancements in AO have greatly improved the capabilities of ground-based astronomical imaging. For example, instruments such as the Gemini Planet Imager on the Gemini South Telescope in Chile which combine high-order AO systems with coronagraphs has enabled direct imaging of exoplanets around their parent stars

(Graham et al., 2007).

However, there are still many problems that remain for high-precision ground-based astronomy. For example, AO hasn't addressed scintillation, which is a significant problem for exoplanet transit photometry (Föhring et al., 2019). In this thesis, three projects are presented which all relate to the improvement of ground-based high precision exoplanet transit follow-up observations. The motivation for each project is outlined below.

1.1.1 Scintillation Correction

For ground-based high precision photometry of bright stars, scintillation noise is often the dominant noise source and severely limits the detection of small-scale intrinsic intensity variations. This is one reason why predominantly only Hot Jupiters can be detected from ground-based exoplanet transit observations.

Scintillation correction would also greatly improve the multi-spectral transit photometry of exoplanets. From measurements of the absorption and emission lines during an exoplanet transit at different wavelengths, the molecules in the planet's atmosphere can be determined. These measurements help to develop our understanding of atmospheric processes including atmospheric chemistry, the greenhouse effect, the physics of clouds and winds. Most significantly, these studies could lead to the discovery of life on other planets. Such studies require large telescopes in order to provide high Signal-to-Noise Ratios (SNRs) in order to detect small changes in the transit photometry between the wavebands. Observations of these bright stars will often be limited by scintillation noise.

Atmospheric scintillation correction could also lead to further ground-based studies becoming possible. These include the study of exoplanet atmospheres from the twinkling of stars during exoplanet transits and studies of the solar atmosphere by observing the occultations of stars by the solar limb (Dravins et al., 1997a).

Additionally, the diameters of stars could be more accurately measured during lunar occultations (Knoechel and von der Heide, 1978).

Therefore, correcting and reducing scintillation noise will provide a large improvement in ground-based high precision photometry. Various scintillation correction techniques have been proposed with varying success. These include the use of a ferroelectric liquid-crystal spatial light modulator to control the transmittance of a telescope pupil (Love and Gourlay, 1996), using the achromatic nature of scintillation (Kornilov, 2011) and conjugate plane photometry (Osborn et al., 2011). However, as of yet, no facility instrumentation for scintillation correction is in use.

1.1.2 Differential Photometry

High-precision transit photometry is also limited by systematic noise (Pont et al., 2006). There are multiple possible sources of systematic noise in astronomical photometry. These include atmospheric transparency variations due to changes in pressure and aerosols which produces systematic noise in light curve observations proportional to 1/f, where f is the frequency (Young et al., 1991).

The most common data reduction technique to correct systematic trends in light curves is the method of differential photometry. This technique corrects the systematics by normalising the light curve of the star of interest with the light curve of one or more comparison stars in the FOV. The ideal comparison star should be similar in colour and brightness to the target star and close to the target star in the field.

However, whilst this method successfully reduces systematic noise, the random intensity fluctuations due to shot noise and scintillation noise of the target star and of the comparison star(s) add in quadrature. This significantly limits the magnitude of the comparison star that can be used, as fainter comparison stars will add more random noise to the calibrated target star light curve.

1.1.3 Optical Sparse Telescope Arrays and scintillation noise

Large ground-based telescopes have many benefits. The most significant advantage is that the total signal from the astronomical source increases with aperture size due to the increased collecting area. In addition, scintillation noise also inversely scales with telescope diameter. Therefore, large telescopes have a significantly increased SNR, enabling much fainter astronomical objects such as distant galaxies to be observed. The increased SNR also means much smaller intrinsic changes in intensity can be detected, and therefore smaller planets can be detected via the transit method.

However, large telescopes have several disadvantages, the most significant of which is their increased cost. In addition, they require large permanent constructions at favourable telescope sites. Such projects often face significant challenges including socio-political opposition. Another significant problem with large telescopes is that observing time is highly competitive.

Sparse arrays of small optical telescopes are in common use for exoplanet surveys such as Wide Angle Search for Planets (SuperWASP) (Pollacco et al., 2006), Multi-site All-Sky CAmeRA (MASCARA) (Lesage et al., 2014) and the Next Generation Transit Survey (NGTS) (Chazelas et al., 2012). Such arrays are ideal for observing large patches of the sky due to the small telescopes' large FOV. Many stars can be observed simultaneously, and automatic pipelines can be used to search for periodic dips in their brightness.

However, another benefit of using such arrays has been recently exploited. By pointing all the telescopes in the array at a single bright target of interest and combining the photometry from all the telescopes in the array, high SNRs can be achieved. For an array of N independent telescopes, averaging their light curves increases the SNR by a factor of $\sqrt{N}$. In the case of bright targets where the photometry is dominated by scintillation noise, the resulting SNR for an array of telescopes will be higher than the SNR for a single telescope of the same equivalent

area of glass. Hence, a higher SNR can be achieved for a fraction of the cost. Simultaneous observations of WASP-166b by NGTS and TESS shows that ground-based multi-telescope arrays are capable of achieving SNRs comparable to those achieved in space (Bryant et al., 2020) (Doyle et al., 2022).

However, since scintillation noise is produced by high altitude turbulence, as this turbulence moves with the wind, the spatial intensity fluctuations can be correlated between neighbouring telescopes. If the photometric noise of the telescope observations are correlated, then the SNR of the observed target will not be increased by the expected $\sqrt{N}$ factor. Hence, a key question about building such telescope arrays is how far apart the individual telescopes need to be placed within the array so that the effects of the correlation of scintillation noise are minimised.

1.2 Synopsis

Chapter 2 discusses the key scientific theoretical background of this thesis. The negative effects of the Earth's atmosphere, specifically in regard to exoplanet transit photometry, are discussed. The physical processes that produce scintillation noise are discussed and the theoretical mathematical expressions are derived. The key numerical methods used to simulate the atmosphere that were used to generate the simulation results presented in this thesis are discussed, including the generation of phase screens and Fresnel propagation. Additional noise sources such as photon noise and systematic noise are also discussed.

Chapter 3 presents the simulation results of a scintillation correction technique proposed by Osborn (2014) that uses a tomographic algorithm to produce a numerical estimate for the intensity fluctuations. The scintillation correction technique is described in detail and the impact of several parameters including the exposure time, the asterism configuration, number of reference stars and the number of reconstructed layers used is explored. The sky coverage of the technique is investigated and the results of simulating a tomographic LGS facility are given.

Chapter 4 presents the first on-sky results for tomographic scintillation correction. The method was demonstrated on the Isaac Newton Telescope (INT), a 2.54m telescope in La Palma, Spain. Details of the experimental set-up and data reduction are given. The on-sky results for two observing runs with two different asterisms are presented and detailed discussions of the limitations of the experiment are given.

Chapter 5 details a simple data reduction technique that reduces noise in differential photometry by the temporal binning of the comparison star signals. A significant problem with differential photometry data reduction is that whilst it corrects systematic noise, the random intensity fluctuations of the star of interest and of the comparison star add in quadrature thus adding noise to the calibrated light curve. This significantly limits the magnitude of the comparison star that can be used. The temporal binning of the comparison star light curves before performing the differential photometry reduces the addition of random intensity fluctuations due to the shot noise and scintillation noise of the comparison star to the calibrated target light curve, whilst still correcting the low-order systematic trends. Hence, much fainter comparison stars can be used.

Chapter 6 investigates the effects of scintillation noise correlation between neighbouring telescopes in an optical sparse telescope array. Arrays of telescopes have multiple benefits including an increased SNR at a fraction of the cost as well as a large FOV. These benefits are investigated with simulation results and on-sky results using INT pupil-plane images.

Chapter 7 summarises and concludes the results from this thesis and discusses future work to be undertaken.

Chapter 2

Theory

2.1 Seeing and Scintillation

2.1.1 Atmospheric Turbulence

The atmosphere is comprised of layers of air of different temperatures and hence different refractive indices. Atmospheric optical turbulence is produced by the mixing of these layers to create layers of spatially and temporally varying refractive indices. As starlight propagates through this optical turbulence it becomes distorted, thus limiting ground-based astronomy observations.

Since atmospheric turbulence is a random process, it can only be described statistically. The most common model used to describe turbulence is the Kolmogorov model which was first proposed by Andrei Kolmogorov in 1941 (Kolmogorov, 1991) and later developed by Tatarski in 1967 (Tatarski, 1967).

A flow becomes turbulent when the Reynold's number reaches a critical value of ~ 1300. The Reynold's number depends only on the characteristic dimensions of the flow and is given by:

$$Re = \frac{V_0 L}{\nu_0}, \tag{2.1}$$

where V_0 is the velocity of the flow, L is the characteristic size of the flow and ν_0 is the kinematic viscosity of the fluid (Roddier, 1981).

From this Kolmogorov developed a simple theory of turbulence based on a cascading effect in which energy is added to the turbulent layer on large spatial scales, L_0, known as the outer scale, to form eddies. For the atmosphere, this energy comes from solar heating and wind shear. These then break down into smaller and smaller eddies until the Reynolds number reaches a small enough number, at which point the energy is dissipated. This occurs once spatial scales of l_0, the inner scale, are reached (Kolmogorov, 1991).

The outer scale has been found to be on average ~ 20 m (Wilson, 1998). For small telescopes the outer scale is therefore negligible since it is much larger than the telescope diameter. In addition, the inner scale, which is only a few millimetres in diameter (Roddier, 1981), is obscured by the Fresnel-zone size - the spatial scale of the intensity fluctuations of the starlight after propagation through the turbulent atmosphere - which is often several centimetres in diameter. Therefore, the characteristic scale that is most significant for most observations is the telescope aperture (Dravins et al., 1997a).

Between these two scales, in the inertial range, the rate of viscous dissipation, ϵ_0, is equal to the rate of production of turbulent energy. Therefore, the velocity of the eddies, v, at this scale, L, is dependent only on L and the dissipated energy ϵ_0. Since, ϵ_0 has dimensions of energy per unit mass per unit time, Kolmogorov showed that from dimensional analysis:

$$v \propto \epsilon_0^{\frac{1}{3}} L^{\frac{1}{3}}. \tag{2.2}$$

Therefore, in terms of spatial frequency κ, for $L_0^{-1} \ll \kappa \ll l_0^{-1}$, the kinetic energy, $E(\kappa)d\kappa$, is proportional to $v(\kappa)^2$. Hence (Roddier, 1981):

$$E(\kappa) \propto \kappa^{-\frac{5}{3}}. \tag{2.3}$$

In three dimensions, the energy dissipated at spatial frequency κ is therefore proportional to $\kappa^{-\frac{11}{3}}$ (Roddier, 1981).

From this relationship, Tatarski derived the Kolmogorov phase power spectrum, given by (Roddier, 1981):

$$\Phi(\kappa) = 9.7 \times 10^{-3} k^2 C_n^2(h) \kappa^{-\frac{11}{3}}, \tag{2.4}$$

where $C_n^2(h)$ is the refractive index structure constant as a function of height, h, with units $\mathrm{m}^{-2/3}$ and k is the wavenumber, $k = \frac{2\pi}{\lambda}$. This relationship has been confirmed empirically for multiple situations, including the atmosphere (Lumley and Panofsky, 1965) (Nightingale and Buscher, 1991). Hence, The Kolmogorov model is used to simulate atmospheric turbulence by producing phase screens with the Kolmogorov power spectrum. In addition, it is used in tomographic reconstruction matrices to estimate the 3D turbulence profile above a telescope aperture.

The von Karman power spectrum is a modification of the Kolmogorov power spectrum which includes the effect of the finite outer scale, given by:

$$\Phi(\kappa) = 9.7 \times 10^{-3} k^2 C_n^2(h) \left| \kappa^2 + \left(\frac{2\pi}{L_0} \right)^2 \right|^{-\frac{11}{6}}, \tag{2.5}$$

Modifications to include the inner scale can also be included, however the aperture sizes considered in this thesis are far greater than the inner scale and therefore its effect is negligible.

A point source of light at a large distance (such as a star) can be considered to produce a plane wave. As it propagates to the ground it is distorted by the optical turbulence. If the atmosphere is considered to be a sum of discrete layers, then the phase shift induced by the refractive index fluctuations $n(x, h)$ in a turbulent layer of thickness δh is given by (Roddier, 1981):

$$\phi(x) = k \int_h^{h+\delta h} n(x, h) dh, \tag{2.6}$$

The output wavefunction after passing through this layer is then:

$$\Psi(x) = \exp(i\phi(x)). \tag{2.7}$$

As the plane wave passes through the turbulent volume, these phase distortions accumulate. For short exposures, the phase aberrations are frozen in time resulting in a distorted speckle image. For long exposures, these aberrations are averaged to produce a smooth Gaussian PSF.

The spatial variance of the difference in refractive index between two points separated by ρ is given by the structure function:

$$D_n(\rho) = \langle |\mathbf{n}(\mathbf{r}) - \mathbf{n}(\mathbf{r}+\rho)|^2 \rangle = C_n^2(h)\rho^{\frac{2}{3}}, \tag{2.8}$$

where $\mathbf{r}$ is the position, ρ is the separation and $C_n^2(h)$ is the refractive index structure constant. Hence, $C_n^2(h)$ is a measure of the local refractive index inhomogeneities and hence a measure of the optical turbulence strength. The integral of the structure constant between two heights gives the total turbulence strength in that range. The total turbulence strength is often expressed by the Fried parameter (Fried, 1966). This is defined as:

$$r_0 = \left(0.423k^2 \sec(\gamma) \int_0^\infty C_n^2(h)dh\right)^{-\frac{3}{5}}, \tag{2.9}$$

where γ is the zenith angle. This equates to the aperture over which propagation through the atmosphere would result in one radian square of phase variance. Typical values of r_0 vary from 5 cm in poor seeing conditions to 20 cm in excellent seeing conditions (Wilson, 1998).

2.1.2 Zernike Polynomials

The Zernike polynomials are a complete set of continuous polynomials that are orthogonal over a unit circle, which were developed by Fritz Zernike in 1934 to describe the phase contrast method for testing mirrors (von F. Zernike, 1934).

The even polynomials are given by (Noll, 1976):

$$Z_j(\rho,\theta) = \sqrt{n+1}R_n^m(\rho)\sqrt{2}cos(m\theta), \tag{2.10}$$

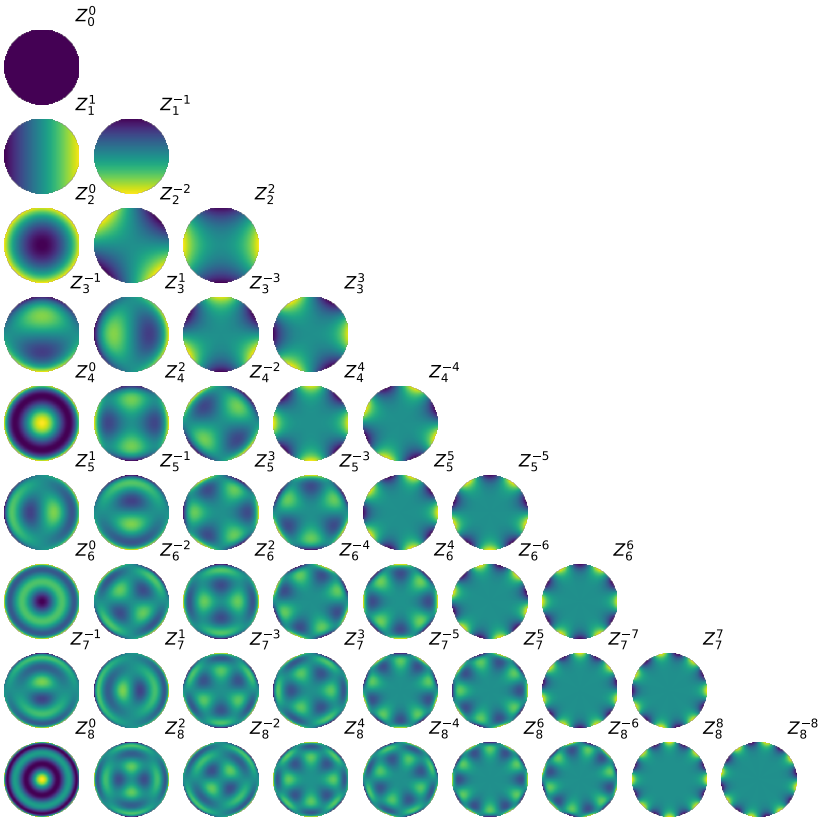

Figure 2.1: The first 45 Zernike polynomials in terms of $Z_n^{\pm m}$. The order is given by n and each row contains $n+1$ polynomials.

the odd polynomials are given by:

$$Z_j(\rho,\theta) = \sqrt{n+1}R_n^m(\rho)\sqrt{2}sin(m\theta), \tag{2.11}$$

and in the case where $m = 0$:

$$Z_j(\rho,\theta) = \sqrt{n+1}R_n^0(\rho), \tag{2.12}$$

where R_n^m are the radial polynomials defined by:

$$R_n^m(\rho) = \sum_{k=0}^{\frac{n-m}{2}} \frac{(-1)^k(n-k)!}{k!(\frac{n+m}{2}-k)!(\frac{n-m}{2}-k)!}\rho^{n-2k}, \tag{2.13}$$

where ρ is the radial distance where $0 \leq \rho \leq 1$, θ is the azimuthal angle, j is a mode ordering number and is a function of n and m where m and n are positive integers with $n \geq m$ and $n - |m|$ is even.

The Zernike basis is a useful basis for describing aberrations in optical systems and atmospheric turbulence. The first 45 Zernike polynomials are shown in Fig. 2.1.

Each represent a different phase aberration. For example, Z_1^1 and Z_1^{-1} represent tip and tilt, and Z_2^0 defocus. Using the centre of the circle as an origin of a reference frame, it can be noted that polynomials with index $+m$ are symmetric with the horizontal axis, whereas polynomials with index $-m$ are antisymmetric. They have the same overall shape, but a different orientation. Therefore, any combination of these two paired polynomials will be independent of any angle of rotation with respect to the centre of the circle (Capalbo et al., 2020). In addition, from the figure, it is clear that the higher order Zernike modes are sensitive to smaller spatial scales.

As a result of these properties, an arbitrary function $\phi(R\rho, \phi)$ over a circle with radius R, can be described by:

$$\phi(R\rho, \theta) = \sum_j a_j Z_j(\rho, \theta), \tag{2.14}$$

where $\rho = r/R$ and a_j is the coefficient associated with the Zernike mode $Z_j(\rho, \theta)$. Hence, a set of atmospheric phase aberrations can be described by the coefficients a_j.

2.1.3 Scintillation Theory

The twinkling of stars, known as scintillation, whilst inspiring the likes of Mozart and Van Gogh, has puzzled philosophers for centuries. Many astronomers have come up with theories of its origins; Aristotle believed the effect to be due to a weakness in the eye, Leonardo Da Vinci believed it to be an optical illusion, whilst Johannes Kepler believed it was the stars themselves changing in brightness. It wasn't until the eighteenth century that Isaac Newton correctly attributed the effect of scintillation to atmospheric turbulence (Sofieva et al., 2013).

The general theory for ground based scintillation was developed by Tatarski (1967) and has been expanded upon by Roddier (1981) and Young (1969). Extensive studies have been carried out by Mikesell (1955), Dainty et al. (1982) and more

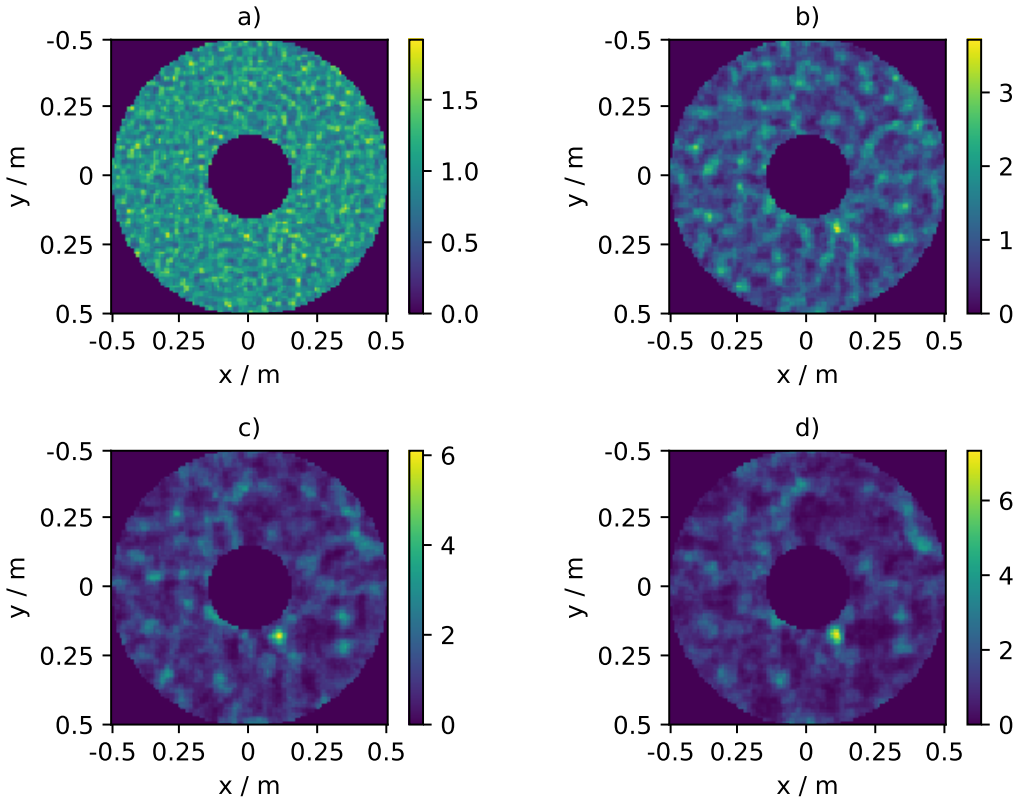

Figure 2.2: An example of a scintillation pattern produced by the propagation of a wavefront over distances a) 1 km, b) 5 km, c) 10 km, d) 15 km.

recently Dravins et al. (1997a), Dravins et al. (1997b), Dravins et al. (1998) who looked at the impact of wavelength and telescope aperture on the scintillation noise measured.

High altitude optical turbulence can focus or de-focus the incoming starlight leading to 'flying shadows' crossing the telescope pupil. These fluctuations occur both because the 'flying shadow' patterns move with the wind as well as the optical turbulence intrinsically changing (Dravins et al., 1997a). In most modelling, Taylors' frozen flow hypothesis is assumed where the time taken for the patterns to cross the telescope pupil is considered to be significantly smaller than the time taken for the optical turbulence to evolve (Taylor, 1938).

Since scintillation is an effect of propagation, it is mainly caused by turbulence in the upper atmosphere. This was confirmed empirically by Mikesell in 1955 in

which he used lamps on high altitude balloons to simulate artificial stars (Mikesell, 1955). The scintillation measured for these artificial stars were less than that of the adjacent real stars, suggesting scintillation originates from turbulence at higher altitudes. It is for this reason that good photometric conditions can be observed during bad seeing; the angular seeing results from the strongest turbulence layer which is often much closer to the ground (Osborn et al., 2010) whilst scintillation is produced by turbulence in the upper atmosphere. Consequently, comparison stars cannot ordinarily be used to correct for scintillation, since the respective wavefronts of the two stars will not have sufficient overlap at high altitudes. Hence, the iso-photometric angle, the angle in which the scintillation is strongly correlated, will be much smaller than the average star separation.

The size of the intensity fluctuations in the scintillation pattern is given by the radius of the first Fresnel zone, $r_f = \sqrt{\lambda z}$, where λ is the wavelength of the light and z is the propagation distance from the turbulent layer. As z increases, the spatial intensity fluctuations become larger in terms of their spatial extent (Osborn et al., 2015). This is demonstrated in Fig. 2.2 where the scintillation pattern for a layer at 1 km, 5 km, 10 km and 15 km are plotted.

The amount of scintillation is measured by the scintillation index. This is given by the variance of the relative intensity fluctuations of the source:

$$\sigma_I^2 = \frac{\langle I^2 \rangle - \langle I \rangle^2}{\langle I \rangle^2}, \tag{2.15}$$

where I is the intensity as a function of time and $\langle \cdot \rangle$ represents an ensemble average. Using the normalised intensity ensures that the scintillation index does not depend on the magnitude of the star. The scintillation RMS fractional noise is then the square-root of the scintillation index. Scintillation can therefore be studied either by measuring the scintillation index or the direct scintillation patterns (Dravins et al., 1997a).

The theoretical scintillation index is given by the integral of the scintillation power

spectrum:

$$\sigma_I^2 = \int_0^\infty W(f)df, \tag{2.16}$$

where $W(f)$ is the irradiance power spectrum defined by Kornilov (2012) as:

$$W(f) = 9.7 \times 10^{-3} \times 4 \times (2\pi)^3 \int_0^\infty C_n^2(z)\phi(f)S(z,f)A(f)fdf, \tag{2.17}$$

where $S(z,f)$ is the Fresnel filter function which accounts for the propagation and is given by $sin(\pi\lambda z f^2)^2/\lambda^2$. It is for this reason that the intensity fluctuations have an intrinsic spatial scale of $r_f = \sqrt{\lambda z}$. $\phi(f)$ is the frequency component of the refractive index power spectrum, i.e. for Kolmogorov $\phi(f) = f^{-\frac{11}{3}}$. $A(f)$ is the aperture filter function and is given by:

$$A(f) = |\mathcal{F}(P(x,y))|^2, \tag{2.18}$$

where $P(x,y)$ is the pupil function for Cartesian coordinates x and y. For a circular pupil function which is equal to one for $x^2 + y^2 < \frac{D^2}{4}$ and zero elsewhere, the aperture filter function is given by $(2J_1(\pi Df)/(\pi Df))^2$.

Hence, for telescopes with an aperture of $D \gg r_f$, where r_f is the Fresnel radius, the scintillation index for short exposures can be estimated as (Sasiela, 2012):

$$\sigma_I^2 = 17.34D^{-7/3}(\cos(\gamma))^{-3} \int_0^\infty h^2 C_n^2 dh, \tag{2.19}$$

where D is the telescope aperture, γ is the zenith angle, h is the altitude of the turbulent layer and $C_n^2(h)$ is the refractive index structure constant.

For long exposure times, defined as $t \gg t_{cross}$ where t_{cross} is the time taken for the layer to cross the telescope pupil, the scintillation index is given by (Sasiela, 2012):

$$\sigma_I^2 = 10.66D^{-4/3}t^{-1}(\cos(\gamma))^{\alpha} \int_0^\infty \frac{h^2 C_n^2}{V_\perp(h)} dh, \tag{2.20}$$

where t is the exposure time and $V_\perp(h)$ is the wind velocity profile. The value of α depends on the wind direction and will be -3 when the wind is transverse to the azimuthal angle of the star and -4 when it is longitudinal.

In the case of short exposure times, the intensity speckles will appear frozen in the pupil. However, for long exposures the speckles will move across the pupil during the exposure, resulting in temporal averaging. The degree of temporal averaging will depend on the wind speed and the exposure time. The exposure time at which the scintillation index can be described by equation 2.20 will therefore depend on the atmospheric turbulence profile and the aperture size of the telescope.

From the above equations, it can be noted that, as telescope aperture and exposure time increase, scintillation decreases proportional to $D^{-4/3}t^{-1}$. The variance of the intensity fluctuations due to shot noise is proportional to $D^{-2}t^{-1}$. Hence, as the telescope aperture size is increased, scintillation noise becomes more dominant. Scintillation correction is therefore increasingly important for large telescopes.

In the absence of systematic errors, for bright stars, scintillation noise is the dominant noise source. The magnitude at which photon noise becomes dominant is dependent on the telescope aperture, with smaller telescopes becoming shot noise limited at lower magnitudes. For example, it has been found that scintillation dominates for stars of magnitude below $V \sim 10.1$ mag for a 0.5m telescope, and at $V \sim 11.7$ mag for a 4.2m telescope under median atmospheric conditions in La Palma (Föhring et al., 2019). Across the sky there are close to 330,000 stars brighter than $V = 10$ (Hog et al., 2000) and therefore a large number of stars for which photometric observations will be scintillation limited.

2.1.4 Turbulence Profiles: SCIDAR

Since scintillation patterns are the result of light interacting with the Earth's turbulent atmosphere, measuring instantaneous stellar scintillation patterns can give insight into the atmospheric turbulence (Sofieva et al., 2013). SCIntillation Detection and Ranging (SCIDAR) (Vernin and Roddier, 1973) is a triangulation technique that uses stellar scintillation patterns to determine the turbulence profile above the telescope.

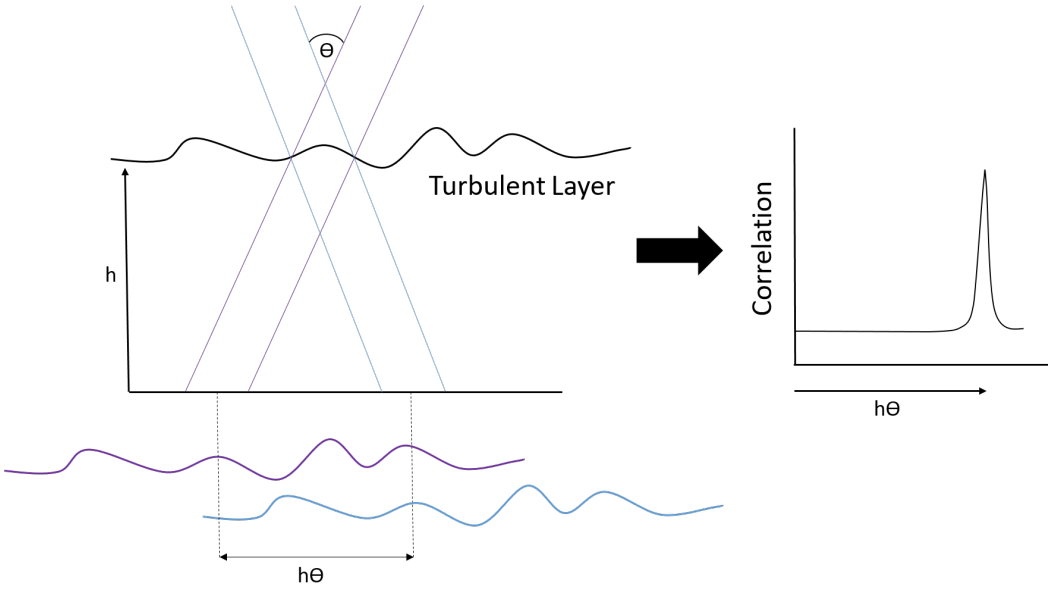

Figure 2.3: A schematic showing the SCIDAR method. For two stars separated by angle θ, the scintillation patterns from a turbulent layer at altitude h for each star will be separated by $h\theta$ at the ground. The cross correlation of the scintillation pattern measured by each star will have a peak at $h\theta$.

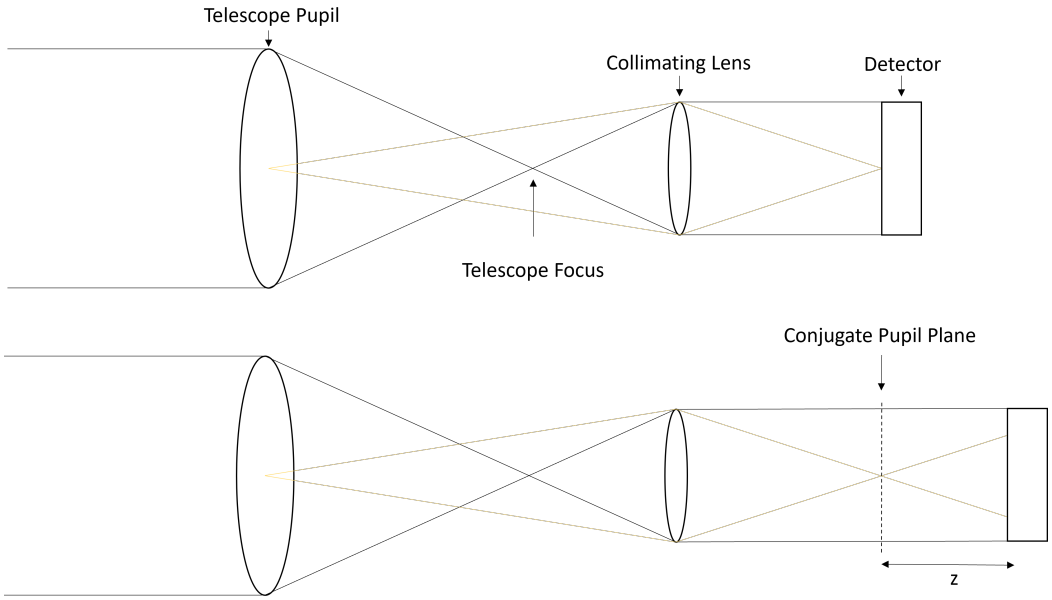

Figure 2.4: A ray diagram showing the concept of optical conjugation. In generalised-SCIDAR the turbulence near the ground can be imaged by moving the detector behind the conjugated pupil plane.

SCIDAR is an instrument that measures turbulence strength as a function of height. It works by observing two stars with angular separation θ. A turbulent layer at height h will produce two copies of the intensity fluctuation pattern at the ground which will be separated by a distance of $h\theta$. Cross-correlating the intensity patterns of these two stars allows the heights and strengths of the turbulent layers to be measured (Osborn et al., 2018).

In generalised-SCIDAR, a conjugate position of at least 1 km below the conjugate plane is used to extend the propagation distance of the light path such that the phase aberrations induced by the surface turbulent layer can be measured (Shepherd et al., 2013). Fig. 2.4 shows a ray diagram demonstrating this concept.

Stereo-SCIDAR is a further development of the SCIDAR technique where each star is imaged on a separate camera which improves the SNR of the profile and also allows for a greater difference in magnitude between the two stars. This significantly increases the sky coverage of the turbulence profiler.

The maximum altitude that SCIDAR can observe is given by:

$$h_{max} = \frac{D}{\theta}, \tag{2.21}$$

where D is the telescope diameter and θ is the angle between the two stars. For a given telescope, θ should be chosen such that h_{max} is $\sim$20 km since this is the maximum height of the tropopause and therefore most optical turbulence (Osborn et al., 2018).

The vertical resolution of SCIDAR is limited by the minimum separation that can be measured for the auto-correlation peaks (Avila et al., 2008). Therefore, the larger the telescope aperture, the higher the profile resolution, and the higher h_{max}. Hence, this technique is optimal for large telescopes.

Assuming Taylor's 'frozen' flow hypothesis, as the turbulent layer moves with the wind, then the scintillation pattern will cross the telescope pupil with the same velocity as the turbulent layer. Therefore, calculating the cross covariance maps

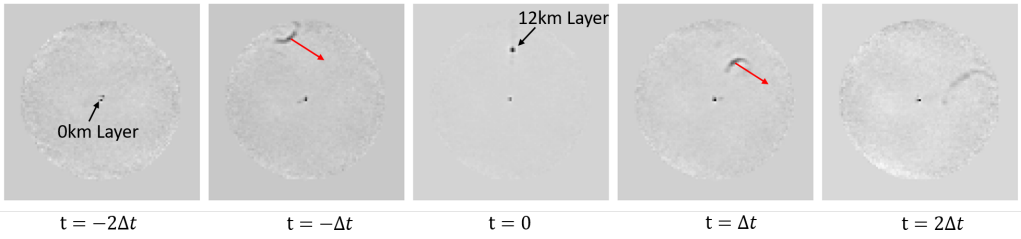

Figure 2.5: An example of stereo-SCIDAR cross covariance maps as a function of time off-set collected on the Isaac Newton Telescope (INT) in September 2021.

with a temporal offset allows an estimate for the wind velocity profile to be determined. This is done by measuring the relative locations of the covariance peaks of the turbulent layers with time.

Fig. 2.5 shows an example of cross covariance maps as a function of time off-set from SCIDAR data collected on the Isaac Newton Telescope (INT) in September 2021. The stationary central peak is due to dome seeing. A second strong layer at approximately 12 km with a well-defined velocity, shown by the red arrows, can be seen moving across the covariance map with time.

2.2 Numerical Simulations

The Monte Carlo method is a class of computational algorithm that uses randomness to solve problems. This is done by repeatedly sampling random instances of a model which has defined statistics, to obtain an accurate result. This technique is ideal for testing systems with multiple degrees of freedom, all of which have defined statistics, such as atmospheric turbulence.

Layers of atmospheric turbulence are modelled by random phase screens placed at discrete layer heights. These screens are moved according to the wind direction and speed of each layer. The statistics of the atmosphere including the C_n^2 associated with each layer, the layer altitudes, wind directions and speeds used in simulation in this thesis are all based on real turbulence profile observations from historic SCIDAR data for La Palma and Paranal.

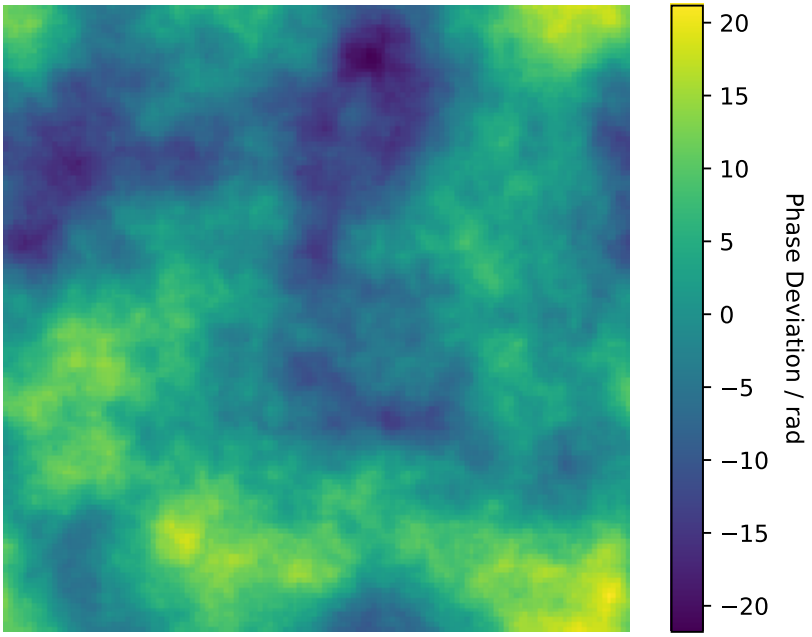

Figure 2.6: An example phase screen.

Scintillation intensity fluctuations are simulated using the Fresnel propagation of the phase screens. Long exposures are simulated by taking multiple instantaneous instances of the atmosphere and averaging the intensity fluctuations over the total exposure time. The number of sub-samples used to model each exposure integration was optimised by plotting the measured scintillation index as a function of the number of samples used.

2.2.1 Phase Screen Generation

The phase modulations of a plane wavefront after passing through an optical turbulence layer in the atmosphere are simulated using random phase screens. Random screens are produced by filtering Gaussian white noise with a spatial power spectrum such as the Kolmogorov or Von Karman spectrum. The phase screen is given by (Ellerbroek and Cochran, 2002):

$$OPD(x) = c\Re\Big(\mathcal{F}[\sqrt{\Phi(\kappa)}(r(\kappa) + ir'(\kappa))\Big), \tag{2.22}$$

where $\mathcal{F}$ is the 2D spatial Fourier transform, $\Phi(\kappa)$ is the spatial power spectrum of the turbulence, κ is the spatial frequency, r and r' are zero mean, unit variance, real-valued white noise functions, and c is a scaling factor for the strength of the screen.

For von Karman turbulence, where the outer scale is included, the spatial power spectrum is given by:

$$\Phi(\kappa) = \left|\kappa^2 + \left(\frac{W}{L_0}\right)^2\right|^{\frac{-11}{6}}. \tag{2.23}$$

where W is the equivalent extent of the screen in meters. The scaling factor c is then given by:

$$c = \frac{0.1517}{\sqrt{2}}\left(\frac{W}{r_0}\right)^{\frac{5}{6}} \tag{2.24}$$

which scales the strength of the phase screen to a value of r_0. The resulting phase screen is given in radians of phase for the particular wavelength λ. For each layer in the simulation, a unique phase screen is used.

The fast Fourier transform means that the phase screen will be periodic. Therefore, the width of the screen should be significantly larger than the telescope aperture and larger than L_0. Otherwise, the strength of turbulence from the low order modes will be underestimated. Fig. 2.6 shows an example of a phase screen generated using the python package `AOtools` (Townson et al., 2019).

2.2.2 Fresnel Propagation

To simulate scintillation, a model for the propagation of light through the turbulent atmosphere is needed. The Fresnel near field approximation can be used since the wavelength of light is much smaller than the wavefront perturbations.

The propagation is described by the Fresnel diffraction integral, which is given by (Schmidt, 2010):

$$U(x_2, y_2) = \frac{e^{ikz}}{i\lambda\delta z}\int_{-\infty}^{\infty}\int_{-\infty}^{\infty} U(x_1, y_1) e^{\frac{ik}{2\triangle z}[(x_2-x_1)^2+(y_2-y_1)^2]} dx_1 dy_1, \tag{2.25}$$

where $U(x_2, y_2)$ is the observation-plane optical field, $U(x_1, y_1)$ is the source-plane optical field, $r_1 = x_1\hat{i} + y_1\hat{j}$ is the source plane and $r_2 = x_2\hat{i} + y_2\hat{j}$ is the observation plane, separated by a distance $\triangle z$.

Eq. 2.25 can be rewritten in the form of a convolution of the source-plane field with the free-space amplitude spread function:

$$U(x_2, y_2) = U(x_1, y_1) \otimes \left[\frac{e^{ikz}}{i\lambda\delta z} e^{\frac{ik}{2\triangle z}(x_1^2 + y_1^2)} \right]. \tag{2.26}$$

This equation can then be solved using the convolution theorem via two Fourier transforms (Schmidt, 2010).

There are three main approaches to solving this equation, namely, one-step Fresnel propagation, two-step Fresnel propagation and angular spectrum propagation. The latter is the solution used to model the propagation in the simulations throughout this thesis. These different methods have different quadratic phase factors in their Fourier transforms and therefore different sampling constraints. The angular spectrum method is found to be more accurate for short distances, whilst Fresnel propagation is better for long distances. Given the turbulence profile is composed of multiple layers, the individual propagation distances are relatively short. The intensity pattern at the ground is then proportional to $|U(x_2, y_2)|^2$.

2.2.3 Simulating Scintillation

The method of phase screen generation and Fresnel propagation is thoroughly tested to ensure that the simulated turbulence profiles generate the expected scintillation index. This was tested by generating an atmosphere comprised of one turbulent layer at 10 km characterised by an $r_0 = 0.1$ m, and moving with wind speed 5 ms^{-1}. The same atmosphere was tested over a range of telescope aperture sizes to ensure the scintillation index agrees with the theoretical scintillation index.

Fig. 2.7 and Fig. 2.8 show the results of this investigation for a short exposure time of 0.01 s and a long exposure time of 1 s respectively. The theoretical scintillation

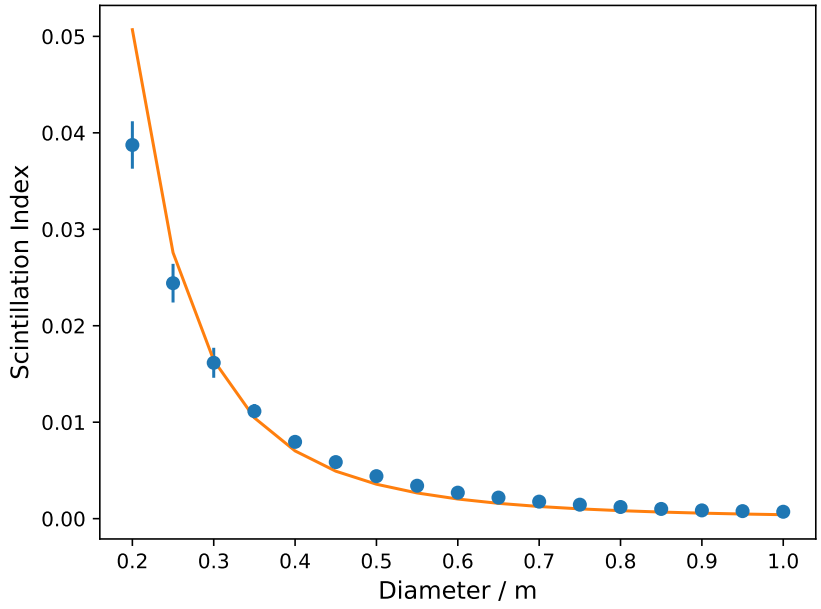

Figure 2.7: The scintillation index measured against telescope aperture size for 0.01 s exposure plotted with the theoretical curve.

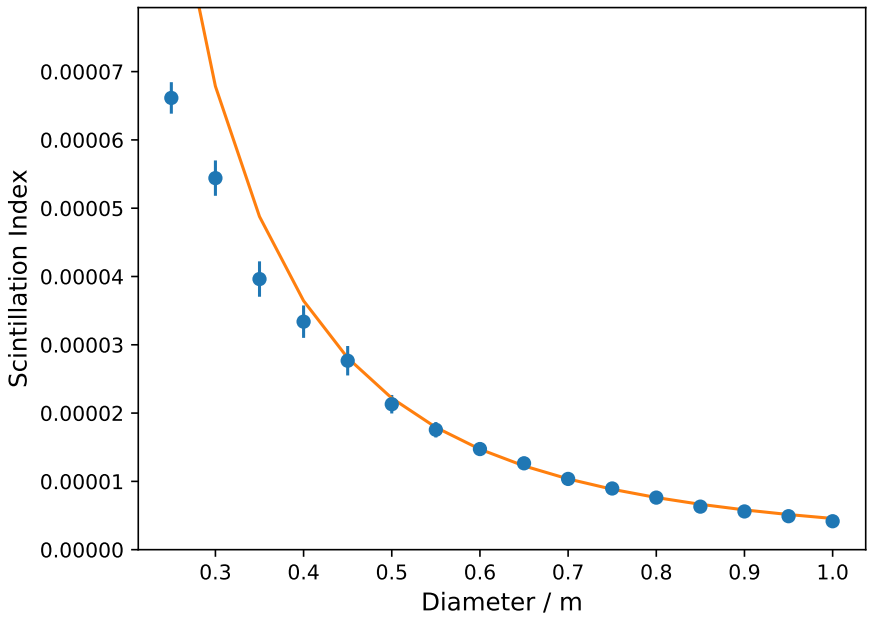

Figure 2.8: The scintillation index measured against telescope aperture size for 1 s exposure plotted with the theoretical curve.

index is plotted using equations 2.19 and 2.20 respectively. There is a close match for large telescope apertures. For small apertures, the simulated scintillation index and the theoretical scintillation index deviate. This is because the theoretical scintillation index equations 2.19 and 2.20 are true for the case where $D >> r_f$. For a 10 km layer in the visible, $r_f = 7.4$ cm and hence, for the small telescope apertures, the theoretical equations are not accurate in these cases. As the aperture size increases and tends to $D >> r_f$, the measured scintillation indices follow the theoretical curves. Therefore, it can be concluded that the simulation is consistent with the theory.

2.3 Photometry and Signal-to-Noise Ratio

2.3.1 Aperture Photometry

Aperture photometry is a standard method used to perform photometry on astronomical images. A circular aperture is centred on the source and the total flux within this aperture is integrated. An annulus is placed around the source in order to estimate the local background signal. To correct the background, the measured median background signal is then multiplied by the number of pixels in the central source aperture, and removed from the integrated source signal. Between frames, the star position can move due to atmospheric effects and telescope shake. Therefore, for each frame, the star is re-centred using a centroiding technique.

In crowded fields, this technique is more challenging, as the light from background stars can contaminate the aperture and annulus measurements. In addition, the measured centroid location can be skewed by the presence of other stars. These effects can be reduced by masking background stars.

In the process of performing aperture photometry, multiple sources of noise are induced, including both random noise fluctuations and systematic noise. These noise sources are discussed in the following two subsections.

2.3.2 CCD Equation

There are four main sources of photometric noise that are uncorrelated in both angle and time. These are:

- Photon noise, also known as shot noise, is the inherent noise due to the quantised nature of light and depends on the magnitude of the star. Photon detection can be considered as independent events that follow a random temporal distribution. As such, the number of photon counts detected have a random Poisson distribution (Hasinoff, 2014). The number of photons detected by a detector, N, over an exposure time, t, therefore has a probability distribution of:

$$P(N = k) = \frac{e^{-\lambda t}(\lambda t)^k}{k!} \tag{2.27}$$

  where λ is the expected number of photons per unit time interval. As such, for a signal level of N, the associated error is given by $\sqrt{N}$. Since the number of photons measured is proportional to the exposure time used, the noise scales as $1/\sqrt{t}$. Hence, as exposure time increases, the relative shot noise decreases. Photon noise is dominant for targets in the magnitude range in which the stars are not bright enough to be scintillation limited, but that are not faint enough to be dominated by background and readout noise (Mary, D. L., 2006) (i.e. photon noise dominates for $V \approx 10 - 15$). For example, under the condition outlined in Fig. 2.9 for a 0.5 m telescope, photon noise is the dominant noise source between $V \approx 11 - 14$, after which the readout noise becomes significant.

- Sky background is the background light from other sources measured in mags/arcsec^2. Sky background noise is the shot noise from this background light. The most significant source of sky background is from airglow - produced when the atoms and molecules in the Earth's atmosphere become excited and emit light. This source contributes approximately 65% to the sky

brightness. In addition, it is a significant problem for observations in the near-IR which is dominated by vibrationally excited OH molecules. This source of sky background is unavoidable for ground-based astronomy. However, the most obvious source of sky background noise is the Moon. Light from the sun is reflected by the moon and then scattered by the Earth's atmosphere. Sky background is thus much higher when there is a full moon compared with a new moon. For example, for La Palma on a moonless night at Zenith, V = 21.9 mags/arcsec^2 and on a full moon night V = 17.9 mags/arcsec^2 (Benn and Ellison, 1998). Background light can also come from the glow from cities and from zodiacal light.

- Readout noise is a source of noise induced by reading out from an array detector, such as a Charged Coupled Device (CCD) detector. It is a combination of noise in the conversion of charge into voltage and of noise in the amplification electronics that convert the signal from analogue to digital. This noise source is always present and is signal independent. It is independent of the integration time used, however it is strongly dependent on the pixel rate (Dussault and Hoess, 2004). This noise follows Gaussian statistics. It is characterised by a variance of σ_r^2 in each pixel. The readout noise contribution in a photometric observation is therefore dependent on the number of pixels used in the aperture photometry.

- Dark current is a source of noise due to the variation in the number of electrons thermally generated in the CCD detector silicon structure (Dussault and Hoess, 2004). Dark noise also follows Poisson statistics, and is equal to the square root of the number of thermally excited electrons. As such, this noise source can be significantly reduced by cooling the CCD.

The total photometric Signal-to-Noise Ratio (SNR) measured using a CCD (or Complementary metal-oxide-semiconductor (CMOS)) detector is given by the CCD equation.

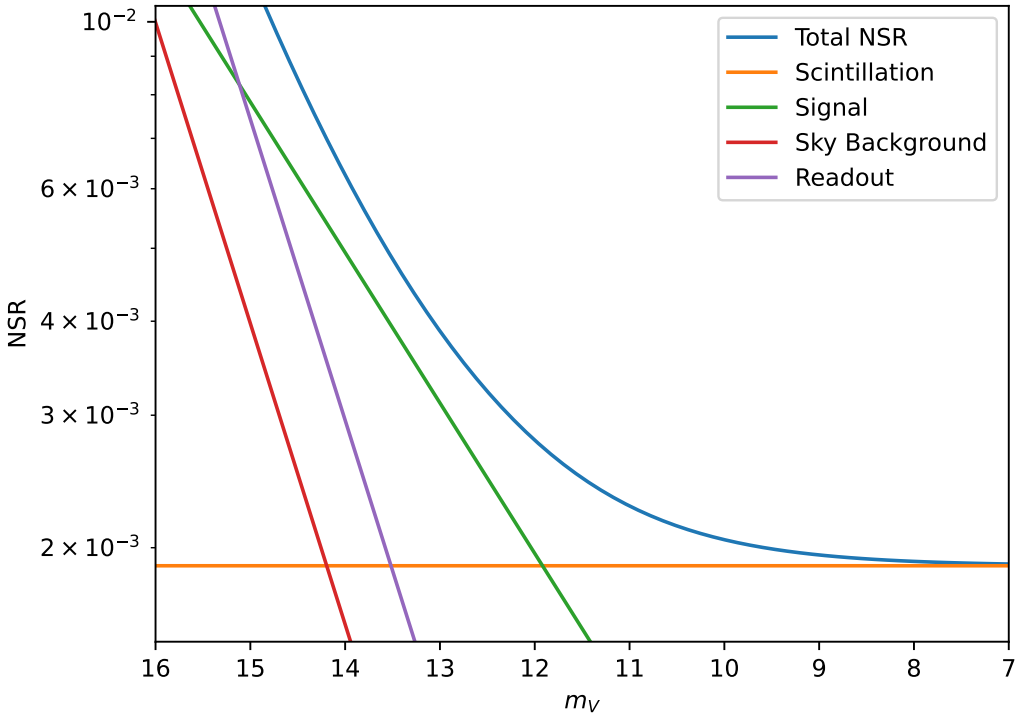

Figure 2.9: The noise contributions to the NSR as a function of the target magnitude for a 0.5 m robotic telescope in La Palma, Spain, in the V band assuming typical atmospheric conditions and a first or third quarter moon with a 10 s exposure time.

The CCD equation is given by (Howell, 1989):

$$SNR = \frac{S_*}{\sqrt{S_* + n_{pix}(\sigma_r^2 + B + D)}} , \tag{2.28}$$

where S_* is the source signal, n_{pix} is the number of pixels in the photometric aperture, σ_r is the readout noise, B is the sky background signal and D is the detector dark current. The Noise-to-Signal ratio (NSR) is given by $1/SNR$.

This equation does not include the effect of scintillation noise which must be added in quadrature. The total noise in the photometry, σ, is then given by:

$$\sigma = \sqrt{(NSR)^2 + \sigma_I^2}. \tag{2.29}$$

Figure 2.9 shows the relative noise contributions to the NSR as a function of the target magnitude. The plot was made for the Pt5m telescope (Hardy et al., 2015), a 0.5 m robotic telescope in La Palma, Spain, in the V band assuming typical

atmospheric conditions and a first or third quarter moon with a 10 s exposure time. Scintillation noise is clearly dominant for bright stars below $V \approx 10$.

2.3.3 Systematic noise

In addition to random, 'white' noise, astronomical aperture photometry is also subject to systematic or 'red' noise. Systematic noise severely limits ground-based exoplanet transit detections (Pont et al., 2006). There are multiple sources for such systematic noise, both due to atmospheric and instrumental effects. These include changes in airmass during the observation, atmospheric transparency variations, temperature variations across the CCD, telescope tracking and optical irregularities across the field such as dust in the imaging optics.

Whilst instrumental systematic noise can be avoided as much as possible by keeping the target on the same pixels throughout the observation, systematic noise produced by the Earth's atmosphere is harder to correct.

As starlight passes through the Earth's atmosphere, molecular absorption and scattering from molecules and aerosols attenuate the incoming light (Zou et al., 2010). Such transparency variations have a power spectrum proportional to $1/f$ (Young et al., 1991) where f is the temporal frequency.

From Hill et al. (1994), the average atmospheric transparency variations have a power spectrum given by:

$$log(P(\nu)) = -8.59 - 1.19\log(f). \tag{2.30}$$

Here the coefficients were determined empirically from observations at the Observatorio del Teide, Tenerife. It should be noted that the measurements of this power spectrum were taken during the day for solar studies. It is unclear if the transparency variations would have the same power at night since aerosol inhomogeneities are much weaker (Young et al., 1991), but it is assumed that it will follow the same linear relationship with the log frequency.

Whilst, on average, the power spectrum of the transparency variations follow Eq. 2.30, on a given night the atmospheric transparency variations could be significantly higher or lower. In addition, the measured transparency can also vary seasonally (Zou et al., 2010). There is also dependence of the transmission on wavelength (Buton et al., 2013). Following Mann et al. (2011), it is assumed that a scaling factor can be applied to Eq. 2.30 to estimate the power spectrum for the waveband used.

2.3.4 Differential Photometry

Stars vary in brightness both due to intrinsic and extrinsic causes. These extrinsic variations in magnitude are caused by external phenomena such as clouds, seeing, atmospheric transparency variations and systematic instrumental effects (Milone and Sterken, 2011) as described above. In order to measure intrinsic variations in the brightness of an astronomical source, one needs to distinguish between the two.

Differential photometry is a technique that has been used for over a century (Stebbins, 1910) to correct for these extrinsic variations in magnitude (Howell and Jacoby, 1986). The premise is to measure the difference in brightness of an astronomical source when compared with one or more non-varying reference sources.

For photometry on array detectors such as CCDs, the reference stars, also known as comparison stars, are often observed simultaneously in the same frame. This allows correction of any atmospheric effects that change with time. From this, any inherent changes in magnitude of the astronomical source can be determined. When properly applied, differential photometry techniques can obtain high accuracies with errors as low as ± 0.001 magnitude (Howell, 2006), (Southworth et al., 2009).

Whilst using differential photometry does correct systematic trends in the target light curve, the process itself can also induce some small scale systematic effects such as first-order and second-order atmospheric extinction.

First-order atmospheric extinction is caused by the non-negligible difference in

airmass between the target and comparison star. For long observations, lasting several hours, the differential airmass will change (Mann et al., 2011). This results in the addition of a systematic trend to the calibrated light curve. To minimise this effect, comparison stars close to the target of interest should be chosen.

Second-order extinction is an additional source of systematic trend, caused by the difference in the spectral energy distribution over the pass-band between the target star and comparison star (Young et al., 1991). This effect is proportional to $\Delta\lambda^2$ and depends on the reddening of the Earth's atmosphere. As such, it changes from night to night. This can be minimised by selecting comparison stars close in colour to the target star.

In addition, comparison stars can only be used to correct systematic trends that are correlated with the target star. Flat fields can be used to correct field-dependent anomalies in the telescope optics and reduce effects of vignetting and pixel-to-pixel sensitivity variations. In addition, ensuring that the target image is always centred on the same pixels can reduce instrumental systematic trends.

2.4 Tomographic Wavefront Sensing

Tomography is a 3D imaging technique which can be used to profile a volume. A classic example of this technique is a Computerized Tomography (CT) scan, which is used in medicine to build a 3D image of the body by combining a series of X-ray images taken from different angles.

Tomographic reconstruction in Adaptive Optics (AO) was first proposed by Tallon and Foy in 1990 (Tallon and Foy, 1990). Their proposition was to use the light from several guide stars to probe the instantaneous 3D phase perturbations in the atmosphere and to reconstruct the turbulent volume by solving an inverse problem.

Several adaptive optics methods that use tomography to correct image distortions are currently being developed including Multi Object AO (MOAO) (Gendron et al.,

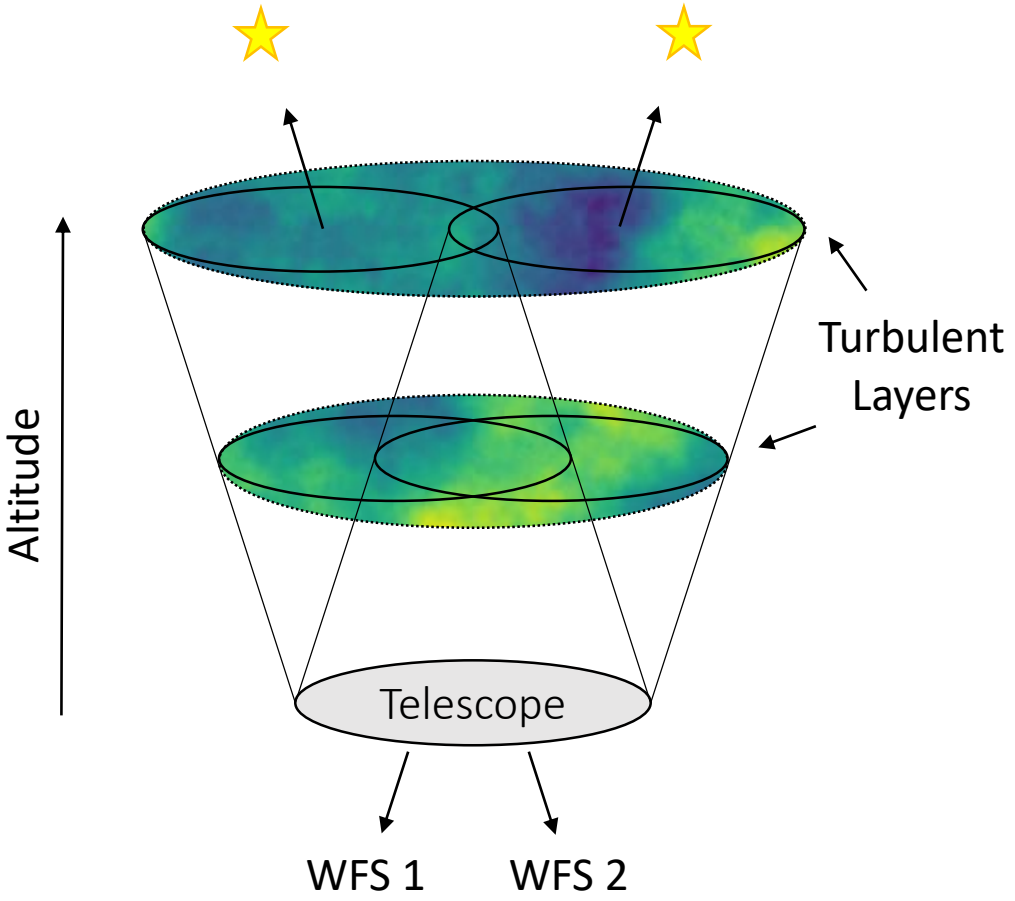

Figure 2.10: A schematic showing the concept of MCAO. Multiple WFS probe the turbulent atmosphere, and a DM is conjugated to each turbulent layer.

2005), Laser Tomography AO (LTAO) (Fusco et al., 2010) and Multi-Conjugate AO (MCAO) (Rigaut and Neichel, 2018).

2.4.1 Tomographic Algorithm

MCAO was initially proposed by Beckers (1988) to increase the field of view of AO systems. It works by stacking several Deformable Mirrors (DMs) in a series, each of which is optically conjugated to a particular altitude in the turbulent volume. A tomographic reconstruction algorithm is used to produce a 3D model of the turbulent volume above the telescope from the WFS measurements. The AO correction for each layer can then be applied to its respective DM. See Fig. 2.10 for a schem-

atic demonstrating this technique. This 3D model of the phase aberrations can also then be used to correct for scintillation noise. This is done by propagating the reconstructed phase numerically to the ground to produce an estimate for the scintillation pattern.

The MCAO tomographic algorithm described here was developed by Fusco et al. (2001) and uses a minimum-mean-square-error estimator that minimises the mean residual phase variance in the FOV of interest. The basis of this model is outlined as follows.

The atmosphere can be modelled as a discrete sum of turbulent layers located at different heights (Roddier, 1981). Hence, the total optical phase aberration seen across the telescope pupil for angular vector direction $\boldsymbol{\alpha}$ in the near field approximation can be given as:

$$\Phi(\boldsymbol{r}, \boldsymbol{\alpha}) = \sum_{j=1}^{N_t} \phi_j(\boldsymbol{r} + h_j \boldsymbol{\alpha}), \tag{2.31}$$

where $\boldsymbol{r}$ is the pupil coordinate, N_t is the number of turbulent layers and h_j is the height of the j^{th} layer.

The wavefront sensor measurements are assumed to be perfect, except for an additional error term due to shot noise. For a wavefront sensor observing in direction $\boldsymbol{\alpha_i}$, the measured phase is then given by:

$$\Phi^m(\boldsymbol{r}, \boldsymbol{\alpha_i}) = \sum_{j=1}^{N_t} \phi_j(\boldsymbol{r} + h_j \boldsymbol{\alpha_i}) + n_i(\boldsymbol{r}), \tag{2.32}$$

where $n_i(\boldsymbol{r})$ is the noise in the WFS measurement, which is assumed to have a Poisson distribution. The reconstructed phase for an arbitrary direction $\boldsymbol{\alpha}$ is then given by:

$$\hat{\Phi}(\boldsymbol{r}, \boldsymbol{\alpha}) = \sum_{k=1}^{N_{DM}} \hat{\phi}_k(\boldsymbol{r} + h_k \boldsymbol{\alpha}), \tag{2.33}$$

where h_k are the altitudes of the conjugated DMs.

These equations can be rewritten in matrix form as:

$$\Phi(\boldsymbol{r}, \boldsymbol{\alpha}) = \boldsymbol{M}_{\alpha}^{N_t} \boldsymbol{\phi}, \tag{2.34}$$

$$\Phi^m(\boldsymbol{r}, \boldsymbol{\alpha_i}) = \boldsymbol{M}_{\alpha_i}^{N_t} \boldsymbol{\phi} + n_i, \tag{2.35}$$

$$\hat{\Phi}(\boldsymbol{r}, \boldsymbol{\alpha}) = \boldsymbol{M}_{\alpha}^{N_{DM}} \hat{\boldsymbol{\phi}}, \tag{2.36}$$

where $\boldsymbol{\phi}$ is a vector of phase aberrations induced at each height, $\hat{\boldsymbol{\phi}}$ is a vector of the reconstructed phase at each height and where $\boldsymbol{M}_{\alpha_i}^{N_t}$, $\boldsymbol{M}_{\alpha_i}^{N_{DM}}$ are the respective matrices that perform the sum of these vectors.

The phase estimator to be minimised is the averaged quadratic difference between the reconstructed phase and the true phase over the FOV, $\boldsymbol{\alpha}_{FOV}$:

$$\epsilon = \left\langle \int_{\boldsymbol{\alpha}_{FOV}} \left\| \hat{\Phi}(\boldsymbol{r}, \boldsymbol{\alpha}) - \Phi(\boldsymbol{r}, \boldsymbol{\alpha}) \right\|^2 d\boldsymbol{\alpha} \right\rangle_{\Phi, noise}, \tag{2.37}$$

where $\langle \cdot \rangle_{\Phi, noise}$ represents a mathematical expectation on both turbulence and WFS noise outcomes.

Using the matrix forms given above, the equation to be minimised is:

$$\epsilon = \left\langle \int_{\boldsymbol{\alpha}_{FOV}} \left\| \boldsymbol{M}_{\alpha}^{N_{DM}} \hat{\boldsymbol{\phi}} - \boldsymbol{M}_{\alpha_i}^{N_t} \boldsymbol{\phi} \right\|^2 d\boldsymbol{\alpha} \right\rangle_{\Phi, noise}. \tag{2.38}$$

The reconstruction matrix is the matrix, $\boldsymbol{W}$, that fulfils the following equation:

$$\hat{\boldsymbol{\phi}} = \boldsymbol{W} \boldsymbol{\Phi}^m. \tag{2.39}$$

Using Eq. 2.35 and then substituting Eq. 2.39 into Eq. 2.38 gives:

$$\epsilon = \left\langle \int_{\alpha_{FOV}} \left\| \boldsymbol{M}_{\alpha}^{N_{DM}} (\boldsymbol{W} \boldsymbol{M}_{\alpha_i}^{N_t} \boldsymbol{\phi} + \boldsymbol{W} \boldsymbol{n}) - \boldsymbol{M}_{\alpha_i}^{N_t} \boldsymbol{\phi} \right\|^2 d\boldsymbol{\alpha} \right\rangle_{\Phi, noise}. \tag{2.40}$$

This is minimised with respect to $\boldsymbol{W}$ to give:

$$\begin{aligned} \boldsymbol{W} = \left[\int_{\alpha_{FOV}} (\boldsymbol{M}_{\alpha}^{N_{DM}})^T \boldsymbol{M}_{\alpha}^{N_{DM}} d\boldsymbol{\alpha} \right]^+ \times \left[\int_{\alpha_{FOV}} (\boldsymbol{M}_{\alpha}^{N_{DM}})^T \boldsymbol{M}_{\alpha}^{N_t} d\boldsymbol{\alpha} \right] \\ \times \boldsymbol{C}_{\boldsymbol{\phi}} (\boldsymbol{M}_{N_{GS}}^{N_t})^T [\boldsymbol{M}_{N_{GS}}^{N_t} \boldsymbol{C}_{\boldsymbol{\phi}} (\boldsymbol{M}_{N_{GS}}^{N_t})^T + \boldsymbol{C}_{\boldsymbol{n}}]^{-1}, \end{aligned} \tag{2.41}$$

where $+$ and T denotes the generalised pseudo inverse and the transpose respectively and where $\boldsymbol{C}_{\boldsymbol{\phi}}$ and $\boldsymbol{C}_{\boldsymbol{n}}$ are the turbulence (Noll, 1976) and noise covariance matrices (Rigaut and Gendron, 1992).

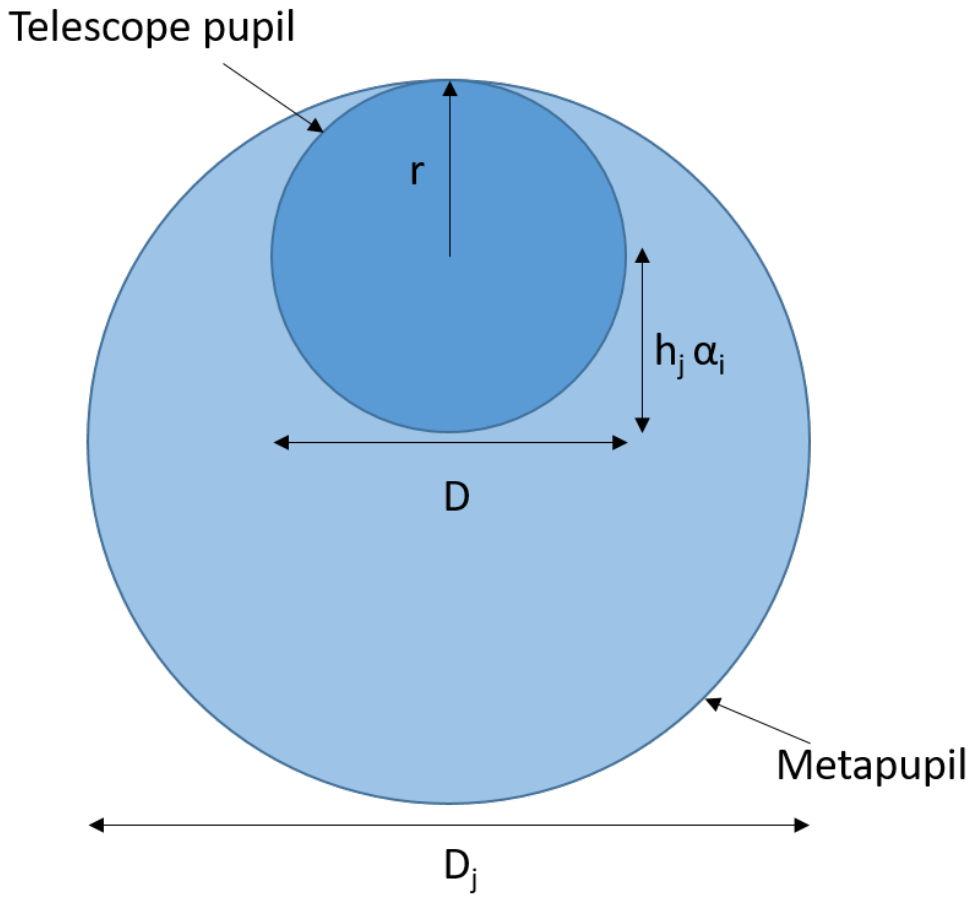

Figure 2.11: A schematic showing the de-centered part of the meta-pupil at altitude h_j seen by the WFS in direction $\boldsymbol{\alpha_i}$.

If $\boldsymbol{M}_{\alpha}^{N_{DM}} = \boldsymbol{M}_{\alpha}^{N_t}$, such that the DMs are exactly conjugated to the individual turbulent layers, $\boldsymbol{W}$ is simplified to:

$$\boldsymbol{W}_{N_{\mathrm{DM}}=N_t} = \boldsymbol{C_\phi}(\boldsymbol{M}_{N_{\mathrm{GS}}}^{N_t})^{\mathrm{T}}[\boldsymbol{M}_{N_{\mathrm{GS}}}^{N_t}\boldsymbol{C_\phi}(\boldsymbol{M}_{N_{\mathrm{GS}}}^{N_t})^{\mathrm{T}} + \boldsymbol{C_n}]^{-1}. \tag{2.42}$$

The MCAO algorithm can be performed in a range of different bases set, the most common of which being the Zernike basis. In the Zernike basis, $\boldsymbol{\phi}$ and $\hat{\boldsymbol{\phi}}$ are simply vectors of Zernike coefficients. $\boldsymbol{C_\phi}$ is the Zernike Kolmogorov turbulence covariance matrix given by Noll (1976) and $\boldsymbol{C_n}$ is the noise covariance matrix given by Rigaut and Gendron (1992). $\boldsymbol{M}_{\alpha}^{N_t}$ is a matrix that consists of the decomposition of the de-centered Zernike polynomials $[Z_{l,j}(\boldsymbol{r} + h_j\boldsymbol{\alpha})]$ on to a Zernike basis defined on

the telescope pupil (see Fig. 2.11). A full description of this matrix is given by Ragazzoni et al. (1999).

In this thesis, a model approximation is used in which it is assumed that all the turbulent layers are perfectly conjugated with the DMs. In this case, the turbulence profile is modelled by a small number of turbulent layers called Equivalent Layers (ELs). The EL positions and strengths are calculated by sampling of the $C_n^2(h)$ profile into N_{EL} slabs. Using this simplified turbulence model, all the equations remain valid, with N_t and N_{DM} replaced by N_{EL} . In this case, the reconstruction matrix is given by:

$$\boldsymbol{W_{MA}} = \boldsymbol{C_\phi}(\boldsymbol{M}_{N_{\mathrm{GS}}}^{N_{\mathrm{EL}}})^{\mathrm{T}}[\boldsymbol{M}_{N_{\mathrm{GS}}}^{N_{\mathrm{EL}}}\boldsymbol{C_\phi}(\boldsymbol{M}_{N_{\mathrm{GS}}}^{N_{\mathrm{EL}}})^{\mathrm{T}} + \boldsymbol{C_n}]^{-1}. \tag{2.43}$$

If it is assumed that the atmospheric turbulence follows Kolmogorov statistics, then $\boldsymbol{C_\phi}$ is a generalisation of the Kolmogorov turbulence covariance matrix such that (Fusco et al., 2001):

$$\boldsymbol{C_\phi} = \begin{pmatrix} \langle \phi_1, \phi_1^T \rangle & 0 & 0 & 0 & 0 \\ 0 & \ddots & 0 & 0 & 0 \\ 0 & 0 & \langle \phi_j, \phi_j^T \rangle & 0 & 0 \\ 0 & 0 & 0 & \ddots & 0 \\ 0 & 0 & 0 & 0 & \langle \phi_{N_t}, \phi_{N_t}^T \rangle \end{pmatrix} \tag{2.44}$$

where $\langle \phi_j, \phi_j^T \rangle$ is the Kolmogorov covariance matrix for the jth layer given by Noll Noll (1976).

$\boldsymbol{C_{\mathbf{n}}}$ is a generalisation of the noise covariance matrix such that (Fusco et al., 2001):

$$\boldsymbol{C_{\mathbf{n}}} = \begin{pmatrix} \langle \boldsymbol{n_1}, \boldsymbol{n_1}^T \rangle & 0 & 0 & 0 & 0 \\ 0 & \ddots & 0 & 0 & 0 \\ 0 & 0 & \langle \boldsymbol{n_i}, \boldsymbol{n_i}^T \rangle & 0 & 0 \\ 0 & 0 & 0 & \ddots & 0 \\ 0 & 0 & 0 & 0 & \langle \boldsymbol{n_{NGS}}, \boldsymbol{n_{NGS}}^T \rangle \end{pmatrix} \tag{2.45}$$

where $\langle \boldsymbol{n_i}, \boldsymbol{n_i}^T \rangle$ is the noise covariance matrix for the *ith* GS.

The noise covariance matrix for each guide star is given by:

$$\langle \boldsymbol{n_i}, \boldsymbol{n_i}^T \rangle = (\boldsymbol{D}^T \boldsymbol{D})^{-1} \sigma_{m_i} \tag{2.46}$$

where $(\boldsymbol{D}^T \boldsymbol{D})^{-1}_{ij} = \pi \sum_{k=1}^{min(i,j)} \gamma^x_{ik} \gamma^x_{jk} + \gamma^y_{ik} \gamma^y_{jk}$ which describes the noise on the Zernike coefficients where $\gamma_{j,j'}$ are the gamma matrices given by Noll (1976) and σ_{m_i} is the WFS noise measurement (Rigaut and Gendron, 1992).

The WFS noise measurement is assumed to be shot noise dominated and is given, in radians, by Rigaut and Gendron (1992):

$$\sigma^2_m = \left(\frac{\lambda_{ws}}{\lambda}\right)^2 \frac{1}{d^2} \frac{2\pi}{N_{ph}}, \tag{2.47}$$

for $d < r_{0_{ws}}$, where d is the subaperture diameter, λ_{ws} is the WFS wavelength, λ is the science wavelength and N_{ph} is the number of detected photons per square meter per exposure.

For $d \geq r_{0_{ws}}$ the WFS noise measurement is given by:

$$\sigma^2_m = \left(\frac{\lambda_{ws}}{\lambda}\right)^2 \frac{1}{r^2_{0_{ws}}} \frac{2\pi}{N_{ph}}, \tag{2.48}$$

where $r_{0_{ws}}$ is the Fried parameter for λ_{ws}.

2.4.2 Limitations of MCAO

One of the biggest limitations of MCAO is its sky coverage. MCAO requires at least three bright guide stars within a FOV of a couple of arcminutes in diameter. To correct scintillation the high turbulent layers needs to be sufficiently reconstructed and hence the WFS observations must overlap at high altitudes, further limiting sky coverage.

The MAD project which used Natural Guide Stars (NGS) identified 50–100 scientifically interesting objects which could be observed with MCAO and almost all of these were close to the Galactic Plane (Marchetti et al., 2007). Therefore, the sky coverage is extremely limited.

The most effective solution is to use LGS. However, even with the use of LGS, some NGS are still required to measure the tip-tilt due to the tip-tilt indetermination problem. This occurs because the LGS measures the same turbulence on the uplink as when the light returns, meaning an equal and opposite tilt is applied and therefore cancels out, making it impossible to measure (Rigaut and Gendron, 1992). The NGS required to compensate for tip/tilt indetermination can be much fainter as they are only needed to measure the global tip-tilt over the whole telescope aperture. LGS also suffer from focal anisoplanatism which would need to be considered in the optimisation. This effect is described in detail in 3.5.1.

Another limitation of the tomographic reconstructor is that it assumes Kolmogorov statistics, in which the outer scale of turbulence is assumed to be infinite and therefore can be ignored. However, for large telescopes, its effects could become significant. It has been observed that for large telescopes (8-10 m) the outer scale will reduce the scintillation (Osborn et al., 2015). Therefore, the estimated scintillation noise predicted from the MCAO reconstructor may be overestimated for large telescopes, thus incorrectly calibrating the intensity.

MCAO is also limited by several sources of error. These include the generalised fitting error, the tomographic error and the aliasing error (Rigaut and Neichel, 2018).

The fitting error is due to the fact that only a finite number of turbulent layers are being corrected. For a DM conjugated at height h, any distortion at a height of $h + \delta h$ will be blurred by a size of θh where θ is the angle between the guide stars. As the vertical distance between the DM and a turbulent layer increases, fewer and fewer high spatial frequencies can be corrected in the layer.

The tomographic error is due to the fact that some parts of the turbulent volume are only being probed by one guide star. This limits the tomography since, where there is no overlap, the reconstructor cannot determine at which height the phase perturbation is located. Another fundamental limitation comes from modes which

are 'unseen'. These are modes that when combined over multiple layers get cancelled out and so are not seen by the WFS. This can lead to serious problems in the scintillation correction, as the estimated intensity pattern will be inaccurate. Using inaccurate estimates to calibrate the uncorrected intensity could end up inducing more noise into the light curve.

The aliasing error in AO is caused by the fact that high-order aberrations are seen by a WFS as a low-order aberration. In tomography, aliasing is also caused by the fact that any layer above the highest conjugated DM will be seen by the WFSs and wrongly interpreted as layers inside the volume considered. This creates an additional error called a generalized aliasing error (Rigaut and Neichel, 2018).

Despite these limitations it has been shown that, for a true atmospheric profile, only a small number of layers (2 or 3) are required to obtain an accurate reconstruction of the phase in the whole field of view. Furthermore, it has been found that only three guide stars are needed to obtain good performance (Fusco et al., 1999).

2.5 Wavefront Sensors

2.5.1 Shack Hartmann Wavefront Sensors

An important component for AO is the wavefront sensor. In astronomy, the light source is often either an NGS or LGS. The WFS must therefore be suitable for incoherent light sources. In the case of NGS, being able to use faint sources is favourable and therefore the WFS must have a high photon efficiency.

The Shack Hartmann wavefront sensor (SHWFS) is a wavefront sensor commonly used in AO. A SHWFS is composed of an array of lenses, each with the same focal length, focused onto an array detector (often a CCD), which produces a grid of spots with a regular separation corresponding to the array of subapertures (Platt and Shack, 2001). For a uniform illumination, if the sensor is placed at the geometric focal plane of the lenslet, the integrated gradient of the wavefront across

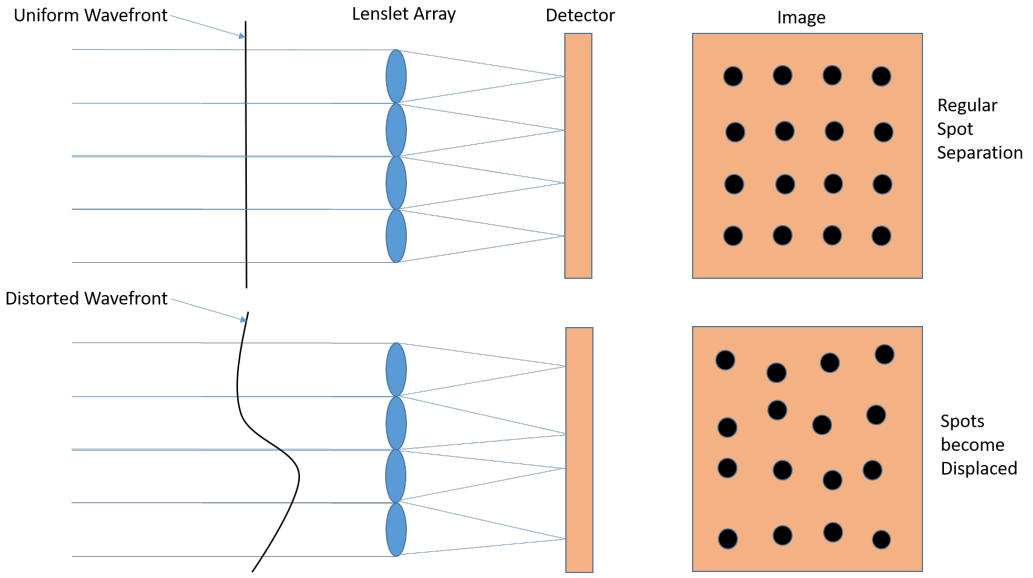

Figure 2.12: A schematic showing the principles of a SHWFS. An array of lenslets samples the wavefront. The phase aberration is reconstructed from a set of local phase gradient measurements.

the lenslet is proportional to the displacement of the centroid. Consequently, any phase aberration can be reconstructed from a set of local phase gradient measurements. This is demonstrated in Fig. 2.12. By sampling the wavefront with an array of lenslets, all of these local tilts can be measured and the whole wavefront reconstructed.

2.5.2 Centre of Gravity

To measure the displacement of the SHWFS spots, a centroiding method must be used. The most common technique is a Centre of Gravity (CoG) centroid algorithm. For each subaperture, the CoG is calculated with the following equation:

$$x = \frac{\sum_{i,j} x_{i,j} I_{i,j}}{\sum_{i,j} I_{i,j}}, \quad y = \frac{\sum_{i,j} y_{i,j} I_{i,j}}{\sum_{i,j} I_{i,j}}, \tag{2.49}$$

where $I_{i,j}$ is the intensities of light on the detector pixels. The main disadvantage of this method is that it is very sensitive to high background noise. This can be improved by thresholding the subaperture spot image to remove the background. A

threshold is set such that all pixels with values below the threshold are set to zero. The amount of thresholding is an additional parameter that must be optimised.

2.5.3 Zernike Decomposition

The MCAO tomographic reconstruction requires the WFS measurements to be returned as Zernike coefficients. Therefore, the WFS spot measurements must be converted to the Zernike basis. This requires a modal decomposition method.

A distorted wavefront in the pupil plane can be expanded onto a sum of orthogonal basis functions such as the Zernike polynomials $\{Z_i\}$ as:

$$\phi(Rr) = \sum_{i=2}^{\infty} a_i Z_i(r), \tag{2.50}$$

where R is the telescope radius, r is the position vector in polar coordinates and a_i are the coefficients.

A Shack-Hartmann wavefront sensor works by dividing the pupil into k subapertures. The gradient of the wavefront at each subaperture is returned using a centroiding algorithm. Taking the derivatives in x and y for each side in equation (2.50) and averaging in each subaperture gives:

$$\left.\frac{\partial \phi(Rr)}{\partial x}\right|_l = \sum_{i=2}^{\infty} a_i \left.\frac{\partial Z_i(r)}{\partial x}\right|_l, \tag{2.51}$$

$$\left.\frac{\partial \phi(Rr)}{\partial y}\right|_l = \sum_{i=2}^{\infty} a_i \left.\frac{\partial Z_i(r)}{\partial y}\right|_l, \tag{2.52}$$

where $l = 1, 2, ...k$ (ming Dai, 1996). The derivatives of Noll normalised Zernike polynomials are given by Noll (1976):

$$\frac{\partial Z_i(r)}{\partial x} = \sum_{j'} {\gamma^x}_{jj'} Z_{j'}, \tag{2.53}$$

$$\frac{\partial Z_i(r)}{\partial y} = \sum_{j'} {\gamma^y}_{jj'} Z_{j'}, \tag{2.54}$$

where ${\gamma^x}_{jj'}$ and ${\gamma^y}_{jj'}$ are matrices defined in Noll (1975).

Equations (2.51) and (2.52) can be rewritten in matrix form as:

$$\boldsymbol{S} = \boldsymbol{G}\boldsymbol{A}, \tag{2.55}$$

where $\boldsymbol{S}$ is a vector of the wavefront sensor slopes in x and y, $\boldsymbol{A}$ is a vector of the Zernike coefficients and $\boldsymbol{G}$ is a matrix that contains the average gradients of Zernike functions in each subaperture (ming Dai, 1996). This can be rearranged to give the Zernike coefficients:

$$\boldsymbol{A} = \boldsymbol{G}^{+}\boldsymbol{S}, \tag{2.56}$$

where $\boldsymbol{G}^{+} = (\boldsymbol{G}^{\boldsymbol{T}}\boldsymbol{G})^{-1}\boldsymbol{G}^{\boldsymbol{T}}$ is the inverse of $\boldsymbol{G}$. When $(\boldsymbol{G}^{\boldsymbol{T}}\boldsymbol{G})^{-1}$ is singular, singular-value decomposition (SVD) is used to invert $\boldsymbol{G}$.

In order to perform the SVD, the maximum number of modes that can be obtained from the slopes is limited to the number of subapertures used. In practice, fewer modes can be accurately measured. This is due to cross coupling and aliasing of the higher order Zernike modes.

Chapter 3

A Scintillation Correction Technique using Tomographic Wavefront Sensing: Simulation

3.1 Introduction

High precision ground-based time-resolved photometry is vital for a range of studies that look for small intrinsic variations in the intensity of astronomical sources. These include observations of exoplanet transits, variable stars and stellar seismology. However, such observations can be significantly limited by the effects of the Earth's atmosphere.

As the light from an astronomical source passes through the atmosphere, high altitude regions of optical turbulence induce wavefront aberrations, which then propagate to produce spatial intensity fluctuations across the telescope pupil. These spatial intensity patterns change over time as the turbulence evolves and translates with the wind (Dravins et al., 1997a). This results in photometric noise known as scintillation, which can be seen by the naked eye as the twinkling of the stars. For time-resolved photometry on large telescopes, these intensity variations can be on the scale of $\sim 0.1\%$ to $\sim 1\%$ (Osborn et al., 2015) averaged over exposures of a

few seconds. This significantly limits the ability to measure intrinsic variations of bright objects on short time-scales.

For bright stars, where scintillation is the dominant noise source, the observations are scintillation limited (Föhring et al., 2015). Hence, if this noise can be corrected, substantially higher precision ground-based photometry could be achieved. This could greatly enhance ground-based exoplanet transit follow-up observations, such as the multi-spectral photometry of exoplanet transits used to determine the composition of the exoplanet's atmosphere (Madhusudhan et al., 2014). Atmospheric scintillation correction could also lead to new avenues of research, such as second-order Adaptive Optics for the direct imaging of exoplanets (Dravins et al., 1998).

However, correcting scintillation noise is a significant challenge. Since scintillation is produced by high altitude turbulence, the range of angles over which it is correlated is very small (Kornilov, 2012). Therefore, it cannot often be corrected directly through differential photometry, as the probability of there being a bright star within the iso-photometric angle, the angle in which the scintillation is strongly correlated, is small. This angle is often smaller than the isoplanatic angle. Several scintillation correction techniques have been proposed, including conjugate plane photometry (Osborn et al., 2011), the use of a ferroelectric liquid-crystal spatial light modulator to control the transmittance of a telescope pupil (Love and Gourlay, 1996), using the achromatic nature of scintillation (Kornilov, 2011) and differencing signals from binary stars (Ryan and Sandler, 1998), although currently no such technique is in common practice.

Osborn (2014) proposed a new scintillation correction technique for large telescopes, that uses the Wavefront Sensor (WFS) data from multiple guide stars near the astronomical source of interest to tomographically reconstruct the phase aberrations above the telescope. This 3D model of the phase aberrations can be used numerically with Fresnel propagation to produce an estimate for the scintillation pattern across the telescope pupil. This estimated scintillation pattern can then be used

to correct the measured photometric data for the fluctuations due to scintillation. The model is able to correct the scintillation in any direction within the Field of View (FOV) and at any wavelength, and thus all objects within the field can be corrected simultaneously.

A significant advantage of this proposed method is that, if desired, the numerical scintillation correction can be applied using the wavefront sensors of any existing tomographic Adaptive Optics (AO) systems without the need for any additional instrumentation. In addition, this technique can be applied entirely in post-processing and can therefore be optimised for any observation. Only the WFS data and an estimate for the turbulence profile is required to perform the scintillation correction, no real-time adaptive optical correction is needed. In addition, a separate turbulence profiler is not necessarily needed, as the turbulence profile can be estimated from the WFS telemetry data if it is performed at a high enough frame rate.

The proposed technique by Osborn (2014) required extensive testing and an on-sky demonstration. A simulation was produced in advance of an on-sky test on the Isaac Newton Telescope (INT) to model the performance of this technique, its limitations and subsequently to find a suitable target for the on-sky experiment. In this chapter, the results of this investigation are presented. The tomographic algorithm used has been described in detail in section 2.4.

Section 3.2 describes the tomographic scintillation correction method. In section 3.3 the simulation is presented, and its assumptions are discussed. The results from simulation are presented in section 3.4, including the optimisation of key observing parameters. Section 3.5 describes the negative effects of using LGS and the implementation of these in the simulation, and finally the results of simulating the 4LGS facility on the VLT are presented. A brief discussion and conclusion to the chapter is given in section 3.7.

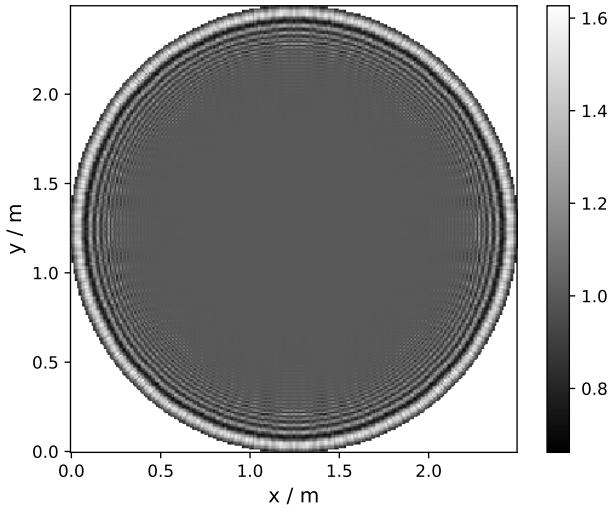

Figure 3.1: An example of the diffraction rings produced by the Fresnel propagation of a 2.5 m circular aperture over 10 km in the V band.

3.2 Scintillation Correction Method

As shown in section 2.4, if the altitudes and relative strengths of the turbulent layers above the telescope pupil are known, the WFS data from multiple guide stars can be used with a tomographic reconstruction matrix to produce a 3D model of the instantaneous phase aberrations above the telescope in the Zernike basis. These reconstructed phase aberrations can be used with Fresnel propagation to compute an estimate for the spatial intensity fluctuations across the pupil for each frame. Integrating the estimated instantaneous spatial scintillation pattern over the aperture for each frame gives the estimated intensity. This estimate of the intensity fluctuations can then be used to normalise the measured photometry.

Large metapupils at each reconstructed layer are needed for the scintillation estimation. This is due to the Fresnel propagation producing diffraction rings at the edge of the propagated pupil, as shown in Fig. 3.1. Hence, a pupil larger than the telescope aperture is used in the Fresnel propagation to produce a reconstructed scintillation pattern over a larger area from which the telescope pupil can be cut-out. This prevents the addition of significant noise from the diffraction rings at the

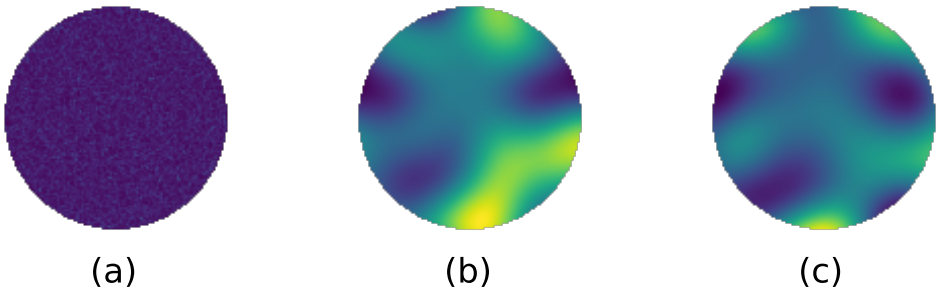

Figure 3.2: (a) A simulated scintillation pattern, (b) the low pass filtered simulated scintillation pattern and (c) the tomographically reconstructed simulated scintillation pattern.

edge of the reconstructed scintillation pattern.

Since scintillation is produced by the high altitude turbulence, only the high altitude reconstructed layers need to be propagated. Fortunately, since the metapupil size is proportional to the altitude, as shown in Fig. 2.10 and Fig. 2.11, the reconstructed layers of interest are over large metapupils.

The wavefront sensor effectively acts as a low-pass spatial filter, such that only low order phase aberrations are measured. Since the timescale of the intensity fluctuations is determined by the spatial scale and wind speed associated with the high altitude turbulence, the temporal intensity fluctuations that can be corrected depends on the spatial scales that can be reconstructed. Therefore, only the low temporal frequency intensity variations can be corrected. This is demonstrated in Fig. 3.2 which shows (a) a simulated scintillation pattern, (b) the low pass filtered simulated scintillation pattern and (c) the tomographically reconstructed simulated scintillation pattern. Comparing (a) and (c) it is not obvious that the tomographic reconstruction is accurate since the scintillation pattern in (a) is visually dominated by high spatial frequencies. However, comparing the low pass filtered scintillation pattern in (b) with the tomographically reconstructed pattern in (c), it can be seen that the tomography is accurately reconstructing the low spatial frequencies in the scintillation pattern.

The application of tomographic wavefront sensing for scintillation noise correction places different requirements on the angular separation of the stars within the asterism. This is because scintillation is produced by only high altitude turbulence. At higher altitudes, there is less overlap between the WFS measurements, as seen in Fig. 2.10. The altitude at which the guide star measurements no longer overlap is given by $h_{max} = \frac{D}{\theta}$, where D is the telescope diameter and θ is the angle between the guide stars. Hence, for scintillation correction the stars must be much closer to one another than is required for traditional AO (where the ground layer is often dominant), in order to provide good sampling of these high layers. As such, this method is better for large telescopes, for which the higher layers are better sampled. Turbulent layers above the altitude at which the WFS measurements no longer overlap will not be sampled and will add noise to the tomographic reconstruction.

Since compact asterisms are required, the sky coverage for scintillation correction using Natural Guide Stars (NGS) is severely limited, with most targets of interest not having sufficiently bright stars nearby to perform the correction. Hence, in practice this technique requires Laser Guide Stars (LGS), a technology becoming increasingly available at more telescope sites.

However, a key benefit to this method is that it can be easily applied to any existing LGS tomographic AO system. The latest large and extremely large telescopes will all be equipped with tomographic AO systems, such as the MORFEO (Ciliegi, 2021) and HARMONI (Thatte et al., 2010) for the ELT, which are ideal bases for this scintillation correction technique. The instrumentation could be setup to apply the scintillation correction in real time, or it can be applied entirely in post-processing using the WFS telemetry and the turbulence profile from WFS data. Correction in post-processing is ideal as the data reduction can be optimised for each observation and, so long as regular turbulence profiling is done, the tomographic reconstruction matrix can be updated as often as necessary.

3.3 Simulation

3.3.1 Simulation Flow Chart

To test this proposed method, a numerical Monte Carlo simulation was produced. A flow chart of this simulation is shown below.

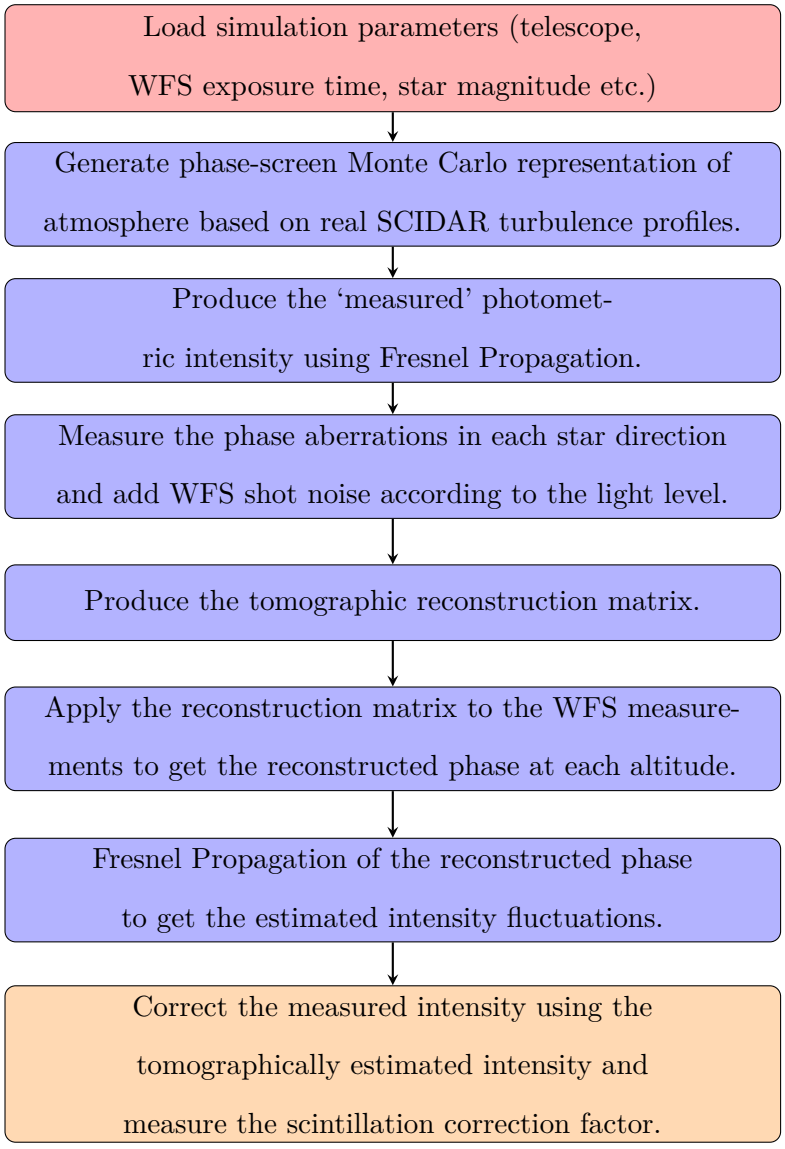

The scintillation correction factor, the factor by which the scintillation index is reduced, C_{scint}, is used to measure the performance of the method and is given by:

$$C_{\text{scint}} = \frac{\sigma_I^2}{\sigma_{|I-I_r|}^2}, \tag{3.1}$$

where I is the measured intensity and I_r is the reconstructed intensity.

3.3.2 Assumptions

Several assumptions were made in the numerical simulation, which are outlined below. All the simulations were performed in the V band unless stated otherwise.

- Taylor's frozen flow hypothesis - the turbulent layers translate with the wind and do not intrinsically evolve.
- The wavefront sensors measure the Zernike modes perfectly. The measurements are assumed to be only limited by shot noise, which is added to the measurements dependent on the light level. It is assumed the Zernike decomposition of the WFS measurements is perfect.
- The same number of Zernike modes are used in the reconstruction of each turbulent layer.
- The photometry is perfect and limited only by scintillation noise. There is no systematic noise.
- The presence of the secondary mirror and its supports are ignored.
- The atmospheric turbulence is assumed to follow Kolmogorov statistics.
- It is assumed that the atmospheric turbulence profile above the telescope pupil is measured perfectly and simultaneously.

Due to the above assumptions, the simulation results produce an upper limit for the performance that can be achieved on-sky and in practice it is likely the correction will be lower.

3.3.3 Turbulence Profiles

SCIDAR data was used in simulation to provide accurate representations of the atmosphere. The profiles used are shown in Fig. 3.3. These profiles were produced using hierarchical clustering of SCIDAR data (Farley et al., 2018) observed in 2015 on the INT, La Palma, Spain. Each profile contained 100 layers which were binned into fewer layers using the optimal grouping method. This grouping method was chosen as it has been found to produce the most accurate atmosphere models (Saxenhuber et al., 2017). The number of layers used depended on the simulation parameters, with fewer layers used for large telescope simulations to save computational time. Hence, details of the number of layers used are given in each subsection.

The wind velocity and direction information for each profile is limited due to the difficulty in measuring such parameters. Therefore, where information was limited, the wind velocity profile in Fig. 3.4 was used as an estimate for the wind velocity at each altitude. This wind velocity distribution was measured for the night of 2013 September 13, JKT, La Palma, and shows a typical wind distribution for this site.

3.4 Results

3.4.1 Exposure Time

One of the most important parameters of the instrument to optimise is the exposure time. This is because the exposure time limits the signal measured, and therefore the magnitude of the reference stars that can be used in the tomographic reconstruction. Hence, the exposure time plays a significant role in the sky coverage. However, if the exposure time is too long, the scintillation signals that are to be corrected are averaged out and therefore the correction factor is reduced.

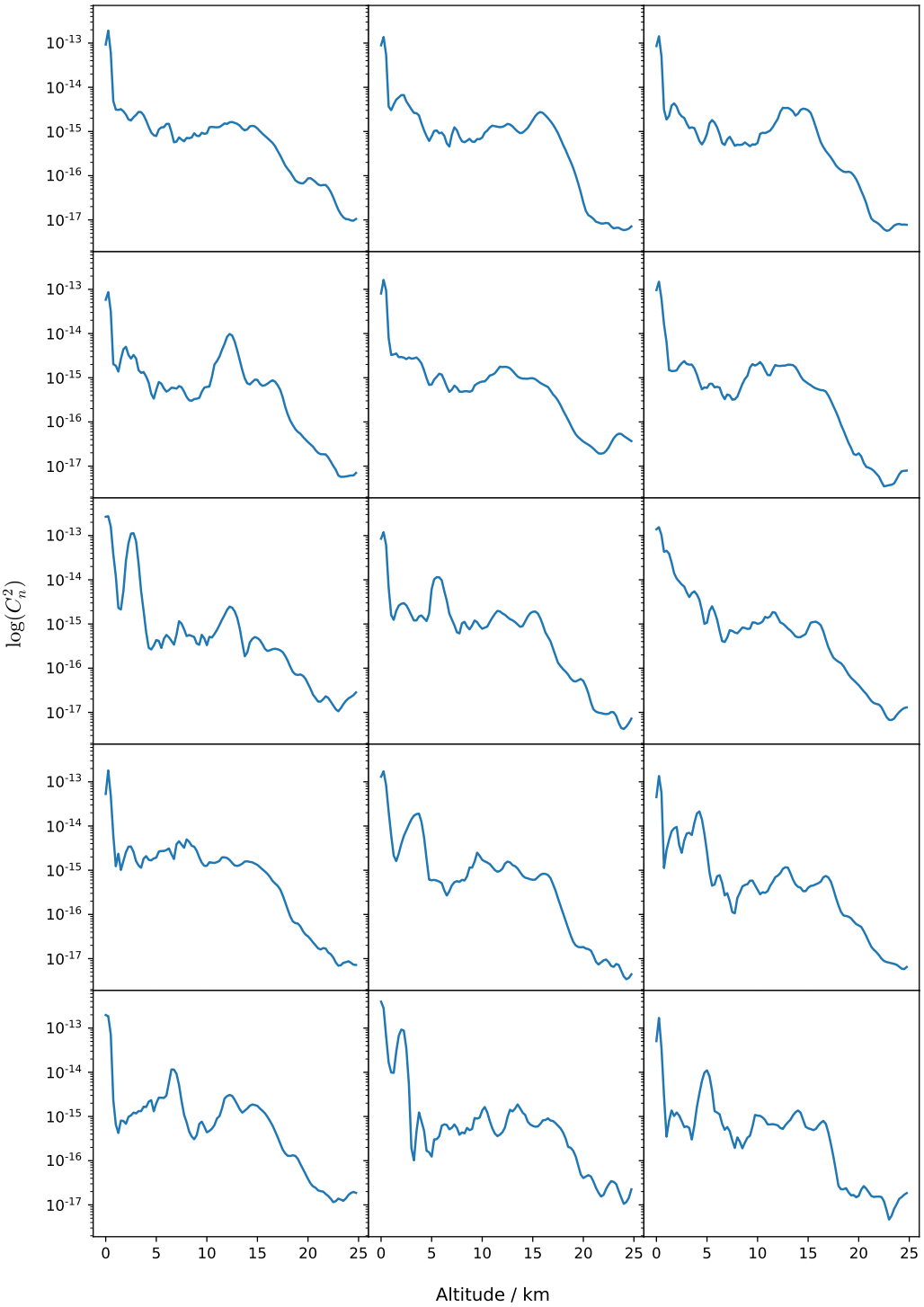

Figure 3.3: The fifteen $C_n^2(h)$ profiles measured in La Palma, Spain, as a function of altitude used in the numerical simulation (Farley et al., 2018).

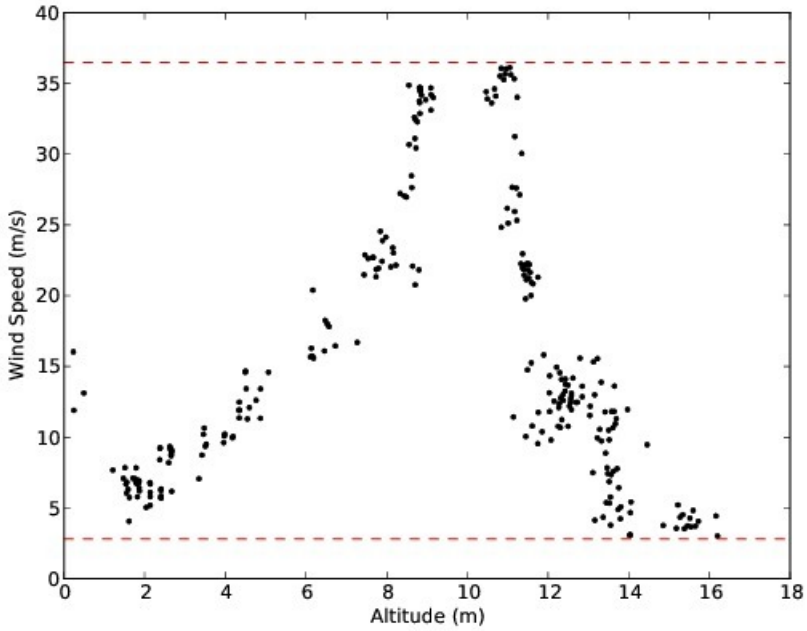

Figure 3.4: The wind velocity profile used in the simulation taken from Shepherd et al. (2013). This wind velocity distribution was measured for the night of 2013 September 13, JKT, La Palma and is a good example of a typical wind profile for this site.

The finite exposure time was simulated by averaging a number of instantaneous frames. For example, to simulate an exposure of 0.1 s, each WFS measurement was taken as an average of twenty instantaneous frames separated at intervals of 0.005 s. It should be noted that the exposure time results therefore depends significantly on the number of frame sub-samples used and therefore the sampling of the phase screens and the velocities of the turbulent layers. The number of sub-samples to use for a given exposure time was established by measuring the residual error in the Zernike coefficient measurement of the phase aberrations as a function of sub-samples. The number of sub-samples at which there is no significant reduction in the residual error is selected as a suitable number to simulate a long exposure.

A simulation for an INT scale telescope was produced. A two layer atmosphere was used in numerical simulation, with one layer at 0 km with speed 5 ms^{-1} and another at 10 km with speed 10 ms^{-1}. The layers had equal weighting, and the total

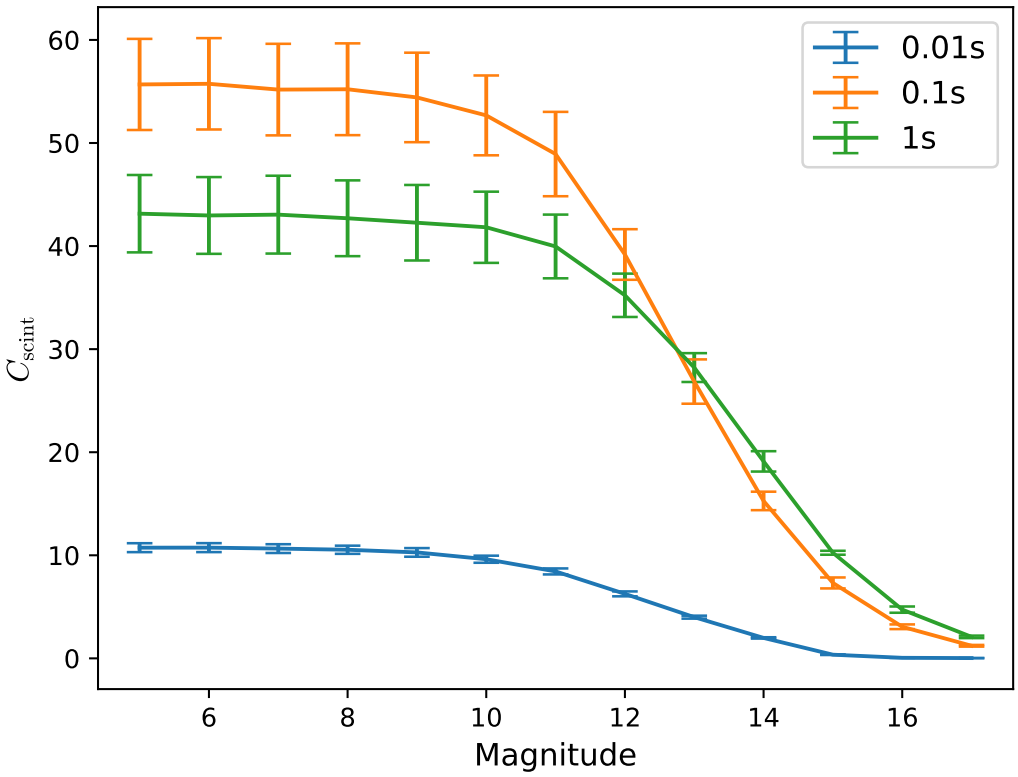

Figure 3.5: The scintillation correction factor as a function of the WFS reference star magnitude for a range of exposure times for the INT. A two layer atmosphere was used, with one layer at 0 km with velocity 5 ms^{-1} and another at 10 km with velocity 10 ms^{-1}. The layers had equal weighting, and the total atmosphere was characterised by $r_0 = 0.2$ m. Four stars were used in a square with sides of 10" and a total of 52 Zernike modes were used.

atmosphere was characterised by $r_0 = 0.2$ m. An asterism of four stars was used, located in a square with sides of 10" to correct a central bright star of magnitude $V = 5$. In total 52 Zernike modes were used for the WFS measurements and in the tomographic reconstruction, which is the maximum number of modes that can be reliably measured by an 8×8 WFS. For each light curve, 100 exposures were used from which C_{scint} was measured.

Figure 3.5 shows the scintillation correction factor as a function of the WFS reference star magnitude for a range of exposure times. For all exposure times, the correction achieved starts to decrease significantly for magnitudes fainter than $V = 11$. For longer exposure times, fainter stars can still achieve some correction. However,

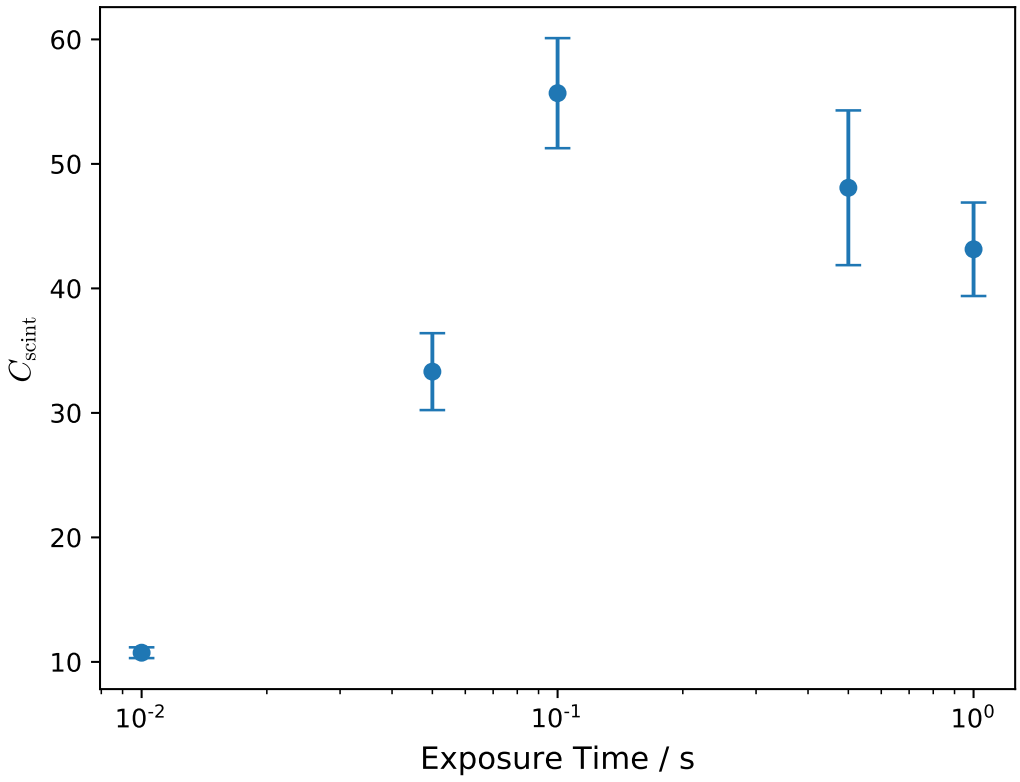

Figure 3.6: The scintillation correction factor as a function of the WFS exposure time for the INT. A two layer atmosphere was used in simulation, with one layer at 0 km with velocity 5 ms^{-1} and another at 10 km with velocity 10 ms^{-1}. The layers had equal weighting, and the total atmosphere was characterised by $r_0 = 0.2$ m. Four stars of 8th magnitude were used in a square with sides of 10" and a total of 52 modes Zernike were used.

a maximum in the correction factor is achieved for an exposure time of 0.1 s. This relationship is demonstrated in more detail in Fig. 3.6 which shows the C_{scint} as a function of exposure time for four $V = 8$ magnitude stars used in the tomographic reconstruction.

The performance that is achieved depends strongly on the exposure time. This may be understood by considering the power spectra of the Zernike focal modes. The defocus term of the high altitude turbulence makes the largest contribution to the intensity fluctuations in the telescope aperture. Fig. 4.11 shows the simulated power spectrum of the defocus Zernike term for a range of aperture sizes.

The frequency corresponding to the peak in this power spectrum depends on the

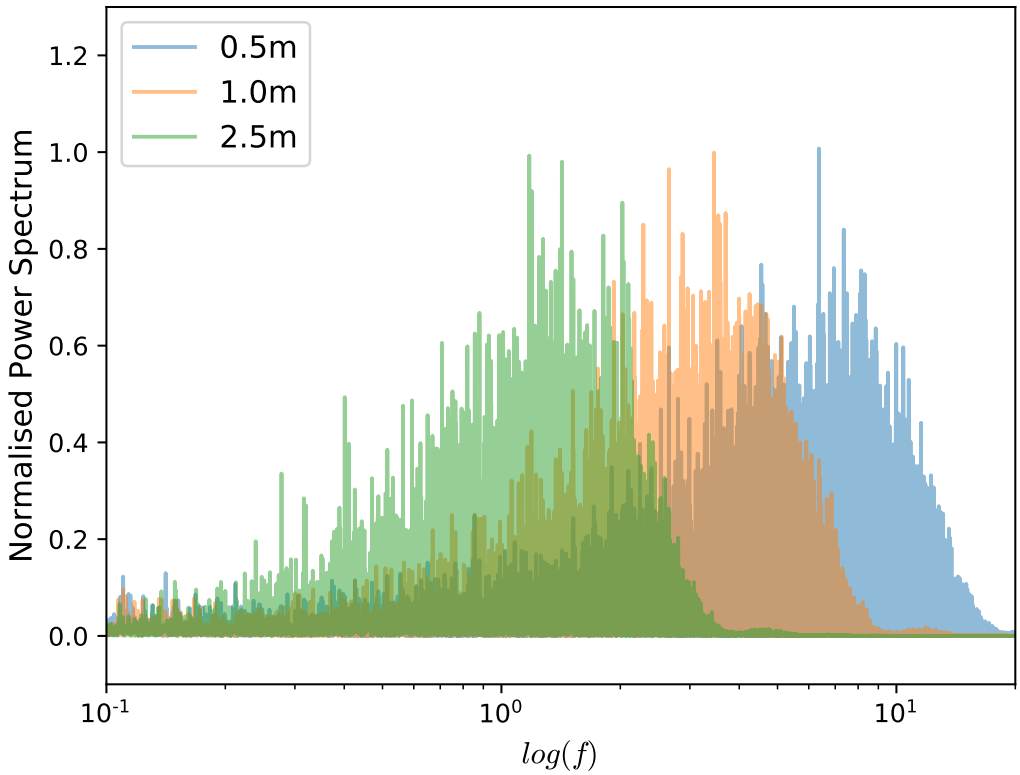

Figure 3.7: The power spectrum of the defocus Zernike mode measured for simulated atmospheric phase aberrations with an $r_0 = 0.1$ m, as a function of frequency f, for a 0.5 m, 1.0 m and 2.5 m telescope. The power spectrum has been normalised by dividing by the maximum value, such that the location of the peaks can be easily compared.

wind speed of the high altitude layer and the size of the telescope aperture. If the exposure time is short, then the power is dominated by shot noise and thus low correction is achieved. If however a long exposure time is used then only the power in the low frequency tail is measured and corrected and hence a lower correction factor is achieved.

Hence, an optimum exposure time exists, for a given aperture size and high layer wind speed, where the scintillation correction factor will be maximised. As shown in Fig. 3.7, the location of the peak scales with aperture size. Larger apertures have a peak at a lower frequency and thus a longer exposure time. Hence, on the largest telescopes, large scintillation correction factors can be achieved for long exposure times.

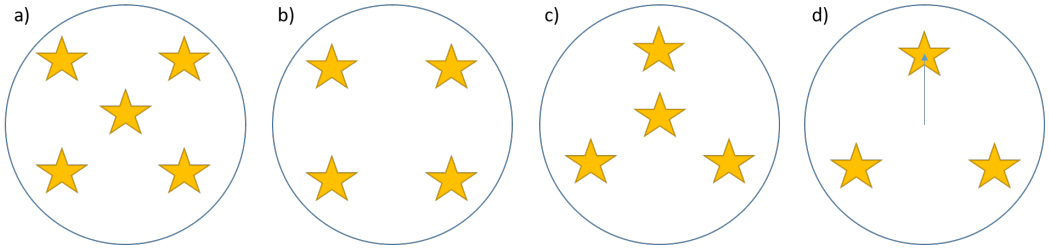

Figure 3.8: The star configurations tested in simulation. In configurations (a) and (c) the target star measurements are also included in the tomographic reconstruction, whereas for (b) and (d) only the reference stars are used.

3.4.2 Configurations

Once the exposure time had been considered, the asterism configuration could be investigated. This included the number of stars used, their angular separation, relative orientation, and their magnitude. A Monte Carlo simulation with an exposure time of 0.1 s was used for an INT scale telescope. The aim of this investigation was to find a suitable asterism for the on-sky experiment.

The configuration of stars investigated can be seen in Fig. 3.8. In total, four configurations were investigated. In configurations (a) and (c) the target star measurements are also included in the tomographic reconstruction, whereas for (b) and (d) only the reference stars are used.

Similarly to section 3.4.1, a Monte Carlo simulation of a 2.5 m telescopes with a two layer atmosphere was used, with one layer at 0 km with speed 5 ms^{-1} and another at 10 km with speed 10 ms^{-1}. The layers had equal weighting and the total atmosphere was characterised by $r_0 = 0.2$ m. Once again, 52 Zernike modes were used in WFS measurements and in the tomographic reconstruction. Each light curve was simulated with 100 exposures from which C_{scint} was measured.

Fig. 3.9 shows the average C_{scint} over all angular separations for each configuration as a function of the star magnitudes. The correction decreases rapidly after a magnitude of $V \approx 12$ which agrees with the results from section 3.4.1. The performance of the four configurations does not vary significantly, however configuration

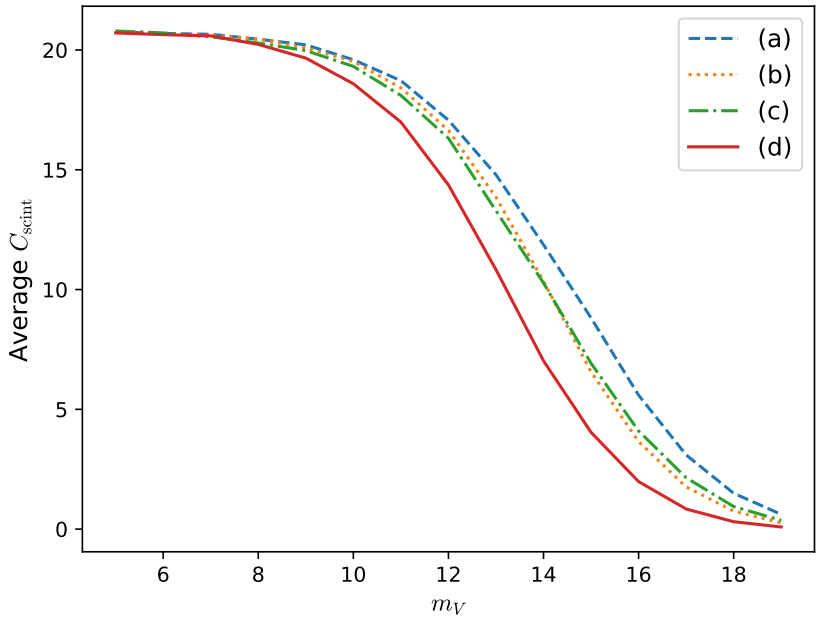

Figure 3.9: The average C_{scint} versus the WFS reference star magnitude, m_V. The results are plotted for four asterism configurations, which are detailed in Fig. 3.8.

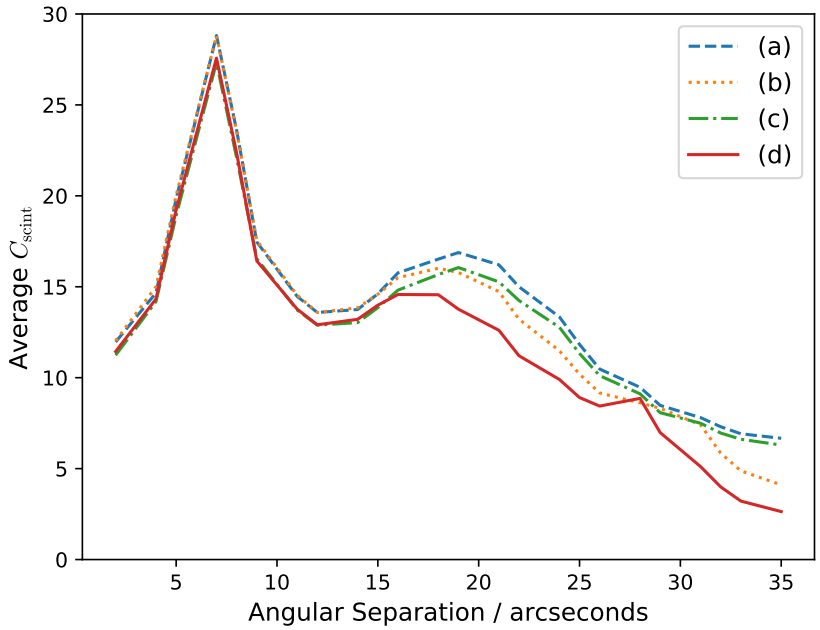

Figure 3.10: The average C_{scint} versus the angular star separation in the asterism. The results are plotted for four asterism configurations, which are detailed in Fig. 3.8.

(a) which has the most stars consistently achieves a higher C_{scint}.

Fig. 3.10 shows the average C_{scint} over all star magnitudes for each configuration as a function of the angular separation of the stars. The results for all configurations show a sharp peak around 7". Below this angle, the scintillation correction factor is low. This is due to the effects of the diffraction rings produced in the propagation of the small metapupils, an example of which is shown in Fig. 3.1. Hence, a limit on the smallest asterism that can be used exists. After the strong peak, there is a slow decline. The dip between 10"-15" is a feature that arises from using the Zernike polynomials. It's possible that with many layers in the atmosphere this feature will average out. As the metapupil size increases, the sampling of the high altitudes is reduced and hence the level of correction is also reduced. The results of this investigation will therefore depend on the altitude of the dominant high layer turbulence and on the number of layers used. However, the general trend remains the same.

When comparing the different configurations, it was found that adding or using more WFS stars makes little difference. Any advantage in having more stars is seen in the case of faint stars or at a large asterism separations. Fusco et al. (1999) found similar results for tomographic AO when comparing the simulated Strehl ratio against the number of stars used in the tomographic reconstruction. They found little improvement when using more than three stars.

In reality, however, natural guide star asterisms are unlikely to be spaced in an equilateral triangular configuration. To investigate how the relative star positions affects the C_{scint} achieved, a simulation was produced using three reference stars. Two of the stars' positions were fixed in location and the third star position was varied. The same simulation parameters were used as for the previous results in this section.

The C_{scint} as a function of the relative position of the third star with respect to the second reference star is plotted in Fig. 3.11. These results show that C_{scint}

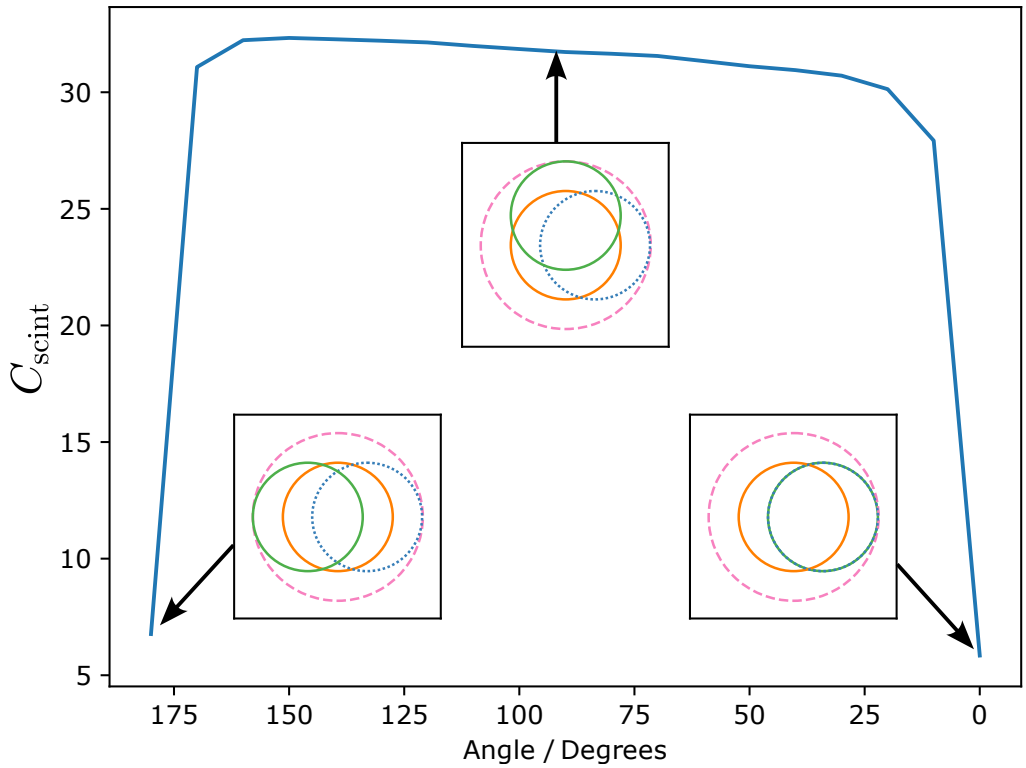

Figure 3.11: The C_{scint} against the location of the third star. The relative overlap of the three stars measurements at 10 km is plotted for clarity.

rapidly decrease if the three stars are placed in a line. This can be understood by the symmetry of the focal Zernike modes, since by only sampling along one axis of the metapupil, it is not possible to distinguish between the 2nd order Zernike modes. Therefore, this places a further restriction on the on-sky asterisms that can be used.

3.4.3 Target Asterisms

The results from section 3.4.2 were used to find a suitable asterism for the on-sky experiment on the INT. However, finding suitable targets for the INT is challenging due to its relatively small aperture size of 2.54 m. A minimum of three stars are required to perform the tomography, and in order to sample turbulent layers up to $\sim$ 20 km on the INT, a maximum angular separation of 21" between the stars is required. Therefore, an asterism of at least three bright stars (below $V = 11$) all

Table 3.1: The star magnitudes and relative positions of the potential target asterisms for observations at the INT. The brightest star was selected as the target (star 2) and placed at the centre of the tomographic metapupils. The two additional reference stars' (star 1 and 3) angular positions are given relative to the target.

Target	V magnitude			Relative angular separations / "		
	star 1	star 2	star 3	star 1	star 2	star 3
Trapezium	6.384	5.061	6.55	[11.84, 6.30]	[0,0]	[-9.54, 8.53]
HD 206267	7.527	5.73	7.477	[-12.96, 18.72]	[0,0]	[19.09, -5.90]
HD 25298	9.981	9.469	10.507	[2.05, 11.88]	[0,0]	[-15.80, -12.96]

Table 3.2: The RA, Dec, and visibility period for the potential on-sky asterisms'. The average scintillation RMS correction achieved in simulation is also given.

Target	RA	Dec	Visibility in La Palma	Simulated σ_I reduction
Trapezium	05h 35m 24s	-5° 27' 0"	August-March	3.2 ± 0.2
HD 206267	21h 38m 58s	+57° 29' 20"	April-December	2.4 ± 0.2
HD 25298	04h 0m 55s	-10° 26' 58"	August-March	2.7 ± 0.3

within 21" is needed. One of the three stars must be bright enough to be scintillation limited for photometry in order to act as the target object. Additionally, the three stars ideally should be configured such that they are not in a line and that the direction of the brightest (target) star should be well sampled by the tomography.

Hence, only a handful of potential targets were found. Table 3.1 shows the three best potential on-sky targets that are visible from La Palma that meet the criteria discussed above. Each of these target asterisms were tested in simulation (details of which are discussed in the next section). Table 3.2 shows the visibility period and the average scintillation RMS correction achieved in simulation. Based on these results, of the three asterisms found, the most suitable is the Orion Trapezium Cluster. The Trapezium Cluster is a tight open cluster of stars in the heart of the Orion Nebula and is a favourite target amongst tomography demonstrations (Marchetti et al., 2007). Three of the stars from this cluster were chosen to perform the tomography.

Fig. 3.12 shows a diagram of the Orion Trapezium Cluster. To perform the tomo-

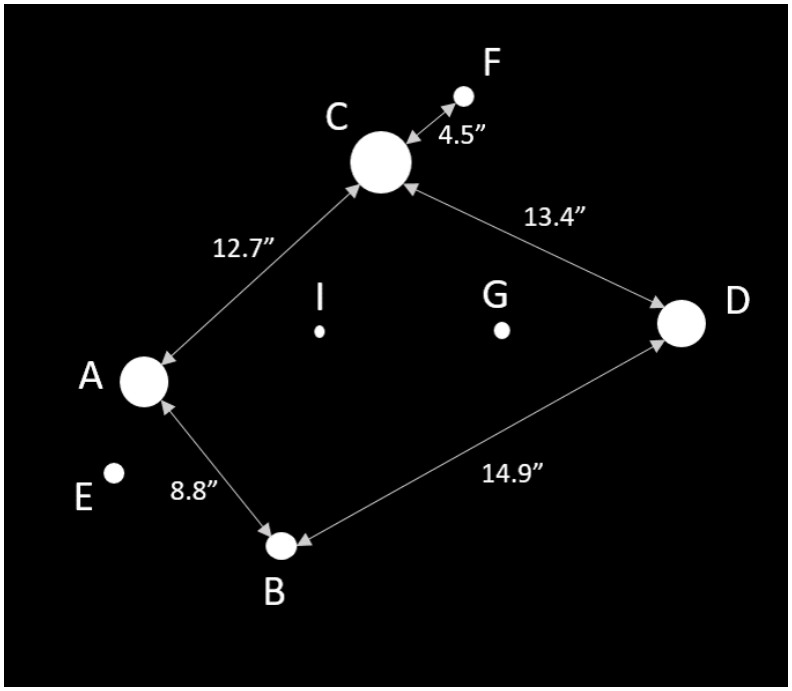

Figure 3.12: A schematic showing the Orion Trapezium Cluster. Each label defines the name of the star, with Theta-1 Orionis A given by label A, Theta-1 Orionis B given by label B and Theta-1 Orionis C given by label C etc. The stars used to perform the tomography are Orionis A, C and D.

graphy, only three stars from this cluster were used. Theta-1 Orionis A, D and C were used to perform the tomography and Theta-1 Orionis C, the brightest star, was used as the target. The configuration of the three stars was chosen such that the target star was at the centre of the tomographic metapupils to reduce the noise produced by the artificially imposed diffraction rings. In the next section, the correction method is simulated using this asterism with multiple atmospheric layers to determine the expected performance of this technique on-sky.

3.4.4 Layers

Another important question for the optimisation of the tomography is the number of turbulent layers that should be used in the tomographic reconstruction matrix. Up until this point, only 2 layer atmospheres have been used to save computational time. In this section, more accurate representations of the atmosphere are

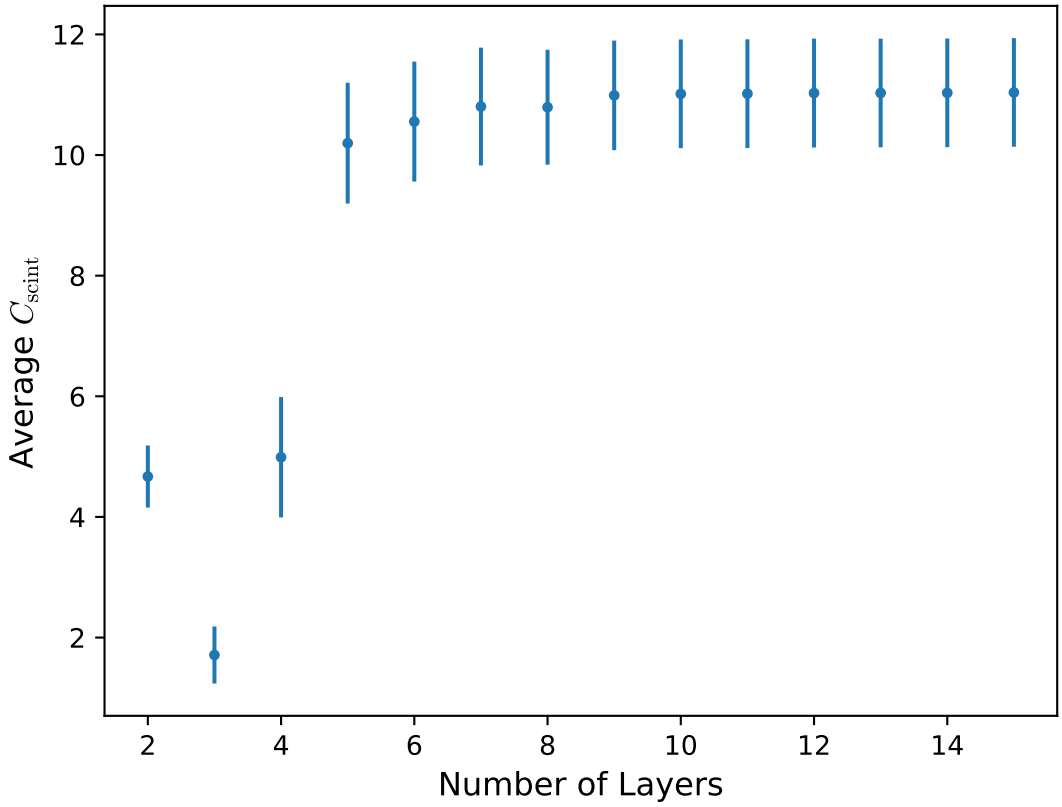

Figure 3.13: The average simulated Scintillation Correction Factor as a function of the number of layers used in the tomographic reconstruction matrix for each turbulence profile. The atmosphere for each profile was modelled with 15 layers considered.

The number of layers required in the tomographic reconstruction was estimated using the 15 turbulence profiles measured on the INT in La Palma shown in Fig. 3.3. Each profile contained 100 layers which were grouped using the optimal grouping method (Saxenhuber et al., 2017) to produce a 15 layer atmosphere. The Orion Trapezium was used in the simulation to test the correction that can be achieved for a real target. For each atmosphere, the intensity of the target star was measured for a 0.1 s exposure time and a total of 100 frames. The intensity was then corrected using a range of turbulence models with N layers where N = 2,3,...,15 in the reconstruction matrix. In each case, the altitudes and relative strengths of the turbulent layers were estimated using the optimal grouping method. For each profile, to avoid noise caused by diffraction rings, only layers above 1 km were

included in the Fresnel propagation to produce the estimated scintillation pattern.

Fig. 3.13 shows the average scintillation correction factor as a function of the number of layers used in the tomographic reconstruction. On average, it was found that a minimum of five layers were needed in the tomographic reconstruction algorithm to accurately estimate the scintillation noise. Beyond five layers the average C_{scint} levels off and therefore there is little benefit to using more layers in the reconstruction matrix. This is to be expected, as often the turbulence profile is dominated by only a few strong layers. The optimal number of layers to use will depend on the current turbulence profile and can be estimated visually.

The results from this simulation give an estimate for the scintillation correction that could be expected on-sky for the Trapezium Cluster. It was found that using five layers in the reconstruction matrix on average reduced the scintillation RMS by a factor of 3.2 ± 0.2. Using all fifteen layers only increases the factor to 3.3 ± 0.1 which confirms that only five layers are needed in the reconstruction matrix to accurately model the turbulence profile.

Fusco et al. (1999) found little improvement in their phase estimation when using more than three layers. However, it is expected that for scintillation correction more layers would be needed. This is because it is the high altitude layers that produce the scintillation, whereas for AO correction, it is primarily the strong layer near the ground that contribute the most to the phase distortions. Therefore, it is likely that the two applications have different requirements, with scintillation correction requiring more layers.

This simulation assumed perfect knowledge of the turbulence profile. Specifically, it assumes that the turbulent layer altitudes and relative strengths have been perfectly measured and that the only error in the correction therefore arises from estimating the atmosphere with fewer layers. In the next section, the precision required for the turbulence profile is investigated.

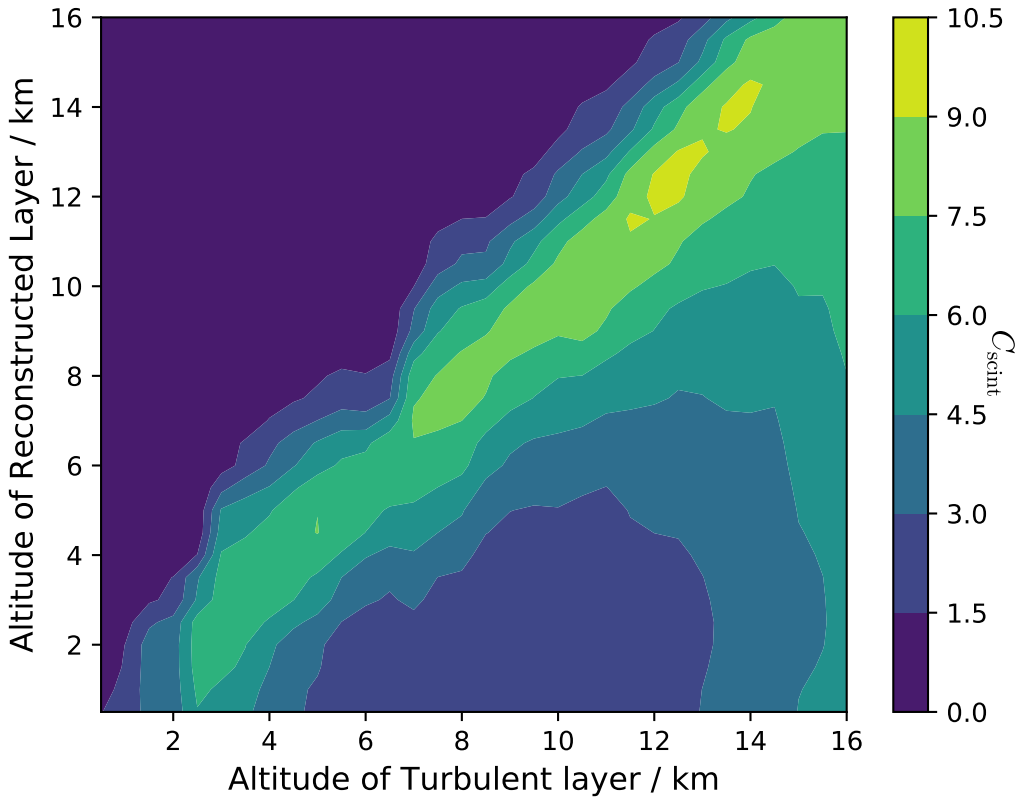

Figure 3.14: The simulated C_{scint} as a function of the true turbulence altitude and the altitude used in the tomographic reconstruction matrix. Three layers were used, one layer at the ground with a weighted strength of 40% of the total C_n^2, a layer at 20 km with a weighted strength of 20% of the total C_n^2, and a layer in the middle which was varied from 500 m to 16 km with a weighting of 40% of the total C_n^2.

3.4.5 Turbulence Profile Knowledge

An important measurement for the tomographic scintillation correction technique is the turbulence profile. Knowledge of the altitude of the turbulent layers is vital for both performing the tomographic reconstruction, and in performing the Fresnel propagation to produce the scintillation pattern estimation. Hence, it is essential that measurements of the turbulent layer altitudes are accurate. In these simulations, perfect knowledge of the turbulence profile has been assumed, but a key question is to what precision must the altitudes be known?

The required precision for the turbulent layer altitudes was investigated by sim-

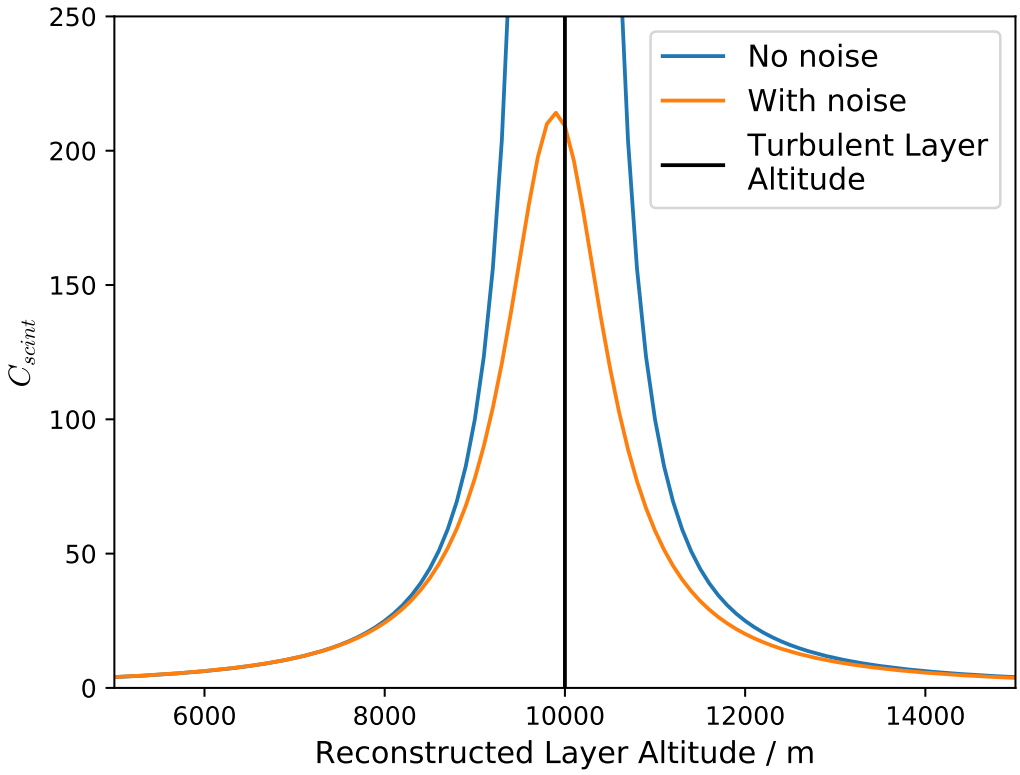

Figure 3.15: The simulated C_{scint} for a turbulent layer at an altitude of 10 km as a function of the turbulent layer altitude used in the tomographic algorithm for a perfectly reconstructed layer in blue and for a reconstructed layer with noise in orange. This demonstrates how underestimating the turbulent layer altitude is favoured in the tomographic reconstruction as any noise in the reconstructed signal scales with the propagation distance.

ulating atmosphere models and varying the altitudes used in the tomographic reconstruction matrix - i.e. assuming imperfect knowledge of the turbulence profile. An atmosphere with three layers was used, characterised by an r_0 of 0.2 m. The model consisted of one fixed layer at the ground with a weighted strength of 40% of the total C_n^2, a fixed layer at 20 km with a weighted strength of 20% of the total C_n^2, and a layer in-between which was varied from 500 m to 16 km with a weighting of 40% of the total C_n^2. Perfect knowledge of the fixed layers was assumed in the tomographic reconstruction matrix, with no knowledge of the third layer position.

Fig. 3.14 shows the C_{scint} measured as a function of the true turbulent layer altitude on the x-axis and the turbulent layer altitude used in the reconstruction on the y-

axis. From this plot, it can be seen that the scintillation factor reduces rapidly when the reconstructed altitude is higher than the true altitude of the turbulent layer. Since the scintillation noise is proportional to the propagation distance, this result implies that overestimating the scintillation noise results in a lower C_{scint}. When the altitude of the reconstructed layer is lower than the true altitude of the layer, the C_{scint} reduces much more slowly. This is due to the presence of noise in the reconstructed turbulent layer. This is demonstrated further in Fig. 3.15 which shows the simulated C_{scint} for a turbulent layer at an altitude of 10 km as a function of the turbulent layer altitude used in the tomographic algorithm for a perfectly reconstructed layer in blue and for a reconstructed layer with noise in orange. In the presence of noise, underestimating the turbulent layer altitude is favoured in the tomographic reconstruction, as any noise in the reconstructed signal scales with the propagation distance in the Fresnel propagation.

The average standard deviation along the x-axis in Fig. 3.14 is 2.1 km, implying that such precision is needed for the turbulent layer altitudes in the tomographic reconstruction, however this is clearly skewed towards a lower reconstruction altitude. A stereo-SCIDAR instrument on the INT can measure the turbulence profile with a precision of 250 m intervals, and therefore is well within the requirements for the tomographic reconstruction.

3.4.6 Wavelength

Up until now, all the simulations have been performed in the V band. However, a promising application of the scintillation correction technique is multi-spectral observations of exoplanet transits in order to determine details of the exoplanet atmosphere. Hence, an important investigation is the scintillation correction performance as a function of wavelength.

A simulation was produced that uses the same seeded random phase screens in different wavebands to determine how the scintillation correction varies with wavelength.

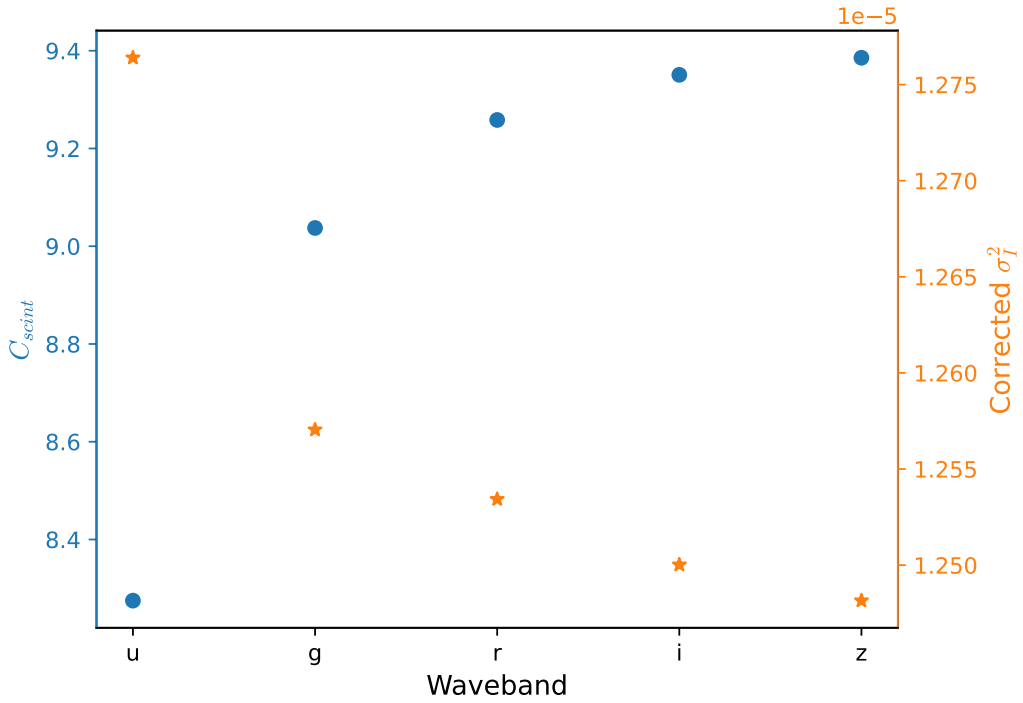

Figure 3.16: The C_{scint} on the left and the corrected scintillation index on the right as a function of the waveband used. The u, g, r, i and z bands were used in simulation on the same simulated atmosphere.

The wavebands chosen were the u, g, r, i and z bands. The median five layer profile for the La Palma SCIDAR data was used in numerical simulation. Fig. 3.16 shows the C_{scint} on the left and the corrected scintillation index on the right against the waveband used. It was found that the longer wavelengths resulted in a higher C_{scint} and resulted in a lower corrected scintillation index. This is to be expected, since the spatial scales of the intensity fluctuations will be larger for longer wavelengths as the Fresnel radius scales with wavelength. The correction technique favours lower spatial orders and hence longer wavelengths.

3.4.7 Sky Coverage

Another key question is whether substantial sky coverage can be achieved for this technique using NGS. For a large telescope, longer exposure times and wider asterisms can be used and hence a larger sky coverage might be expected.

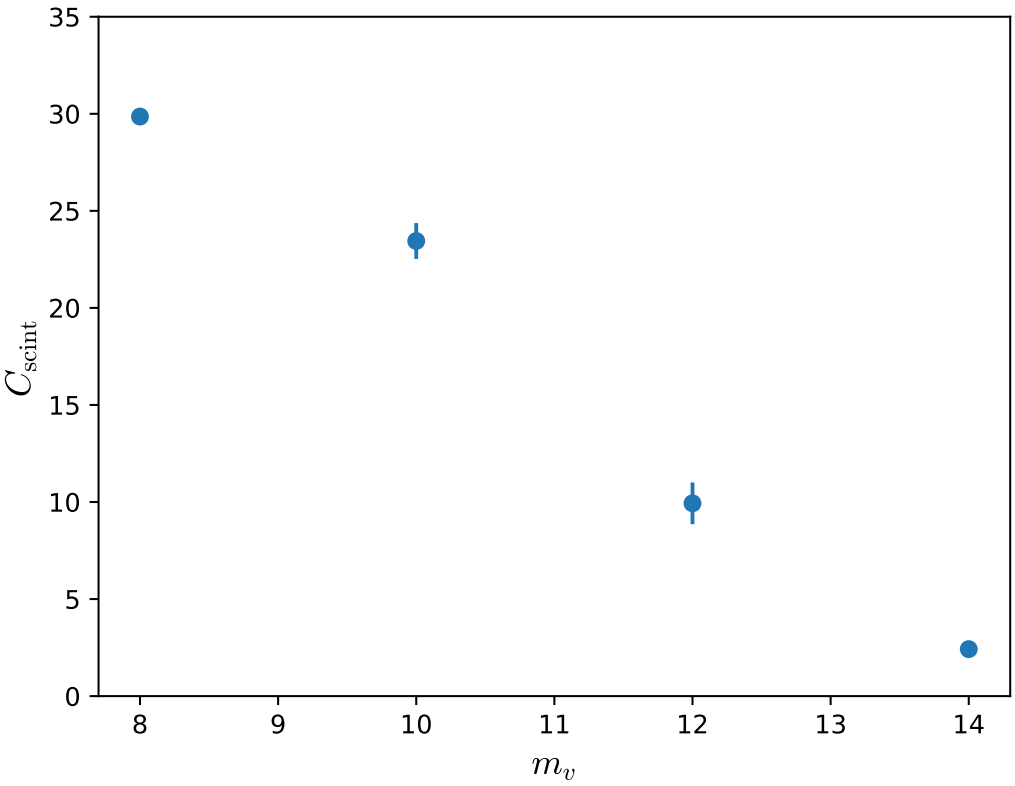

Figure 3.17: The scintillation correction factor against the magnitude of the reference stars used to perform the tomography for a VLT scale NGS tomographic system.

To determine the sky coverage for a tomographic AO system on a large telescope, a simulation for an 8 m class telescope was produced. Eighteen Paranal SCIDAR profiles each with 5 layers were used. A configuration with a very bright scintillation limited target star (V=5) was chosen, with 4 stars in a square with sides of 63 arcseconds. The magnitude of the 4 reference stars was varied from 8 to 14. A 1 s exposure time and a 16×16 WFS was used for each guide star from which 100 Zernike modes (a more than sufficient number of modes, well within what could be reasonably measured) were used in the tomographic reconstruction. It was assumed the observation was near zenith. The scintillation correction factor was then plotted against the reference star magnitudes. The results of this simulation are shown in Fig. 3.17.

The scintillation correction factor reduces significantly as the reference stars used to

perform the tomography get fainter. Hence, brighter stars (V $\leq$ 10) are required to perform the tomography with sufficient accuracy. As such, the expected sky coverage for an NGS tomographic system would be negligible, despite the fact that a longer exposure time and wider asterism are used. In addition, even if there were enough stars within the asterism required, the probability of it being in a suitable configuration would be small. Therefore, the use of LGS are required. The 4LGSF of the VLT, which have magnitudes $V \sim 8$ and therefore provide more than enough flux for this application. Fortunately, the majority of the newest large and extremely large telescopes, such as the ELT, will be equipped with LGS facilities for tomographic AO and therefore this requirement will already be met.

3.5 Laser Guide Stars

In practice, the likelihood of finding enough bright natural guide stars within the field of view of interest is small, and the likelihood of the bright stars being in a suitable configuration for the tomography is even smaller. Therefore, artificial reference stars are needed (Rigaut and Neichel, 2018). Several such artificial stars have been proposed, including using planes equipped with bright lights (Linnick, 1957). The more practical solution is to use lasers, which was first proposed by Foy and Labeyrie (1985).

Sodium LGS are artificial stars produced by the excitation of the sodium layer (at approximately 90 km) in the mesosphere by lasers. The excited sodium atoms re-emit the laser light, to produce an artificial star. The back-projected light can then be used for sensing the wavefront aberrations (Clare et al., 2010).

Although laser guide stars can provide a full sky coverage, they have several effects that need to be accounted for. These are the cone effect, tip/tilt indeterminacy and spot elongation. The details of each of these effects are discussed below.

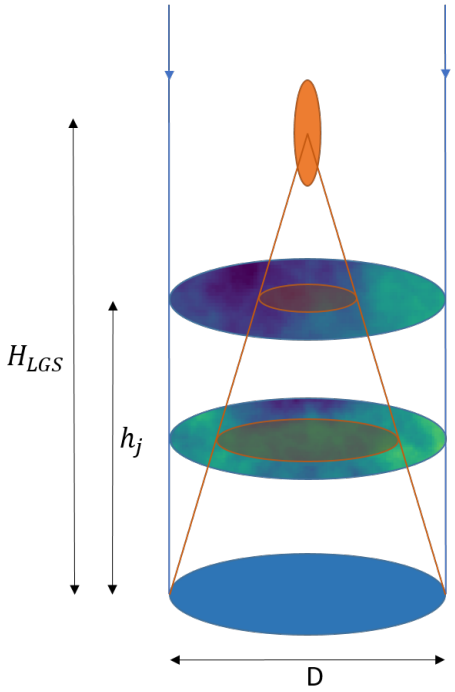

Figure 3.18: The focal anisoplanatism (cone effect) produced by the finite height of an LGS.

3.5.1 Focal Anisoplanatism

A significant problem with using LGS is the cone effect or focus anisoplanatism. For NGS, the light propagates through the atmosphere in a cylinder as the star can be considered to be an infinite distance away. However, an LGS is a point source at a finite height (90 km) and therefore the light propagates through the atmosphere in a cone shape. This means high altitude turbulent layers are sampled by a smaller area. This is demonstrated in Fig. 3.18. This difference in sampling causes errors in the measurement of the optical phase aberrations of the incoming wavefronts. This is a problem for scintillation correction, since it is the high altitude layers, which are less sampled, that produce the scintillation noise, and are therefore the layers of interest.

Hence, for an LGS, the measured phase in direction $\boldsymbol{\alpha_i}$ is given by:

$$\Phi^m(\boldsymbol{r}, \boldsymbol{\alpha_i}) = \sum_{j=1}^{N_t} \phi_j \left(\left(\frac{H_{LGS} - h_j}{H_{LGS}} \right) \boldsymbol{r} + h_j \boldsymbol{\alpha_i} \right) + n_i(\boldsymbol{r}), \tag{3.2}$$

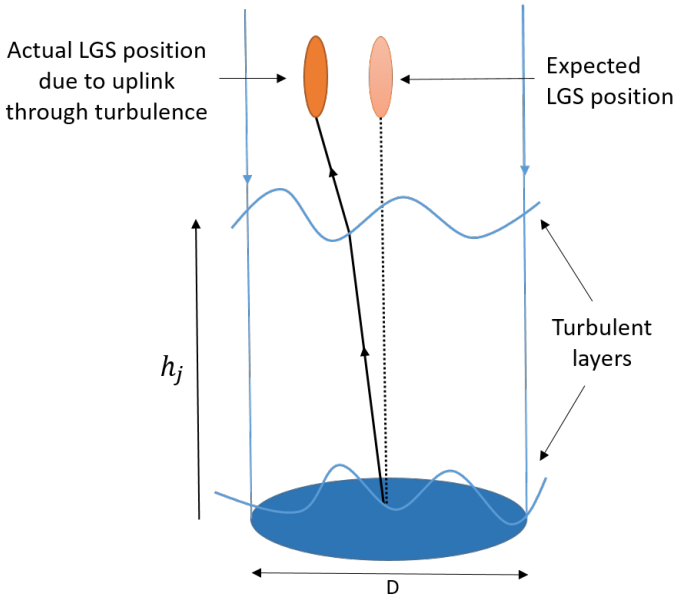

Figure 3.19: The tip/tilt indetermination due to the uplink of the LGS beacon through turbulence.

where H_{LGS} is the altitude of the LGS, h_j is the altitude of the turbulent layer j (Rosensteiner and Ramlau, 2013). This equation was used to simulate the WFS measurements for each LGS. The projection matrix, $M_{N_{GS}}^{N_{EL}}$, was also edited to include the cone effect in the reconstruction matrix.

3.5.2 Tip/Tilt Indetermination

For an LGS, it is impossible to determine the tip/tilt modes of the atmospheric turbulent layers, as the position of the LGS has been affected by the up-link of the laser light as it passes through the atmosphere on its way up to the sodium layer. This effect is demonstrated in Fig. 3.19. The wavefront sensor measurements are given by the sum of the perturbations in both directions, thus making it impossible to determine the tip/tilt mode of the wavefront on the down-link.

This can be mitigated by using an NGS close to the target to measure the tip/tilt modes (Rigaut and Neichel, 2018). However, any differential in the tip/tilt between the LGS reference stars used to perform the tomography cannot be measured.

For the simulations, it was found that the tip/tilt was not needed in the reconstruction matrix to get an accurate estimate for the scintillation noise. Since the asterisms used are relatively small, any differential tip/tilt measured between the LGS at the turbulent layers are small, and therefore it is primarily the focal Zernike modes that contribute to the scintillation noise. Hence, the tip/tilt indetermination is not a significant problem for scintillation correction. However, it could be a problem if larger asterisms are used. In practice, it is likely the observer may also want to do AO correction on the target and therefore a faint NGS would be needed.

3.5.3 Temporally Varying Sodium Layer Altitude

The atomic density distribution within the sodium layer is constantly changing, which means the altitude of the sodium layer, and therefore the LGS, varies over time. The sodium layer altitude can vary throughout an observation from as much as 85-105 km (Marin et al., 2015). These altitude variations translate into focus variations, which cannot be distinguished from atmospheric focus changes (Rigaut and Neichel, 2018). Hence, to measure the focal Zernike modes, the altitude of the LGS must be known. In addition, the LGS altitude is needed to accurately model the cone effect in the tomographic reconstruction matrix - if the altitude is varying, then the relative sampling of each turbulent layer changes.

Not only is the varying altitude a problem, but the differential focus error between the LGS is also significant. The obvious solution to this problem is to have an off axis telescope observing the LGSs. The absolute altitude of the LGSs can be derived by a triangulation method using NGS trails behind the laser streaks (Neichel et al., 2013). Since the tomographic reconstruction is done in post-processing, the varying altitude of the LGSs effects on the sampling of each turbulent layer can then be included in the tomographic reconstruction. Hence, in the simulations it has been assumed that the altitudes of all the LGS are known and hence the focal modes can be measured perfectly.

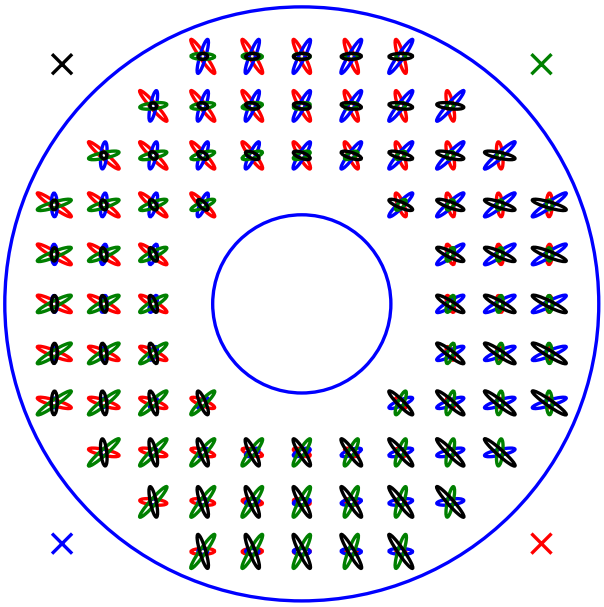

Figure 3.20: The spot elongation for each LGS in each subaperture. Each LGS location is noted by a coloured cross. The spot elongation in each subaperture for each LGS is given by an ellipse in its corresponding colour.

3.5.4 Spot Elongation

Another effect of using LGS that needs to be taken into account in the simulation is the elongation of the Shack–Hartmann wavefront sensor subaperture images. This effect is due to the finite thickness of the sodium layer and parallax, resulting in elongated cigar shaped WFS spots. This increases the noise in the slope measurements for each direction and also induces a correlation between the x and y directions (Clare et al., 2010). The spot elongation for four LGS on a WFS is shown in Fig. 3.20.

The elongation of the Shack–Hartmann spots is given by the vector $\boldsymbol{\beta} = (\beta_x, \beta_y)$, where the magnitude β is the projection of the Full-Width Half Maximums (FWHM) of the sodium profile in the field of view (Tallon and Foy, 1990). The spot elongation is therefore given by (Clare et al., 2010):

$$\boldsymbol{\beta} = \frac{\cos(z)\boldsymbol{bt}}{h^2}, \tag{3.3}$$

where z is the zenith angle, $\boldsymbol{b}$ is the baseline vector between the launch telescope and the subaperture, t is the thickness of the sodium layer, and h is the mean height of the sodium layer above the telescope. Hence, the spot elongation will also vary over time as the sodium layer height and thickness changes.

When there is no elongation, the WFS subaperture images can be considered as a symmetric Gaussian with a FWHM of θ. For an LGS, the subaperture images become elongated such that the FWHM becomes θ and $\sqrt{\theta^2 + \beta^2}$ along the main axis. The noise covariance matrix $\boldsymbol{C_n^{lgs}}$ will become a block diagonal of 2×2 covariance matrices of x and y coordinates for each subaperture. The noise covariance matrix $\boldsymbol{C_K}$ of the kth WFS subaperture is then given by (Tallon and Foy, 1990):

$$\boldsymbol{C_k} = \sigma_n^2 \begin{pmatrix} 1 + \beta_x^2/\theta^2 & \beta_x\beta_y/\theta^2 \\ \beta_x\beta_y/\theta^2 & 1 + \beta_y^2/\theta^2 \end{pmatrix}, \tag{3.4}$$

where σ_n^2 is the variance of the error on the centroid measurements.

To get the noise on the Zernike coefficients, the noise covariance matrix must be converted to the Zernike basis. This is done using the Zernike reconstruction matrix, M_{zr}, such that:

$$\boldsymbol{C_{nzr}^{lgs}} = \boldsymbol{M_{zr}} \boldsymbol{C_n^{lgs}} \boldsymbol{M_{zr}^T}. \tag{3.5}$$

This new noise covariance matrix was used in the simulation to both model the noise of the WFS measurements and to model the noise in the tomographic reconstruction matrix. The height of the LGS was assumed to be 90 km with a thickness of 10 km (Neichel et al., 2013). It was assumed that these did not vary during the observation.

3.5.5 Implementation on LGS AO facility

Based on the results for the sky coverage, it is clear that an ideal application of this method requires an LGS facility. However, whilst LGS provide full sky coverage, there are several disadvantages to their use including the cone effect, the tip/tilt indetermination problem and spot elongation. The 4LGSF on the VLT was

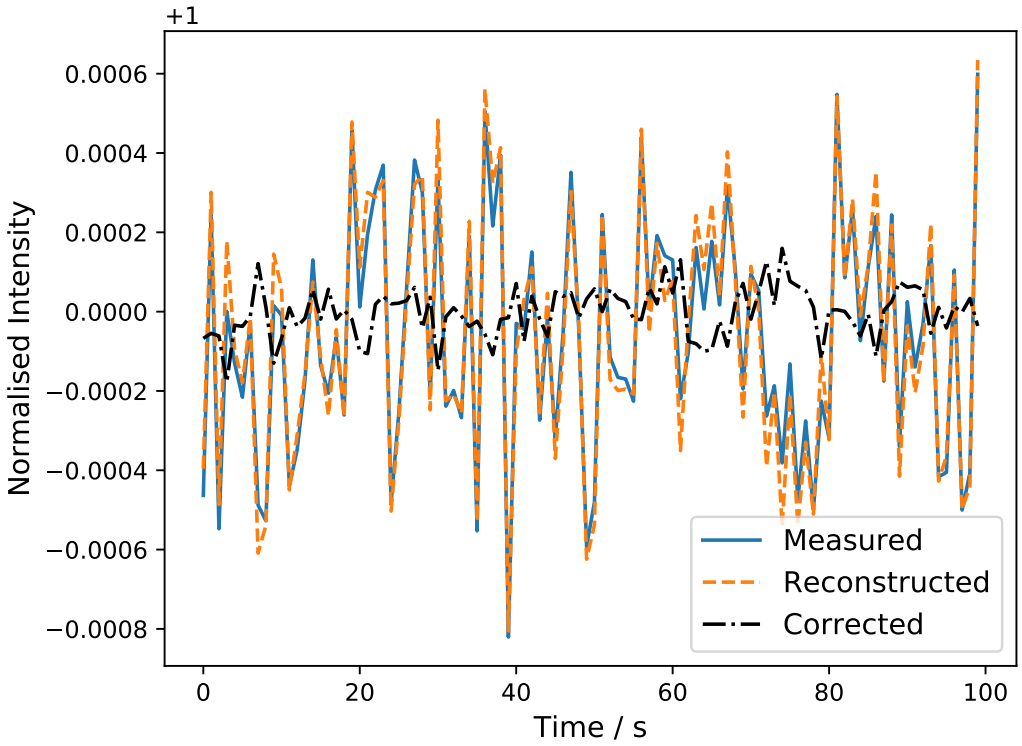

Figure 3.21: An example simulated light curve for the 4LGSF on the VLT. The measured normalised intensity, tomographically reconstructed normalised intensity and corrected intensity are plotted.

simulated with these effects included to estimate the scintillation correction that can be achieved on a full tomographic AO system with LGS.

To summarise, the cone effect was included by setting an LGS height of 90 km in the WFS measurements and in the reconstruction matrix as described by Rosensteiner and Ramlau (2013). The LGS spot elongation was included in the WFS noise model using the noise covariance matrix defined by Clare et al. (2010). The tip/tilt indetermination was included in the simulation by excluding tip/tilt from the tomographic reconstruction matrix. On-sky, the target NGS could be used to measure the tip/tilt. It is expected that any differential tip/tilt between the LGS at the high altitude layers are likely small, as there is significant overlap in the WFS measurements. It is assumed that the height of the LGS are known, and hence the remaining Zernike modes can be measured perfectly.

The VLT was simulated with the four LGS in a square with sides of 63" with a scintillation limited target star in the middle and it was assumed that the observation was near zenith. A one second exposure time was used and 100 Zernike modes were employed in the tomographic reconstruction. The expected shot noise for a magnitude $V = 8$ LGS with a 16×16 WFS was added to the measured Zernike modes for each guide star. Eighteen turbulence profiles measured in Paranal (Farley et al., 2018) were used in simulation, each compressed to 5 layers using an optimal grouping algorithm. A total data acquisition of 100 s was simulated for each turbulence profile.

Fig. 3.21 shows an example of the measured normalised intensity, reconstructed intensity and corrected intensity for one of the turbulence profiles. The noise has been substantially reduced in the corrected light curve. The correlation between the measured and reconstructed intensity is 0.98 which results in a scintillation correction factor of 22 - a reduction in the scintillation RMS noise by a factor of 4.7. It was found that on average for all the turbulence profiles the scintillation RMS noise was reduced by a factor of four. This is slightly reduced from the factor of 5.5 ($C_{scint} = 30$) that was measured for the same configuration with $V = 8$ NGS in Fig. 3.17.

These simulations assume perfect knowledge of the turbulence profile and sets the number of reconstructed layers equal to the number of layers in the atmosphere. In addition the WFS measurements are assumed to be limited only by shot noise. Therefore, these simulations give an upper limit of the performance that can be expected for an LGS facility.

Whilst a tomographic AO system will be operating at very high frame rates, the wavefront and the intensity temporally average in the same way. Hence, the reconstructed intensity can be temporally binned (so long as the scintillation remains the dominant noise source) to apply correction over longer exposures for the photometric data.

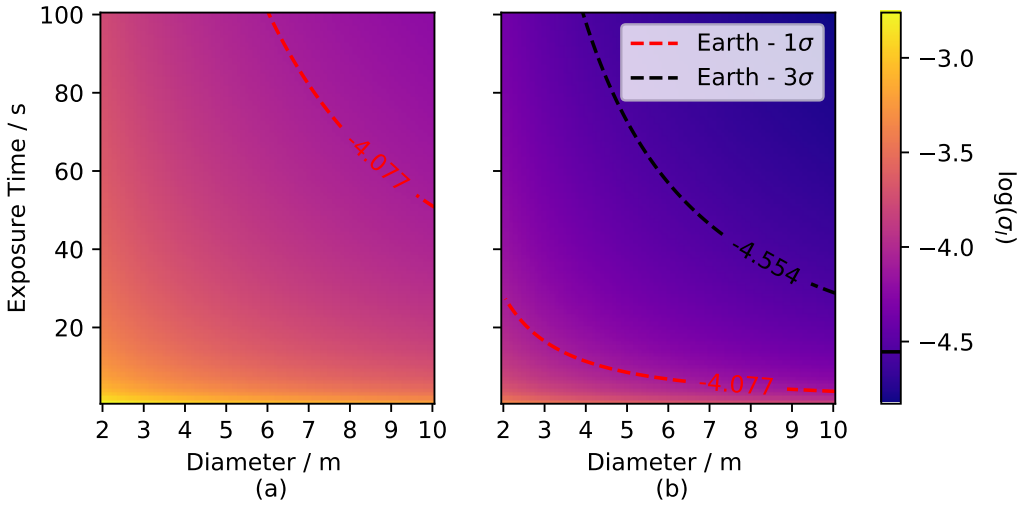

Figure 3.22: The theoretical scintillation noise as a function of exposure time and aperture size used (a) without any correction and (b) with scintillation correction by a factor of four.

3.6 Exoplanet detections with scintillation correction

Based on simulations of the tomographic scintillation correction technique on the VLT with 4LGS, it is expected that the scintillation noise RMS could be reduced by a factor of four. A key question is what impact such a noise reduction would have on astrophysical measurements using time-resolved photometry, for example, the detection and measurement of transiting exoplanets.

Fig. 3.22 compares the scintillation noise as a function of exposure time and aperture diameter with and without scintillation correction, assuming a reduction in the scintillation noise RMS by a factor of four. The scintillation noise was estimated using Eq. 2.20 for median atmospheric conditions in La Palma. Without scintillation correction, high SNRs for observations of Earth sized planets around sun like stars can only be achieved with large telescopes and long exposure times of more than a minute. Reducing the scintillation noise by a factor of four enables such observations with a good SNR on much smaller telescopes and with much shorter exposure times of less than 10 s.

In practice, a lot of the scintillation limited stars will likely have larger radii than the Sun, and therefore to detect an Earth sized planet from the ground would require less noise. However, reducing the scintillation noise by a factor of four will significantly reduce the error in ground-based exoplanet parameters, since the scatter on the astrophysical parameters of the exoplanet transit scales linearly with the scintillation noise within a gradient in the range of 0.68 – 0.80 (Föhring et al., 2019).

3.7 Discussion and Conclusions

In summary, simulations of a scintillation correction technique for large telescopes using tomographic wavefront sensing show promising results. The importance of the WFS exposure time on the scintillation correction has been investigated, as well as the configuration and magnitudes of the reference stars used to perform the tomography. It was found that only three stars are needed for a reasonable correction, which is in agreement with the findings of Fusco et al. (2001) for tomographic AO. Based on these investigations, three suitable asterisms were found for the on-sky demonstration at the INT.

The Trapezium cluster was used to determine the expected on-sky performance for a real target asterism. Fifteen SCIDAR turbulence profiles observed in La Palma were used in the numerical simulation, each with 15 layers. An average reduction in the scintillation RMS of 3.2 ± 0.2 was achieved in simulation. It was found that, on average, five layers were necessary to sufficiently model the turbulence profile in the tomographic reconstruction matrix and that the turbulence profile needs to be measured with a precision of approximately 1 km.

Results from simulation show that even for the largest telescopes, a significant sky coverage cannot be achieved using NGS. Hence, for most targets of interest, LGS are required. Simulations of the 4LGSF facility on the VLT show that high

scintillation correction factors of up to ~ 25 could be achieved, with an average correction factor of ~ 16 across 18 turbulence profiles.

Chapter 4

First on-sky demonstration of a scintillation correction technique using tomographic wavefront-sensing

4.1 Introduction

The previous chapter investigated the scintillation correction technique proposed by Osborn (2014). These simulations found three suitable targets for the INT observations, where the high altitude turbulent layers are well sampled. Simulating the Orion Trapezium Cluster suggested that the scintillation RMS could be reduced by a factor of 3.4.

A simple experiment that uses a single SHWFS and a SCIDAR instrument was devised to test the tomographic scintillation correction technique on-sky. An observing run of five nights on the INT in La Palma was done in September 2021 and a second observing run of five nights was done in May 2022.

In this chapter, the results from these on-sky experiments are presented. These

results have been published (Hartley et al., 2023a) and presented at a conference (Hartley et al., 2022). Section 4.3 details the data acquisition and in section 4.4 the data reduction techniques used in this demonstration are discussed. In section 4.5 the on-sky results from the 2021 run are presented and compared to simulations. In section 4.6 the results from a simulation investigating the importance of updating the tomographic reconstruction matrix regularly is presented. These results are discussed and concluded in section 4.8. In section 4.7 the results from the May 2022 run on a different target are presented and discussed.

4.2 Performance Metrics

The performance of the correction technique is determined by measuring the Pearson r correlation coefficient between the measured intensity and the tomographically reconstructed intensity. The Pearson r coefficient measured between two variables x and y is given by:

$$r = \frac{\sum(x_i - \bar{x})(y_i - \bar{y})}{\sqrt{\sum(x_i - \bar{x})^2 \sum(y_i - \bar{y})^2}}, \tag{4.1}$$

which is equivalent to:

$$\mathrm{Cor}(x, y) = \frac{\mathrm{Cov}(x, y)}{\sqrt{\sigma_x^2 \sigma_y^2}}, \tag{4.2}$$

where $\mathrm{Cov}(x, y)$ is the covariance between x and y.

The performance is also measured in terms of the 'scintillation correction factor' which is the factor by which the scintillation index has been reduced. The reduction in the measured scintillation index that can be expected is directly related to the correlation coefficient measured between the measured photometry and the reconstructed intensity.

The corrected light curve will have a measured variance of:

$$\langle |I - I_r|^2 \rangle = \langle I \rangle^2 + \langle I_r \rangle^2 - 2\langle I, I_r \rangle = \sigma_I^2 + \sigma_{I_r}^2 - 2\mathrm{Cov}(I, I_r), \tag{4.3}$$

where I is the measured intensity and I_r is the reconstructed intensity. Assuming that $\sigma_I^2 \approx \sigma_{I_r}^2$, then:

$$\langle |I - I_r|^2 \rangle = 2(\sigma_I^2 - \mathrm{Cov}(I, I_r)). \tag{4.4}$$

The scintillation correction factor, which is defined as C_{scint}, is given by:

$$C_{\mathrm{scint}} = \frac{\sigma_I^2}{\sigma_{|I-I_r|}^2}, \tag{4.5}$$

which is equivalent to:

$$C_{\mathrm{scint}} = \frac{\sigma_I^2}{2(\sigma_I^2 - \mathrm{Cov}(I, I_r))} = \frac{1}{2(1 - \mathrm{Cor}(I, I_r))}. \tag{4.6}$$

The correlation coefficient and the scintillation correction factor are the metrics used to measure the performance of this technique. To achieve any correction in scintillation noise a correlation coefficient of greater than 0.5 is required. In order to halve the scintillation RMS noise, a scintillation correction factor of 4 is needed and thus a correlation coefficient of 0.875 is required. Fig 4.13 shows the relationship between the scintillation correction factor and correlation coefficient, helping to visualise the correlation coefficient required for scintillation correction levels. It also indicates the effect of noise on the data reduction optimisation as discussed in Section 4.5.3.

4.3 On-Sky Experiment

The data presented in this chapter were recorded on the 19th of September 2021 using the INT at the Roque de los Muchachos Observatory in La Palma. This proof of concept experiment was designed with a single WFS and stereo-SCIDAR turbulence profiler attached to the INT. The single 10×10 WFS was used to measure the wavefront aberrations for all three of the stars. The WFS data was also used to perform the aperture photometry. This greatly simplified the data acquisition as only a single camera was needed to collect all of the tomographic

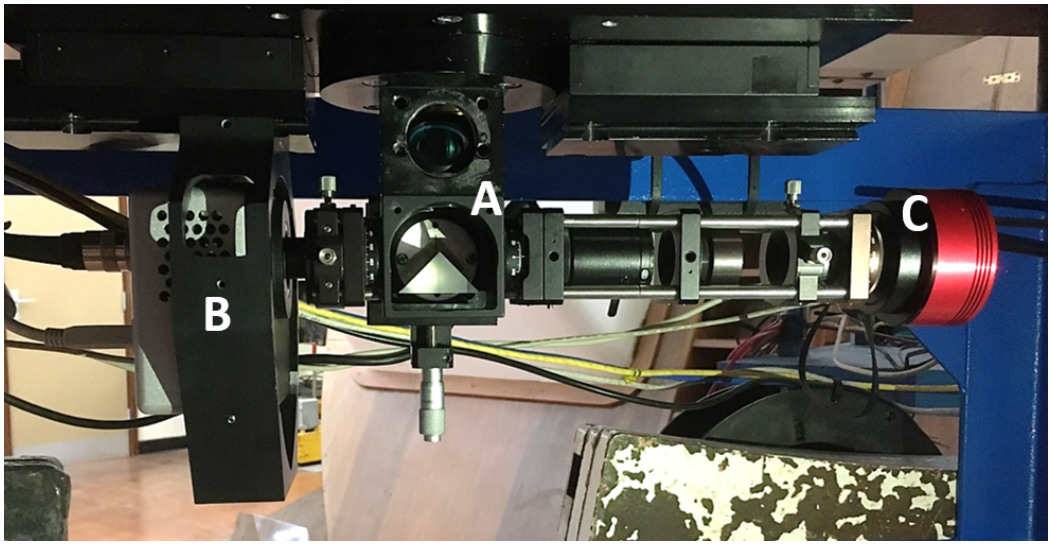

Figure 4.1: A photo of the instruments connected to the INT. Label A shows the prism that is used to divert the telescope focus into one instrument or the other, label B shows the SCIDAR instrument and label C shows the WFS optics and detector.

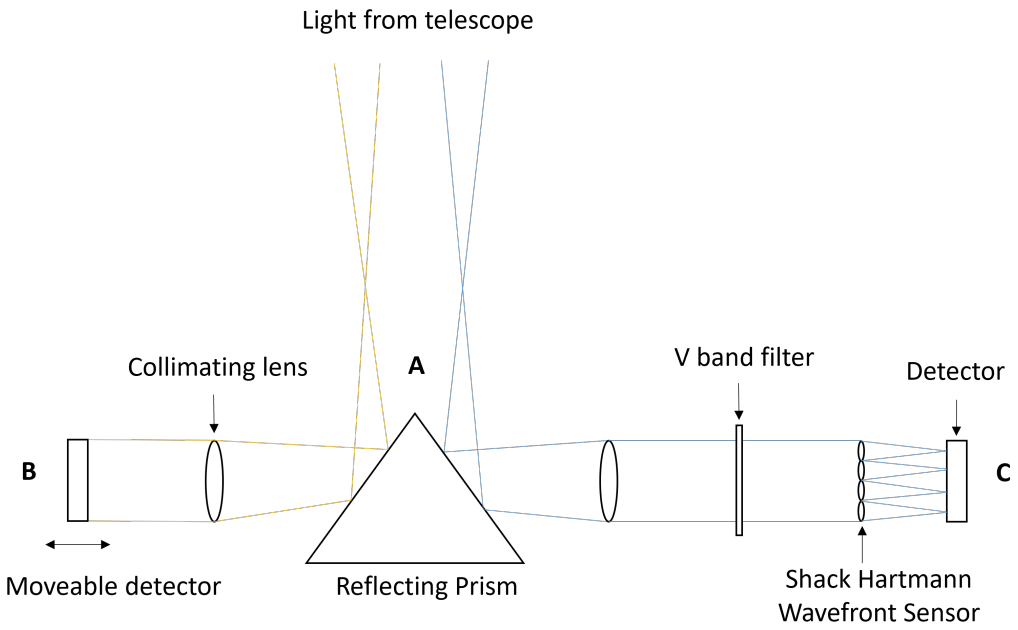

Figure 4.2: A ray diagram showing the instruments connected to the INT. Label A shows the prism that is used to divert the telescope focus into one instrument or the other, label B shows the SCIDAR instrument and label C shows the WFS optics and detector.

and photometric data and ensured the two were synchronised. Fig. 4.1 shows a photograph and Fig. 4.2 shows a ray diagram of the SCIDAR and WFS instruments attached to the INT. The SCIDAR measurements and WFS data measurements were taken in succession with the reflecting prism at label A used to switch between the two instruments by offsetting the telescope. Hence, the profiling and WFS measurements were not taken simultaneously.

The WFS optics comprised of a collimating lens, V band filter, a lenslet array and a detector. A ZWO ASI 1600MM camera was chosen as a suitable detector for the WFS frames due to the CMOS camera's large format, meaning all the stars WFS data can be encompassed, and fast readout with low read-out noise meant that short exposure times could be used. The photometric performance of the camera is also of good standard, although it was found that the bias level varied from frame to frame. Hence, a bias level was measured and subtracted for each frame.

At this time of year, in September, the Trapezium Cluster did not rise until early in the morning, reaching an altitude of 40 deg around 5:30 am. Hence, the observations were taken at a low elevation angle. Throughout the observations, the Trapezium was rising and thus changes in airmass added systematic trends to the photometry.

In simulation it was found that the technique works well using exposure times much longer than those typically used for AO correction. This is because both the wavefront measurements and intensity fluctuations average over time in the same way. Therefore averaging the wavefront measurement does not bias the reconstructed intensities. Hence, good correction can still be achieved with longer exposure times so long as the temporal fluctuations remain detectable. In addition, because the correction is performed in post-processing and open loop, a very short exposure time is not necessary. A range of exposure times were used to investigate the correction performance as a function of exposure time used. The WFS data was collected in contiguous data packets of 50 frames with exposure times of 0.01 s, 0.1 s and 1 s. In simulation a 0.1 s exposure time resulted in the highest scintilla-

tion correction factors. This can be understood by considering the power spectrum of the intensity fluctuations and is discussed further in section 4.5.4.

4.4 Data Reduction

There are multiple steps to performing the data reduction which are outlined below. Each step was optimised to achieve the best performance.

1. The centroids for each of the three stars of interest are measured from the WFS data.
2. The aperture photometry of the target star is measured from the WFS frames.
3. The measured star centroids are converted to Zernike modes using a Zernike decomposition matrix.
4. The SCIDAR data is used to estimate the turbulence profile and an optimal grouping method (Saxenhuber et al., 2017) is used to compress the profile to fewer layers.
5. The tomographic reconstruction matrix is produced using the estimated turbulence profile and star cluster geometry and is applied to the measured Zernike slopes to get the reconstructed phase at each altitude.
6. The reconstructed phase is used numerically with Fresnel propagation to produce an estimate for the scintillation pattern across the telescope pupil.
7. The measured target light curve is normalised using the summed estimated scintillation patterns and the correlation coefficient and scintillation correction factor is measured.

In this section, each step in the data reduction pipeline is given in more detail with information on the optimisation performed for each step.

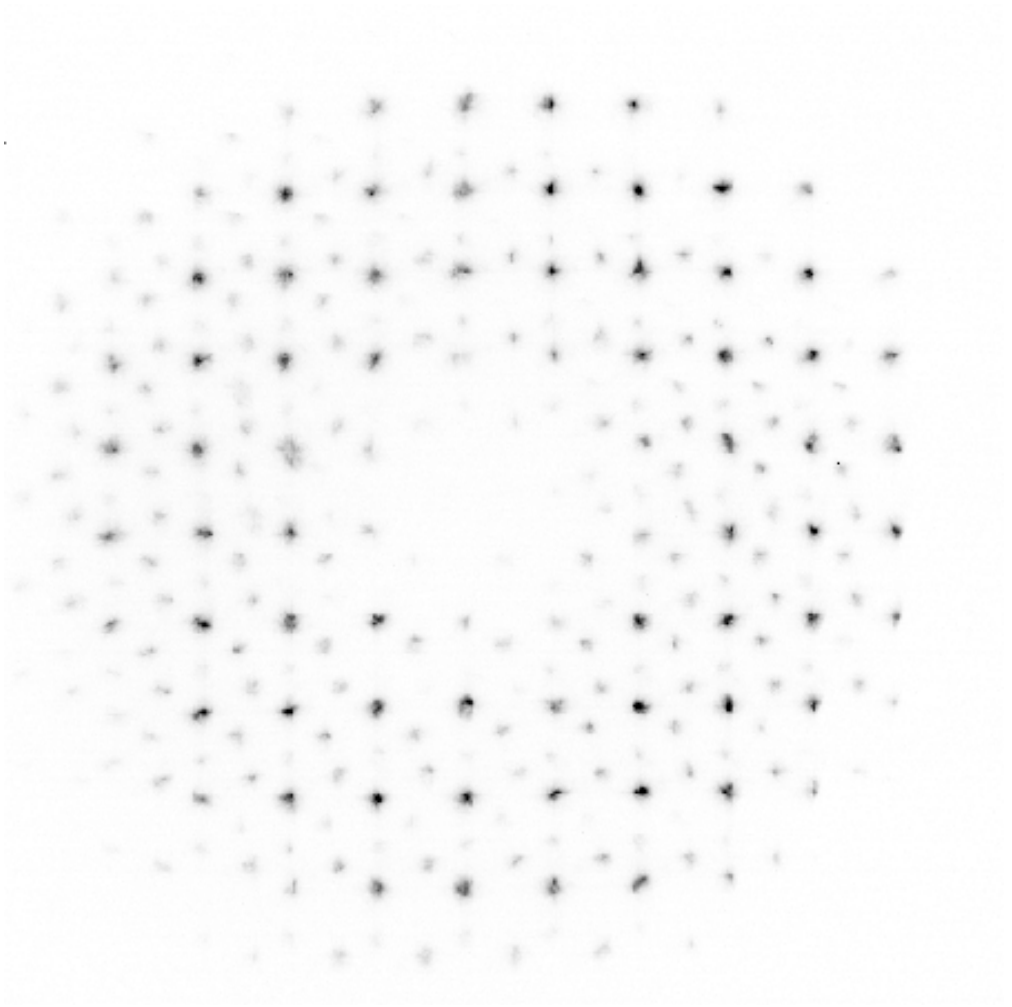

Figure 4.3: Example of a 0.1 s WFS frame. The colours have been inverted and a maximum pixel value set such that the fainter stars can be more easily seen.

4.4.1 Centroiding

The use of a single WFS to measure the spot centroids for all three stars, whilst greatly simplifying the data acquisition, created more challenges for measuring the centroids and performing the aperture photometry. Fig. 4.3 shows an example image of a 0.1 s WFS frame. The image produced by each subaperture is crowded, with 4 stars in each. As such, windowing was required to prevent contamination from neighbouring stars and masking was used.

As can be seen in Fig. 3.12, there is a faint companion star next to Theta-1 Orionis

Table 4.1: A table of the average photometric SNR measured for the target star in each subaperture for each exposure time.

Exposure Time	0.02 s	0.1 s	1 s
Measured SNR	13	21	50

C labelled as F. This faint star, V = 10.2, can also be seen in the WFS data. Due to its close proximity to the target star, it is included in the aperture photometry. Hence, some noise is introduced. However, this star is significantly fainter than the target star and hence any noise addition will be small.

The target star is significantly brighter than the other reference stars and if it strays into the window of the neighbouring star, its intensity significantly skews the measured centroid. As such, once the centroids of the target star had been measured, a mask was applied to each frame to block out the light of the target star for each subaperture, thus reducing contamination from the target star in measuring the centroids for the other, fainter stars.

The Centre of Gravity (CoG) method was used with optimal windowing and thresholding. The optimisation was performed by maximising the scintillation correction performance. Each subaperture had a width of 42 pixels. A window centred on the average spot position of each star corresponding to each subaperture was used. A window of 18×18 pixels for the brighter target star and 16×16 pixels for the companion stars was found to be optimal, with a threshold of 0.4. Fig. 4.4 shows the C_{scint} achieved for a data packet against the window size. A peak around 16 pixels can be seen. For windows larger than 20 pixels the correction drops significantly due to contamination from the neighbouring stars. Fig. 4.5 shows the C_{scint} against threshold value for a single data packet. The threshold required is relatively low. This is likely due to the stars being very bright and in small windows. Therefore, the background noise is low. In total, 75 subapertures were used in the tomographic reconstruction. Table 4.1 shows the average photometric SNR measured for over all subapertures for each exposure time.

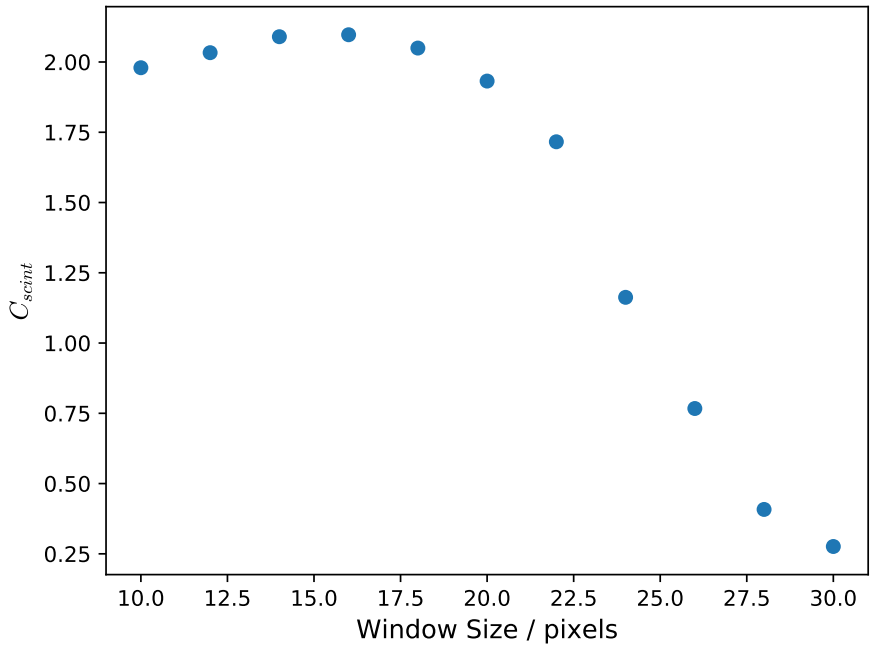

Figure 4.4: The scintillation correction factor achieved for a 0.1 s data packet as a function of the WFS CoG windowing used.

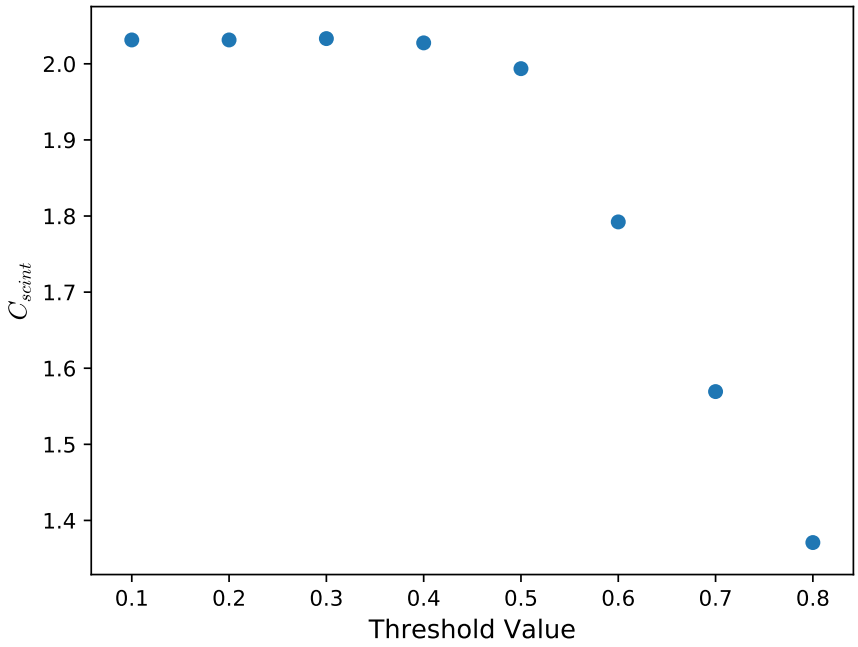

Figure 4.5: The scintillation correction factor achieved for a 0.1 s data packet as a function of the WFS CoG thresholding used.

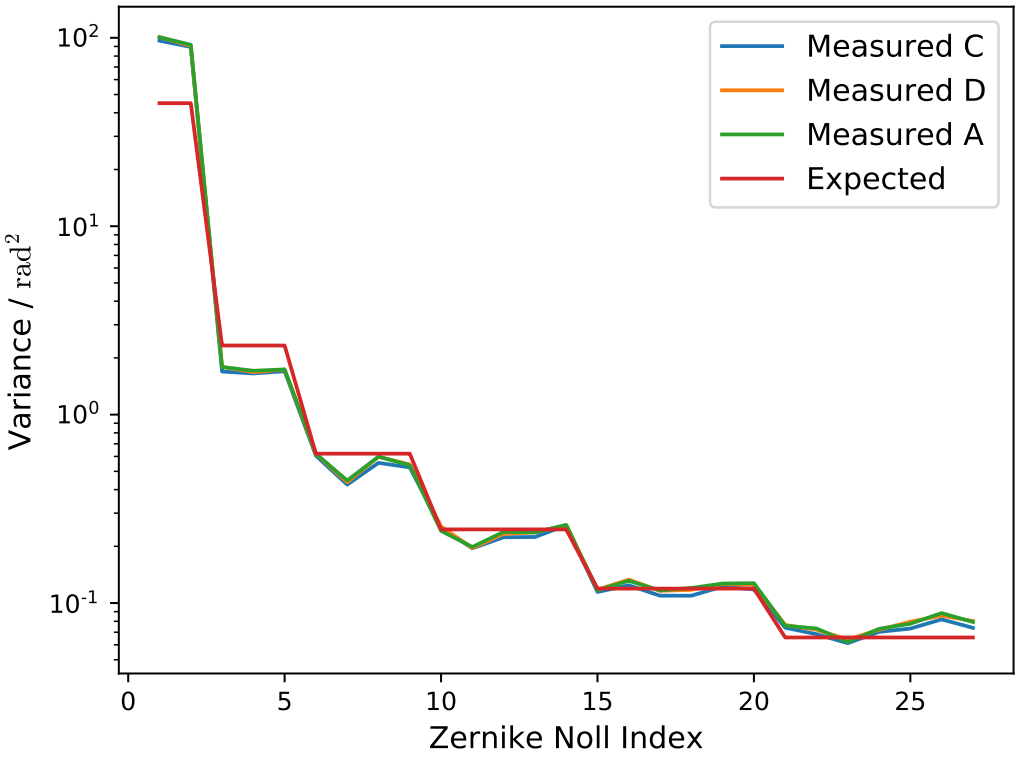

Figure 4.6: The measured Zernike mode variance for Theta-1 Orionis C, D and A. The expected variance for $r_0 = 0.16$ m is also plotted.

4.4.2 Zernike Decomposition

Converting the centroids to Zernike modes was done using a Zernike decomposition matrix. As shown in Fig. 4.6, the measured variance of the reconstructed Zernike modes across the telescope aperture for each star closely follows the expected variance for Kolmogorov turbulence, for $r_0 = 0.16$ m measured from the SCIDAR profiles (Noll, 1976). This suggests the Zernike decomposition (ming Dai, 1996) has been implemented accurately and that the average r_0 value has not changed significantly over the data run. The excess variance for the first order modes (tip/tilt) is likely due to tracking errors.

Since scintillation noise is produced by the low order spherical modes of the incoming wavefront in high turbulent layers, the most significant modes that need to be measured are the low order spherical modes. Fig. 4.6 shows that the atmospheric

phase variance associated with low order modes is much greater than for higher order modes, as expected. Using higher order modes adds noise to the reconstruction whilst providing little additional atmospheric correction.

The number of Zernike modes used in the tomographic reconstruction matrix was optimised for each individual data packet by finding the maximum scintillation correction as a function of the number of modes used to perform the correction. All the layers were reconstructed with the same number of Zernike modes. The average measured scintillation correction factor as a function of the Noll index for the 0.1 s data packets is shown in Fig. 4.7. A peak around 8 modes is seen. Including higher orders in the reconstruction matrix, reduces the scintillation correction factor achieved. This suggests that only low orders are required for the scintillation correction. This is to be expected as the defocus term (j=4) of the high altitude turbulence makes the largest contribution to the intensity fluctuations.

4.4.3 Photometry

Aperture photometry was performed on the target star in each subaperture and summed over all the subapertures. An annulus was used to measure the median background value for each subaperture to correct any field dependent background noise.

The crowding of WFS images resulted in several challenges in performing the photometry. Firstly, the crowded field severely limited the size of the aperture that could be used to perform the photometry. In addition, measuring an accurate sky background was challenging due to nearby stars contaminating the annulus. To overcome this, a mask was applied to the annulus to try to avoid contamination by neighbouring stars skewing the measured background. A standard SNR versus aperture plot could not be used to determine the optimum aperture size to use since beyond a certain size the aperture was contaminated with the light from the neighbouring stars. Hence, the size of aperture used had to be optimised based on

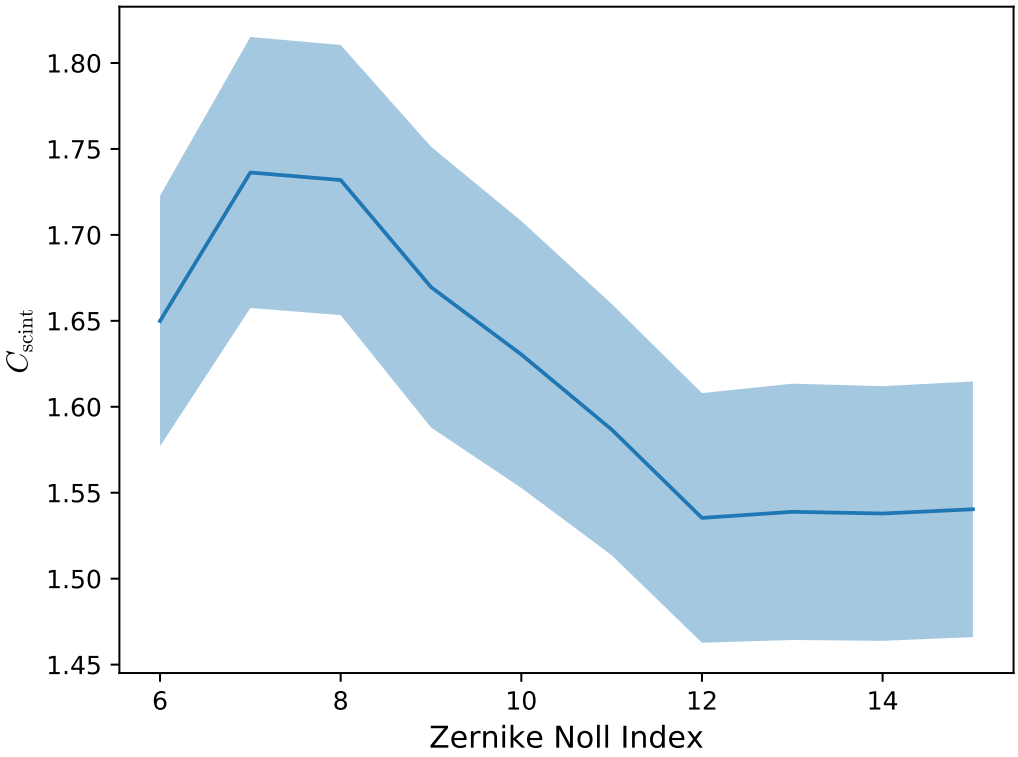

Figure 4.7: The average measured scintillation correction factor as a function of the Noll index for the 0.1 s data packets. A peak around 8 modes suggest that only low orders are required for the scintillation correction.

the tomographic scintillation correction performance achieved. In addition, measuring the photometry with the subapertures also increased the total read-out noise. However, it is still an insignificant noise source in comparison to the scintillation noise as shown in table 4.2.

The light curve obtained also contained slowly varying systematic trends. These are most likely due to changes in the airmass during the observation as the observations were taken at low elevations, as well as irregularities across the field. These could not be corrected via standard differential photometry due to the addition of random intensity fluctuations from the fainter comparison stars since the shot noise of the fainter comparison stars will dominate the measurement. Hence, a curve fitting algorithm was used to correct these low order systematic trends. A low order polynomial was fit to the entire light curve and used to remove the systematic

Table 4.2: A table to compare the measured scintillation index and SNR to the expected scintillation index and SNR from the theory.

Exposure Time	0.01 s	0.1 s	1 s
Expected Scintillation Index	1.9×10^{-5}	4.4×10^{-5}	4.4×10^{-6}
Average Measured Scintillation Index	3.7×10^{-5}	4.2×10^{-5}	7.6×10^{-6}
Average Measured Scintillation RMS	6.1×10^{-3}	6.5×10^{-3}	2.8×10^{-3}
Expected Shot Noise RMS	4.7×10^{-4}	2.1×10^{-4}	6.0×10^{-5}
Read-out Noise RMS	6.2×10^{-5}	1.2×10^{-5}	1.2×10^{-6}

trends (Poddaný et al., 2010) (Tamuz et al., 2005). This is not ideal as it is difficult to distinguish between systematic trends and low order scintillation variations. However, the power spectrum of the low order systematic trends shown in Fig. 4.11 clearly shows the power is in much lower frequencies than the frequency of the peak in the power of the scintillation. Thus, it is likely to be primarily low order systematics that were corrected and not scintillation noise. In addition, this correction maximised the scintillation correction performance achieved.

The expected scintillation index was estimated using the median of the measured SCIDAR turbulence profiles in equations 2.19 or 2.20. As can be seen in Table 4.2, the average measured scintillation index is close to the expected scintillation index for the turbulence profile for the 0.1 s data. In addition, the measured scintillation noise far exceeds the expected shot noise and read noise and thus it can be confidently concluded that the observations are limited by scintillation noise.

4.4.4 Turbulence Profiles

To perform the tomography, the turbulent layer heights and relative strengths must be known. The turbulence profile is required to produce the projection matrices and the Zernike Kolmogorov turbulence covariance matrix in the tomographic reconstruction matrix given in section 2.4.

The median SCIDAR data taken 8 minutes before the start of the WFS run was used to estimate the turbulence profile above the telescope during the WFS observations. The median SCIDAR profile was then grouped into layers using the

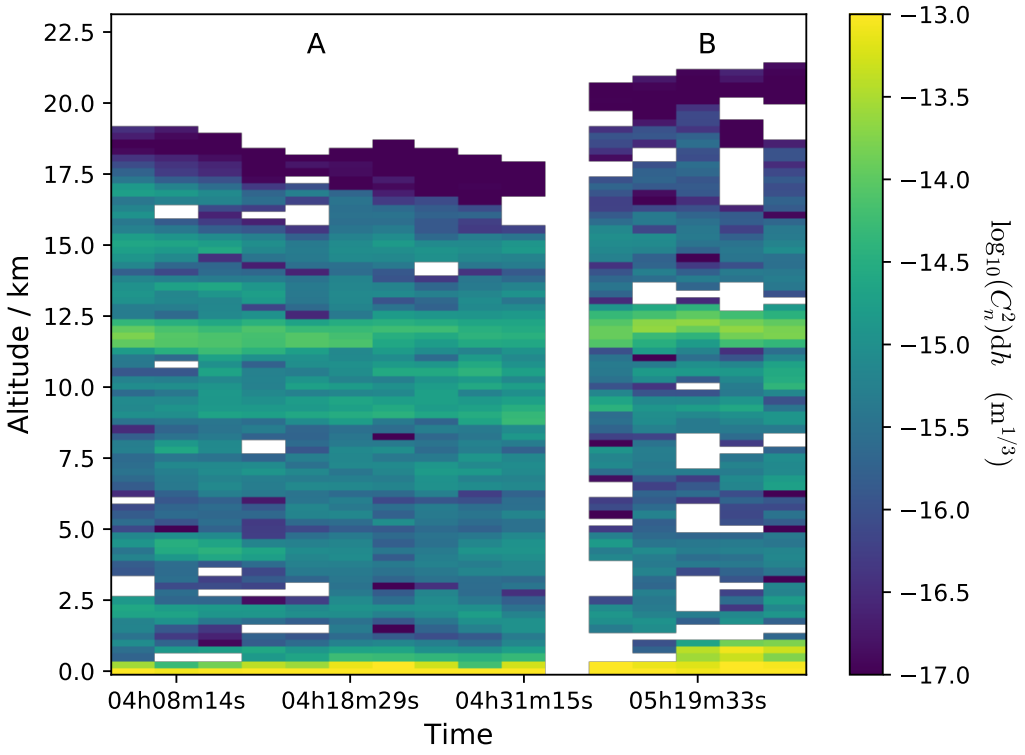

Figure 4.8: The turbulence profiles measured over 1.5 hours of the night of the 19th of September. The observations are split into observing period A and B with a gap between the observations plotted. A strong turbulent layer is seen at the ground and at 12 km.

optimal grouping algorithm. This grouping method was selected as it was found to be optimum in terms of tomographic performance (Saxenhuber et al., 2017).

Fig. 4.8 shows the turbulence profiles measured on the night beginning 19th of September 2021. The turbulence profiles observed at 4am in observation period A, have a strong layer at the ground and a strong layer around 12 km but with many weaker layers in-between. After 5am, in observing period B, the strength of the high altitude layer has increased and there are clearly two dominant layers, one at the ground and one at 12 km. Hence, this chapter focusses on the WFS data collected from 5:30 am onward, where the profile is dominated by two strong layers and thus the tomographic reconstruction is simplified.

It should be noted that the turbulence conditions were not optimal for this demonstration. Whilst there is a dominant turbulent layer at 12 km, it does not produce

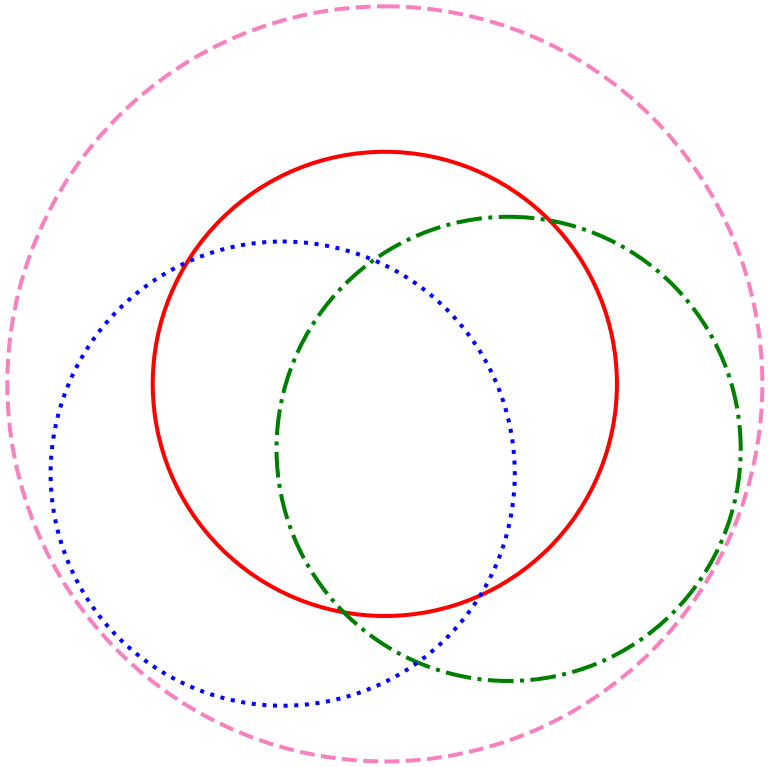

Figure 4.9: The overlap in WFS measurements for the three stars used in the tomographic reconstruction at 12 km. The target star, Orionis C, is placed in the centre of the meta-pupil and is shown in red, with Orionis D in green dash-dotted, and Orionis A in blue dotted.

strong scintillation due to its low C_n^2 value of 5.9×10^{-14} m$^{-2/3}$. In addition, the profile is heavily dominated by the strong ground layer and the substantial dome seeing.

Fig. 4.9 shows there is significant overlap between the WFS measurements at the 12 km layer and hence good sampling of this dominant layer for the tomographic reconstruction in the overlapped region is achieved. However, there is a large region that is not sampled by the stars which will limit the correction that can be achieved.

4.4.5 Tomographic Reconstruction

The tomographic reconstruction matrix, given in Eq. 2.38, was produced using the median five layer turbulence profile measured for the five profiles measured

between 5:14 and 5:24 am and the geometry of the Orion Trapezium Cluster. Five layers were used in the reconstruction matrix as no benefit was found in using more layers. A reconstruction matrix was produced for each data packet using the optimal number of Zernike modes.

The reconstruction matrix was then applied to the measured Zernike coefficients for all three of the stars to produce an estimate for the phase aberrations at each of the five altitudes. A python package, `AOtools` (Townson et al., 2019), was used to Fresnel propagate the reconstructed high layer phase aberrations metapupils to the ground to produce an estimate for the scintillation intensity fluctuation pattern at the ground. The telescope pupil was then cut out from the scintillation pattern metapupil (thus avoiding the artificial diffraction rings at the edge) and summed to estimate the intensity. This is then repeated for each frame to produce a temporal estimate of the intensity variance. For each data packet, C_{scint} and r are computed.

4.5 On-Sky Results: Orion Trapezium

4.5.1 Example Light Curve

In order to remove some of the high frequency noise such that the correlation can be more clearly seen, the light curves were temporally binned by a factor of 2. Hence, the effective exposure times used are 0.02 s, 0.2 s and 2 s.

Fig. 4.10 shows the measured normalised intensity and the reconstructed normalised intensity for the best performing 0.2 s data packet. This data packet has an SNR of 197 and a scintillation RMS noise of 5.1×10^{-3}. For a star of magnitude 5.13 in the V band, for a 0.2 s exposure time for the instruments used a shot RMS noise of 1.6×10^{-4} is expected. Hence, it can be confidently concluded that the overall SNR is dominated by scintillation.

The correlation coefficient between the measured and reconstructed intensities of this data packet is 0.86. The strong correlation between the measured and recon-

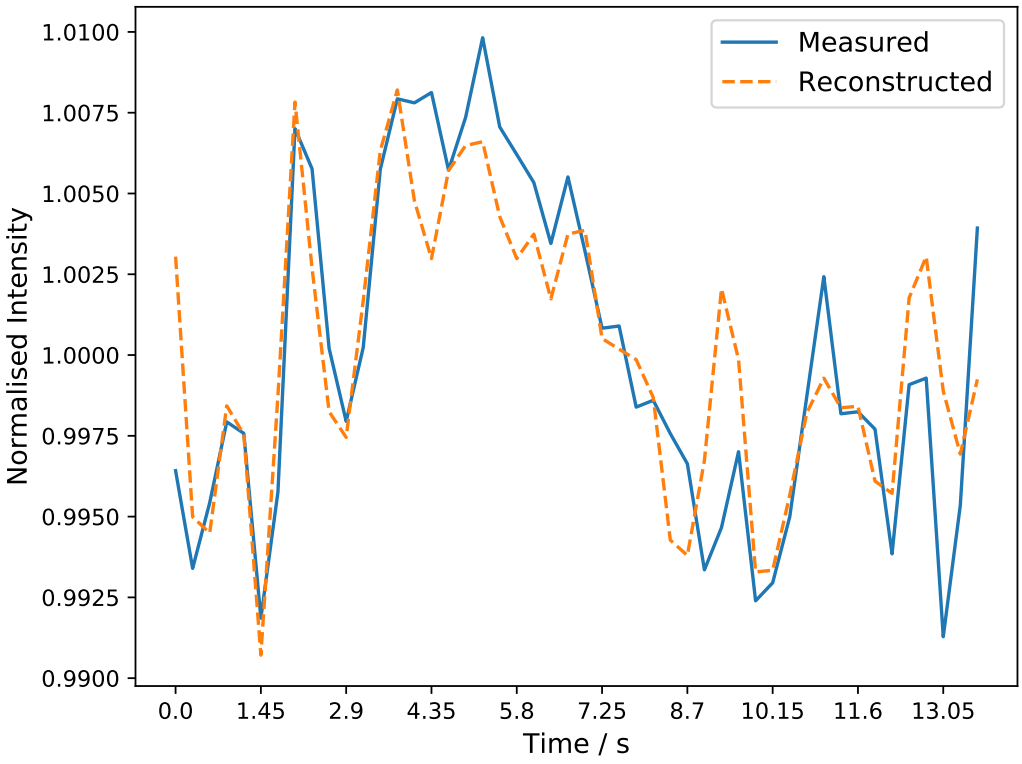

Figure 4.10: The measured normalised intensity and the normalised tomographically reconstructed intensity for the best performing 0.1 s data packet. The intensity was temporally binned by a factor of 2.

structed light curves shows that the tomographic reconstruction is correctly estimating the low frequency intensity variations. Normalising the measured photometry of this data packet with the reconstructed intensity reduced the scintillation index by a factor of 3.41, corresponding to a reduction in the scintillation RMS noise by a factor of 1.85.

4.5.2 Power Spectrum

Fig. 4.11 shows the average power spectra of the uncorrected and corrected light curves for the 0.1 s data packets for which a correction of at least 2 in the variance was achieved. The power at low frequencies has been significantly reduced in the corrected light curve. In addition, the power spectra for the measured defocus Zernike term of the high altitude turbulent layer at 12 km is also plotted. The

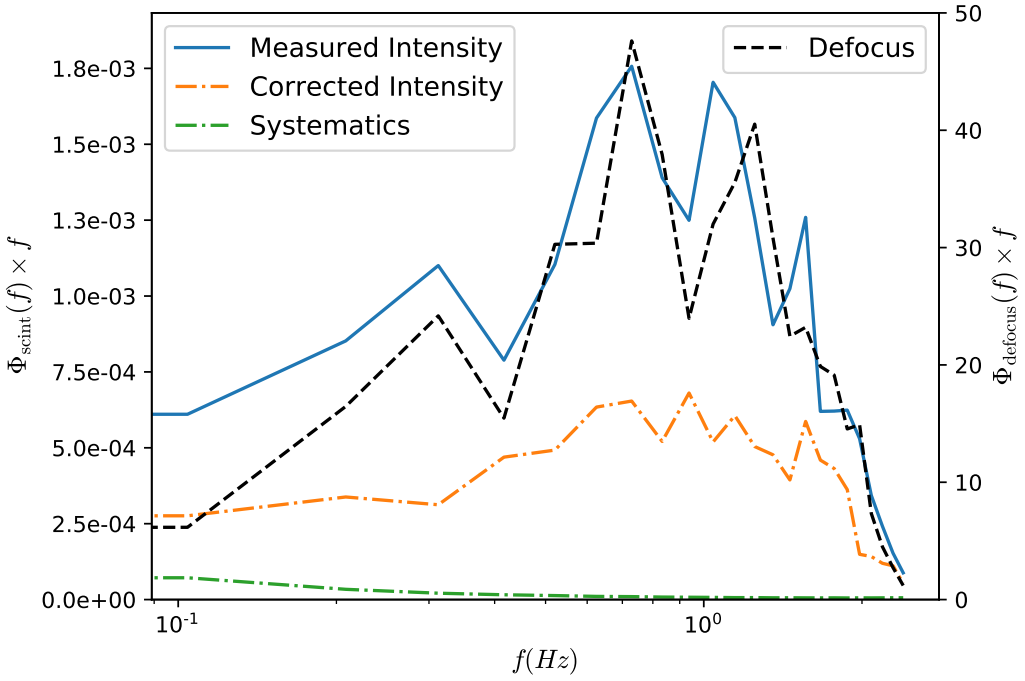

Figure 4.11: The average power spectra for the measured and corrected light curves is plotted using the left y-axis. The power spectrum for the measured systematic trends is also plotted. The power spectrum for the defocus Zernike mode measured for the 12 km turbulent layer is also plotted using the right y-axis.

shape of the power spectra of the measured intensity strongly resembles the power of the high altitude defocus Zernike term. This has been discussed in section 3.4.1. Since there is no significant power above a few hertz, exposure times of a few tenths of a second can be used.

Since this on-sky proof of concept experiment has several limitations, the fact that such high correlation has been measured and that an average correction in the scintillation variance of ~ 2 has been achieved, demonstrates the potential of the correction technique. It is expected that with a full tomographic WFS system, substantially greater scintillation noise correction would be achieved.

4.5.3 Performance Metrics Results

Fig. 4.12 shows a histogram of the measured correlation coefficient. The median correlation coefficient that was measured for all the data packets was 0.67 with a

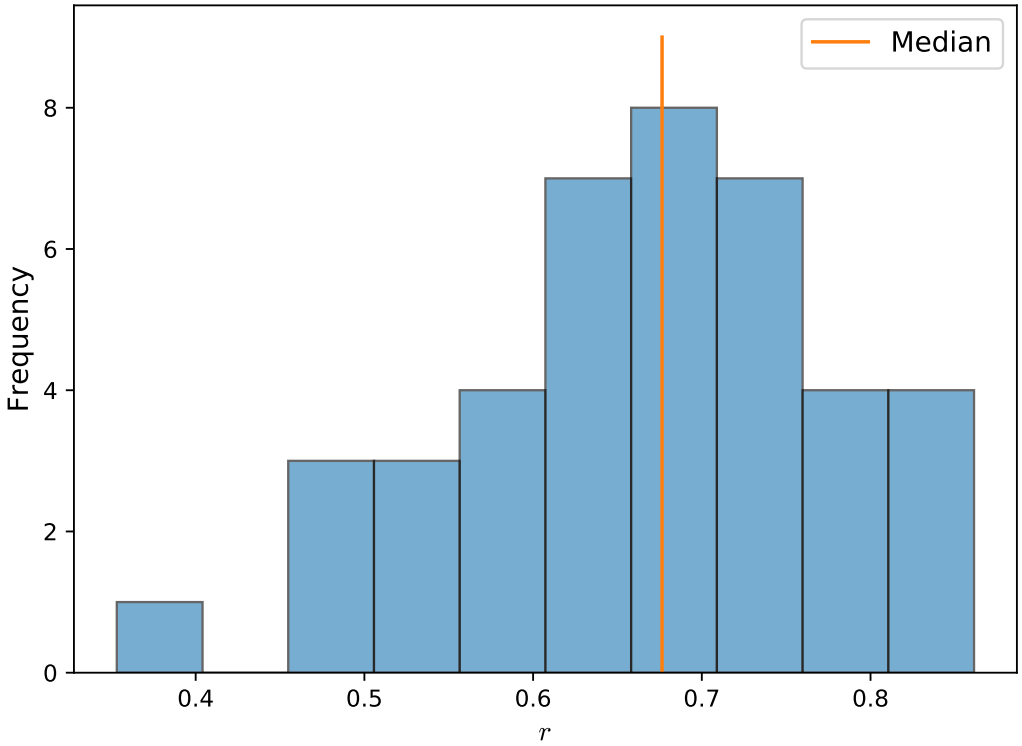

Figure 4.12: A histogram of the measured correlation coefficient between the measured intensity and tomographically reconstructed intensity. The median of the measured correlations is also plotted.

standard deviation of 0.11. The maximum correlation coefficient recorded was 0.86. These relatively high correlations show that the tomography is correctly estimating the phase aberrations of the high altitude layers and thus the scintillation pattern. To achieve any correction in the scintillation, a correlation coefficient of more than 0.5 is needed, which is achieved 88% of the time.

There is a considerable scatter in the correlation coefficient measured. Simulations show that some statistical scatter is to be expected for measurements of short data packets. However, the observed scatter is much larger than would be expected. This may be explained by variations in the turbulence profile from packet to packet. This may be particularly problematic for the ground layer and dome seeing which vary significantly.

Fig. 4.13 demonstrates the relationship between the correlation measured and the

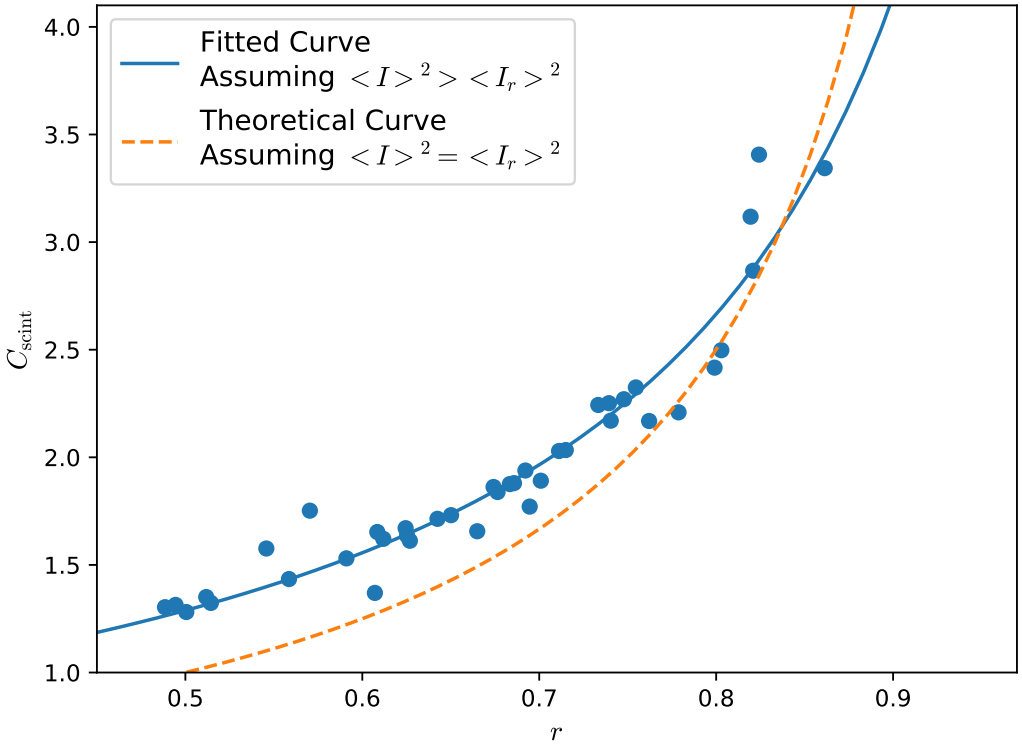

Figure 4.13: The measured correlation coefficient as a function of the measured Scintillation correction Factor with the theoretical curve for $\langle I \rangle^2 = \langle I_r \rangle^2$ and the fitted curve where $\langle I \rangle^2 > \langle I_r \rangle^2$.

scintillation correction performance. The theoretical curve from Eq. 4.6, which assumes $\langle I \rangle^2 = \langle I_r \rangle^2$, is plotted in orange. The measured performance, with a fitted curve in blue where $\langle I \rangle^2 > \langle I_r \rangle^2$ in Eq. 4.5, achieves slightly higher performance at low correlations. This is likely favoured in the optimisation of the data reduction parameters due to the presence of noise in the reconstructed signal, as discussed in section 3.4.5. It is likely there are small scaling errors in the Fresnel propagation due to not having exact knowledge of the true turbulence profile for each data packet. As demonstrated in Fig. 3.14, overestimating the altitude of the high altitude turbulence layer significantly limits the C_{scint} achieved and hence in the optimisation, underestimating the turbulence layer altitudes, and hence the variance of the reconstructed signal, is favoured.

Assuming $\langle I \rangle^2 = \langle I_r \rangle^2$, to halve the scintillation index, a correlation coefficient of at least 0.75 is needed. A scintillation correction factor of 2 or more was achieved

Table 4.3: The measured average and peak C_{scint} for each exposure time.

Exposure Time	0.02 s	0.2 s	2 s
Average C_{scint}	1.35 ± 0.03	1.92 ± 0.08	1.48 ± 0.15
Peak C_{scint}	1.54	3.41	3.53

for 35% of the 0.2 s data packets.

4.5.4 Exposure Time

Table. 4.3, shows the average scintillation correction factor and peak correction factor measured as a function of the exposure time used. The 0.2 s data results in the largest correction factor. This result agrees with our findings from numerical simulation given in section 3.4.1 and is expected from the power spectrum given in Fig. 4.11.

The 0.02 s data has the lowest correction factor whilst the 2 s data still achieves good performance. This demonstrates that relatively long exposures can be used to perform tomographic reconstruction in this way. Hence, exposure times and frame rates can be used which are closer to those typically used for time-resolved photometry rather than AO correction. It should be noted that the optimum exposure time for this technique increases with telescope size. Hence, for larger telescopes longer exposures can be used.

4.5.5 Expected Performance Simulation

A numerical simulation was produced to determine the expected scintillation correction performance for the measured SCIDAR profiles in observing period B in Fig. 4.8. This was used to determine whether the correction achieved is close to what could be expected for such turbulence profiles and, in particular, whether the correction is limited due to the lack of simultaneous profiling.

The profiles given in section 4.4.4 were used to estimate the expected performance. Each profile was grouped into fifteen layers using the optimal grouping technique.

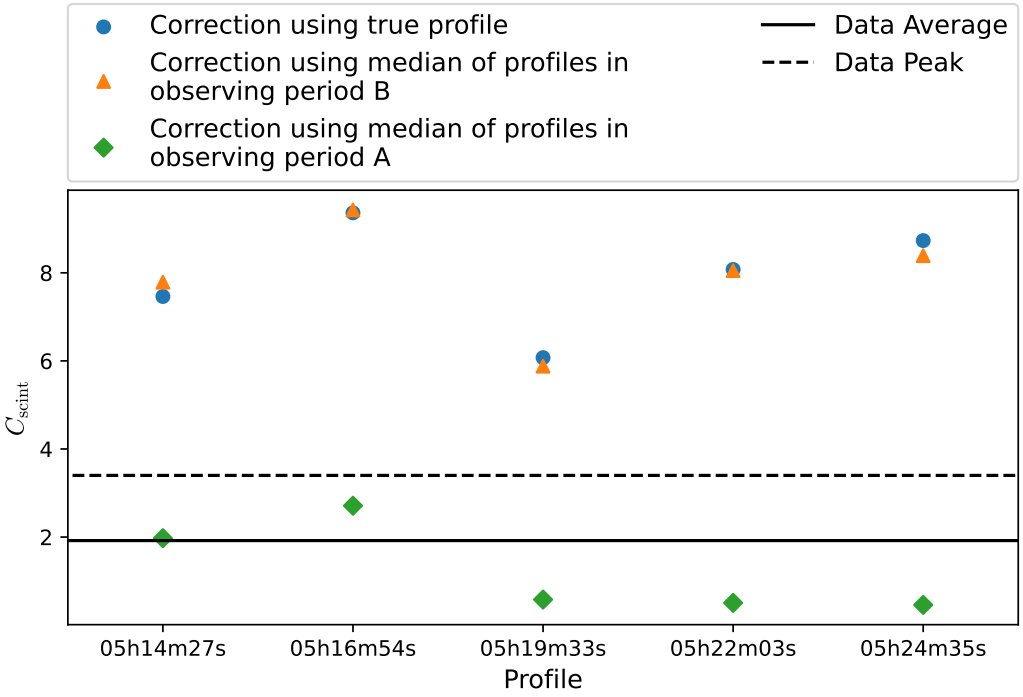

Figure 4.14: The measured scintillation correction factor in simulation for each turbulence profile. The performance is plotted for several reconstruction matrices using either the true turbulence profile, the median of the profiles measured in observing period A and the median of the profiles measured in observing period B. The average and peak performance for the WFS data collected after 5:30am is also plotted.

These profiles were used to simulate a Monte Carlo phase screen representation of the atmosphere. The simulation assumes that the WFS can measure the atmospheric Zernike terms perfectly with only shot noise added to the WFS data. In addition, the simulated target light curve is completely scintillation limited with no other noise sources. The simulation also assumes perfect measurement of the turbulence profile.

The tomographic reconstruction was then performed on each profile using a five layer estimate for the turbulence profile. Five layers were chosen to correct the fifteen layer profiles in simulation in order to include some tomographic model error in the simulation and thus simulate a more realistic performance that can be achieved. In practice, C_n^2 is a continuous function which is approximated with a discrete number of layers, N, in the reconstruction matrix, and thus there will

always be some model error. It was found that with $N > 5$ layers there is little difference in the performance and therefore the model error is small.

The median five layer profile observed between 5:14 am and 5:24 am in observing period A was also used to correct the simulated intensity. This was to test the performance of the median profile over the 5 profiles measured and to justify its use for the data collected as little change in the performance is seen. In addition, the median five layer profile measured by the SCIDAR run between 4:05 am and 4:30 am in observing period B was used to determine how significantly the profile has changed over the 45 minutes between the two SCIDAR runs.

As can be seen in Fig. 4.14, the measured performance varies from profile to profile. The median profile in observing period B shows reasonable performance, whilst using the median profile in observing period A, measured 45 minutes prior, performs badly. This can be expected, as the profile has changed between the two runs as seen in Fig. 4.8. This demonstrates the necessity for regular profiling to perform accurate tomographic reconstruction.

Comparing the scintillation correction performance obtained using the real data with the expected performance from the simulation of the SCIDAR profiles shows that the measured performance is lower. This is to be expected as the simulation assumes perfect measurement of the turbulence profile above the telescope as well as perfect photometry and Zernike wavefront sensing. Hence, the simulation provides an upper limit for the scintillation correction that can be expected.

The average and peak scintillation correction results for the data are on average better than those measured in simulation using the median profile in observing period A. This suggests that the turbulence profile has not changed as significantly between the SCIDAR observing period B and the wavefront sensing. However, it may have still changed enough to reduce the correction performance. It is expected that simultaneous turbulence profiling would provide improved performance, and would allow the reconstruction matrix to be updated as regularly as is required.

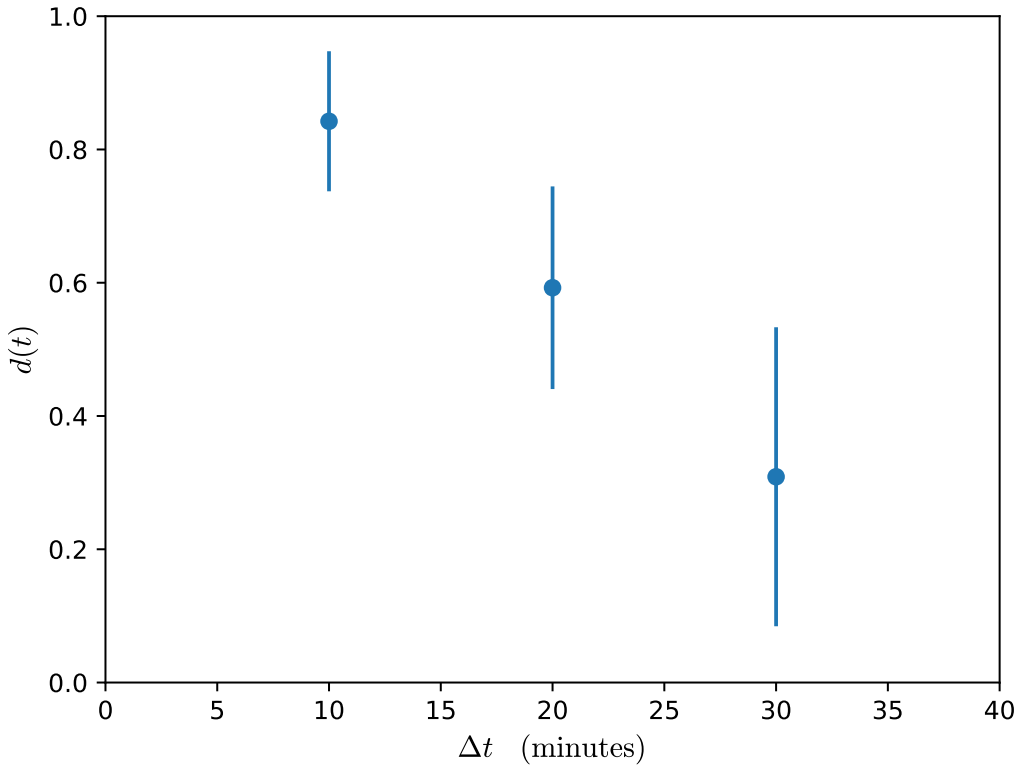

Figure 4.15: The fractional reduction in the scintillation correction factor between $t = \Delta t$ and $t = 0$ as a function of time. The error bars are the standard error of all the profiles used.

4.6 Implications for facility implementation

In this section, results from simulations are presented to demonstrate the expected scintillation correction performance that could be achieved on a full tomographic AO system.

4.6.1 Updating the Tomographic Algorithm

Based on the on-sky results, it is important to assess how regularly the tomographic reconstruction matrix needs to be updated.

Farley et al. (2020) explored how regularly the tomographic reconstruction matrix must be updated for AO on the ELT, with results suggesting that 20 minutes is

optimal. The same turbulence profile data has been used to see how the scintillation correction performance changes with the time interval.

It is expected that for scintillation correction, the turbulence profile used will need to be updated more regularly than for AO correction. This is because for scintillation correction, not only is knowledge of the turbulence profile necessary to perform the tomography, but it is also needed to perform the Fresnel propagation. Hence, accurate knowledge of the turbulent layer heights is vital.

A numerical simulation was performed using SCIDAR profiles measured in Paranal in 2018. The tomographic error performance using the Trapezium asterism was measured over time. The tomographic error was compared for a tomographic reconstruction matrix using the current $t = \Delta t$ profile and the $t = 0$ profile. Profiles where the change in the relative tomographic error was close to the median value were selected. These median profiles at time t were simulated using a Monte Carlo phase screen representation of the atmosphere and the tomographic scintillation correction was performed both with the $t = \Delta t$ profile and the $t = 0$ profile, where $\Delta t = 10, 20$ & 30 minutes.

To quantify the difference in the performance achieved, the fractional change in the scintillation correction factor between using the $t = \Delta t$ profile and the $t = 0$ profile in the tomographic reconstruction matrix was measured such that:

$$d(t) = \frac{C_{\text{scint}}(t = 0)}{C_{\text{scint}}(t = \Delta t)} \tag{4.7}$$

Fig. 4.15 shows $d(t)$ as a function of time. The reduction in performance increases with the time interval. After 20 minutes there is already a 40% reduction in performance when the reconstruction matrix is not updated. This increases to 70% after 30 minutes. It is clear that using the current profile results in optimum performance and therefore regular simultaneous turbulence profiling on the timescale of ~ 10 minutes is required.

For the on-sky data presented in section 4.5 there was a lag between the SCIDAR observation and the start of the WFS run of 8 minutes. In addition, the WFS

data was collected over half an hour period. Hence, assuming the profile changed by a median amount over this time, and that on average $t \approx 20$; then based on Fig. 4.15, the correction measured is $\sim 40\%$ smaller than what could be achieved with simultaneous profiling. Therefore, with simultaneous turbulence profiling, the results presented in section 4.5.1 could have achieved an increased average C_{scint} of 3.2 and peak of 5.7. This would shift the on-sky results much closer to the optimal values given in Fig. 4.14.

4.7 On Sky Results: HD206267

In May 2022 the tomographic scintillation correction experiment was repeated on a different, less optimal target asterism, HD206267. The exact same experimental set-up described in section 4.3 was used.

4.7.1 Target

The on-sky target, HD206267, is a triple star system in the constellation of Cepheus. Full details of the asterism are given in section 3.4.3 and Fig. 4.16 shows a schematic of the system. HD 206267 is the central star which has an apparent magnitude of $V = 5.74$ and was used as the target on which the tomographic scintillation correction was applied. The two companion stars used as reference stars for the tomography, TYC 3975-1821-1 and TYC 3975-1823-1, have magnitudes of $V = 7.51$ and $V = 7.46$ respectively.

Fig. 4.17 shows the overlap in the WFS measurements at an altitude of 12 km. Comparing this to Fig. 4.9, which shows the overlap for the Trapezium Cluster, it is clear that the sampling of the high altitude turbulent layers is substantially reduced for the HD206267 target. Hence, it is likely the correction achieved will be reduced.

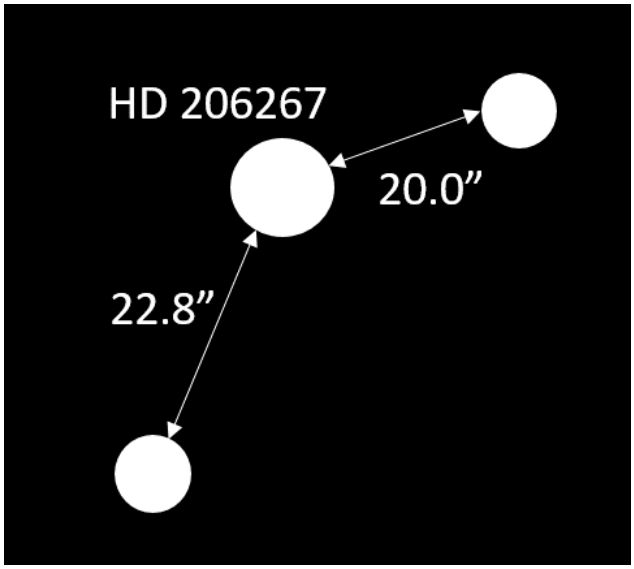

Figure 4.16: A schematic showing the triple star system HD 206267.

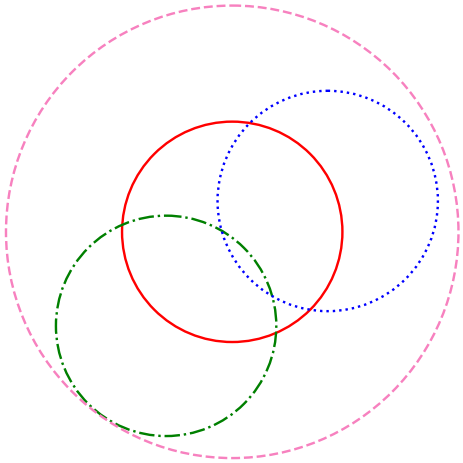

Figure 4.17: A schematic showing the overlap in the WFS measurements of the triple star system HD 206267 at an altitude of 12 km.

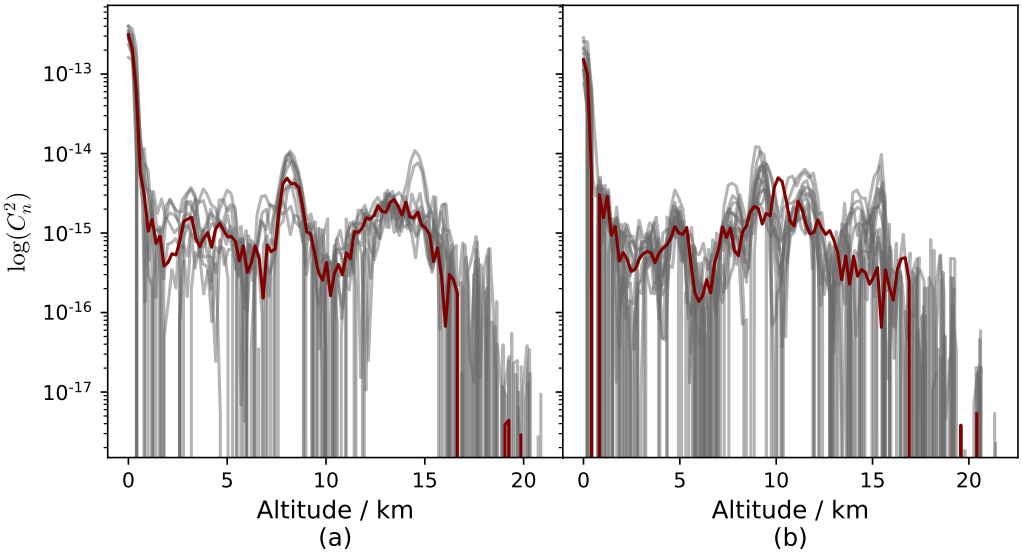

Figure 4.18: The SCIDAR turbulence profiles measured after 4am on (a) the 15/05/2022 and (b) 16/05/2022. The median profile for each night is plotted in maroon.

Table 4.4: A table of the performance of the scintillation correction achieved for the data collected observing HD206267 in May 2022.

Date & time	Data Packets	Median Correlation	Average C_{scint}	Peak C_{scint}
04:00 15/05/22	22	0.60 ± 0.18	1.61 ± 0.11	2.88
05:15 15/05/22	25	0.37 ± 0.18	1.17 ± 0.04	1.85
05:55 15/05/22	46	0.46 ± 0.15	1.22 ± 0.05	3.02
04:00 16/05/22	21	0.57 ± 0.10	1.55 ± 0.11	3.12
04:35 16/05/22	16	0.47 ± 0.12	1.28 ± 0.06	1.91
05:19 16/05/22	28	0.44 ± 0.17	1.29 ± 0.07	2.83

4.7.2 Results

The results for the 0.2 s WFS data-packets collected on the 15th and 16th of May are presented. Fig. 4.18 shows the SCIDAR turbulence profiles measured after 4:00 am on (a) the 15/05/2022 and (b) 16/05/2022 with the median profile for each night plotted in maroon. For each data-set, the median five layer SCIDAR turbulence profile observed preceding the WFS data observation was used.

Despite this asterism being fainter and larger than the Orion Trapezium Cluster, significant scintillation correction was still achieved. The average correlation and C_{scint} given in table 4.4 is reduced in comparison to the Orion Trapezium Cluster.

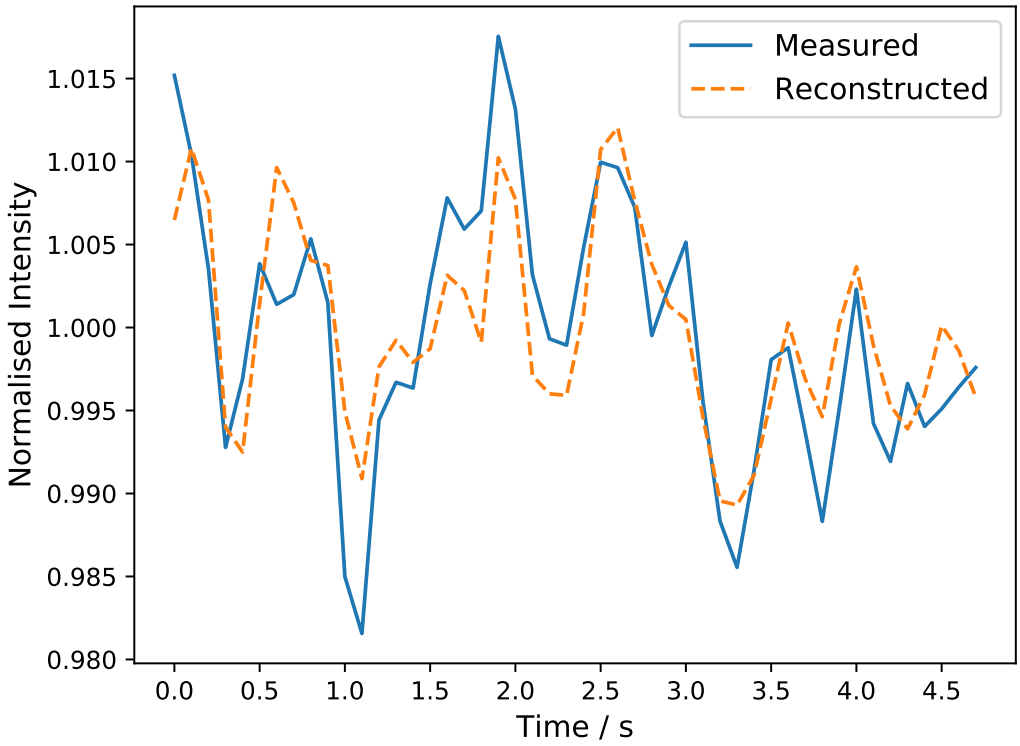

Figure 4.19: The measured normalised intensity and the normalised tomographically reconstructed intensity for the best performing 0.1 s data packet for HD206267. The light curve was temporally binned by a factor of 2.

However, the peak C_{scint} measured within each observing time slot is significant.

Fig. 4.19 shows the light curve with the best performing scintillation correction for HD206267. The measured scintillation RMS noise is 7.75×10^{-3} which is significantly larger than the expected shot noise for a $V = 5.74$ star of 1.98×10^{-4}. Hence, it is clear that the data packet is scintillation noise dominated. This data packet had a strong correlation of 0.82 which is clear from Fig. 4.19. Correcting the measured photometry results in a reduction in the scintillation index of $C_{scint} = 3.12$ which corresponds to a reduction in the scintillation RMS noise by a factor of 1.77.

4.8 Discussion and Conclusions

For bright targets, high-precision ground-based photometry can be severely limited by atmospheric scintillation noise. The first ever on-sky demonstration of a scintillation correction technique has been presented. A simple proof-of-concept experiment was performed, observing the Orion Trapezium cluster using a single wavefront sensor and SCIDAR instrument on the Isaac Newton Telescope. The results from this experiment have successfully proved the concept, although the correction achieved is relatively low. An average reduction in the scintillation RMS noise by a factor of 1.92 was achieved for the 0.1 s data. However, the on-sky experiment has highlighted a number of ways in which the correction performance can be improved for a facility system.

It was found that the turbulence profiles measured with SCIDAR changed substantially between observations and using an out of date profile severely limits performance. It is expected that the scintillation correction performance would be greatly improved if simultaneous turbulence profiling is available.

A separate turbulence profiler is not necessarily needed. In the proof of concept experiment, a SCIDAR instrument was used to estimate the turbulence profile. It was not possible to estimate the profile from the WFS data because long exposure times were used. However, the profile could be obtained from the WFS telemetry data if high frame rates are used. For a full tomographic AO facility, bursts of WFS data at high frame rates could be measured and used to estimate the turbulence profile every $\sim 10 - 15$ minutes. This technique could be easily applied to any existing and future tomographic AO facilities without the need for any additional hardware.

Another significant limitation to this demonstration is that the photometry was performed using the WFS frames. The crowded field limited the photometric aperture size that could be used and the ability to measure an accurate sky background

value. In addition, any long timescale systematic trends in the photometry limit the scintillation correction performance that can be achieved. Differential photometry cannot be used to correct these trends as random noise from the comparison star is added during the calibration. Hence, the systematic trends had to be removed using a simple polynomial curve fitting algorithm. Whilst this does a good job at removing low order trends, any high order trend cannot be corrected this way as it is impossible to differentiate between scintillation noise and other noise sources.

Despite these limitations, a strong correlation between the uncorrected and tomographically reconstructed intensities was measured with a maximum correlation of 0.86 achieved. It is expected that, with optimal instrumentation, this method would achieve substantial scintillation correction.

The HD206267 target was less optimal compared to the Orion Trapezium Cluster as the reference stars used in the tomography are a magnitude fainter and are separated by a much larger angle. This is clearly seen when comparing the overlap in the WFS measurements at an altitude of 12 km for the Trapezium (shown in Fig. 4.9) and the HD206267 star system (as shown in Fig. 4.17). The high altitude turbulence has far less sampling and therefore the level of correction is lessened. Hence, despite these limitations, the fact that the tomographic reconstruction has successfully corrected the scintillation noise demonstrates the viability of this method.

It is expected that with a full tomographic wavefront sensing facility on a large telescope, with simultaneous turbulence profiling, significant scintillation correction could be achieved.

Chapter 5

Optimised temporal binning of comparison star measurements for differential photometry

5.1 Introduction

High-precision time resolved photometry is central to the study of variability of astronomical objects. However, ground-based observations are limited by effects of the Earth's atmosphere, including scintillation, absorption and scattering. These introduce random intensity variations which are correlated on a range of timescales and with a range of angular correlations.

Differential photometry aims to correct these systematic errors due to atmospheric and instrumental effects (Howell, 1992). This technique has been particularly important for the studies of exoplanet transits (Pont et al., 2006), eclipsing binaries (Pluzhnik, E. A., 2005) and micro-lensing events (Giannini et al., 2017).

For ground-based differential photometry, the comparison star should be close to the target star in order to maximise the correlation for systematic trends. However, it should also be bright in order to minimise shot noise (Mann et al., 2011). It is difficult to meet both these requirements simultaneously, especially for large

telescopes where the field of view (FOV) is more likely to be limited.

Furthermore, differential photometry cannot normally be used to correct scintillation noise since the angular correlation of the intensity fluctuations is very small (Kornilov, 2012). Hence, the probability of there being a bright comparison star within the iso-photometric angle is small - on the order of a few arcseconds.

Although the use of comparison stars can be effective at removing systematic trends, the random noise for the comparison star and target star (such as photon and scintillation noise), add in quadrature, thus increasing the random noise in the calibrated light curve (Koppelman, 2005). For the brightest targets, the random noise will typically be dominated by scintillation noise and will be independent of the magnitude. If the comparison star is also scintillation limited, then the variance of the noise in the calibrated light curve will be increased by a factor of 2 (see Fig. 2.9). For fainter comparison stars, where photon noise dominates, the NSR of the calibrated light curve will be increased by a larger factor. This significantly limits the number of comparison stars that can be used to perform effective differential photometry.

Since in many cases the timescale of the systematic variations due to the atmosphere will be much longer than the cadence of the observations (Young et al., 1991), the comparison star data can be temporally binned before applying the calibration to the target star. Therefore, the NSR of the calibrated light curve will be significantly improved. This method can be applied to any dataset with cadences of up to a few tens of seconds recorded in good photometric conditions and allows the use of much fainter comparison stars without detriment. This is especially advantageous when observing with large telescopes which tend to have a limited FOV. In all cases, it is assumed that it is not possible to reduce the cadence of the observations of the science target.

For light curves affected by short periods of high frequency trends, e.g. due to intermittent cirrus clouds, the temporal binning can be applied everywhere apart

from these periods. Hence, the improvement in NSR can still be achieved for a majority of the calibrated light curve.

In this chapter, a data reduction pipeline for implementing the method is described, which optimises the number of frames to be temporally binned for the comparison star. Some example results for time-resolved photometric data are presented. Finally, results of applying this technique on an exoplanet transit light curve of WASP-166b are presented (Doyle et al., 2022) and the results for a range of comparison star magnitudes are compared. This work was accepted for publication by the Monthly Notices of the Royal Astronomical Society in September 2023 (Hartley and Wilson, 2023).

5.2 Theory

5.2.1 Total noise

The total noise in the light curve depends on the exposure time. The scintillation and photon noise will decrease with the exposure time. On the other hand, the noise due to the atmospheric transparency variations will increase with exposure time and hence the cadence of the light curve (Mann et al., 2011), as shown by Eq. 2.30. Therefore, for a given observation, there will be an optimal exposure time that minimises the total noise. Fig. 5.1 shows an example of the theoretical photometric noise as a function of the exposure time.

The plot was calculated assuming a star of magnitude 10 in the V band observed using the Pt5m telescope. It is assumed that the systematic noise was due only to atmospheric transparency variations described by Eq. 2.30.

The minimum in Fig. 5.1, only exists because of systematic trends in the light curve. Without such effects, the noise would continue to decrease with exposure time as the scintillation and shot noise decrease. Therefore, measuring the noise as a

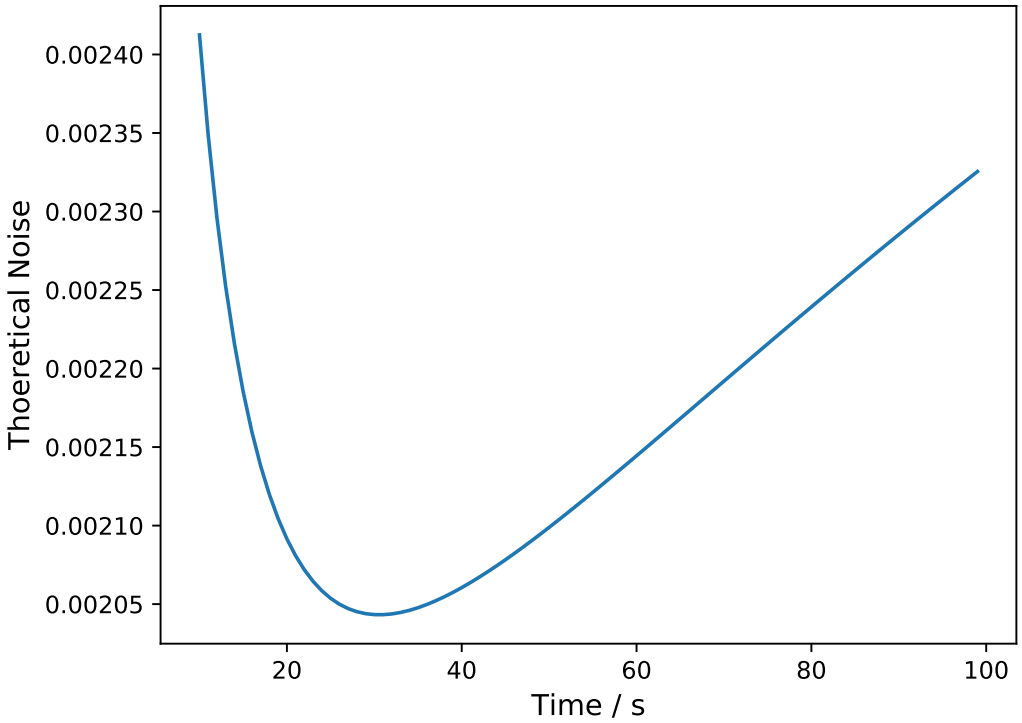

Figure 5.1: The theoretical noise as a function of the exposure time used. The plot was calculated assuming a star of magnitude 10 in the V band observed using the Pt5m telescope in standard atmospheric conditions for La Palma, Spain. It is assumed that the systematic noise was due only to atmospheric transparency variations described by Eq. 2.30.

function of the exposure time can give information on the atmospheric transparency fluctuations at the telescope site.

This optimal exposure time will also vary depending on the magnitude of the star, with fainter stars having a longer optimal exposure time, as shown in Fig. 5.2. This is because for fainter stars, photon noise becomes more dominant.

5.2.2 Sky Coverage

As discussed in the theory chapter, section 2.3.4, the ideal comparison star should be close in the field to the target star and of a similar colour. Ideally, the star should be bright so as to minimise the addition of shot noise to the calibrated light curve.

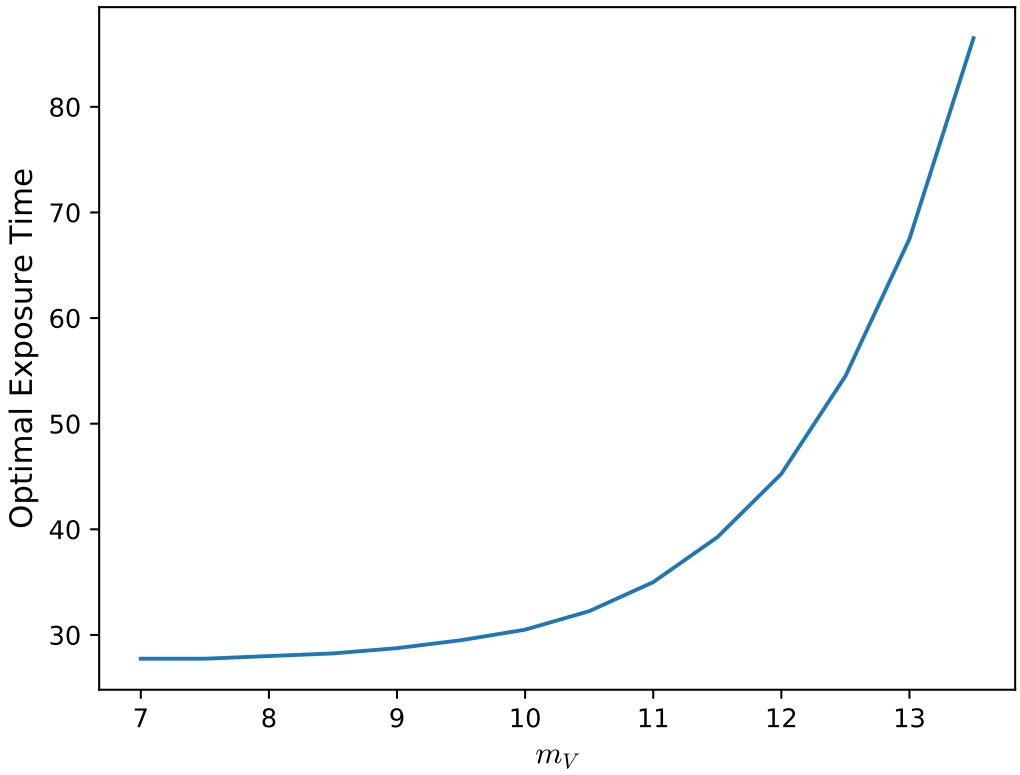

Figure 5.2: The optimal exposure time as a function of star magnitude. The plot was simulated assuming a star of magnitude 10 in the V band observed using the Pt5m telescope in standard atmospheric conditions for La Palma, Spain. It is assumed that the systematic noise was due only to atmospheric transparency variations described by Eq. 2.30.

The FOV of a telescope depends on the focal length and the physical size of the detector. For fixed values of the focal ratio, the FOV will scale inversely with the aperture size. Since most telescopes are produced for a range of fixed focal ratio values, larger telescopes will often have a smaller FOV.

Fig. 5.3 shows the average probability over the whole sky of finding a star of magnitude less than or equal to m_V within the FOV for a 20 cm, 1 m and 2.54 m telescope for a fixed f-ratio of 10, and a ZWO ASI1600 detector. The vertical lines represent an estimate for the magnitude below which the photometric noise in a star light curve will be dominated by scintillation noise. For the two larger telescopes, where the FOV is smaller, the probability of there being a bright star is small. For the 20 cm telescope, there is a significantly higher probability of finding

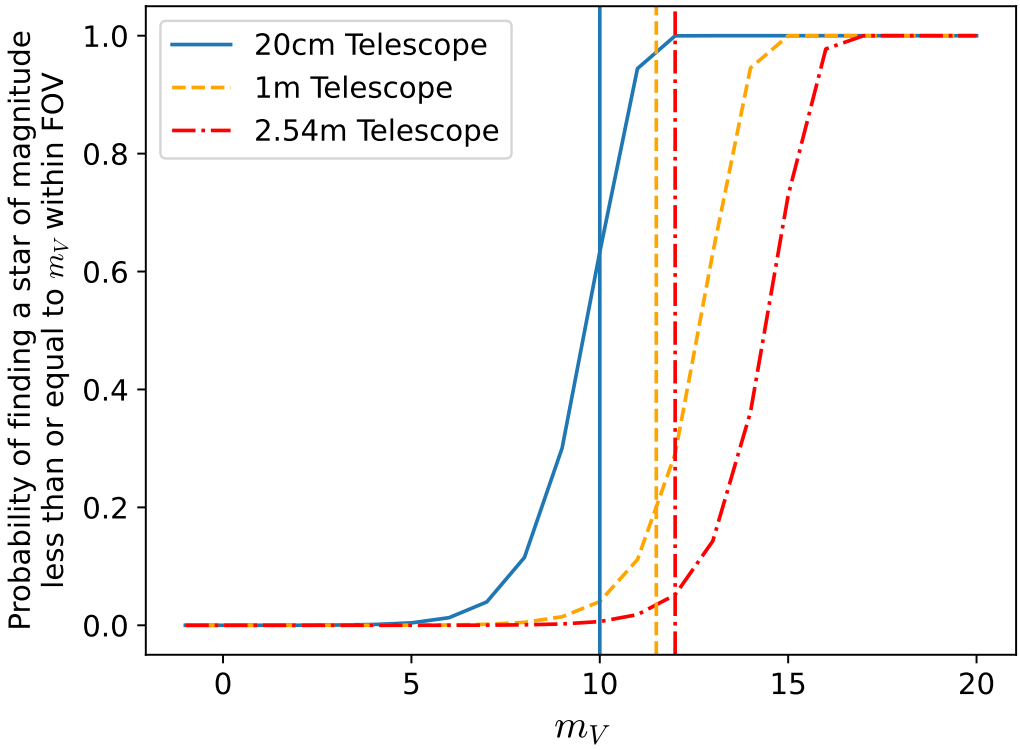

Figure 5.3: The average probability of finding a $V \leq m_V$ star within the FOV for a 20 cm, 1 m and 2.54 m telescope. The vertical lines correspond to an estimate for the magnitude below which the photometric noise is dominated by scintillation.

bright stars within its FOV.

The ideal comparison star would need to be as close as possible to the target star in order to minimise first-order extinction effects. Furthermore, ideally the comparison star should not be too near the edge of the detector to avoid the star drifting out of the frame over the observing period and to avoid vignetting effects. Therefore, the true probability of finding a suitable bright comparison star within the field is even more limited.

5.2.3 Temporal binning of comparison stars

Comparison stars are vital for high precision photometry. However, the calibrated light curve, although corrected for systematic noise, will now have increased random noise. This is because the NSR of the target star and of the comparison star add

in quadrature.

Several advanced systematic correction techniques have previously been proposed and used. This includes the averaging of multiple comparison stars (Boyd, 2007), therefore averaging the random fluctuations. However, as the telescope aperture increases, the FOV decreases, thus reducing the likelihood of finding multiple suitable comparison stars to choose from.

Other techniques use curve fitting algorithms that measure low frequency trends in the comparison star light curve to remove low order trends in the data (Poddaný et al., 2010). Whilst this method will not add any random noise, the technique makes assumptions about the order of the systematic noise and could miss periods of high frequency noise. The Kepler mission identifies systematic noise terms by searching for photometric trends common to a large ensemble of stars, specifically looking for trends with transit-length timescales (Petigura and Marcy, 2012).

In this chapter, a new technique that takes advantage of the reduction in photon and scintillation noise with integration time is proposed. Since the systematic trends tend to be low in frequency, the comparison star signal can be binned in time with a moving average such that its noise is minimised. An integration time that minimises the noise in the comparison star light curve exists, an example of this is shown in Fig. 5.1. Temporally binning the signal by this optimal factor reduces the random noise in the comparison star's light curve whilst retaining the low frequency trends. The temporally binned comparison star's light curve can then be used to normalise the photometry of the star of interest, thus correcting the systematic trends, whilst minimising the addition of random noise.

Temporal binning is a technique widely used in astronomical photometry (Doyle et al., 2022) to reduce the NSR, however, it has traditionally been applied to the calibrated light curve as a whole. It should be noted that in our proposal, the light curve of the scientific target is not temporally binned and hence its cadence is unchanged. Only the comparison star signal is temporally binned. Our aim is that

the NSR of the final calibrated light curve should be limited only by the random noise of the target star signal.

The comparison star is temporally binned with a moving average such that it has the same number of data points as the target signal. Using a moving average does introduce wings at the start and end of the light curve where the data cannot be averaged by N_{Bins} frames. However, in most applications, the period of interest will still have an improved NSR. Hence, when using this method one should ensure that there are additional frames at the start and end of the observation run such that the period of interest is well covered.

For situations where both the target star and comparison star are bright and where scintillation noise is dominant, the NSR of the calibrated light curve can be reduced by a factor of up to $\sqrt{2}$. This is because in standard differential photometry, both stars will contribute equal noise variance to the calibrated target. If the scintillation fluctuations can be completely removed from the comparison star signal, the NSR of the calibrated target will therefore be reduced by a factor of $\sqrt{2}$. For fainter comparison stars where there is additional photon noise, the NSR of the calibrated target light curve can be reduced by up to $\sqrt{N_{Bins}}$ where N_{Bins} is the number of frames which have been temporally binned for the comparison star. The optimum temporal binning for a given observation, an example of which is shown in Fig. 5.1, will depend on the magnitude of the comparison star used and on the Power Spectral Density (PSD) of the systematic trends in the light curve.

The systematic trends in the light curve are not caused by the atmospheric transparency alone, there is additional systematic noise produced by the instrumentation optics and detectors. The atmospheric transparency variations and scintillation noise can also vary significantly from night to night. Therefore, it is very challenging to determine a theoretical value for the optimal degree of temporal binning.

The optimal degree of temporal binning to apply to the comparison star light curve is determined by finding the temporal binning factor that minimises the NSR of

the calibrated target light curve. However, since the target of interest will likely have intrinsic variation in its magnitude, a different non-varying star must be used to determine the optimal temporal binning factor. A pipeline to determine the optimal binning required for a given observation was developed and is detailed in section 5.3.2.

For this technique, it is assumed that the observations are taken in good photometric conditions. It is assumed the photometry does not contain high frequency systematic trends for example due to cirrus clouds, and that the primary source of systematic noise is due to atmospheric transparency variations. This technique cannot be applied for sources with blending.

This technique can be applied to either aperture photometry or PSF-fitting since the trade-off and optimisation between the shot/scintillation noise and the systematic noise due to atmospheric transparency variations will still be the same. Hence, this technique can be applied to either case. In the examples in this chapter, only aperture photometry is presented.

5.3 Method

5.3.1 Quantifying systematic noise

The amount of systematic noise in the light curves can be estimated by a method known as RMS binning (Pont et al., 2006). The systematic noise is measured by splitting the signal up into N bins and calculating the average standard deviation of the signal within each bin Fohring et al. (2013). For random white noise the standard deviation is proportional to the square root of the number of bins, $\sigma \propto 1/\sqrt{N}$.

In the presence of systematic noise, the gradient will deviate from that expected for pure white noise gradient. Hence, measuring the gradient indicates the amount of systematic noise in the light curve. This technique can also be used to visu-

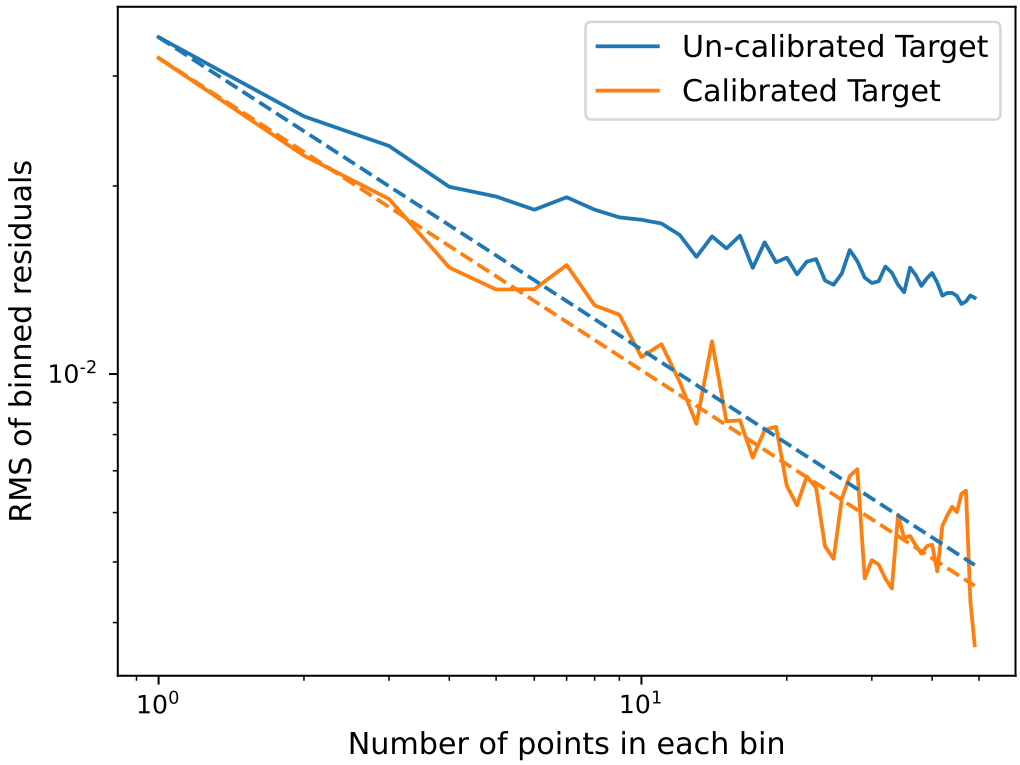

Figure 5.4: An example of the light curve RMS residual as a function of the number of points in each bin for the un-calibrated and calibrated light curve for an $m_V = 8.2$ star using an $m_V = 9.9$ comparison star in the Pinwheel cluster observed on the 2021 December 20 using the Pt5m telescope. The dashed lines show the expected relationship for a light curve with only white noise.

ally determine whether the use of a comparison star has significantly reduced the systematic noise in the calibrated light curve. Plotting the RMS binning of the un-calibrated target light curve alongside the calibrated target light curve can be used to test whether using differential photometry has reduced the systematic noise for the target.

Fig. 5.4 shows an example of performing the RMS binning for an un-calibrated and calibrated light curve. The dashed lines show the expected relationship for a light curve with only white noise. The un-calibrated light curve deviates significantly from the expected relationship for white noise, indicating that it is dominated by systematic noise. The calibrated light curve however is much closer to the expected white noise relationship. As such, it can be confidently assumed that

the comparison star used has successfully corrected the systematic trends. Hence, this method can be used to aid comparison star choice and to optimise the data reduction techniques used.

5.3.2 Pipeline

As discussed in Section 5.2.3, the optimum degree of binning cannot be determined theoretically, as the atmospheric conditions vary from night to night. Therefore, a pipeline was developed to determine the optimal number of frames that should be binned for a given data-set.

Since the scientific target of interest will likely vary in magnitude, a test star should be used to determine the optimal temporal binning factor, N_{Opt}, of the comparison star signal. Hence, in total, three stars are required. One must also determine whether the test star light curve and the comparison star light curve have systematic trends in common, which are likely common to the target.

A simulation was used to develop and test this pipeline. Simulated light curves with systematic trends, shot noise, read noise and scintillation noise were produced for stars of different magnitudes.

The following pipeline was developed and tested using both simulated and observed star light curves. The steps below are used to determine the optimal temporal binning required to minimise the NSR of the calibrated target star:

1. Perform the aperture photometry on the target star.
2. Select two other stars from the frame - a comparison star and a test star. These should be non-varying stars close to the target of interest, and ideally bright.
3. Perform the aperture photometry on the comparison star and test star.

4. The cross spectrum of the light curves for the comparison and test stars are used to assess whether there are common systematic trends in the light curves that need correcting.

5. Visually check the photometric light curves for any obvious high frequency trends – if there are periods of high frequency systematic trends, do not apply the temporal binning during these periods.

6. The selected comparison star is used to calibrate the test star with incremental binning i.e. start with no binning, then bin every two frames etc. The NSR of the calibrated test star is plotted as a function of the temporal binning applied to the comparison star light curve. This is used to find the binning factor N_{Opt} that results in a minimum in the measured NSR of the calibrated test star light curve.

7. The RMS versus binning method described in section 5.3.1 should be used on the un-calibrated and calibrated test star light curves to check that the use of the comparison star has reduced the systematic noise.

8. If the comparison star is deemed suitable in Step 7, then the target signal can now be calibrated using the comparison star light curve temporally binned by the optimal binning factor N_{Opt} found in Step 6.

This pipeline could be combined with other techniques. For example, if multiple comparison stars are available, the stars' signals could be averaged before applying the binning. In addition, the pipeline can be further optimised by allowing varying binning values in different parts of the light curve. For example, periods with higher frequency systematic trends could have less temporal binning than periods with lower frequency trends.

5.4 Simulations

For the available on-sky data, the minimum in the measured NSR is often very shallow (see Fig. 5.11). As such, it is hard to determine how the minimum location varies with the magnitude of the comparison star. Therefore, a simulation was used to produce light curves with second-order polynomial trends (such as Fig. 5.6) to produce more well defined N_{Opt} (such as Fig. 5.7).

Simulations were also used to investigate the impact of short periods of high frequency systematic noise e.g. due to cirrus clouds. This was done in simulation, since no data was collected in such conditions. All the data were either collected in good photometric conditions or during continuous poor conditions to the extent where the method could not be used at all.

5.4.1 Test Star magnitude

Since the target of interest will likely have intrinsic variations, ideally another 'test' star should be used to determine the optimal temporal binning required. For a large telescope, the number of stars to choose from may be limited and therefore the test star may need to be relatively faint. In addition, the test star should be close to the target of interest to maximise the correlation for systematic trends. A simulation was used to check whether the magnitude of the test star has a significant impact on determination of the optimal binning factor.

Light curves for a range of star magnitudes were produced, each with the same systematic trends, and random Poisson noise added according to the light level. Each star was used as a comparison star for each of the other light curves. The NSR of the calibrated test star against the temporal binning of the comparison star was measured and the binning that corresponds to the minimum NSR was recorded.

Fig. 5.5 shows the optimal binning required as a function of the comparison star magnitude and test star magnitude. The binning required does not appear to depend substantially on the test star magnitude used and depends primarily on the comparison star magnitude. Therefore, the test star does not need to have a similar magnitude to the target of interest. This is as expected, as the test star NSR is constant and therefore does not affect the position of the minimum. However, the brighter the test star magnitude, the better since the light curve should be dominated by the systematics trends that need to be corrected and not shot noise.

In reality, it is unlikely that the systematic trends in the light curves will be completely identical, as each star will likely have some localised systematic trends. Hence, a test star close to the target of interest on the detector should be selected to minimise the first-order atmospheric extinction and any other field dependent systematic trends.

5.4.2 High order (rapidly varying) trends

An important benefit of this method is that it can be optimised for each observation. For light curves with sudden rapid high order trends, for example due to intermittent cirrus cloud in otherwise photometric conditions, the comparison star can be temporally binned in the photometric periods and not binned (or less severely binned) in the periods that contain high order trends.

Fig. 5.6 shows an example systematic trend used in simulation. The systematic noise is primarily low in frequency, with a sudden high frequency trend at around 100 s. A magnitude $V = 8$ target star along with 4 comparison stars with $V = 9, 10, 11$ & 12 were simulated, all with this same systematic trends. Shot noise was added as appropriate for the star magnitude for a 1 s exposure time on the Pt5m telescope. The comparison stars were temporally binned everywhere except during the high frequency period at 98-102 s.

Fig. 5.7 shows the measured NSR of the calibrated light curve for each comparison

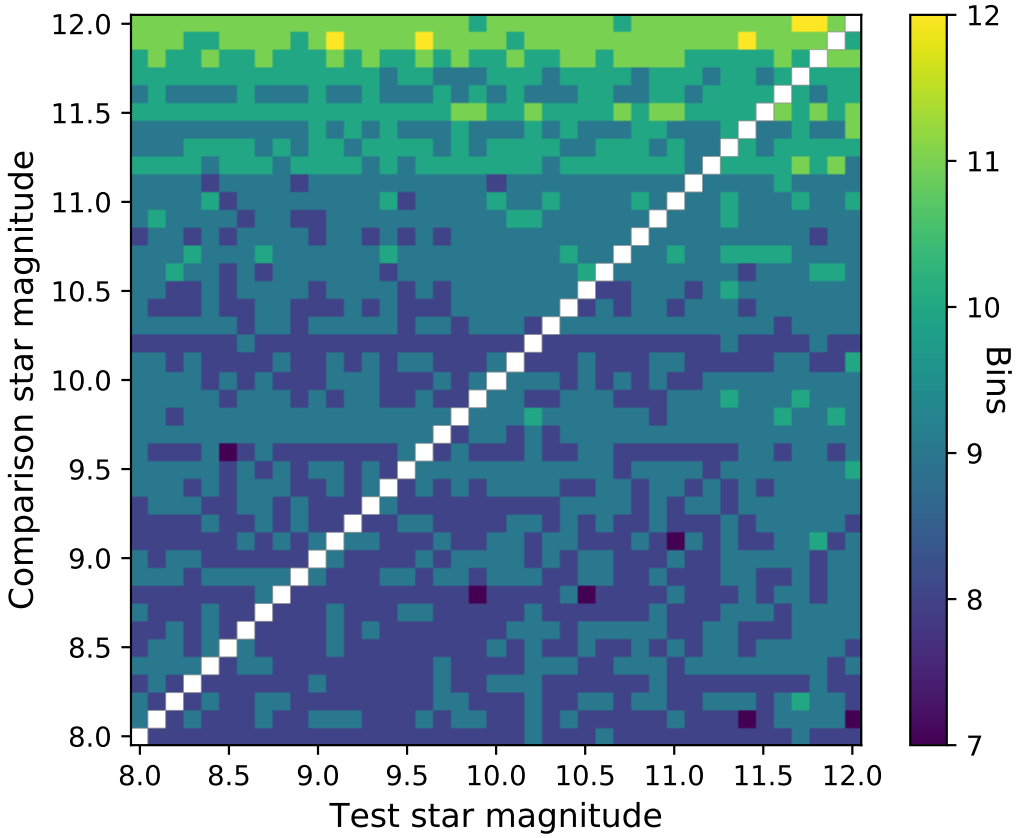

Figure 5.5: A matrix of the simulated optimised temporal binning factor, N_{Opt}, for a given comparison star magnitude as a function of the magnitude of the test star.

star against the temporal binning of the comparison star. In addition, the NSR for the calibrated light curve using a 2nd order polynomial fit to correct the systematic trends is plotted. A minimum can be clearly seen for each comparison star. The steep increase in NSR for long integration times results from the shape of the low frequency systematic trend. In all cases temporally binning the comparison star everywhere bar the high frequency period outperforms the use of a low order curve fitting algorithm and achieves a significantly reduced NSR at the minima. However, the curve fitting algorithm outperforms temporal binning of the comparison stars when more than 20 frames are temporally binned. This demonstrates the importance of selecting the optimum temporal binning for a given observation.

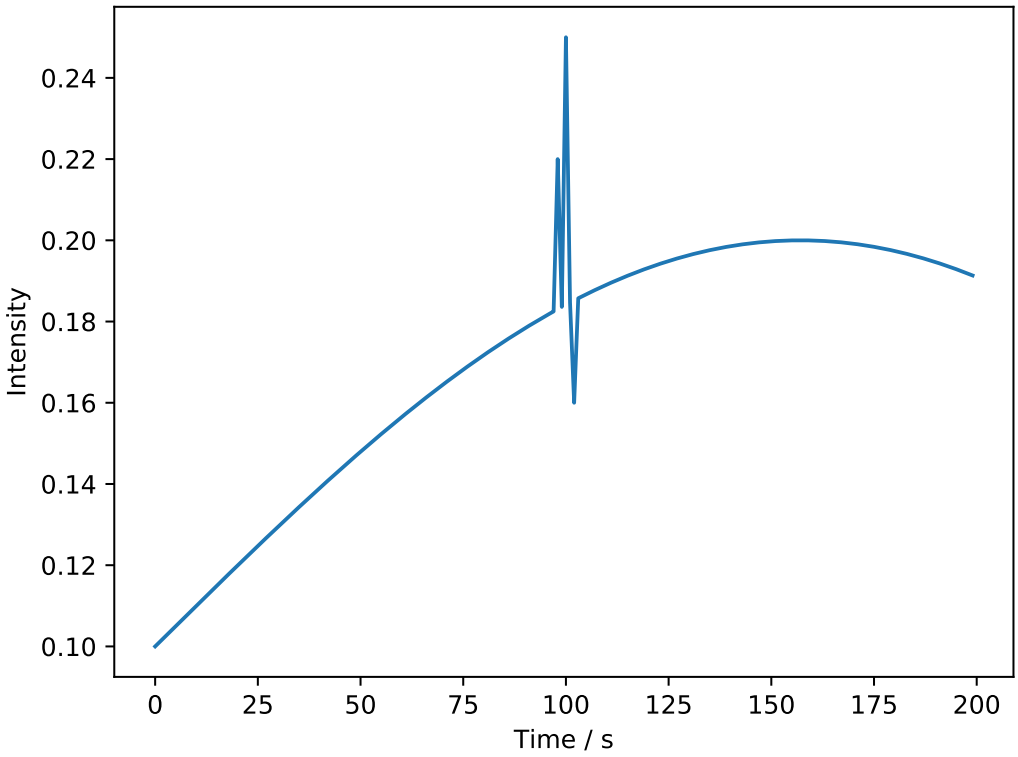

Figure 5.6: A simulated systematic trend with a low frequency 2nd order variation for a majority of the observing period and a high frequency trend between 98 s and 102 s.

5.5 Results

The pipeline described in section 5.3.2 was tested with multiple on-sky data-sets described in section 5.5.1 and in simulation. In this section, the key results of testing this technique with on-sky data are presented, including the application of the technique to two exoplanet transit light curves. Bright targets are of most interest for this technique, since in these cases the calibrated signal is significantly limited by the magnitude of the comparison star. Whilst this technique is still useful in the case of a faint target, often a comparison star with a similar magnitude or brighter than the target will be within the FOV, and therefore the calibrated signal will still be dominated by the shot noise of the target signal.

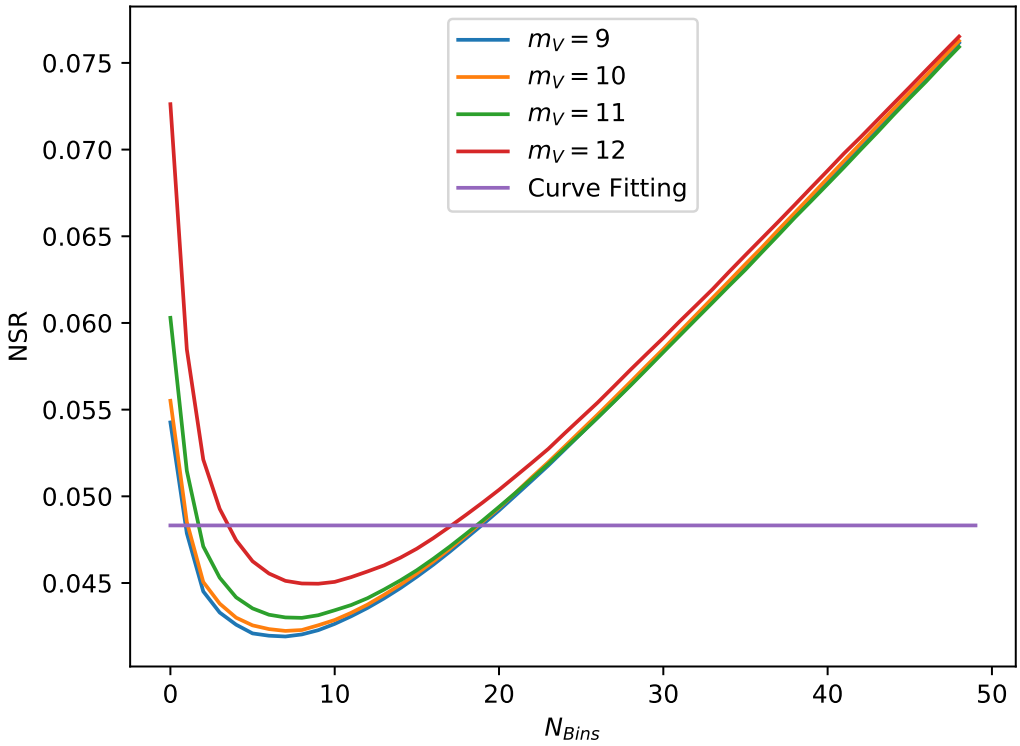

Figure 5.7: The NSR of the calibrated target light curve as a function of the temporal binning of the comparison star light curve for different magnitudes. The simulated comparison star light curve is temporally binned everywhere apart from the region of a rapid high frequency trend around 100 s. The purple line shows the measured NSR for the calibrated target star where a 2nd order polynomial fit has been used to correct the systematic trends.

5.5.1 Data-sets

Here, the results from applying this pipeline to a variety of data-sets are presented. Details of the instrument used for each data-set are given below.

5.5.1.1 Pt5m

Pt5m is a robotic 0.5 m telescope at the Roque de los Muchachos Observatory in La Palma, Spain (Hardy et al., 2015). This was used to collect the majority of the data used in this chapter. This telescope provides imaging in standard photometric bands, with a FOV of 10.2 × 6.9 arcmins.

M36 (The Pinwheel Cluster, RA 05 h 36 m 16 s and Dec +34°08'36.5"), was chosen

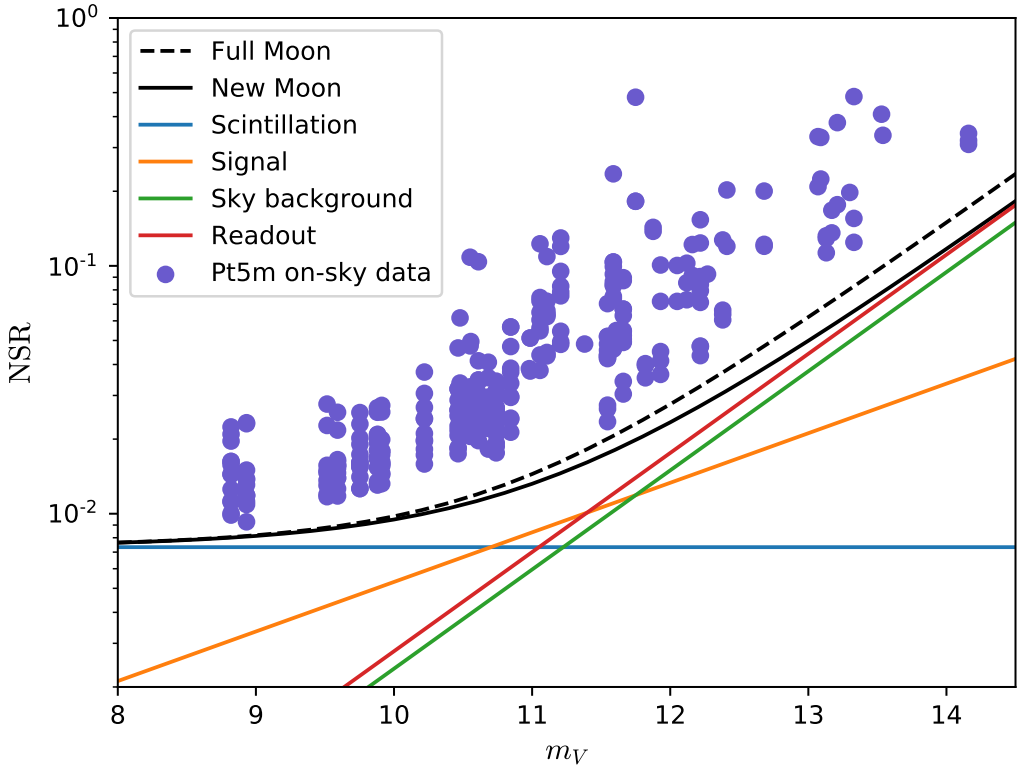

Figure 5.8: The measured NSR for light curves observed in the Pinwheel Cluster using the Pt5m telescope in the V band under typical atmospheric conditions for La Palma, Spain with an exposure time of 1 s are plotted (as blue data points) as a function of the stellar magnitude. The expected noise contributions from different sources including scintillation, signal noise, readout and sky background are also plotted as a function of the star magnitude. The total noise is plotted for both full moon and new moon. The measured NSR for the light curves lie above the expected noise for the CCD equation, as the light curves will also contain systematic noise.

as a suitable target because it provides a large number of bright stars within the FOV. This target was observed on 15 nights between December 2020 and April 2021 using the Pt5m telescope. All observations were made in the V band with an exposure time of either 1 s or 2 s. Each observation comprised of 100-300 frames with a cadence of $\sim$ 10 s.

Fig. 5.8 shows the measured NSR for light curves observed in the Pinwheel Cluster with an estimate of the relative noise contributions to the NSR as a function of the stellar magnitude for the Pt5m. The plot was made in the V band assuming typical atmospheric conditions for La Palma, Spain with an exposure time of 1 s.

5.5.1.2 Wide-field camera data

A wide field imager was used to acquire data from the Pt5m dome in La Palma in August and September 2016. The imager comprised a 70 mm f/1.8 lens coupled to a Moravian Instruments G3-11000 CCD camera, providing a field of view of 10×10 degrees.

A series of images were taken over several nights. The data was used to test the technique for the case of very bright stars. The NSR for the brightest stars from each night was measured and the effects of systematic errors on the NSR were investigated.

All observations were centred on RA 21 h 05 m 00 s and Dec +29°00'00". Just over 48 hours of data was collected over a 2 month period. Each night, an average of 600 frames were observed with a 10 s exposure and a cadence of 20 s. The telescope was slightly de-focused to avoid saturation. This data-set was primarily used to investigate the binning of bright comparison stars to achieve the expected NSR reduction factor of $\sqrt{2}$.

5.5.1.3 NGTS data

Exoplanet transit data measured with the Next Generation Transit Survey (NGTS) (Chazelas et al., 2012) was provided by Warwick University. NGTS is a wide-field robotic telescope facility designed to find and characterise transiting exoplanets at the ESO Paranal Observatory, Chile. NGTS is made up of twelve 20 cm robotic telescopes, each with a FOV of 8 square degrees. Each telescope uses a custom NGTS filter (520 – 890 nm).

The WASP-166b data was observed using a 10 s exposure time with NGTS on the 2021 February 18 (Doyle et al., 2022). The data from six of the 20 cm telescopes were averaged (Bryant et al., 2020). A total of 1384 images were collected by each telescope.

5.5.2 Power Spectral Density

This technique exploits the fact that the noise contribution from systematic noise is at low frequencies. On the other hand, if the systematic trends occur at high frequencies, then temporally binning the comparison star will reduce the correction achieved.

A key question therefore is whether stars of different magnitudes share the same low frequency trends i.e. whether there are any frequency dependent effects in the light curve data reduction processing. Therefore, comparing the power spectrum of the target star light curve and comparison star light curve can give useful insight in to whether the comparison star selected is suitable and whether temporally binning the comparison star signal would be beneficial. NGTS data provided from 2021 February 18 was used to investigate how the power spectra from multiple stars in the field varies with magnitude. This data set was chosen due to its large FOV and hence large number of stars to compare.

Fig. 5.9 shows the power spectrum for a bright $m_V = 8.6$ and a fainter star of $m_V = 11.1$. It was found that there are not any significant difference in the power at low frequencies. As expected, for the fainter star, the higher frequencies have much more power due to increased shot noise. This clearly demonstrates the motivation of our proposed method and indicates that, for this observed data, the method is suitable.

Fig. 5.10 shows the power spectrum as a function of star magnitude and frequency for all the stars in the field. The power at the lowest frequencies does not change significantly with the star magnitude. At higher frequencies, there is an increase in power with star magnitude since, as expected, fainter stars have more shot noise.

Hence, it is found that fainter stars share the same low frequency trends as the bright stars and therefore, with temporal binning, substantially fainter stars can be used as comparison stars. However, the data is limited to a single observational set-up and does not have any stars fainter than a magnitude of $m_V = 11.3$. There-

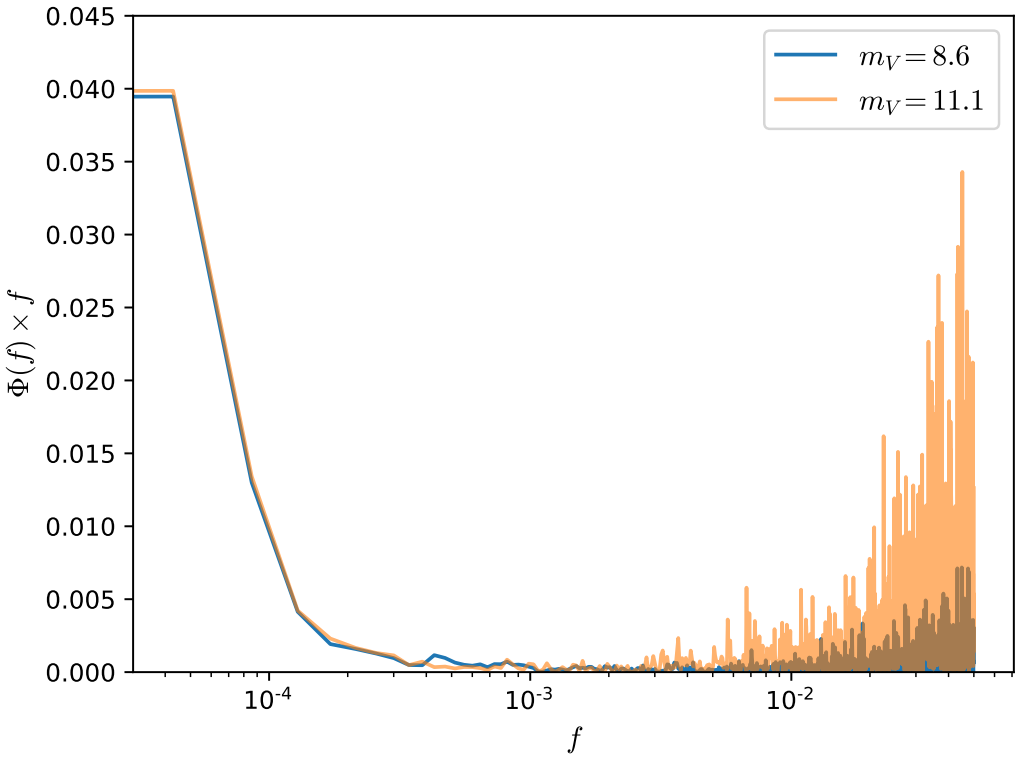

Figure 5.9: The power spectrum, $f\Phi(f)$, as a function of the frequency, f, for two stars of magnitude $m_V = 8.6$ and $m_V = 11.1$ observed with an NGTS telescope on 2021 February 18.

fore, similar studies from other telescopes and instruments would be useful in this context.

5.5.3 NSR

To investigate optimisation of the temporal binning method, the NSR of the calibrated light curve was plotted as a function of the temporal binning for multiple comparison stars of different magnitudes.

The Pinwheel cluster data from the Pt5m telescope was used to test this method. A short exposure time of 1 s was used to ensure that the bright stars did not saturate. The brightest star in the frame (of magnitude V = 8.2) was chosen as a target star, and fainter stars within the FOV were used as comparison stars.

Fig. 5.11 shows the NSR of the calibrated light curve as a function of the temporal

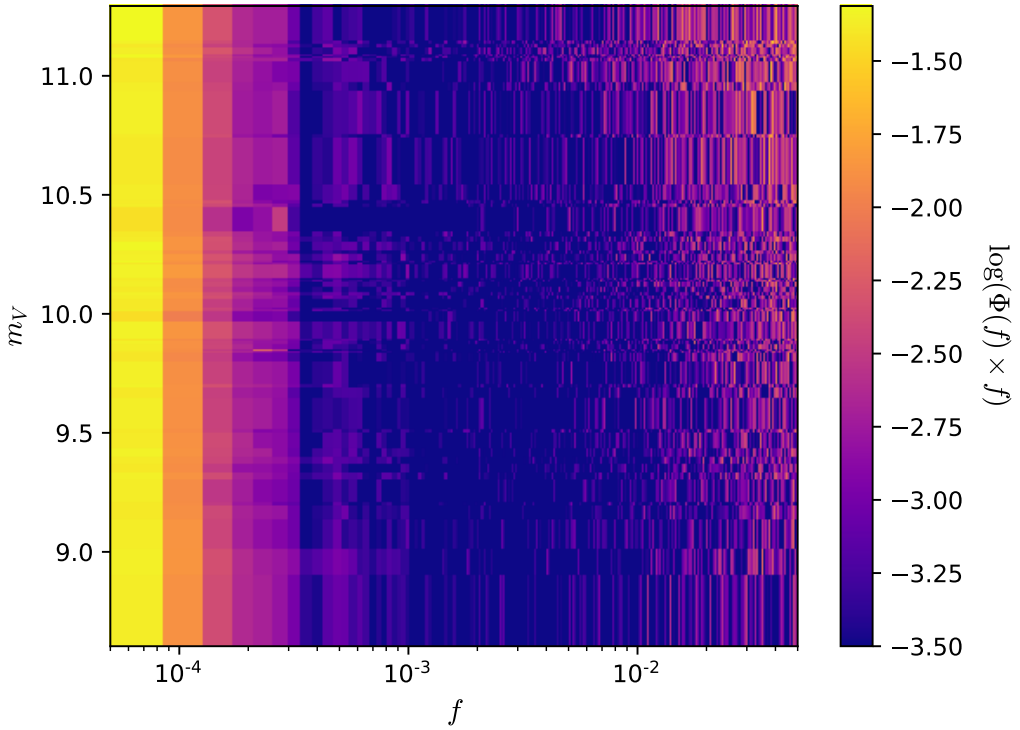

Figure 5.10: The power spectrum, $f\Phi(f)$, as a function of the star magnitude and log frequency, f, observed with an NGTS telescope on 2021 February 18.

binning factor, N_{Bins}, for a range of comparison stars with different magnitudes. The NSR decreases with increasing temporal binning. This is because the contribution of the photon and scintillation noise from the comparison star are reduced.

For the brightest comparison stars, where photon noise is less significant and the noise for the target is limited by scintillation, there is a slow increase in the NSR for long integration times such that a shallow minimum exists. This is because at long integration times the atmospheric transparency variations and other low frequency systematic noise sources start to become significant. For the faintest comparison stars this feature is not seen as the photon noise contribution is far more significant.

In all cases temporally binning the comparison stars' data has reduced the NSR of the final light curve. In addition, there exists a binning factor at which using the comparison star does not add any additional noise to the calibrated light curve. The

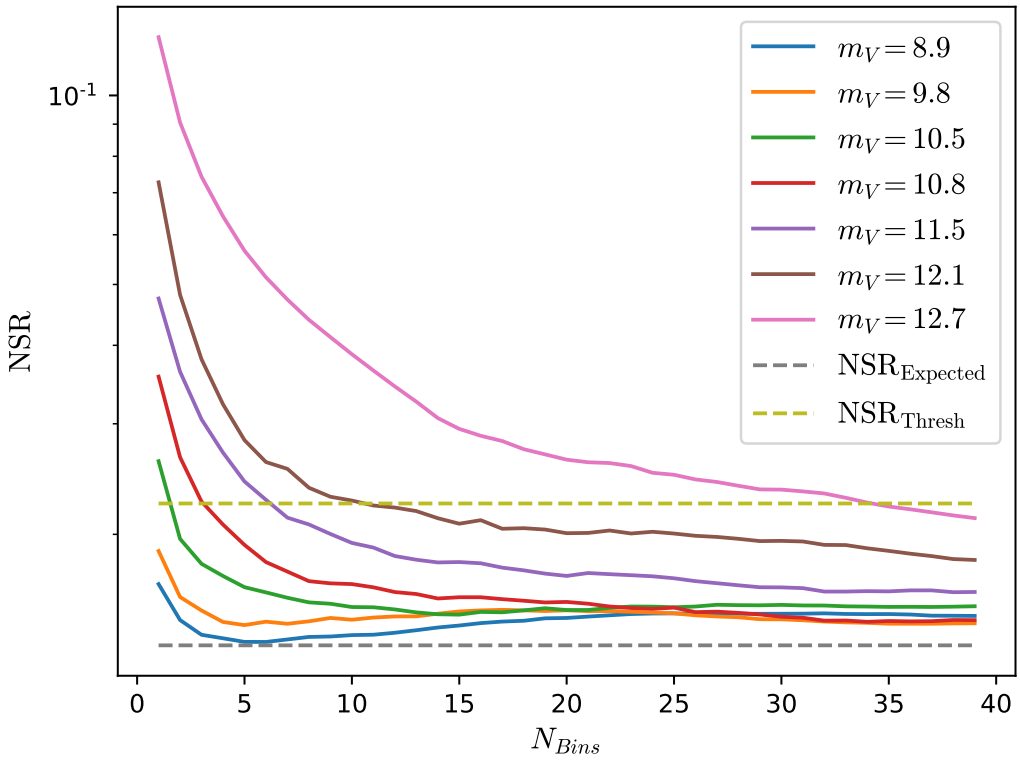

Figure 5.11: The NSR of the calibrated light curve as a function of the temporal binning of the comparison star. Only the comparison star is temporally binned. The threshold, NSR_{Thresh}, at which the addition of the random noise from the comparison star is outweighed by the correction of the systematic noise is also plotted along with the expected NSR which was estimated using the noise sources in the CCD equation given in 2.28 and the estimated scintillation noise for standard atmospheric conditions in La Palma.

yellow dashed line represents the NSR of the raw target star light curve. At this NSR threshold, NSR_{Thresh}, the addition of the random noise from the comparison star is outweighed by the correction of the systematic noise. The temporal binning factor of the comparison star signal that corresponds to this threshold is given by N_{Thresh}. As binning reduces the noise contribution from the comparison star the NSR of the calibrated light curve should tend towards the expected NSR from the CCD equation and scintillation noise, given by the grey-dashed line. The RMS binning method in section 5.3.1 was used to check that the comparison star has reduced the systematic noise.

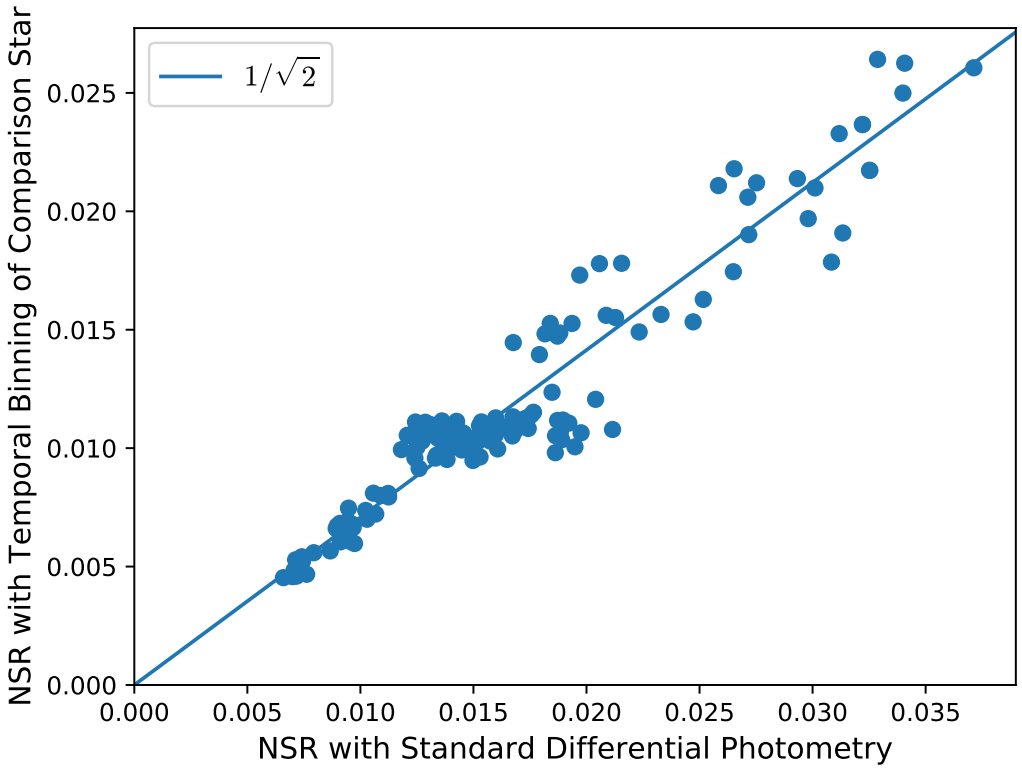

Figure 5.12: The NSR of the calibrated light curves with temporal binning of the comparison star versus the NSR of the calibrated light curve using standard (un-binned) differential photometry, for a range of stars dominated by scintillation noise. These results were produced using observations of the Pinwheel cluster on the Pt5m telescope and data using a wide-field camera in La Palma. Full details of these data-sets are given in section 5.5.1.

5.5.4 Bright Stars

Here, the case where both the target star and comparison star are bright is tested. It is expected that the random noise for both stars will be dominated by scintillation. Hence, it is expected that the NSR for the calibrated light curve will be reduced by a factor of $\sqrt{2}$ if the temporal binning of the comparison star light curve is employed effectively. Two data-sets from La Palma were employed. The first data were collected in 2016 using the wide field camera described in section 5.5.1.2. The second uses the Pt5m data of the Pinwheel Cluster described in section 5.5.1.1. For each data set all of the bright comparison stars which were sufficiently bright to be expected to be dominated by scintillation noise were selected. The brightest

non-varying star from each night was selected as the target star and the remaining scintillation limited stars in the field were used as comparison stars.

Each target star light curve was calibrated using both the raw un-binned comparison star data and then with the comparison star data optimally binned using N_{Opt}. Typically, it was found that $N_{\mathrm{Opt}} = 20$ although in many cases the minimum in the optimisation curve was very shallow. In Fig. 5.12 the NSR of the final light curve using optimised temporal binning against the NSR for standard (un-binned) differential photometry is plotted.

It was found that, on average, temporally binning the comparison star data reduced the NSR of the calibrated target star light curve by a factor of 1.41 ± 0.06, which agrees with the theoretical reduction of $\sqrt{2}$ within error. Hence, even when bright comparison stars are available, binning the comparison star is still beneficial.

5.5.5 Faint Stars

For faint stars, where the signal is photon noise limited, the NSR of the calibrated light curve can be reduced by a much larger factor, with the noise contribution from the comparison star reducing as $\sim \sqrt{N_{Bins}}$. This was investigated using the observations of the Pinwheel Cluster from the Pt5m telescope.

The brightest star, with magnitude $V = 8.2$, was chosen as the target for each night of observations and the remaining stars in the field were used as comparison stars. For each comparison star, the temporal binning factor N_{Thresh}, the point at which the correction of the systematic noise in the calibrated light curve outweighs the addition of random noise was recorded. In addition, the reduction in the NSR of the calibrated light curve at this point, was also recorded. The suitability of the comparison star was confirmed by visually checking that the NSR of the calibrated light curve was reduced to the threshold using the method described in section 5.3.1.

The results are shown in Fig. 5.13, which plots the factor by which the NSR of

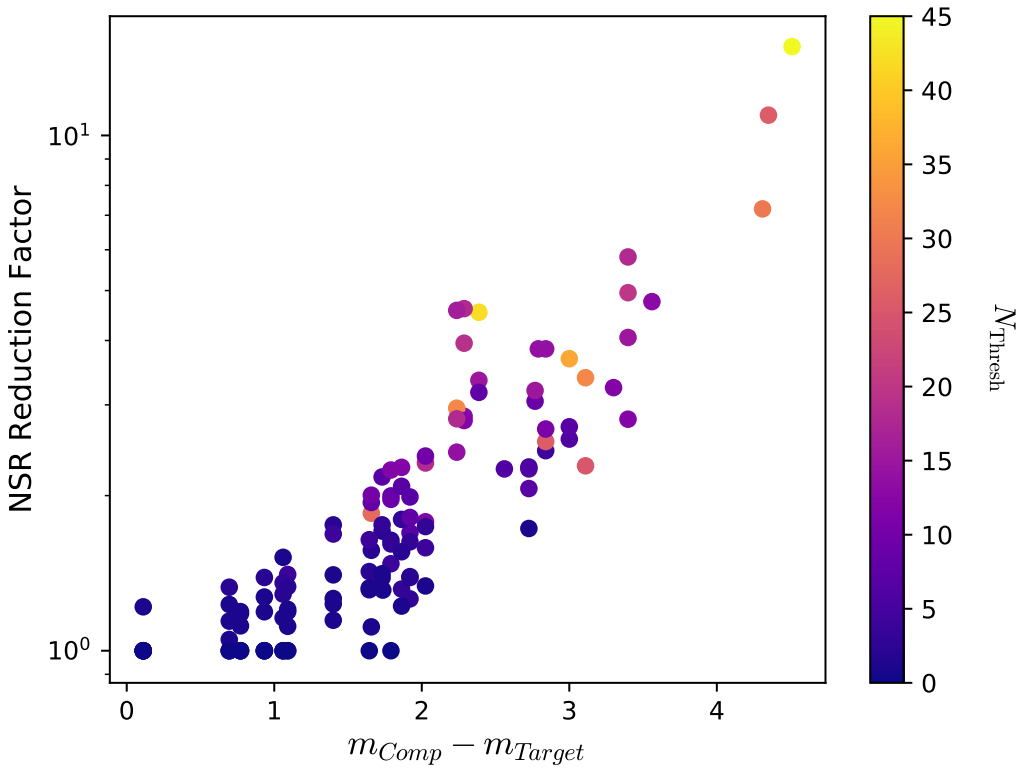

Figure 5.13: The reduction in the NSR versus the difference in magnitude between the comparison star (m_{Comp}) and the target star (m_{Target}). The temporal binning factor N_{Thresh} is given by the colour bar, where N_{Thresh} is the temporal binning required such that the addition of the random noise from the comparison star is outweighed by the correction of the systematic noise. This plot was produced using observations of the Pinwheel Cluster on the Pt5m telescope (see section 5.5.1 for more details).

the calibrated light curve has been reduced by with binning the comparison star before performing the differential photometry. The colour bar shows the degree of temporal binning required, N_{Thresh}, such that the correction of systematic noise with the use of the temporally binned comparison star outweighs the random noise contributions. In some cases, for bright comparison stars, this threshold is reached without any temporal binning.

The results show the expected relationship, where temporally binning bright comparison stars reduces the NSR by a factor $\sim \sqrt{2}$. Temporally binning fainter comparison stars reduces the NSR by a larger factor. The NSR is typically reduced by more than $\sim \sqrt{N}$. This indicates the presence of other random noise

Table 5.1: The comparison stars used, their magnitude in the V band and their distance from WASP-166b.

Star	V	Distance (arcminutes)
TIC-413298649	9.45	44
TIC-408307095	10.29	20
TIC-408306501	11.31	45
TIC-408306605	11.96	33

such as read-out noise and sky background light may be significant. In addition, larger temporal binning factors are required for the faint comparison stars which is to be expected from Fig. 5.2.

For the Pinwheel data, it was found that 44% of the stars in the image field could be used to reduce the NSR of the calibrated light curve to NSR_{Thresh}. In other words, by temporally binning the comparison star, the contribution of random noise was reduced to a negligible level. Furthermore, it has been shown that this is possible for comparison stars up to 4 magnitudes fainter than the target star.

5.5.6 Transit Analysis

5.5.6.1 WASP-166b

The method was tested on an exoplanet transit observation of WASP-166b, a hot Neptune around a magnitude $V = 9.35$ star, observed using a 10 s exposure time at a cadence of 13 s, with NGTS on the 2021 February 18 (Doyle et al., 2022). The data from six of the NGTS telescopes were averaged (Bryant et al., 2020).

A range of comparison stars were selected with magnitudes close to 0, 1, 2 & 3 fainter than WASP-166b. From these stars, a subset of comparison stars closest in position to the target star were selected in order to reduce first order extinction effects. The details for the stars chosen are given in Table. 5.1. The faintest star available has a magnitude of $V = 11.96$.

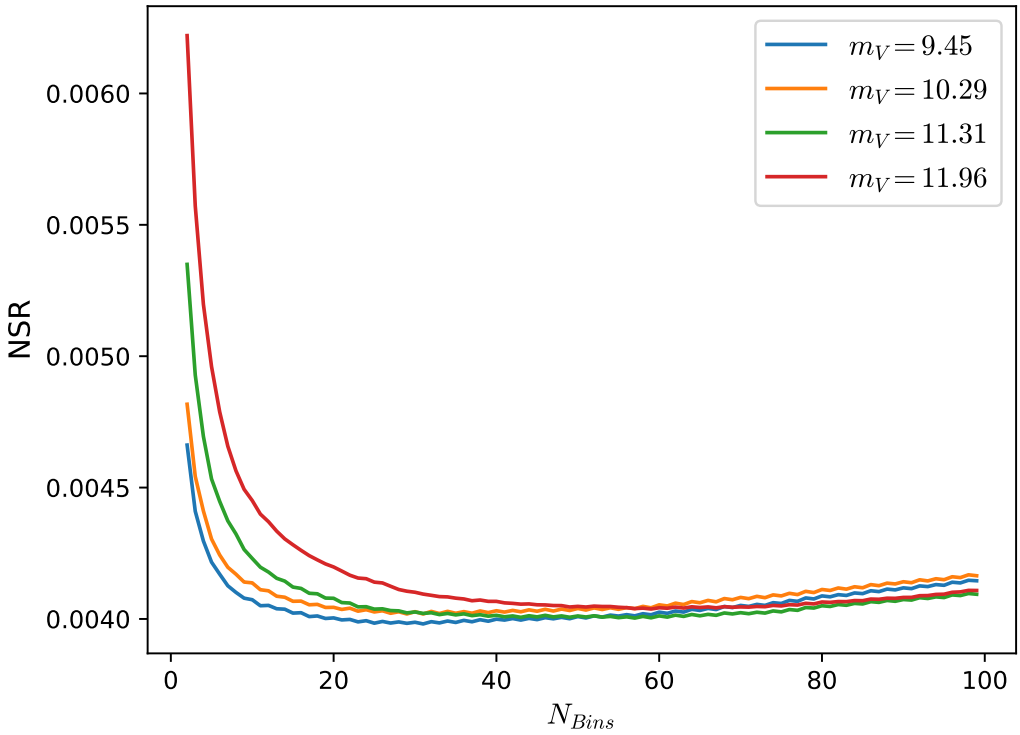

Figure 5.14: The NSR measured for the calibrated light curve for the test star, TIC-408354533, as a function of the temporal binning of the comparison star signal for four comparison stars outlined in table 5.1.

A test star, TIC-408354533, with magnitude $V = 10.29$ and a separation of 482 pixels (equivalent to 40'), from WASP-166b, was selected to find the binning required for each comparison star. Fig. 5.14 shows the measured NSR for the calibrated test star using the comparison stars in Table 5.1. For all curves a shallow minimum can be seen with a binning factor of around 30 for the two brighter stars, and 50 and 70 respectively for the two fainter stars, resulting in the minimum NSR. As the temporal binning is increased beyond this point, the NSR also begins to slowly increase. This is due to the spectrum of the systematic noise, which has increased power at low frequencies.

Fig. 5.15 (a) shows the calibrated light curve using standard differential photometry and (b) shows the calibrated light curve where the comparison star light curves have been temporally binned with N_{Opt} frames. The calibrated light curve was temporally binned in 5 minute intervals such that the transit can be clearly seen

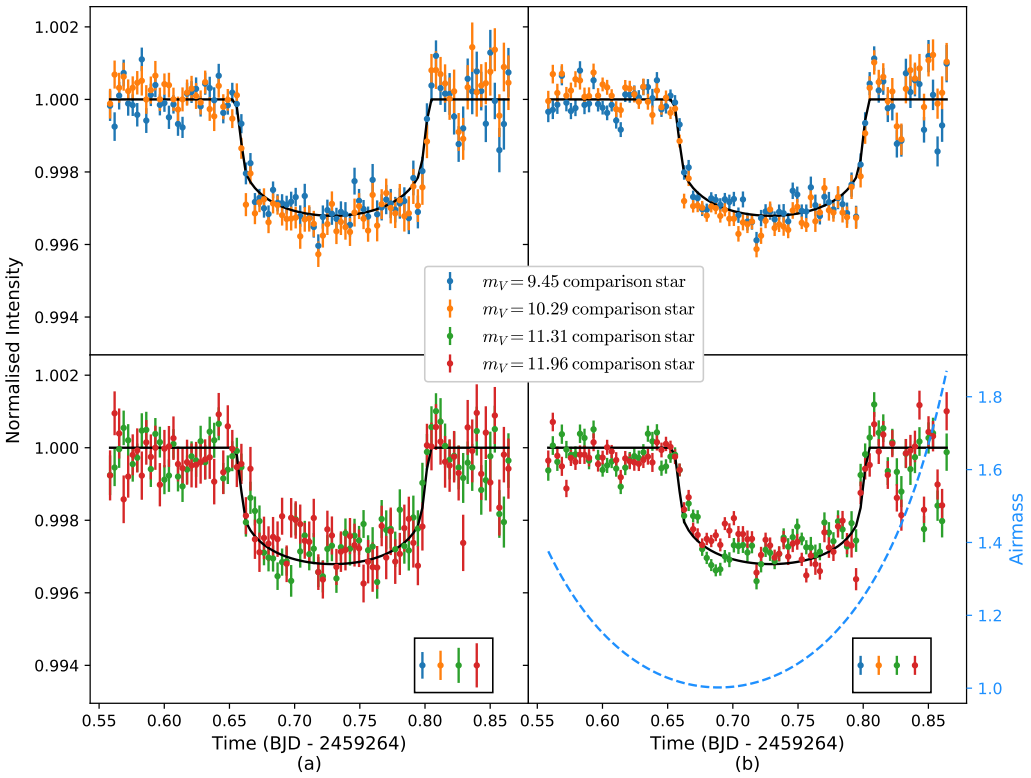

Figure 5.15: The transit light curve for WASP-166b observed on 2021 February 18 with 6 NGTS telescopes. The left-hand plots (a) show the calibrated light curve using standard differential photometry and the right-hand plots (b) show the calibrated light curve where the comparison star light curves have been temporally binned by N_{Opt} frames. The calibrated light curve was then temporally binned in 5 minute intervals such that the transit can be clearly seen and in order to compare the average error between the bins in plot (a) and plot (b). The bottom right-hand plot also has the airmass plotted as the blue dashed line. The average weighted standard error calculated for each time bin as $\sqrt{\frac{1}{\sum_i^n \sigma_i^{-2}}}$ where σ_i is the standard error of telescope i, is indicated by the error bars in the bottom right-hand corner of each subplot. The theoretical transit light curve using the fitted parameters of TESS data presented in Doyle et al. (2022) is also plotted.

and in order to compare the average error between the bins in plot (a) and plot (b). The average error bar, where the error bar for each time bin is calculated as $\sqrt{\frac{1}{\sum_i^n \sigma_i^{-2}}}$ where σ_i is the standard error for telescope i (Hughes and Hase, 2010), for each calibrated light curve is plotted in a black box in the bottom right-hand corner of (a) and (b). Comparing figures (a) and (b) it is clear that temporally binning the comparison stars has reduced the NSR.

The scatter in the average light curve is slightly larger than expected from the individual error bars. This suggests that there is some residual correlated noise that is not being fully corrected via the comparison star measurements for this data. In some parts of the light curve there are clearly some low frequency trends which have not been fully corrected through the differential photometry. These are visible in the un-binned data as well, but are less obvious as the error bars are greater. In addition, the transit depth seems to vary slightly for the different comparison stars. The main reason for this is likely due to the short shoulder measurements which have visible large systematic trends, especially at the egress. This is likely skewing the depth for the different comparison stars. Therefore this effect could be reduced with more data points prior and post to the transit.

Table. 5.2 compares, for each comparison star, the average error bar of the noise in the calibrated light curve where standard differential photometry has been used and where the comparison star light curve has been temporally binned. Table 5.3 compares the average standard error of the calibrated transit light curves data points. Here the effects of residual correlated noise can be seen, such that the reduction factors are lower than in Table. 5.2. For all the comparison stars, temporally binning by N_{Opt} frames has reduced the NSR of the calibrated transit light curve. In addition, with temporal binning, the use of a fainter comparison star performs nearly as well as the brightest comparison star (TIC-413298649).

A Markov chain Monte Carlo (MCMC) method was used to fit the transit photometry of WASP-166b using the `EMCEE` package (Foreman-Mackey et al., 2013) and the `batman` transit model package (Kreidberg, 2015). The parameters obtained by

Table 5.2: The average error bar for the calibrated transit light curve of WASP-166b using standard differential photometry compared with the error bar with temporal binning of the comparison star light curve.

Star	Standard Differential Photometry σ	Temporal Binning σ	Reduction Factor
TIC-413298649	3.7×10^{-4}	2.6×10^{-4}	1.40
TIC-408307095	4.0×10^{-4}	2.6×10^{-4}	1.53
TIC-408306501	4.8×10^{-4}	2.6×10^{-4}	1.84
TIC-408306605	6.1×10^{-4}	2.6×10^{-4}	2.32

Table 5.3: The average scatter for the calibrated transit light curve of WASP-166b using standard differential photometry compared with the average scatter with temporal binning of the comparison star light curve. Here, the effects of residual correlated noise can be seen such that the reduction factors are lower than in Table. 5.2. However, the overall noise is still reduced in all cases.

Star	Standard Differential Photometry σ	Temporal Binning σ	Reduction Factor
TIC-413298649	3.2×10^{-4}	2.9×10^{-4}	1.14
TIC-408307095	3.7×10^{-4}	3.2×10^{-4}	1.17
TIC-408306501	4.4×10^{-4}	3.2×10^{-4}	1.43
TIC-408306605	5.7×10^{-4}	3.8×10^{-4}	1.62

Table 5.4: The MCMC fitted mid-transit time, T_0, for the calibrated transit light curve of WASP-166b using standard differential photometry compared with the temporal binning of the comparison star light curve.

Star	Standard Differential Photometry	Temporal Binning
TIC-413298649	$2459264.73025 \pm 0.00060$	$2459264.73027 \pm 0.00043$
TIC-408307095	$2459264.73002 \pm 0.00051$	$2459264.72988 \pm 0.00037$
TIC-408307086	$2459264.72886 \pm 0.00105$	$2459264.72862 \pm 0.00059$
TIC-413298350	$2459264.73029 \pm 0.00119$	$2459264.73073 \pm 0.00064$

observations of WASP-166b given in Doyle et al. (2022) were used to perform the MCMC simulation. Twenty walkers with 10000 steps per walker, with a burn in of 3000 steps were used. Only the mid-transit time, T_0, the planet radius, R_p, and the limb darkening coefficients were varied, with all remaining parameters fixed. During the MCMC analysis, a linear out-of-transit model with time is fitted to each light curve simultaneously with the transit model.

Table 5.4 shows the results for the fitted T_0 for the calibrated light curve using each comparison star with standard differential photometry and with temporal binning of the comparison star light curve. In all cases temporally binning the comparison star signal results in a higher precision. Doyle et al. (2022) found $T_0 = 2459264.729337 \pm 0.000633$. All of our transit times are consistent with this result and with the TESS prediction within 3σ.

5.5.6.2 TOI-836c

A similar analysis was performed using the telescope data from three NGTS telescopes observing TOI-836c, a sub-Neptune planet around a magnitude $V = 9.92$ K-dwarf star, on 16th of April 2021 (Hawthorn et al., 2023).

Four comparison stars were selected with magnitudes close to 0, 1, 2 & 3 fainter than TOI-836c. The faintest star has a magnitude of $V = 12.77$. A test star, TIC-440869386, with magnitude $V = 10.20$, was used to determine the optimal binning required for each comparison star.

Fig. 5.16 (a) shows the calibrated light curve using standard differential photometry and (b) shows the calibrated light curve where the comparison star light curves have been temporally binned with N_{Opt} frames. Comparing figures (a) and (b) it is clear that temporally binning the comparison stars has reduced the NSR.

Table. 5.5 compares, for each comparison star, the average error bar of the noise in the calibrated light curve where standard differential photometry has been used and where the comparison star light curve has been temporally binned. For all the

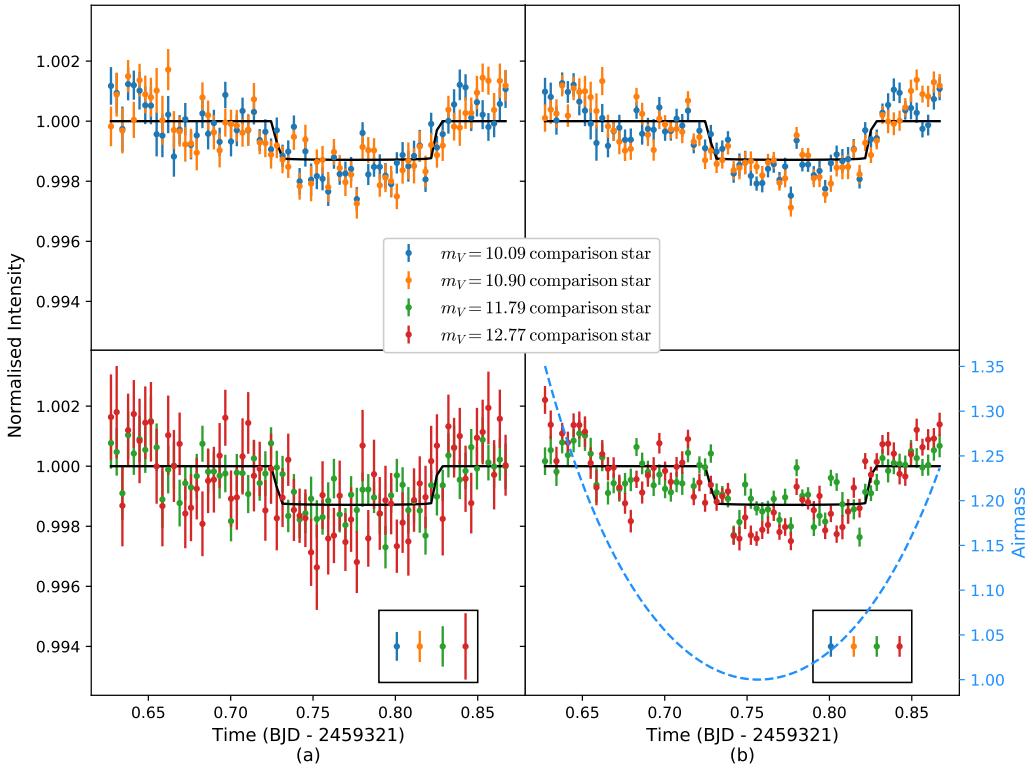

Figure 5.16: The transit light curve for TOI-236c observed on 2021 April 16 with 3 NGTS telescopes. The left-hand plots (a) show the calibrated light curve using standard differential photometry and the right-hand plots (b) show the calibrated light curve where the comparison star light curves have been temporally binned by N_{Opt} frames. The calibrated light curve was then temporally binned in 5 minute intervals such that the transit can be clearly seen and in order to compare the average error between the bins in plot (a) and plot (b). The bottom right-hand plot also has the airmass plotted as the blue dashed line. The average weighted standard error calculated for each time bin as $\sqrt{\frac{1}{\sum_i^n \sigma_i^{-2}}}$ where σ_i is the standard error of telescope i, is indicated by the error bars in the bottom right-hand corner of each subplot. The theoretical transit light curve using the fitted parameters presented in Hawthorn et al. (2023) is also plotted.

Table 5.5: The average error bar for the calibrated transit light curve of TOI-836c using standard differential photometry compared with the error bar with temporal binning of the comparison star light curve.

Star	m_V	Standard Differential Photometry σ	Temporal Binning σ	Reduction Factor
TIC-164844	10.09	4.8×10^{-4}	3.4×10^{-4}	1.39
TIC-166097	10.90	5.2×10^{-4}	3.4×10^{-4}	1.51
TIC-440886598	11.79	6.7×10^{-4}	3.4×10^{-4}	1.96
TIC-440878718	12.77	11.1×10^{-4}	3.4×10^{-4}	3.21

comparison stars, temporally binning by $N_{\rm Opt}$ frames has reduced the NSR of the calibrated transit light curve to the same level. Hence, with temporal binning, the use of a $V = 12.77$ magnitude comparison star does not add any additional random noise fluctuations to the calibrated target light curve, than a comparison star 2.68 magnitudes brighter.

5.5.6.3 Qatar 1b

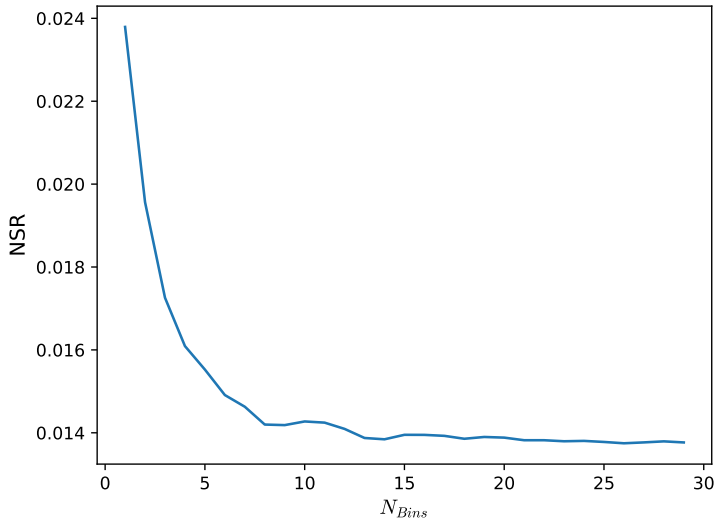

Figure 5.17: The NSR of the calibrated light curve for the test star as a function of the temporal binning factor of the comparison star observed on 2022 June 11 using the Pt5m telescope.

A transit of Qatar-1b, a magnitude $V = 12.84$ star with a transit depth of 0.02 mags, was observed using a 20 s exposure time, with a cadence of 31 s, on the Pt5m

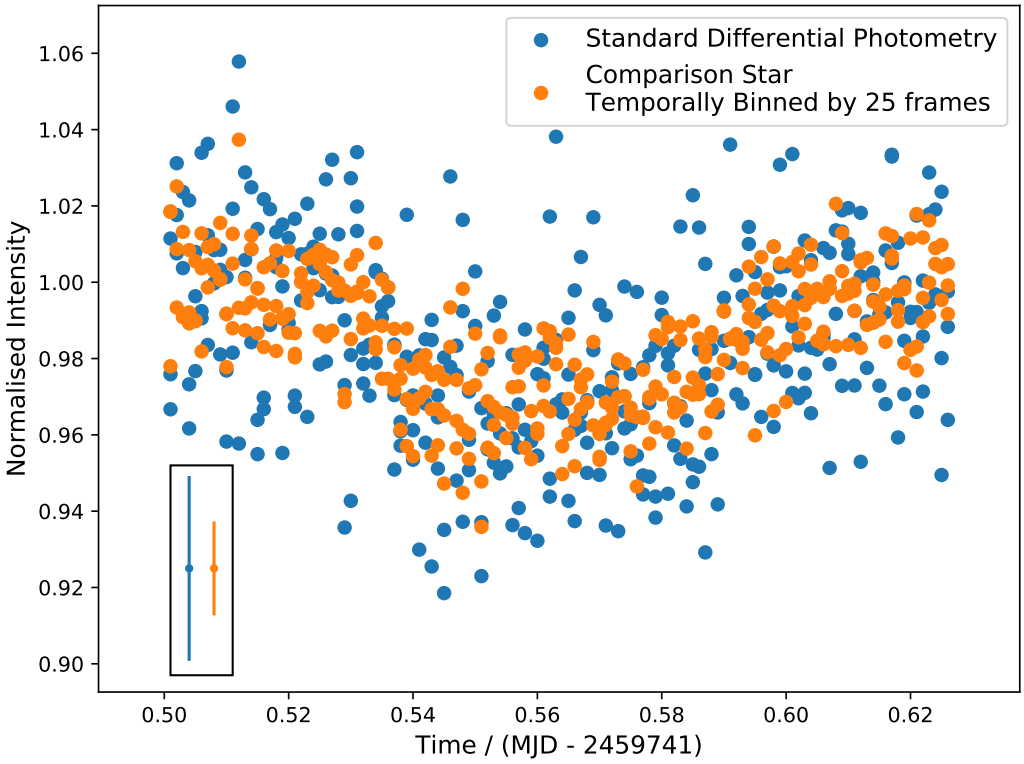

Figure 5.18: The calibrated transit light curve of Qatar-1b observed on 2022 June 11 on the Pt5m telescope using standard differential photometry in blue and where the comparison star has been temporally binned by 25 frames in orange. The standard deviation measured at the wings of the transit for each method is given in the bottom left-hand corner.

telescope on the 2022 June 11. The FOV (10.2×6.9 arcmin) is much more limited for this telescope compared to NGTS. As such, there were far fewer comparison stars to choose from than in the previous example.

A star of magnitude $V = 13.5$ was used to perform the differential photometry. A test star of magnitude $V = 12.98$ was selected from the field to determine the temporal binning required. Fig. 5.17 shows the NSR of the calibrated light curve for the test star against the temporal binning of the comparison star. In this example, no clear minimum in the NSR is visible. This is because the systematic noise is dominated by a linear trend and therefore severe binning still accurately corrects the systematic noise.

Fig. 5.18 shows the calibrated light curve using standard differential photometry

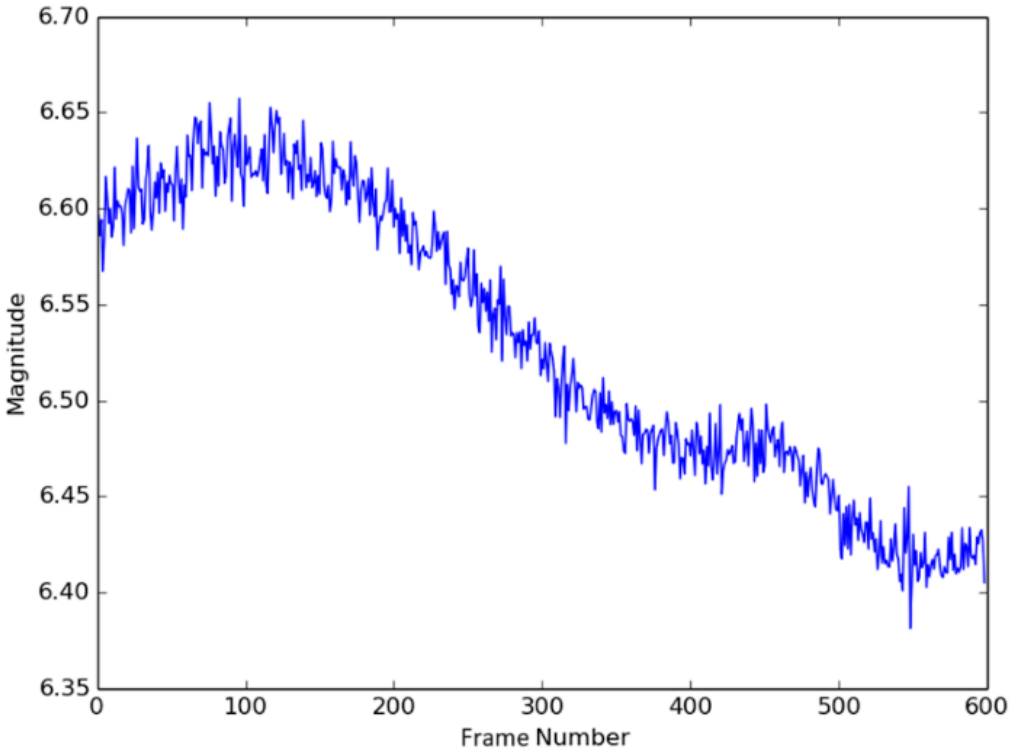

Figure 5.19: The observed light curve for BW Vulpeculae on August the 8th 2016, La Palma, Canary Islands, Spain observed with the wide-field camera setup described in section 5.5.1.2.

and the case where the comparison star has been temporally binned by 25 frames. The NSR of the calibrated light curve using standard differential photometry is 2.1×10^{-2}. Temporally binning the comparison star has reduced the NSR of the calibrated transit by a factor of 2, to an NSR of 1.0×10^{-2}. The NSR of the un-calibrated Qatar-1b transit data was 1.3×10^{-2}. Thus, it has been shown that a fainter comparison star can be used without adding any noise to the final light curve at this cadence.

5.5.7 BW Vulpeculae

BW Vulpeculae or BW Vul, is a Beta Cephei variable star that ranges in brightness between magnitudes $V = 6.44$ and $V = 6.68$ over a period of 4.8 hours in the northern constellation of Vulpecula.

A light curve of BW Vulpeculae, shown in Fig. 5.19, was observed on August the 8th 2016, La Palma, Canary Islands, Spain using the wide-field camera setup described in section 5.5.1.2. A bootstrapping technique was used to measure the location of the minima in the light curve. For each iteration in the bootstrapping, a curve fitting algorithm was used to measure the minima to prevent the location from being skewed by noise.

This technique was performed using a range of comparison stars of varying magnitude. For each comparison star the minima location was measured for the calibrated light curve using standard differential photometry and the calibrated target light curve where the comparison star has been temporally binned by N_{Opt} frames. As a control, the minima was also measured for the un-calibrated BW Vul photometry.

Fig. 5.20 shows the measured minima location of BW Vul for a range of comparison stars. The expected minima location was calculated using previous BW Vul observations (SIMBAD, 2021). For all the comparison stars used, temporally binning the comparison star by N_{Opt} frames results in a more precise measurement of the minima location. Furthermore, in most cases the use of differential photometry has improved the accuracy in the minima measurement.

5.6 Discussion and Conclusions

Choosing a suitable comparison star is of great importance for high-precision photometry since any residual systematics in the differential photometry will add linearly. In addition, the random photon noise and scintillation noise of the star of interest and the comparison star will add in quadrature. The data reduction technique described here significantly reduces the NSR for differential photometry by taking advantage of the fact that power in systematic trends is often at low frequencies compared to the cadence of the light curve. Hence, a minimum exists in the total noise of a light curve as a function of the integration time and cadence. Therefore,

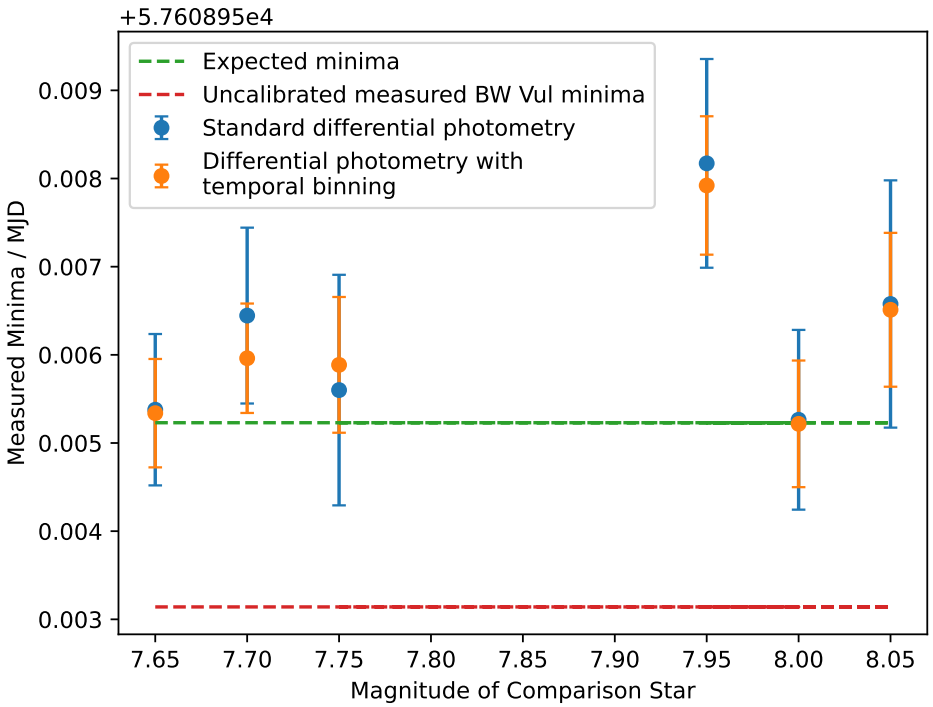

Figure 5.20: The measured minima location of BW Vul for a range of comparison stars using standard differential photometry in blue and with differential photometry with temporal binning in orange. The minima location measured using the un-calibrated BW Vul light curve is given by the red dashed line. The expected minima location, given by the green dashed line, was calculated using previous BW Vul observations in SIMBAD.

the total NSR of the calibrated light curve can be minimised by optimising the temporal binning.

A data pipeline to perform this technique and to optimise the temporal binning used has been described. An example transit light curve of WASP-166b observed using six of the NGTS telescopes has been presented. Light curves using four comparison stars of different magnitude were produced. In all cases temporally binning the comparison star before doing the differential photometry reduced the NSR of the calibrated transit light curve.

One of the main advantages of this binning method is that it allows much fainter comparison stars to be used. This is especially beneficial for less dense fields where

there are few comparison stars available and for large telescopes where the FOV is small. In this case there are often few comparison stars to choose from and therefore calibration methods, such as averaging multiple comparison stars, are limited. This technique is also beneficial for small telescopes where, whilst there are more comparison stars in the FOV to choose from, the scintillation noise is more significant, scaling as $D^{-4/3}$, where D is the aperture size.

This technique can also be implemented in addition to other data reduction methods such as the use of multiple comparison stars and the defocussing technique (Tregloan-Reed and Southworth, 2013) and diffuser technique (Stefansson et al., 2017), thus resulting in even lower NSRs.

It should be noted that this method is only beneficial for observations that are taken in good photometric conditions. The systematic trends in the data must be at low frequencies for the binning of the comparison star to be beneficial. For observations with high frequency systematic noise the comparison star can no longer be binned, as the moving average would smooth out these trends and thus no longer accurately correct the systematic noise for the target star.

For observations that have occasional periods of sudden high frequency trends, binning could still be beneficial. The comparison star data would be temporally binned everywhere except for periods of rapid high frequency trends. As such, the calibrated light curve would still have these periods of high frequency trends corrected by the comparison star. The NSR of the light curve would be improved everywhere except for the high frequency periods where the NSR would be equivalent to the use of standard differential photometry. This flexibility with where the binning is applied is another advantage to this method over the use of low order curve fitting algorithms, as any high order trends can still be corrected.

In addition, it has been demonstrated that this technique works for a range of cadence values up to 30 s. It is expected that this method will work for cadences of the order of tens of seconds in cases dominated by shot noise and scintillation noise.

In addition, the technique has been demonstrated on two exoplanet light curves and have shown that temporal binning of the comparison stars reduces the NSR of the calibrated transit light curve as shown in Table. 5.2 and Table. 5.3. Hence, this data reduction technique is ideal for ground-based follow-up observations of exoplanets around bright stars such as targets found by TESS (Villanueva et al., 2019), Wide Angle Search for Planets (SuperWASP) (Pollacco et al., 2006), Multi-site All-Sky CAmeRA (MASCARA) (Lesage et al., 2014) and NGTS (Chazelas et al., 2012).

Information about telescope sites can also be gained from this technique. Measuring the minima in the NSR v.s. time plots (such as the minima in Fig. 5.14) for a range of standard stars over multiple nights could provide details of the power spectrum of the atmospheric transparency fluctuations of the site and the observed scintillation noise. Therefore, these could be used to perform a statistical survey of seasonal and cyclical variations in photometric quality.

Further research investigating this technique in multiple wavebands is needed. Simultaneous observations in multiple wavebands could be used to investigate how the power spectrum of the atmospheric transparency variations vary with wavelength and therefore the viability of this method in different wavebands.

Chapter 6

Optical sparse telescope arrays and scintillation noise

6.1 Introduction

High-precision, time resolved, ground-based photometry is critical for a wide range of astronomical applications. For example, for exoplanet photometry it is vital for follow-up observations in order to verify the transit detection, to check for variations in the transit timings, and to improve the precision on transit parameters such as the period and depth (Collins et al., 2018). However, such ground-based observations are limited by the effects of the Earth's atmosphere.

Arrays of small telescopes are in common use for exoplanet surveys such as SuperWASP (Pollacco et al., 2006), MASCARA (Lesage et al., 2014) and the Next Generation Transit Survey (NGTS) (Chazelas et al., 2012). Such arrays are designed to observe large patches of the sky using small telescopes' with very large fields-of-view (FOV). Many stars are observed simultaneously and automatic pipelines are used to search for periodic dips in their brightness.

However, another benefit of using such arrays has been recently exploited. By pointing all of the telescopes in the array at a single bright target of interest and combining the photometry from all of the telescopes in the array, high Signal-to-

Noise Ratios (SNRs) can be achieved. For an array of N telescopes, averaging their light curves increases the SNR by a factor of $\sqrt{N}$ if the photometric noise is uncorrelated. Simultaneous observations of WASP-166b by NGTS and the Transiting Exoplanet Survey Satellite (TESS) (Villanueva et al., 2019) shows that ground-based sparse telescope arrays are capable of achieving SNRs comparable to those achieved in space (Bryant et al., 2020) (Doyle et al., 2022).

Not only are arrays of small telescopes able to achieve high SNRs for bright stars, but they also have a much larger FOV than a large telescope. For example, each of the NGTS 20 cm telescopes has a FOV of 8 $\deg^2$. Hence, the likelihood of finding a bright comparison star in the field is significantly increased. Such bright comparison stars are necessary to minimise the addition of random noise fluctuations in differential photometry. As such, arrays of small telescopes could be used for ground based observations of exoplanet transits around bright stars with very high-precision.

However, the $\sqrt{N}$ increase in SNR of using an array of small telescopes is only achieved if the photometric noise from each telescope is independent. Any correlated noise between neighbouring telescopes would significantly reduce the improvement in the measured SNR. Noise sources such as the shot noise of the signal, read-out noise and the shot noise of the sky-background etc. are random and therefore will not be correlated between telescopes. However, for bright targets, the scintillation noise is likely to be the dominant noise source and may be correlated between neighbouring telescopes for long exposure times. This is because scintillation noise is produced by the propagation of the wavefront through high altitude turbulence, producing spatio-temporal intensity fluctuation patterns at the ground (Osborn et al., 2015). Correlation between neighbouring apertures will depend on aperture size, turbulence strength and wind direction and the exposure time, but can be substantial.

These effects all need to be considered when designing a telescope array to perform high-precision ground-based photometry. It has been shown for the NGTS

telescope array that correlation of the photometric noise measured between neighbouring 20 cm telescopes separated by an order of ∼2 m is negligible (Bryant et al., 2020). Here, telescope arrays with much smaller baselines which may be limited by such effects are considered, for example if the telescopes were mounted on a single mount, such as in the Gravitational-wave Optical Transient Observer (GOTO) array (Gompertz et al., 2020).

In this chapter the correlation of scintillation noise between neighbouring telescopes in an array is investigated for a range of parameters including wind direction, exposure time and distance between telescopes. Results from both numerical simulation and observations at the Isaac Newton Telescope (INT) are presented and discussed, and several advantages of using sparse aperture arrays for photometric observations are discussed. The work in this chapter has been published (Hartley et al., 2023b).

6.2 Theory

6.2.1 Sparse Telescope Arrays and Scintillation Limited Stars

For a bright star where scintillation noise is dominant, the benefit of using an array of small telescopes over a single telescope of the same equivalent area for long exposure times can be determined by considering the SNR for both instruments.

To compare the two, consider a single telescope of diameter D and an array of N telescopes, each with diameter D_{sub}. Equating the two areas gives:

$$D = \sqrt{N} D_{\mathrm{sub}}. \tag{6.1}$$

For a bright star, where the noise is limited by scintillation noise, the SNR is proportional to:

$$\mathrm{SNR} \propto \frac{1}{\sigma_I}, \tag{6.2}$$

where σ_I is the RMS scintillation noise.

Hence, for long exposures on a single telescope of diameter D:

$$\mathrm{SNR}_{\mathrm{tel}} \propto (D^{-\frac{4}{3}})^{-\frac{1}{2}} \propto (D)^{2/3}. \tag{6.3}$$

For an array of small telescopes where the photometric noise is uncorrelated between neighbouring telescopes, the scintillation index measured for the entire array is given by:

$$\sigma^2_{I_{\mathrm{array}}} = \frac{\sigma^2_{I_{\mathrm{sub}}}}{N}, \tag{6.4}$$

where $\sigma^2_{I_{\mathrm{sub}}}$ is the scintillation index measured for a single telescope within the array of diameter D_{sub}.

Hence, for an array of telescopes where the photometric noise is uncorrelated:

$$\mathrm{SNR}_{\mathrm{array}} \propto \sqrt{N} \propto \frac{D}{D_{\mathrm{sub}}}. \tag{6.5}$$

Therefore, for long exposure times, the SNR of an array of small telescopes will be greater than the SNR measured by a single telescope of the same equivalent area. This is because $\mathrm{SNR}_{\mathrm{array}} > \mathrm{SNR}_{\mathrm{tel}}$. Hence, an array of small telescopes can achieve the same SNR as a larger telescope with diameter:

$$D = N^{3/4} D_{\mathrm{sub}}, \tag{6.6}$$

for a fraction of the area of glass and hence a fraction of the cost. For example, for bright stars, the SNR of a 2.5 m telescope can be achieved with an array of thirty 20 cm telescopes.

For short exposure times, where $\sigma^2_I \propto D^{-7/3}$, the SNR of a single telescope scales as $D^{7/6}$. Therefore, using an array results in a lower SNR than using a single telescope of the same equivalent area. Therefore, the SNR benefit of using an array of small telescopes is only achieved for long exposure times where $t \gg t_{\mathrm{cross}}$ (for example, on the order of seconds rather than milliseconds).

This SNR for the array given by Eq. 6.5 is only valid if the photometric noise measured for the telescopes are statistically independent. In addition, it should be noted that this increase in SNR performance for an array over a single telescope of

the same total area is only achieved for bright stars where the signal is limited by scintillation noise. For fainter stars, where the photometric noise is dominated by shot noise (Föhring et al., 2019), the SNR depends only on the total area of glass used and therefore no benefit to using an array is obtained.

6.2.2 Scintillation Correlation

The scintillation noise can be correlated between two neighbouring telescopes. If Taylor's frozen flow hypothesis (Taylor, 1938) is assumed, then a high altitude layer of turbulence that is producing the scintillation noise will move a finite distance within the exposure time. As such, the spatial intensity fluctuations can translate from one pupil to the other. The degree of the correlation will be dependent on the averaging of the intensity fluctuations with the exposure time. An example of this spatio-temporal averaging for increasing exposure times is shown in Fig. 6.7. This leads to correlation between the scintillation noise for two apertures.

Several parameters affect the correlation of scintillation noise between neighbouring telescopes. These include:

- Wind direction of the high altitude turbulence relative to the separation vector of the telescopes.
- Exposure time.
- Wind speed of the high altitude turbulent layers.
- Telescope diameter.
- Distance between the telescopes.

The correlation between the measurements of two telescopes is measured using the Pearson Correlation Coefficient, r. The correlation can be calculated both through Monte Carlo simulation and analytically from weak perturbation scintillation theory, both of which are presented here.

6.2.3 Theoretical Scintillation Correlation between Spatially Separated Apertures

From the definition of the scintillation index in Eq. 2.15, for an array of two apertures with intensities I_1 and I_2:

$$\sigma^2_{I_1+I_2} = \frac{\langle (I_1+I_2)^2\rangle - \langle I_1+I_2\rangle^2}{\langle I_1+I_2\rangle^2}. \tag{6.7}$$

If both apertures are the same size, with $\langle I_1\rangle = \langle I_2\rangle = 1$, the term $\langle I_1+I_2\rangle^2 = 2\langle I\rangle^2 + 2\langle I\rangle^2 = 4$. Developing the numerator above, one obtains

$$\sigma^2_{I_1+I_2} = \frac{\langle I^2\rangle + \langle I_1 I_2\rangle - 2}{2}, \tag{6.8}$$

where it has been assumed $\langle I_1^2\rangle = \langle I_2^2\rangle = \langle I^2\rangle$. Using the definition of the single aperture scintillation index one can substitute $\langle I^2\rangle = \sigma_I^2 + 1$, obtaining

$$\sigma^2_{I_1+I_2} = \frac{\sigma_I^2 + \langle I_1 I_2\rangle - 1}{2}. \tag{6.9}$$

Finally, it is noted that the normalised intensity $I = 1 + \delta I$, where δI is a random variable with 0 mean and variance σ_I^2. Hence

$$\langle I_1 I_2\rangle = \langle (1+\delta I_1)(1+\delta I_2)\rangle = 1 + \langle \delta I_1 \delta I_2\rangle \tag{6.10}$$

where $\langle \delta I_1 \delta I_2\rangle$ represents the covariance of scintillation in each aperture. One then obtains

$$\sigma^2_{I_1+I_2} = \frac{\sigma_I^2 + \langle \delta I_1 \delta I_2\rangle}{2}, \tag{6.11}$$

which reduces to Eq. 6.4 in the case of $\langle \delta I_1 \delta I_2\rangle = 0$, i.e. no covariance between apertures. The covariance is therefore given as

$$\langle \delta I_1 \delta I_2\rangle = 2\sigma^2_{I_1+I_2} - \sigma_I^2. \tag{6.12}$$

From standard scintillation theory in the weak perturbation limit (Roddier, 1981), the scintillation index including aperture averaging and exposure time effects can

be obtained by the following integral over altitude and the two-dimensional Fourier plane

$$\sigma_I^2 = 4\int_0^\infty \mathrm{d}h \int_{-\infty}^{\infty} \mathrm{d}^2\mathbf{f}\, \Phi_\phi(h,\mathbf{f}) \sin^2(\pi\lambda h f^2) \times A(\mathbf{f}) \operatorname{sinc}^2(t_{\exp}\mathbf{v}_{\mathrm{wind}}(h)\cdot\mathbf{f}), \tag{6.13}$$

where h represents altitude and $\mathbf{f}$ the two-dimensional spatial frequency vector with $f = |\mathbf{f}|$. The quantity $\Phi_\phi(h,\mathbf{f})$ is the turbulent phase spatial power spectrum for a turbulent layer at altitude h, and the $\sin^2$ filter describes the effect of propagation to the ground. The sinc^2 filter represents temporal averaging of the scintillation according to the wind vector $\mathbf{v}_{\mathrm{wind}}(h)$ for the layer at altitude h (Tokovinin, 2002). The aperture filter $A(\mathbf{f}) = |\mathcal{F}(P(\mathbf{r}))|^2$ is the square modulus of the Fourier transform of the pupil function $P(\mathrm{r})$. For a single circular aperture this is given by

$$A(\mathbf{f}) = \frac{4}{\pi D f^2} J_1^2\left(\pi D f^2\right) \tag{6.14}$$

where J_1 is the Bessel function of the first kind and D is the single aperture diameter. For two apertures separated by the vector $\mathbf{\Delta}$, the convolution theorem of the Fourier transform with two Dirac delta functions can be used to obtain

$$A(\mathbf{f},\mathbf{\Delta}) = \frac{1}{4}A(\mathbf{f})|1+\exp(2\pi i\mathbf{\Delta}\cdot\mathbf{f})|^2 = A(\mathbf{f})\cos^2(\pi\mathbf{\Delta}\cdot\mathbf{f}) \tag{6.15}$$

where the factor of $1/4$ arises from normalisation of the two apertures. For the computation of covariance, combining Eq. 6.12, 6.13 and Eq. 6.15 one obtains

$$\langle\delta I_1\delta I_2\rangle = 4\int_0^\infty \mathrm{d}h \int_{-\infty}^{\infty} \mathrm{d}^2\mathbf{f}\, \Phi_\phi(h,\mathbf{f}) \sin^2(\pi\lambda h f^2) \times A(\mathbf{f})(2\cos^2(\pi\mathbf{\Delta}\cdot\mathbf{f})-1) \operatorname{sinc}^2(t_{\exp}\mathbf{v}_{\mathrm{wind}}(h)\cdot\mathbf{f}), \tag{6.16}$$

which can be straightforwardly numerically integrated. The correlation, $r(\Delta)$ is then obtained by normalising the covariance

$$r(\Delta) = \frac{\langle\delta I_1\delta I_2\rangle(\Delta)}{\langle\delta I_1\delta I_2\rangle(0)} = \frac{\langle\delta I_1\delta I_2\rangle}{\sigma_I^2}. \tag{6.17}$$

It should also be noted that the scintillation index for an arbitrary N-aperture array may be directly calculated by integrating Eq. 6.13 using the aperture filter

$$A_{\mathrm{array}}(\mathbf{f},\{\mathbf{\Delta_i}\}) = \frac{1}{N^2}A(\mathbf{f})\left|\sum_i \exp(2\pi i\mathbf{\Delta}_i\cdot\mathbf{f})\right|^2, \tag{6.18}$$

where the $\boldsymbol{\Delta}_i$ are the spatial co-ordinates of the centre of each aperture of the array.

6.3 Method

The scintillation correlation measured between two telescopes is dependent on the parameters described above. The dependence of these parameters were investigated both in simulation and using INT telescope measurements. The method for each investigation is described below.

6.3.1 Simulation

To investigate the spatio-temporal correlation of scintillation in simulation, a Monte Carlo phase screen representation of the atmosphere was produced using the python package `SOAPY` (Reeves, 2016). The phase screens were used with Fresnel propagation to simulate a scintillation pattern at ground level using the python package `AOtools` (Townson et al., 2019). Small telescope pupils were cut out from this pattern and summed to give the integrated intensity for each pupil.

Turbulence profiles measured using a SCIDAR turbulence profiler instrument (Shepherd et al., 2013) in La Palma and Paranal were used to produce accurate estimations for the strength and altitude of the turbulence layers above the telescope pupils in numerical simulation. The simulated atmospheres were updated and translated based on the turbulent profile wind velocities and directions in order to simulate the effect of the finite exposure time assuming Taylor's frozen flow hypothesis. This was then repeated to produce a light curve with the appropriate temporal intensity fluctuations for each telescope.

The Pearson correlation coefficient was then measured between the neighbouring telescopes to measure the correlation of the intensity fluctuations due to scintillation. It should be noted that new phase screens were generated for each exposure,

such that the temporal correlation measured was strictly dependent on the exposure time used.

6.3.2 Telescope Measurements

Measurements were made at the INT in La Palma, Spain by re-imaging the telescope aperture plane onto a detector using a collimating lens. The detector used was a ZWO 1600 CMOS camera, which allowed the use of short exposures and high frame rates with relatively low readout noise. A SCIDAR instrument was also mounted on the telescope so that turbulence profile measurements could be interleaved with the photometric measurements. The SCIDAR data could then be used in numerical simulation to compare the on-sky photometric results to the simulation, for the prevailing turbulence and wind profile. The pupil-imager and SCIDAR turbulence profiler were mounted in parallel at the Cassegrain focus with a folding mirror used to switch between the two instruments.

The scintillation pattern in the pupil-plane were observed in the V band for a range of exposure times. From these scintillation patterns, an array of small subapertures equivalent to a sparse telescope array could be defined. From these observations the effect of a range of parameters on the scintillation correlation between the subapertures could be measured.

Data were obtained in two observing runs, in September 2021 and May 2022. In the first observation a bright star, Aljanah, with magnitude $V = 2.48$ was selected as a suitable target. Pupil-plane images with exposure times of 0.01 s, 0.1 s and 1 s were collected. Exposure times of more than 1 s would have saturated the detector. The second data run in May 2022 included longer exposure times of 2 s and 3 s using the bright star Seginus, a magnitude $V = 3.02$ star.

6.3.3 Aperture Size

To select a suitable aperture size for a sparse telescope array, careful consideration of the Optical Telescope Assembly (OTA) cost and the cost of the detectors is required.

The cost of a ground-based optical telescope scales with aperture size. Several models have been used to estimate the scaling of cost with aperture size. For example, van Belle et al. (2004) estimated the scaling of cost with the ground OTA size as:

$$\text{Ground OTA Cost} \propto D^{2.46}. \tag{6.19}$$

This relation is given for large telescopes. However, based on the price for commercial telescopes in the 20-100 cm range, a relation of D^3 better reflects the cost scaling.

The correlation measured between pupils with separation also depends on telescope size. This is because the intensity fluctuations are averaged over a larger area and therefore measure larger scales which will be correlated over larger separations. Hence, large telescopes will need to be separated by larger distances.

In addition, the aperture size will also affect the FOV. The FOV often scales inversely with the telescope aperture assuming a constant focal ratio and equivalent detector size. Therefore, for a smaller telescope aperture and larger FOV there will be a higher probability of finding a bright comparison star in the field.

There are two options for the sparse telescope array design. One is to have each telescope in the array on its own mount, as for the NGTS array. This gives the option of independent pointing of the telescopes, but will increase the cost and complexity. The second option is to have all the apertures mounted onto a single large mount, such as the GOTO array. Here, this second option is considered. In this case, the cost of the mount will scale more slowly with the number of telescopes.

The SNR increases with telescope size and the SNR of an array is proportional to

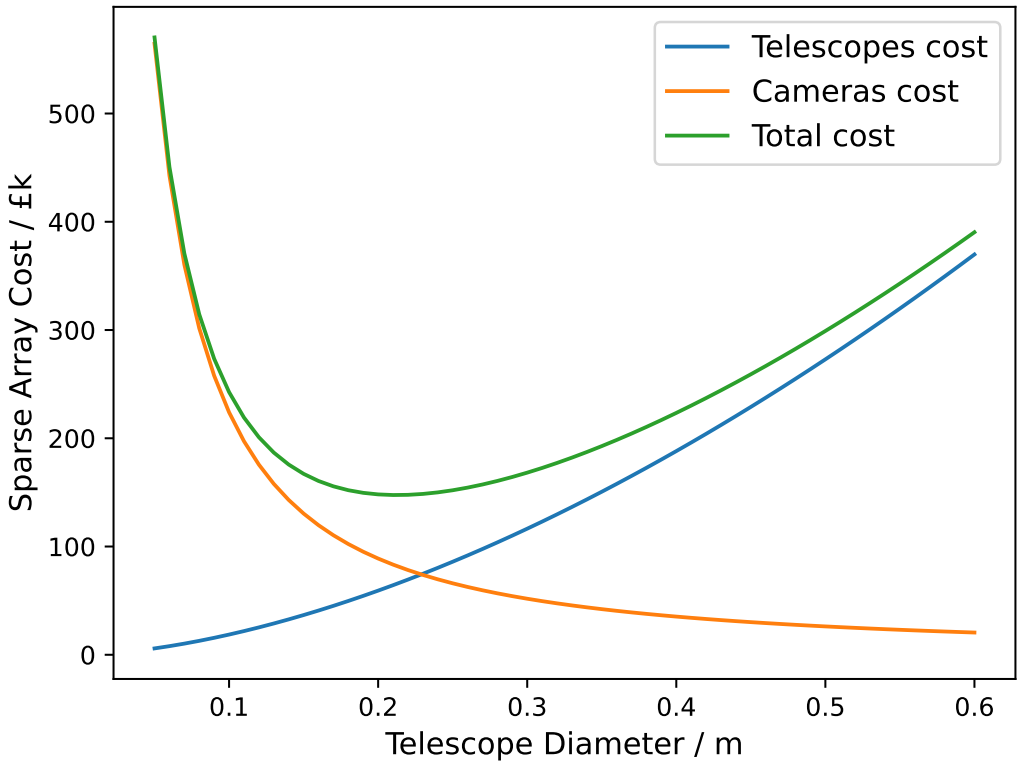

Figure 6.1: The cost of building a sparse telescope array that provides the same scintillation limited SNR as the Isaac Newton Telescope as a function of the diameter of the telescopes in the array. The cost for the telescopes and cameras are given assuming a cost of £3k per camera and assuming the telescope cost scales as D^3.

$\mathrm{SNR}_{\mathrm{tel}}\sqrt{N}$ where $\mathrm{SNR}_{\mathrm{tel}}$ is the SNR of a single telescope in the array. Hence, for very small telescopes, more telescopes in the array to reach the required overall SNR, and therefore more detectors, would be needed.

The telescope aperture used in an array should therefore be optimised to minimise the cost. Fig. 6.1 shows the estimated cost for a sparse telescope array as a function of the telescope diameter, assuming that a scintillation limited SNR for the INT is desired. The cost for the telescopes and cameras are given assuming a cost of £3k per camera and assuming the telescope cost scales as D^3. The number of telescopes N required to match the SNR for the INT was calculated using Eq. 6.6, for a range of values of D_{sub}. For small telescopes, where a larger number of apertures is needed, the sparse array cost is dominated by the cost of the cameras, which

decreases sharply with N and hence, aperture size. As the telescope size increases, the cost of the OTA starts to become more significant and a slow increase in array cost is seen. These two opposing parameters result in a shallow minimum.

Based on this figure, it is proposed that the use of ∼20 cm telescopes is a suitable aperture size for building a sparse telescope array in terms of minimising cost. Additionally, NGTS has already shown that an array of telescopes of this size can achieve SNRs equivalent to that of TESS observations (Bryant et al., 2020). Hence, an aperture size of 20 cm has been used for all the results given in section 6.4.

6.4 Results

In this section, the correlation of scintillation noise between neighbouring telescopes is investigated for a range of parameters. Results from numerical simulations and INT telescope measurements are presented.

6.4.1 Analytical and Numerical Simulation Results

6.4.1.1 Wind Direction

To investigate the significance of wind direction on the correlation of scintillation noise between two pupils, a turbulence profile consisting of a single layer at an altitude of 10 km was modelled with a wind velocity of 15 ms^{-1} and direction 0° for a 1 s exposure time. Two 20 cm telescopes were simulated. For all the results, the telescope pupils are initially superposed such that a correlation coefficient of $r = 1$ is measured. This overlapping of the telescope pupils is possible in simulation but is not physically possible for real apertures. The pupils are then moved apart in a range of directions.

Fig. 6.2 shows a strong correlation between two telescopes separated parallel to the wind direction (0 degrees), even at a separation of 1 m. The numerical simulation

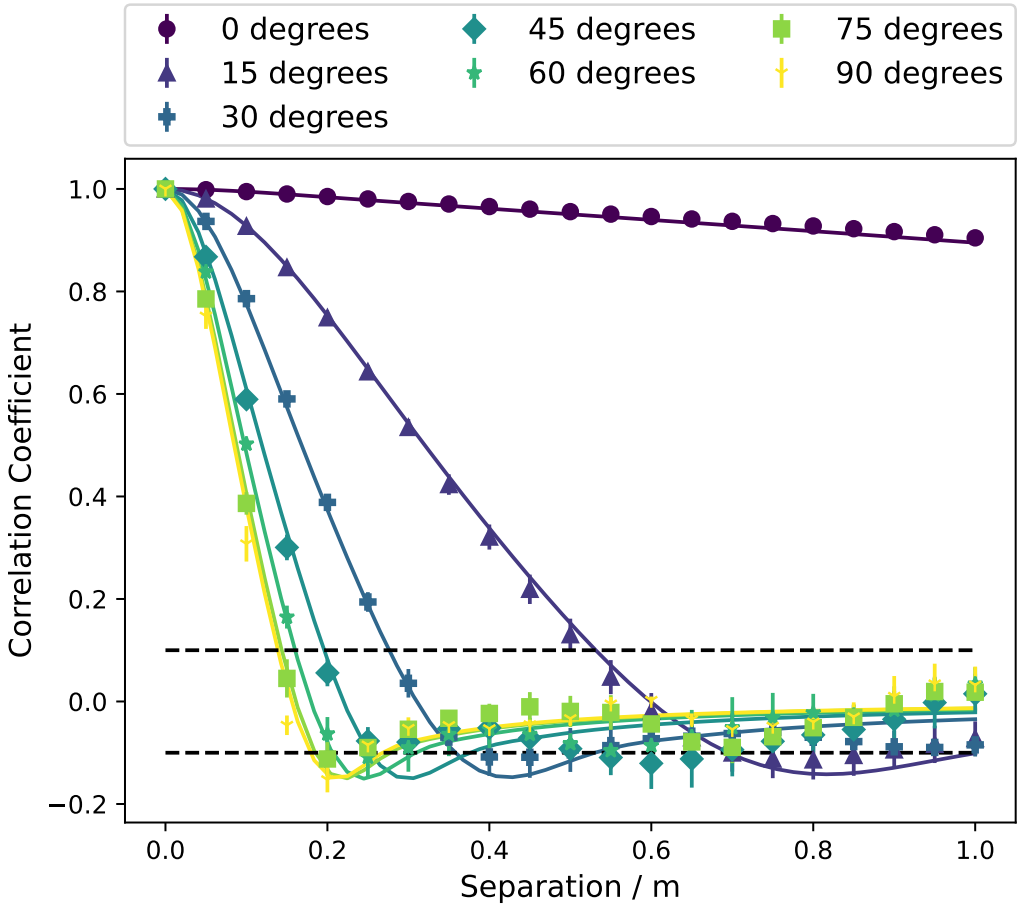

Figure 6.2: The correlation coefficient of the intensity fluctuations due to scintillation between two telescopes as a function of separation along the y-axis (North), which corresponds to 0 degrees (see Fig. 6.3 for reference). A range of wind directions are plotted between 0 and 90 degrees. The error bars represent the standard error in the Monte Carlo simulation. The theoretical scintillation correlation is plotted as the solid lines.

results closely follow the theoretical scintillation correlation, which are plotted as the solid lines. As the telescopes are separated along directions away from the wind direction, the correlation drops significantly with distance. Telescopes that are positioned perpendicular to the wind direction are not correlated at all once the telescope pupils no longer overlap.

Hence, as expected, the wind direction of the high altitude turbulence is arguably the most significant parameter for the scintillation correlation measured between neighbouring telescopes for long exposure observations. Telescopes with baselines

Table 6.1: The median five layer SCIDAR profile measured at La Palma.

Heights (m)	0	250	3500	11250	14750
Weights ($r_0 = 0.20$ m)	0.266	0.585	0.059	0.049	0.041
Wind Direction (degrees)	159	236	238	262	143
Wind Speed (ms^{-1})	6.8	8.7	10.6	12.9	10.5

close to parallel to the wind direction, within $\sim 15°$, will be highly correlated at short separations. This demonstrates the significance of the turbulence wind direction for scintillation correlation. An unfavourable wind direction, i.e. parallel to the separation of the apertures, results in large correlation coefficients between neighbouring telescope pupils.

In reality, the atmosphere is not discrete and typically it will have several significant turbulent layers moving in different directions, averaging out this effect. As such, it is expected that the measured correlation in scintillation noise between neighbouring telescopes will become negligible at much shorter separations if a realistic turbulence profile is assumed rather than a single layer. However, sites will often have a prevailing wind direction for the high altitude turbulence due to atmospheric features such as the jet stream. In principle, telescope arrays could be designed with this in consideration by having longer baselines parallel to the prevailing wind direction.

6.4.1.2 Exposure Time

Another significant factor effecting the correlation of scintillation noise between neighbouring telescopes is the exposure time used. The minimum distance required between neighbouring telescopes will depend on the distance that the high altitude turbulence has moved during an exposure time. For example, for a high altitude turbulent layer moving with a wind velocity of 30 ms^{-1}, for a 1 s exposure time the turbulent layer, and therefore the spatial intensity fluctuations at the ground produced by this layer, will have moved 30 m, whereas for a 0.1 s exposure time it will have only moved 3 m. Hence, this will also be dependent on the wind speed

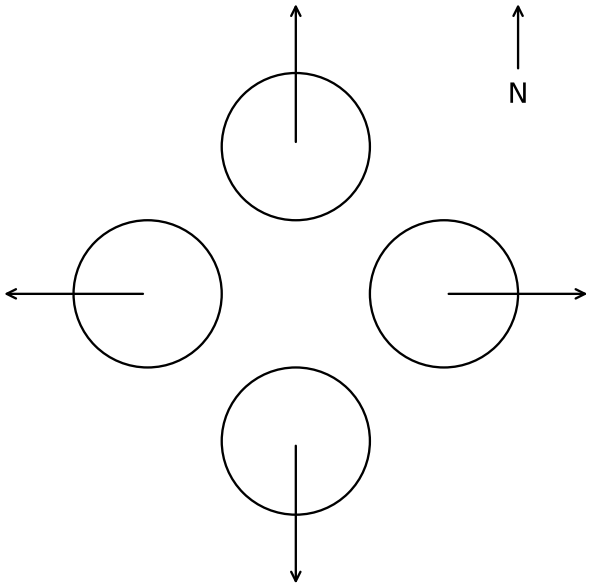

Figure 6.3: The geometry of the telescope positions relative to North used for the calculations shown in Fig. 6.4. The 4 telescopes begin entirely overlapped and are then moved in 2.5 cm steps in the directions indicated by arrows.

of the high altitude turbulent layer.

A numerical simulation based on fifteen different optical turbulence profiles from La Palma (Osborn et al., 2018) was used to investigate how the correlation of scintillation noise between neighbouring telescopes varied with exposure time. These profiles were based on SCIDAR data collected in La Palma in 2015 and were produced using the hierarchical clustering method described by Farley et al. (2018). The median profile is given in Table. 6.1.

Four 20 cm apertures were used in simulation, two separated along the x-axis (parallel to the 90° and 270° directions) and two separated along the y-axis (parallel to the 0° and 180° directions). This is demonstrated in Fig. 6.3. This is the simplest configuration to explore a 2D array.

Fig. 6.4 shows the results of this simulation where the telescopes are (a) along the x-axis (parallel to the high altitude wind direction) and (b) along the y-axis (perpendicular to the high altitude wind direction). The numerical simulation results closely follow the theoretical correlation expected for each exposure time using the

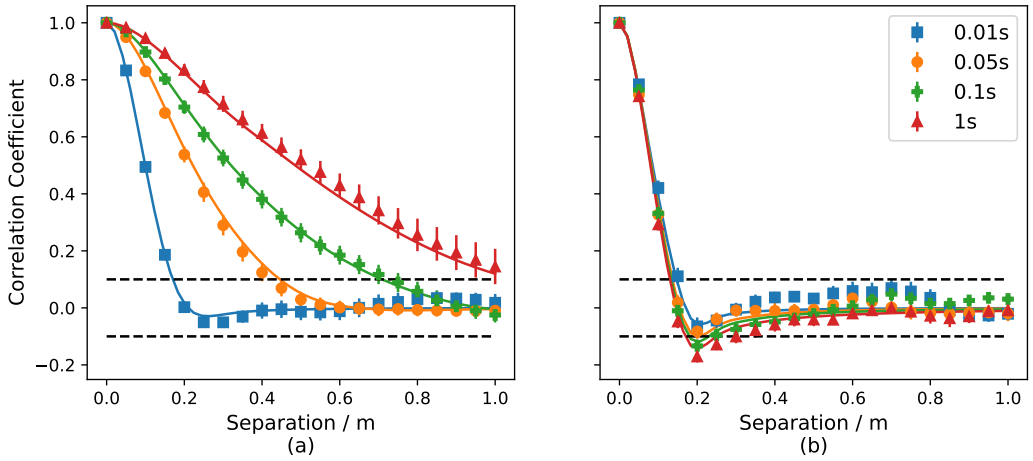

Figure 6.4: The average correlation coefficient of the intensity fluctuations due to scintillation between two telescope as a function of separation (a) along the x-axis (parallel to the high altitude wind direction) and (b) along the y-axis (perpendicular to the high altitude wind direction) for the numerical simulation of fifteen SCIDAR turbulence profiles measured in La Palma for a range of exposure times. The scatter in the correlation due to the variation in the turbulence profiles is represented by the standard error error bars. The theoretical correlation coefficient for the average SCIDAR turbulence profile for La Palma is also plotted as solid lines.

average SCIDAR turbulence profile for La Palma. For the shortest exposure time of 0.01 s, the scintillation correlation drops to zero as soon as the telescopes no longer overlap. As the exposure time increases, the measured correlation in the scintillation noise between the telescopes in (a) increases for all separations, i.e. for longer exposure times, a larger separation between neighbouring telescopes is needed for the scintillation noise to be uncorrelated. This is to be expected, as the atmospheric turbulence will have moved a larger distance over the exposure time, producing intensity correlations over larger spatial scales.

However, if the telescopes are placed perpendicular to the wind direction, as shown in Fig. 6.4 (b), the correlation of scintillation noise falls to zero once the telescopes no longer overlap for all of the exposure times used. There is small deviation between the simulated results and the theoretical scintillation correlation after 0.3 m, however the correlation measured in simulation is still negligible.

Table 6.2: The median five layer SCIDAR profile measured at Paranal.

Heights (m)	0	1750	5500	10250	14500
Weights ($r_0 = 0.21$ m)	0.714	0.106	0.057	0.057	0.066
Wind Direction (degrees)	142	298	278	273	271
Wind Speed (ms^{-1})	7.8	9.1	18.8	24.4	9.9

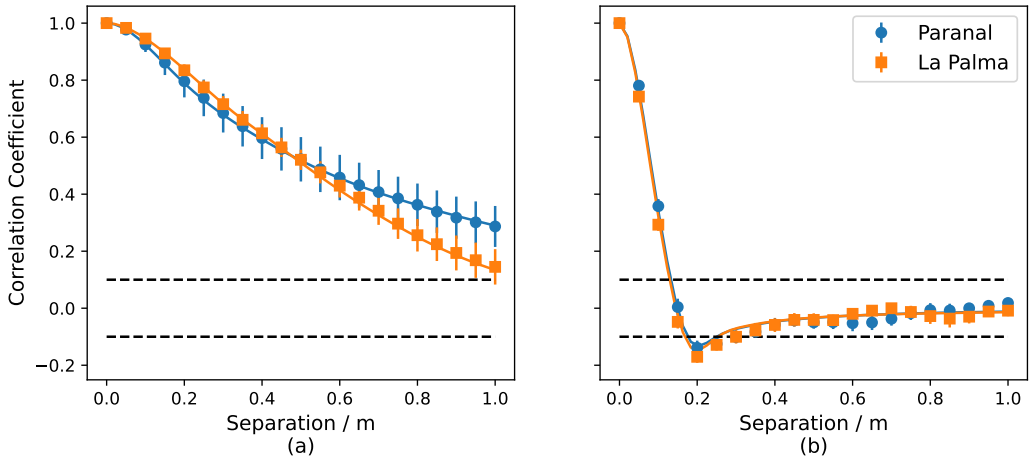

Figure 6.5: The measured correlation in intensity between two telescopes as a function of separation along the (a) the x-axis (East) and (b) the y-axis (North). The average result for fifteen SCIDAR profiles from La Palma and eighteen SCIDAR profiles from Paranal are plotted with the scatter resulting from the variation in the turbulence profiles is shown by the error bars in terms of standard error. The theoretical correlation is given by the solid lines.

6.4.1.3 SCIDAR Profiles Simulation

Optical turbulence profiles from SCIDAR measurements collected at Paranal (Farley et al., 2018) and La Palma (Osborn et al., 2018) were used to compare the two sites. The SCIDAR data suggests that both Paranal and La Palma have similar prevailing wind directions for the high altitude turbulence layers. The median profiles given in Table. 6.1 and Table. 6.2 are shown to indicate the median wind directions.

Fig. 6.5 shows the results from the simulation for the two telescopes placed along (a) the x-axis and (b) the y-axis. The simulation results closely match the theoretical correlation given by the solid lines. Based on the median profiles given in Table. 6.1 and Table. 6.2, the dominant high layer turbulence is along the 262° and

273° direction respectively and therefore is close to parallel to the x-axis. Hence, stronger correlation of the scintillation noise along the x-axis is expected.

The average of the Paranal profiles in Fig. 6.5 (a) have a slightly higher correlation coefficient at large separations, since the median wind direction of the high altitude turbulent layer is closer to parallel to the x-axis than for the La Palma profiles. These results suggest that the prevailing wind direction of the high altitude turbulent layers could be useful information for designing optimised sparse telescope arrays.

6.4.1.4 Telescope Separation

A key question for the use of sparse telescope arrays is the minimum separation required between telescopes within a telescope array so as to reduce correlation of scintillation noise to a negligible level.

To determine the separation required between neighbouring telescopes, an array of 4 telescopes was tested in simulation using 18 Paranal SCIDAR profiles each with 5 layers. The correlation of scintillation for 1 s exposures was measured such that the scintillation variance is expected to be described by Eq. 2.20. The telescopes pupils were initially fully superimposed and were then moved incrementally apart along the x and y axis. This was repeated for five telescope aperture sizes of $D =$ 15 cm, 20 cm, 28 cm, 40 cm & 50 cm.

Fig. 6.6 shows the average SNR for a range of aperture sizes over the 18 Paranal profiles for an array of 4 telescopes as a function of the separation in units of the aperture diameter, D. For all of the aperture sizes, the SNR levels off for separations larger than $\sim 2D$. This suggests a centre-to-centre separation between neighbouring telescopes of at least $2D$ should be used.

It is possible that for longer exposure times (more than 10 s) a larger separation may be required. This is because for longer temporal averaging, larger spatial scales in the scintillation pattern will be more dominant. However, since the targets which

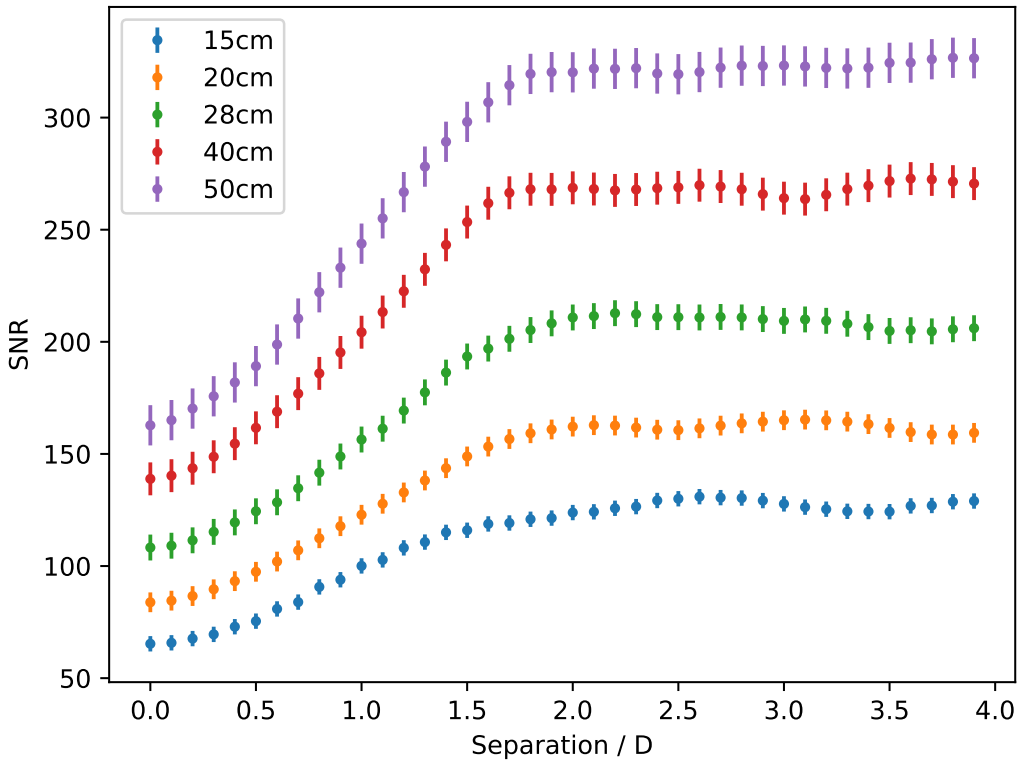

Figure 6.6: The average scintillation limited SNR from simulation for an array of 4 telescopes with diameter D as a function of the centre-to-centre separation between them. The 4 telescopes are positioned as in Fig. 6.3. A range of telescope aperture sizes of $D = 15$ cm, 20 cm, 28 cm, 40 cm & 50 cm are plotted. For all the aperture sizes, the SNR levels off for telescope separations greater than $\sim 2D$.

are limited by scintillation noise are bright, to avoid saturation very long exposure times cannot be used. Therefore, this will rarely be a problem.

6.4.2 Telescope Measurements

The results from section 6.4.1 show how the wind direction, exposure time and distance between neighbouring telescopes all affect the correlation of scintillation between two apertures. However, these simulations have limitations, such as the discrete number of turbulent layers that can be simulated and the assumption of frozen flow. Hence, telescope data was recorded to test this for the real atmosphere.

Examples of pupil plane date for the INT with exposure times of 0.01 s, 0.1 s and 1 s can be seen in Fig. 6.7. The variance in intensity across the pupil is very large

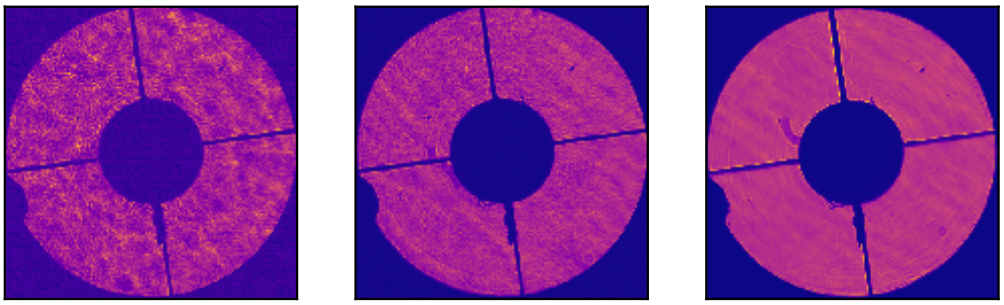

Figure 6.7: Example INT pupil-plane images for the 0.01 s, 0.1 s and 1 s exposures. These show the spatio-temporal averaging of the scintillation pattern for increasing exposure time.

Table 6.3: The median five layer SCIDAR profile measured between 22:00 and 23:00 on 2021 September 19.

Heights	0	211	7175	12028	13927
Weights ($r_0 = 0.16$ m)	0.619	0.240	0.029	0.072	0.040
Wind Direction	130	106	92	84	64
Wind Speed	4.4	2.1	15.7	20.7	16.4

for the 0.01 s data with the speckles clearly visible. For the 0.1 s data, streaks across the pupil can clearly be seen moving in the wind direction of the dominant high layer turbulence. For the 1 s frame the pattern is averaged further, and the intensity variance reduced.

The average of all of the images recorded for each exposure time within a given observation run was used as a flat field image. Some areas affected by dust and small fibres in the optical path which are visible in the 1 s image, were avoided entirely in the data analysis as it could affect the measured scintillation correlation.

6.4.2.1 SCIDAR Turbulence Profile

The stereo-SCIDAR instrument was used to measure the turbulence profile above the INT in between pupil-plane data collections. The median of 12 profiles measured between 22:00 and 23:00 on 2021 September 19 is given in table 6.3. This profile was grouped into five layers using the Optimal Grouping method (Saxen-

huber et al., 2017).

The SCIDAR profile measured is typical for La Palma with a strong ground layer and another strong layer at an altitude of approximately $\sim$ 12 km. It should be noted that measuring the wind direction and speed for the turbulent layers is challenging and can only be performed by tracking strong features over time. As such, wind speed and direction measurements are only available for the dominant layers.

6.4.2.2 Exposure Time, Wind Direction and Aperture Separation

A Monte Carlo algorithm was implemented to investigate the importance of wind direction, exposure time and telescope separation. This worked by randomly selecting start locations within the INT pupil-plane images from which it was possible to offset by at least 0.75 m without leaving the limits of the pupil area or intersecting the shadow of the secondary mirror and its supports. From the pupil plane image, two sub-pupils were cut out and summed to measure the intensity within each pupil. One pupil remained stationary at the start location and the second pupil would then be moved incrementally in the given direction with the intensity being recorded at each location.

In this way the scintillation correlation could be recorded in a range of directions for a range of telescope separations. The Monte Carlo algorithm was run ten times for each direction to ensure the average result was not affected by any flat-field irregularities, for example due to dust within the re-imaging optics. This method was repeated for the data collected for each exposure time.

Data packets comprising 200 frames were collected. Fifteen 0.01 s packets, eleven 0.1 s packets and seventeen 1 s packets were collected between 23:00 and 00:30 on the night of 2021 September 19. The results using the pupil-plane data for 0.01 s, 0.1 s and 1 s exposure times are shown in Fig. 6.8, 6.9 and 6.10 respectively. For very short exposure times, the measured scintillation correlation drops to zero as

soon as the pupils are not overlapping, even along the wind direction. Whereas, for the long exposure data, the measured scintillation correlation along the wind direction increases at larger separations. The increased correlation is seen for orientations within approximately 15° of the aperture separations. Hence, the on-sky data agrees with the simulation results from Fig. 6.2 and Fig. 6.4 for both wind direction and exposure time.

The profile given in table 6.3 was used in a Monte Carlo simulation to compare the scintillation correlation results to the on-sky data for the 1 s exposure time. Fig. 6.11 shows the simulated results. Comparing to Fig. 6.10 it is clear that the simulation overestimates the measured scintillation noise correlation between the two telescope pupils at large separations. This is to be expected as the simulation assumes Taylor's frozen flow hypothesis and approximates the atmosphere as discrete with only five layers whereas in reality the atmospheric turbulence profile is continuous.

Based on these results it can be seen that in most cases neighbouring telescopes within an array will be uncorrelated. Only pairs of telescopes with baselines close to parallel to the wind direction will exhibit significant correlation of the scintillation noise. This drops significantly with separation and is almost negligible after $\sim$ 40 cm. Based on the results in this section, an array of 20 cm within a sparse array should be separated by at least 40 cm from centre to centre. This is in agreement with the results from numerical simulation shown in Fig. 6.6 in section 6.4.1.4 which suggests a separation of $2D$ is required.

6.4.2.3 Optical Sparse Arrays

Based on the results from the previous section, a centre-to-centre separation of approximately twice the aperture diameter will result in minimal correlation between the neighbouring pupils. This separation was used to test the relation between the number of telescopes in an array and the resulting photometric SNR.

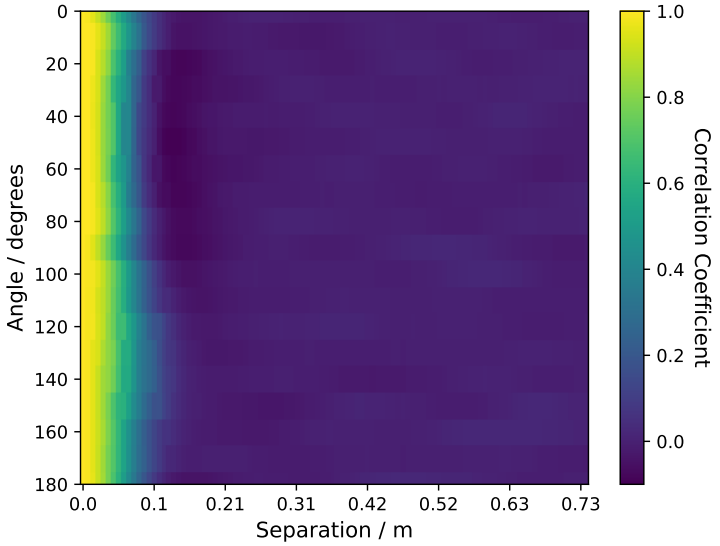

Figure 6.8: The measured correlation between two 20 cm apertures as a function of angle and separation for the INT pupil-plane images with an exposure of 0.01 s.

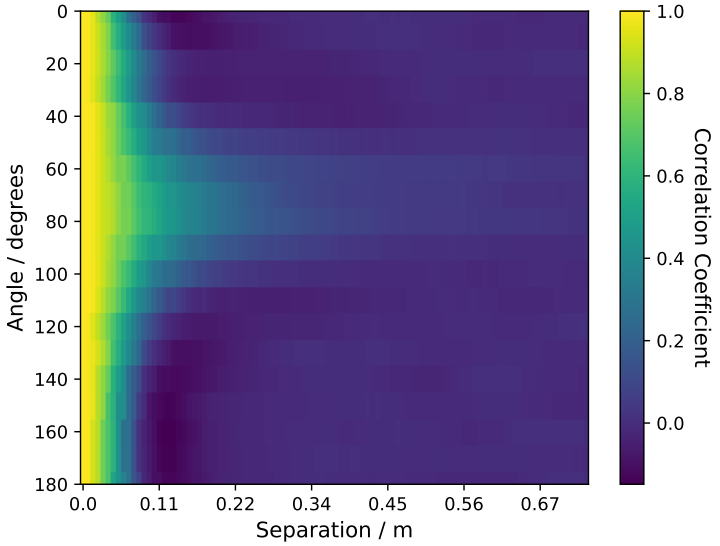

Figure 6.9: The measured correlation between two 20 cm apertures as a function of angle and separation for the INT pupil-plane images with an exposure of 0.1 s.

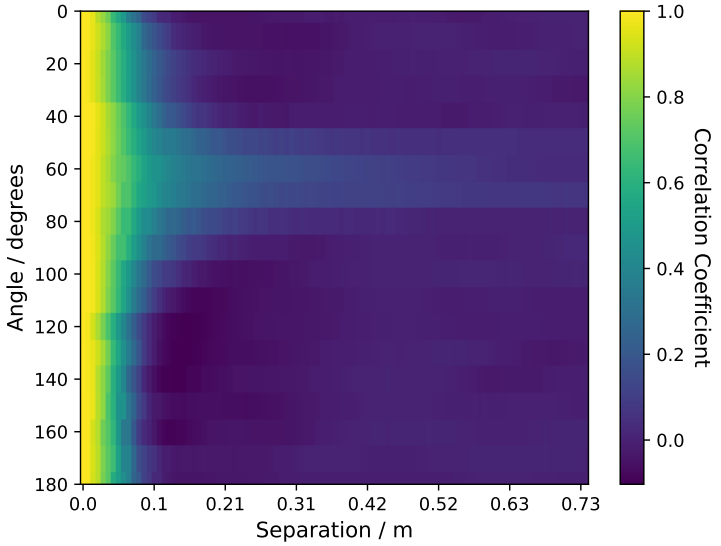

Figure 6.10: The measured correlation between two 20 cm apertures as a function of angle and separation for the INT pupil-plane images with an exposure of 1 s.

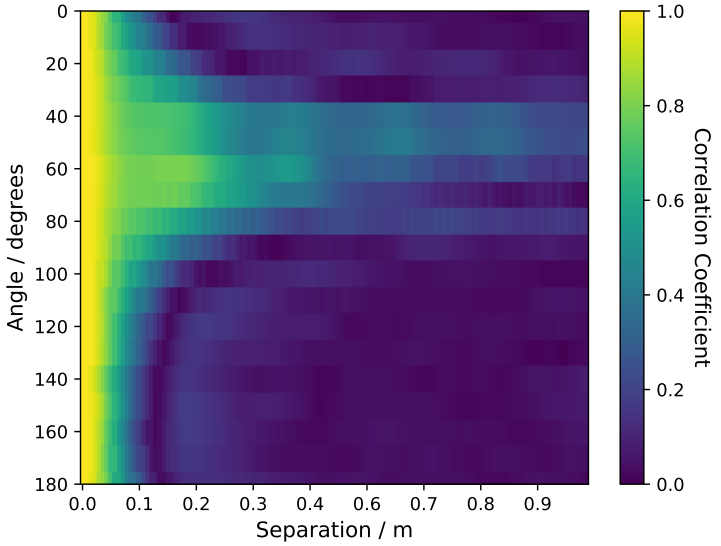

Figure 6.11: The measured correlation between two 20 cm apertures as a function of angle and separation for a numerical simulation using the SCIDAR profile given in table 6.3 and a 1 s exposure time.

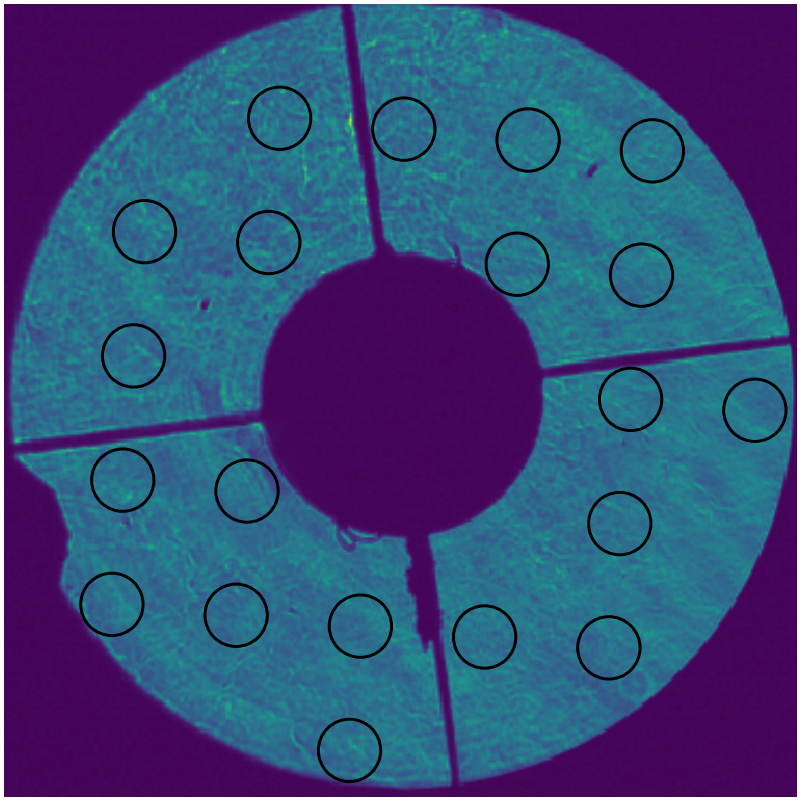

Figure 6.12: Example of using the INT pupil plane images to estimate the SNR for an array, where each black circle represents a telescope pupil in the array. The intensity for each telescope is measured by summing the flux within each circle.

Multiple 20 cm pupils were cut from the pupil-plane data to create an array, each separated by 40 cm. An example is shown in Fig. 6.12 where the telescope pupils used in the array are the black circles. The intensity for each telescope is measured by summing the flux within each circle. The array was rotated and shifted such that the maximum number of pupils can fit within the INT pupil image whilst avoiding the secondary obscuration and any irregularities in the field. The presence of the secondary mirror obscuration limited the number of pupils that could be placed within the array and meant that the average distance between the pupils was slightly larger than 40 cm.

The overall photometric SNR for the whole array found by averaging the intensity over all the telescopes was then plotted against the summed area of the telescopes in the array. In addition, a single telescope of the same summed area of the array was

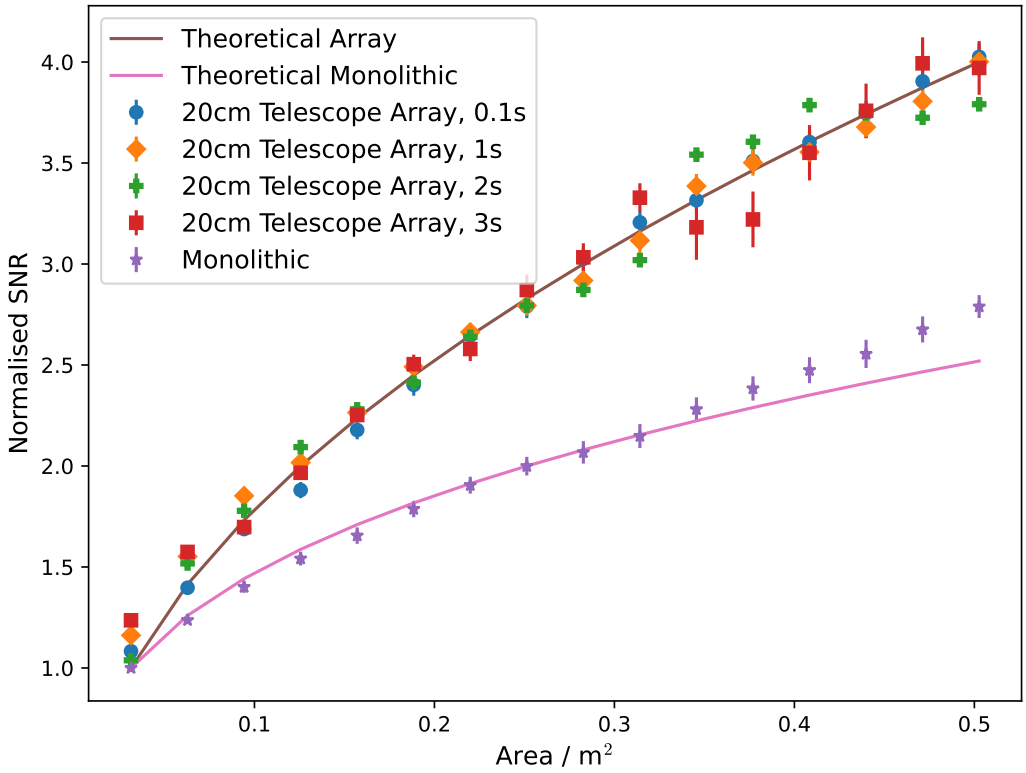

Figure 6.13: The average normalised SNR for a range of exposure times over all the data packets as a function of the total area for an array of telescopes. The average normalised SNR for a monolithic telescope is also plotted as a function of its area. The theoretical SNR for the telescope array and monolithic telescope described by equations 6.5 and 6.3 respectively are also plotted. The SNR for each exposure time was normalised using the average SNR value for a single 20 cm aperture.

cut from the pupil-plane image and the SNR recorded to allow a direct comparison.

Data-packets comprising 200 pupil-plane images were recorded with the INT in May 2022 for a range of exposure times. Thirteen 0.1 s packets, five 1 s, three 2 s and two 3 s packets were collected between 22:50 and 00:00 on the night of 2022 May 15. Fewer long exposure data packets could be collected due to time constraints.

Fig. 6.13 shows the average normalised SNR as a function of the total area of the telescope array, as well as the results for a single telescope of the same area, for a range of exposure times. The SNR for each exposure time was normalised using the average SNR value for a single 20 cm aperture such that the shape of

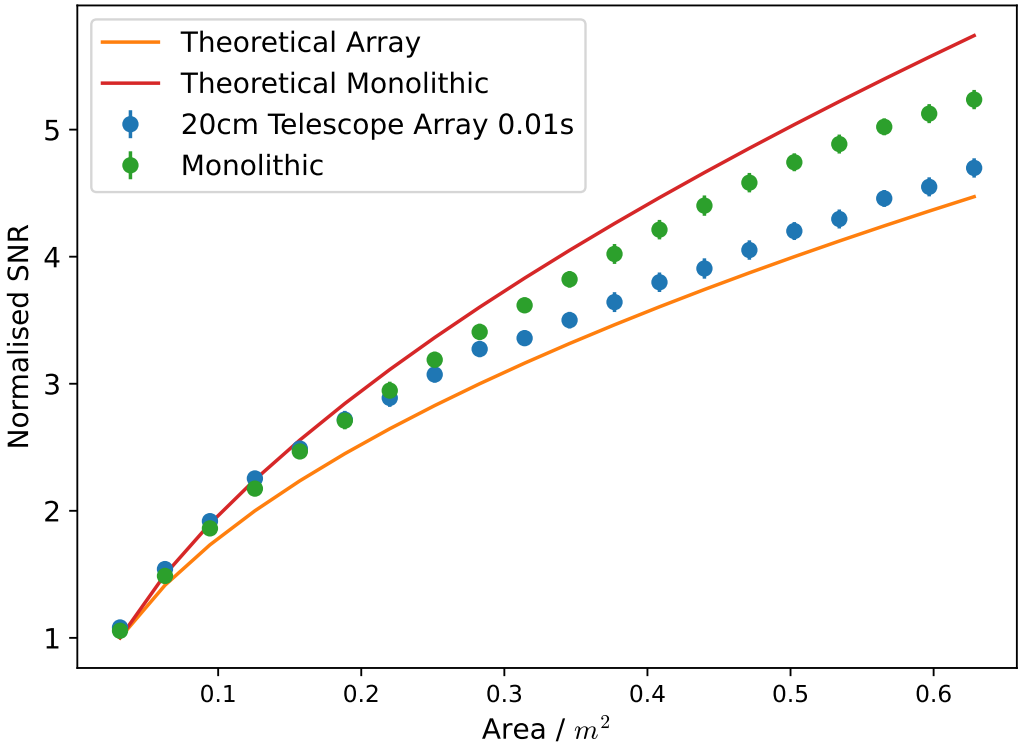

Figure 6.14: The average SNR for an array of 20 cm telescopes in an array as a function of the area of the telescope array and the SNR of a single monolithic pupil as a function of telescope area for a 0.01 s exposure time. The SNR was normalised using the average SNR value for a single 20 cm aperture.

the trends could be easily compared between the different exposure times. The theoretical mean SNR for the telescope array and monolithic telescope described by equations 6.5 and 6.3 respectively are also plotted. For all the exposure times, the SNR measured for the array of telescopes exceeds the SNR measured for the monolithic telescope of equivalent area and all scale as expected from Eq. 6.5. This implies there is negligible correlation of scintillation noise between the pupils.

If however one considers the short exposure regime, for a bright star, the SNR of the telescope array is worse than for a single telescope of the same area, as shown in Fig. 6.14. This is to be expected due to the aperture size dependence on the scintillation index for short exposure times given in Eq. 2.19 as discussed in section 6.2.1. Therefore, the improvement in the SNR for using a telescope array over a single telescope of equal area is only beneficial for long exposure times

where $t \gg t_{\text{cross}}$. Fortunately, for most applications such as exoplanet follow up observations, typical exposure times (> 1 s) fall within this regime.

6.4.3 Sparse Telescope Array Exoplanet Transit Simulation

In this section, a simulated exoplanet transit light curve is presented, demonstrating the SNR improvement that can be achieved for thirty 20 cm telescopes in an array compared to a single 1 m telescope.

Based on equations 2.20 and 6.5, an array of thirty 20 cm telescopes (which has a total glass area of 1 m) should have an SNR equivalent to a single telescope of aperture diameter 2.54 m.

An exoplanet transit light curve of WASP-8b, a hot Jupiter exoplanet that orbits a star similar to the sun with magnitude $V = 9.9$ (Borsato et al., 2021), was simulated. A single layer turbulence profile was used with a wind speed of 15 ms^{-1}, an $r_0 = 0.15$ m and using an exposure time of 10 s. It was assumed that the photometry was limited by scintillation noise and that the scintillation noise between the telescopes was uncorrelated such that the SNR $\propto \sqrt{N}$ where N is the number of telescopes in the array. This relationship was demonstrated by the results measured on-sky in section 6.4.2.3.

Fig. 6.15 shows the results of a Monte Carlo simulation assuming random error due to scintillation alone, for a transit of WASP-8b for an array of thirty 20 cm telescopes and for a single 1 m telescope. The standard error for the wings of the transit is plotted in the bottom right-hand corner for the array, a 1 m telescope and for a 2.54 m telescope. Based on these error bars, an array of thirty 20 cm telescopes can achieve an NSR 50% smaller than a 1 m telescope and achieves an NSR equivalent to a single telescope with a diameter of 2.54 m.

Since the uncertainty of the fitted astrophysical parameters of the exoplanet transit scales linearly with the scintillation noise, with a gradient in the range of $0.68 - 0.80$ (Föhring et al., 2019), using a sparse array of thirty 20 cm telescopes will result in a

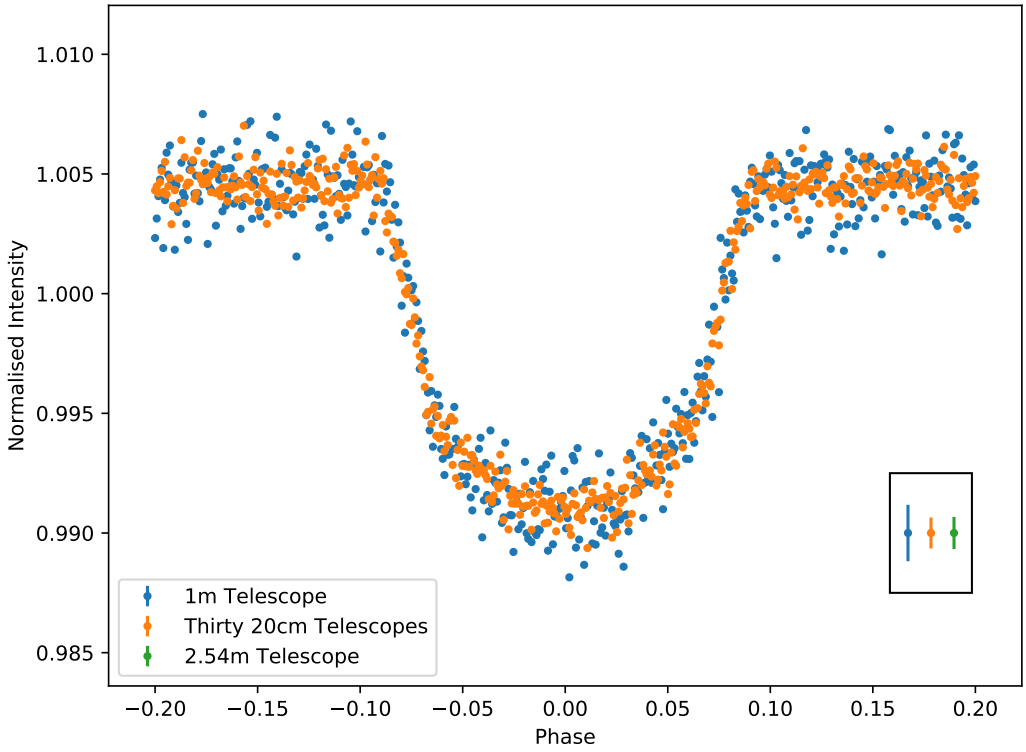

Figure 6.15: Simulated exoplanet transit light curve of WASP-8b for thirty 20 cm telescopes in an array and for a single 1 m telescope. The standard error for the wings of the transit is plotted in the bottom right-hand corner for the array and for a 1 m telescope. In addition, the standard error for a 2.54 m telescope has been added for comparison.

reduction in the uncertainty of the exoplanet transit parameters by approximately 40% when compared with a single telescope of the same equivalent area.

From Fig. 6.1, the cost of the telescope array is approximately £150k, assuming the individual 20 cm OTAs would have a typical cost of £2k and £3k per camera. The cost of a 2.54 m telescope would be substantially higher at approximately ∼£2million. Hence, for bright stars, exoplanet observations with SNRs equivalent to a 2.54 m telescope could be achieved for approximately a tenth of the price by building an array of thirty 20 cm telescopes instead.

In addition, the probability of finding a suitable comparison star within the FOV is much higher for the array of small telescopes. If telescopes with a focal ratio of 10, using the same detector with a pixel width of $3.8\mu m$, are considered, then the

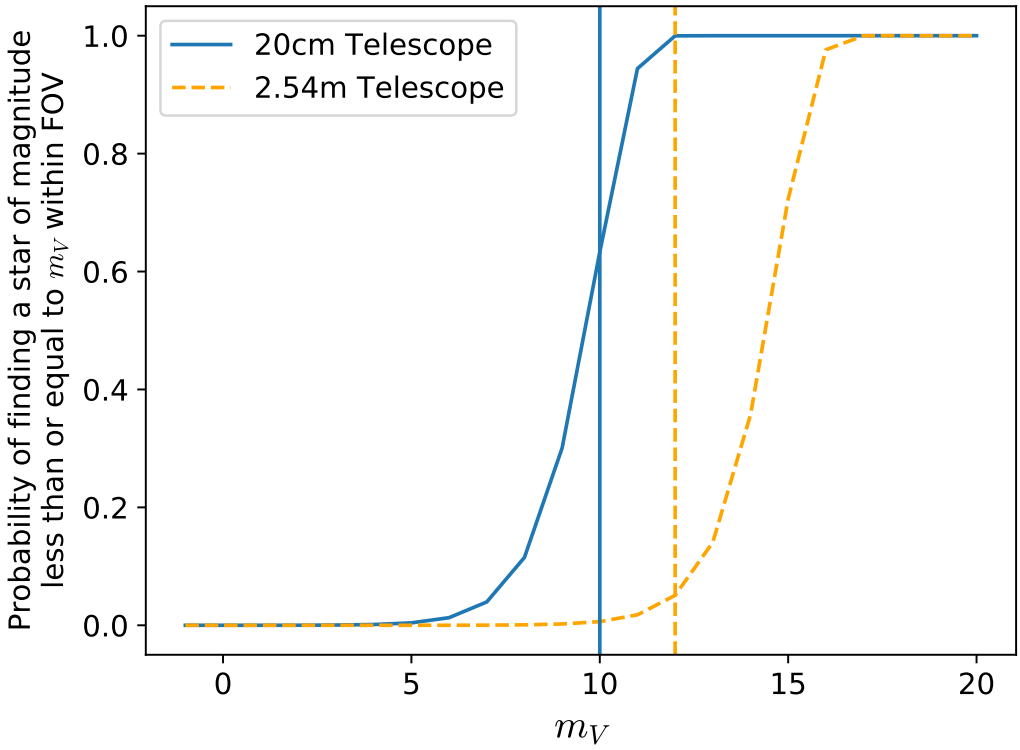

Figure 6.16: The probability of finding a star of $V \leq m_V$ in the FOV of a 20 cm and 2.54 m telescope. The vertical lines represent the magnitude at which the photometric noise is dominated by scintillation noise for each telescope.

area of the FOV for a single 20 cm and 2.54 m telescope will be 0.19 degrees^2 and 0.001 degrees^2 respectively.

Fig. 6.16 shows the probability of finding a star of a given V-band magnitude within the FOV of the 20 cm and 2.54 m telescopes discussed above. The vertical blue and orange lines on Fig. 6.16 indicate the magnitude below which the photometric noise is dominated by scintillation noise for each telescope (Osborn et al., 2015). The 20 cm telescope has a FOV 190 times larger than the 2.54 m telescope and therefore has a much higher likelihood of finding a bright comparison star within the FOV.

The shorter focal length also means that the requirements for the pointing and tracking is reduced, significantly reducing the cost of the array. If the images need to be kept on the same pixels to reduce systematic errors, then good tracking will

be needed. However, the use of defocusing or diffusers (Stefansson et al., 2017) with bright stars would reduce this requirement. In addition, if instrumental systematic errors are independent for the telescopes in the array then the errors will average.

6.5 Discussion and Conclusions

For bright stars for which photometric noise is limited by scintillation noise, arrays of small telescopes have several potential benefits. For long exposure times, an array of N telescopes of diameter $D_{\rm sub}$ can achieve an SNR equivalent to a single telescope of diameter equal to $N^{3/4}D_{\rm sub}$. However, this is only achieved if the scintillation noise is uncorrelated between the telescopes in the array. The cost of the sparse array will be much smaller than for the equivalent monolithic telescope. Furthermore, the small telescopes of the array have a large FOV such that bright comparison stars can be acquired within the same image frame.

The impact of parameters including wind direction, aperture size and the exposure time on the correlation of scintillation noise between neighbouring telescopes has been investigated. It was found in simulation that the scintillation correlation between two telescopes parallel to the high altitude turbulence wind direction was high, even over large physical separations. For on-sky measurements, the correlation between the telescopes reduced more quickly. This is most likely because the simulation has only a few discrete turbulent layers and assumes frozen flow. In reality, the turbulence profile is more continuous and will evolve such that Taylor's frozen flow is not an exact description. Hence, in reality, the scintillation correlation reduces to negligible levels at smaller telescope separations than expected from simulation.

However, in both cases, the measured scintillation correlation fell to near negligible values for a centre-to-centre separation of $\sim 2D$ between telescopes. It has been shown using pupil plane imaging at the INT that the overall SNR for an array of telescopes separated by $\sim 2D$ is $\propto \sqrt{N}$. This implies that the scintillation noise

is not correlated between the neighbouring telescopes. Hence, it is recommended that in practice, a telescope separation of at least $2D$ should be used for a sparse telescope array. Furthermore, for a majority of telescope sites, there will be a dominant high altitude prevailing wind direction. For example, at La Palma, the high altitude turbulence results from the jet stream which has a prevailing wind direction of ENE. Hence, telescope arrays can be designed with the specific site in mind.

One of the most significant benefits for using a telescope array over a larger monolithic telescope is that the same SNR can be reached using a fraction of the glass area and thus also at a fraction of the cost. For example, using thirty 20 cm telescopes can achieve the equivalent SNR as the INT, a 2.54 m telescope. In addition, small telescopes have a much larger FOV, therefore increasing the probability of finding a suitable bright comparison star. Exoplanet transit observations are significantly limited by systematic noise, (Pont et al., 2006) and therefore having a bright comparison star in the field is vital for high-precision photometry.

The increase in SNR for a telescope array compared to a single telescope of the same area is only achieved for long exposure times. For short exposure times, on the order of a few milliseconds, there is no benefit to using a telescope array over a single large telescope. In addition, an increase in SNR is only achieved for bright stars where the photometric noise is dominated by scintillation. In this regime, the SNR of a single telescope scales with the telescope aperture as $D^{2/3}$ whilst the SNR for a sparse telescope array scales with D. For a fainter star where the observation is shot noise limited, the SNR scales linearly with the aperture diameter. Hence, an array of telescopes would perform as well as a single telescope of identical area. Therefore, there is no SNR benefit to using an array over a single telescope for faint, shot noise limited stars. However, the advantages of the reduced cost and increased FOV remain.

Chapter 7

Conclusions

Whilst chapters 4, 5 and 6 each present an independent project, the underlying theme for all the research presented in this thesis is the reduction of noise in ground-based, time-resolved photometry due to atmospheric effects.

In Chapters 3 and 4 the simulation and on-sky results of a scintillation correction technique that uses a tomographic algorithm are presented. Chapter 5 presents a new data reduction technique that used the optimal temporal binning of comparison star light curves to reduce random noise in differential photometry. Finally, Chapter 6 investigates the use of sparse optical telescope arrays to achieve improved SNRs for the observation of bright stars, and the impact that the correlation of scintillation noise between neighbouring apertures has on such arrays.

In this chapter, the key results are summarised and suggestions for future research avenues for each project are presented.

7.1 A scintillation correction technique using tomographic wavefront-sensing

High-precision ground-based photometry can be severely limited by atmospheric scintillation noise. Reducing scintillation noise enables more accurate multi-spectral measurements to be taken as higher SNR values within each waveband can be

achieved. In addition, reducing scintillation noise allows shallower exoplanet primary transits to be observed for bright stars from the ground and possibly even secondary transits.

In this thesis the first ever on-sky demonstration of a scintillation correction technique that uses tomographic wavefront sensing has been presented.

The results from a Monte Carlo simulation are presented that investigate the effect of several parameters, including the WFS exposure time, the number of stars used in the tomographic reconstruction and their angular separation and magnitude, on the expected scintillation correction that can be achieved. Based on these investigations, a suitable target asterism was found for the on-sky experiment on the INT in La Palma, Spain.

Simulations showed that a significant sky coverage using NGS cannot be achieved for an 8 m class telescope, and therefore LGSs are necessary. Fortunately, many of the current and future largest telescopes will be equipped with tomographic AO systems and LGS facilities, such as MORFEO on the ELT. A simulation of the 4 LGS on the VLT found that the scintillation RMS noise could be reduced on average by a factor of four.

Results from a simple on-sky experiment on the INT in La Palma were presented in Chapter 4. A single SHWFS was used to perform the photometry and the tomographic wavefront sensing for three stars in the Orion Trapezium Cluster. The results from this experiment have successfully demonstrated the concept, with a peak reduction in the scintillation index of 3.41 measured.

The on-sky experiment highlighted a number of ways in which the correction performance can be improved for a facility system, including the importance of having up-to-date turbulence profiles for the tomographic reconstruction matrix and Fresnel propagation. It is expected that the scintillation correction performance would be greatly improved if simultaneous turbulence profiling is available. Despite these limitations, strong correlation between the uncorrected and tomographically recon-

structed intensities were measured, with a maximum correlation of 0.86 achieved.

The next step of this research is to test the tomographic scintillation correction technique on a large aperture telescope using LGSs, such as the VLT, where much higher scintillation correction can be expected. Unfortunately, the current VLT set up is not optimal as the NGS used as a target star is observed at a different frame rate to the LGSs without detailed timestamps synchronization. Therefore, in its current set up, the tomographic scintillation correction technique cannot be easily tested. A dedicated experiment would therefore need to be performed.

Additionally, another area of research to investigate is the use of machine learning with this technique. whilst the technique can be performed entirely in post-processing, a real time implementation of this technique is severely limited by the computational time taken to perform the Fresnel propagation. An interesting avenue of research could be training a machine learning algorithm with inputs of WFS data and the resulting intensity fluctuations as outputs. This could greatly improve computational speeds, making a real time application more possible.

7.2 Optimised temporal binning of comparison star measurements for differential photometry

Differential photometry is an important tool used to correct systematic trends due to atmospheric transparency variations in ground-based photometry. However, the NSR of the calibrated light curve could then be limited by the random intensity fluctuations of the comparison star signal, since the shot noise and scintillation noise of the raw light curves add in quadrature.

In this thesis it has been proposed that since the timescale of the systematic variations is much longer than the cadence, in most cases the comparison star signal can be temporally binned before performing the differential photometry, therefore reducing the NSR of the calibrated light curve.

This technique has been demonstrated for several targets of interest, including both exoplanet transits and a variable star. In all cases, the precision in the measurements has been increased by temporally binning the comparison star light curves. This allows the use of much fainter comparison stars. In these observations, it was found that comparison stars of up to four magnitudes fainter than the target star can be used.

This technique however requires the data to be taken in good photometric conditions. Any periods in the data with high frequency trends cannot be improved.

The power in the low frequency transparency variations is not expected to vary with star magnitude. Therefore, it is expected that with temporal binning, much fainter stars can still be used as suitable comparison stars. However, the data was limited and does not have any stars fainter than a magnitude of $V = 11.3$. Therefore, more data with fainter stars is required. Further research to see how the power spectrum of the stellar light curves vary with wavelength should also be performed. All the data presented was observed in the V band. However, the atmospheric transparency variations depend on wavelength. Therefore, this technique may be more or less suitable in other wavebands.

7.3 Optical sparse telescope arrays and scintillation noise

For stars with light curves dominated by scintillation noise, it has been shown that arrays of small telescopes are able to achieve higher SNRs than a single telescope of equal area. For long exposure times, an array of N telescopes of diameter D_{sub} can achieve an SNR equivalent to a single telescope of diameter equal to $N^{3/4}D_{\mathrm{sub}}$ for a bright star. In addition, the cost to build an array of small telescopes is significantly smaller than the cost of building a single large aperture. However, this is only achieved if the scintillation noise is uncorrelated between the telescopes in the array.

Simulations and on-sky pupil-plane data taken on the INT were used to investigate the impact of several parameters, including wind direction, aperture size and the exposure time, on the correlation of scintillation noise between neighbouring telescopes. It was found in simulation that for long exposures, strong correlation of scintillation noise was measured for telescopes separated parallel to the wind direction of the dominant high altitude turbulent layer.

Results from simulation and on-sky suggest that any correlation of scintillation noise between neighbouring telescopes averaged over the array becomes negligible when the telescopes are separated by at least $2D$ from centre-to-centre, where D is the telescope aperture. Hence, future sparse telescope arrays should be designed with such separations.

Arrays of small telescopes could be used to perform follow-up observations of exoplanet transits around bright stars. In addition, an array of telescopes could also be used to improve the SNR, and hence the identification, of satellite light curves (Kerr et al., 2021). In this application, not only is the random noise averaged, the systematic noise due to pixel-to-pixel variation along the satellite trail will also average, thus significantly improving the SNR.

The next step of this research is to measure the correlation of scintillation noise between fully separated neighbouring telescope apertures on-sky. Ideally, turbulence profiles would be acquired in order to compare the measured scintillation noise correlation with that expected from simulation results. In addition, with turbulence profile measurements, the telescopes could be aligned parallel to the wind direction of the dominant high altitude turbulent layer. To avoid the addition of instrumental systematic noise, the observations should be defocused to reduce the effects of pixel-to-pixel variations.

Bibliography

R. Alonso. *Characterization of Exoplanets: Secondary Eclipses*, pages 1–26. Springer International Publishing, Cham, 2018. ISBN 978-3-319-30648-3. doi: 10.1007/978-3-319-30648-3_40-1. URL https://doi.org/10.1007/978-3-319-30648-3_40-1.

R. Avila, J. L. Avilés, R. W. Wilson, M. Chun, T. Butterley, and E. Carrasco. LOLAS: an optical turbulence profiler in the atmospheric boundary layer with extreme altitude resolution. *Monthly Notices of the Royal Astronomical Society*, 387(4):1511–1516, jul 2008. doi: 10.1111/j.1365-2966.2008.13386.x.

H. W. Babcock. The possibility of compensating astronomical seeing. *Publications of the Astronomical Society of the Pacific*, 65(386):229–236, 1953. ISSN 00046280, 15383873. URL http://www.jstor.org/stable/40672682.

J. M. Beckers. Increasing the Size of the Isoplanatic Patch with Multiconjugate Adaptive Optics. In *European Southern Observatory Conference and Workshop Proceedings*, volume 30 of *European Southern Observatory Conference and Workshop Proceedings*, page 693, Jan. 1988.

C. Benn and S. Ellison. Brightness of the night sky over la palma. *New Astronomy Reviews*, 42(6-8):503–507, nov 1998. doi: 10.1016/s1387-6473(98)00062-1. URL https://doi.org/10.1016%2Fs1387-6473%2898%2900062-1.

L. Borsato, G. Piotto, D. Gandolfi, V. Nascimbeni, G. Lacedelli, F. Marzari, N. Billot, P. F. L. Maxted, S. Sousa, A. C. Cameron, A. Bonfanti, T. G. Wilson, L. M. Serrano, Z. Garai, Y. Alibert, R. Alonso, J. Asquier, T. Bárczy, T. Bandy, D. Barrado, S. C. C. Barros, W. Baumjohann, M. Beck, T. Beck, W. Benz, X. Bonfils, A. Brandeker, C. Broeg, J. Cabrera, S. Charnoz, S. Csizmadia, M. B. Davies, M. Deleuil, L. Delrez, O. Demangeon, B. O. Demory, A. L. des Etangs, D. Ehrenreich, A. Erikson, G. A. Escudé, A. Fortier, L. Fossati, M. Fridlund, M. Gillon, M. Guedel, J. Hasiba, K. Heng, S. Hoyer, K. G. Isaak, L. Kiss, E. Kopp, J. Laskar, M. Lendl, C. Lovis, D. Magrin, M. Munari, G. Olofsson, R. Ottensamer, I. Pagano, E. Pallé, G. Peter, D. Pollacco, D. Queloz, R. Ragazzoni, N. Rando, H. Rauer, I. Ribas, D. Ségransan, N. C. Santos, G. Scandariato, A. Simon, A. M. S. Smith, M. Steller, G. Szabó, N. Thomas, S. Udry, V. Van Grootel, and N. Walton. Exploiting timing capabilities of the CHEOPS mission with warm-Jupiter planets. *Monthly Notices of the Royal Astronomical Society*, 506(3):3810–3830, Sept. 2021. doi: 10.1093/mnras/stab1782.

D. Boyd. Differential photometry using multiple comparison stars. *Society for Astronomical Sciences Annual Symposium*, 05 2007.

E. M. Bryant, D. Bayliss, J. McCormac, P. J. Wheatley, J. S. Acton, D. R. Anderson, D. J. Armstrong, F. Bouchy, C. Belardi, M. R. Burleigh, R. H. Tilbrook, S. L. Casewell, B. F. Cooke, S. Gill, M. R. Goad, J. S. Jenkins, M. Lendl, D. Pollacco, D. Queloz, L. Raynard, A. M. S. Smith, J. I. Vines, R. G. West, and S. Udry. Simultaneous TESS and NGTS transit observations of WASP-166b. *Monthly Notices of the Royal Astronomical Society*, 494 (4):5872–5881, 04 2020. ISSN 0035-8711. doi: 10.1093/mnras/staa1075. URL `https://doi.org/10.1093/mnras/staa1075`.

C. Buton, Y. Copin, G. Aldering, P. Antilogus, C. Aragon, S. Bailey, C. Baltay, S. Bongard, A. Canto, F. Cellier-Holzem, M. Childress, N. Chotard, H. K. Fakhouri, E. Gangler, J. Guy, E. Y. Hsiao, M. Kerschhaggl, M. Kowalski, S. Loken,

P. Nugent, K. Paech, R. Pain, E. Pécontal, R. Pereira, S. Perlmutter, D. Rabinowitz, M. Rigault, K. Runge, R. Scalzo, G. Smadja, C. Tao, R. C. Thomas, B. A. Weaver, C. Wu, and Nearby SuperNova Factory. Atmospheric extinction properties above Mauna Kea from the Nearby SuperNova Factory spectrophotometric data set. *Astronomy and Astrophysics*, 549:A8, Jan. 2013. doi: 10.1051/0004-6361/201219834.

V. Capalbo, M. D. Petris, F. D. Luca, W. Cui, G. Yepes, A. Knebe, and E. Rasia. The three hundred project: quest of clusters of galaxies morphology and dynamical state through zernike polynomials. *Monthly Notices of the Royal Astronomical Society*, 503(4):6155–6169, dec 2020. doi: 10.1093/mnras/staa3900. URL `https://doi.org/10.1093%2Fmnras%2Fstaa3900`.

B. Chazelas, D. Pollacco, D. Queloz, H. Rauer, P. J. Wheatley, R. West, J. Da Silva Bento, M. Burleigh, J. McCormac, P. Eigmüller, A. Erikson, L. Genolet, M. Goad, A. Jordán, M. Neveu, and S. Walker. NGTS: a robotic transit survey to detect Neptune and super-Earth mass planets. In L. M. Stepp, R. Gilmozzi, and H. J. Hall, editors, *Ground-based and Airborne Telescopes IV*, volume 8444 of *Society of Photo-Optical Instrumentation Engineers (SPIE) Conference Series*, page 84440E, Sept. 2012. doi: 10.1117/12.925755.

P. e. a. Ciliegi. MAORY: A Multi-conjugate Adaptive Optics RelaY for ELT. *The Messenger*, 182:13–16, Mar. 2021. doi: 10.18727/0722-6691/5216.

R. M. Clare, M. L. Louarn, and C. Béchet. Optimal noise-weighted reconstruction with elongated shack–hartmann wavefront sensor images for laser tomography adaptive optics. *Appl. Opt.*, 49(31):G27–G36, Nov 2010. doi: 10.1364/AO.49.000G27. URL `http://ao.osa.org/abstract.cfm?URI=ao-49-31-G27`.

K. A. Collins, K. I. Collins, J. Pepper, J. Labadie-Bartz, K. G. Stassun, B. S. Gaudi, D. Bayliss, J. Bento, K. D. COLÓN, D. Feliz, D. James, M. C. Johnson, R. B. Kuhn, M. B. Lund, M. T. Penny, J. E. Rodriguez, R. J. Siverd, D. J. Stevens, X. Yao, G. Zhou, M. Akshay, G. F. Aldi, C. Ashcraft, S. Awiphan, Özgür

Baştürk, D. Baker, T. G. Beatty, P. Benni, P. Berlind, G. B. Berriman, Z. Berta-Thompson, A. Bieryla, V. Bozza, S. C. Novati, M. L. Calkins, J. M. Cann, D. R. Ciardi, I. R. Clark, W. D. Cochran, D. H. Cohen, D. Conti, J. R. Crepp, I. A. Curtis, G. D'Ago, K. A. Diazeguigure, C. D. Dressing, F. Dubois, E. Ellingson, T. G. Ellis, G. A. Esquerdo, P. Evans, A. Friedli, A. Fukui, B. J. Fulton, E. J. Gonzales, J. C. Good, J. Gregorio, T. Gumusayak, D. A. Hancock, C. K. Harada, R. Hart, E. G. Hintz, H. Jang-Condell, E. J. Jeffery, E. L. N. Jensen, E. Jofré, M. D. Joner, A. Kar, D. H. Kasper, B. Keten, J. F. Kielkopf, S. Komonjinda, C. Kotnik, D. W. Latham, J. Leuquire, T. R. Lewis, L. Logie, S. J. Lowther, P. J. Macqueen, T. J. Martin, D. Mawet, K. K. Mcleod, G. Murawski, N. Narita, J. Nordhausen, T. E. Oberst, C. Odden, P. A. Panka, R. Petrucci, P. Plavchan, S. N. Quinn, S. Rau, P. A. Reed, H. Relles, J. P. Renaud, G. Scarpetta, R. L. Sorber, A. D. Spencer, M. Spencer, D. C. Stephens, C. Stockdale, T.-G. Tan, M. Trueblood, P. Trueblood, S. Vanaverbeke, S. Villanueva, E. M. Warner, M. L. West, S. Yalçınkaya, R. Yeigh, and R. Zambelli. The kelt follow-up network and transit false-positive catalog: Pre-vetted false positives for tess. *The Astronomical Journal*, 156(5):234, nov 2018. doi: 10.3847/1538-3881/aae582. URL `https://dx.doi.org/10.3847/1538-3881/aae582`.

J. C. Dainty, B. M. Levine, B. J. Brames, and K. A. O'Donnell. Measurements of the wavelength dependence and other properties of stellar scintillation at mauna kea, hawaii. *Appl. Opt.*, 21(7):1196–1200, Apr 1982. doi: 10.1364/AO.21.001196. URL `http://ao.osa.org/abstract.cfm?URI=ao-21-7-1196`.

L. Doyle, H. M. Cegla, E. Bryant, D. Bayliss, M. Lafarga, D. R. Anderson, R. Allart, V. Bourrier, M. Brogi, N. Buchschacher, V. Kunovac, M. Lendl, C. Lovis, M. Moyano, N. Roguet-Kern, J. V. Seidel, D. Sosnowska, P. J. Wheatley, J. S. Acton, M. R. Burleigh, S. L. Casewell, S. Gill, M. R. Goad, B. A. Henderson, J. S. Jenkins, R. H. Tilbrook, and R. G. West. The Hot Neptune WASP-166 b with ESPRESSO - I. Refining the planetary architecture and stellar variability.

Monthly Notices of the Royal Astronomical Society, 516(1):298–315, Oct. 2022. doi: 10.1093/mnras/stac2178.

D. Dravins, L. Lindegren, E. Mezey, and A. T. Young. Atmospheric intensity scintillation of stars, i. statistical distributions and temporal properties. *Publications of the Astronomical Society of the Pacific*, 109:173, feb 1997a. doi: 10.1086/133872. URL `https://doi.org/10.1086%2F133872`.

D. Dravins, L. Lindegren, E. Mezey, and A. T. Young. Atmospheric intensity scintillation of stars. II. dependence on optical wavelength. *Publications of the Astronomical Society of the Pacific*, 109:725, jun 1997b. doi: 10.1086/133937. URL `https://doi.org/10.1086%2F133937`.

D. Dravins, L. Lindegren, E. Mezey, and A. Young. Atmospheric intensity scintillation of stars. iii. effects for different telescope apertures. *Publications of the Astronomical Society of the Pacific*, 110:610–633, 04 1998. doi: 10.1086/316232.

D. Dussault and P. Hoess. Noise performance comparison of ICCD with CCD and EMCCD cameras. In C. B. Johnson, E. L. Dereniak, and R. E. Sampson, editors, *Infrared Systems and Photoelectronic Technology*, volume 5563, pages 195 – 204. International Society for Optics and Photonics, SPIE, 2004. doi: 10.1117/12.561839. URL `https://doi.org/10.1117/12.561839`.

B. L. Ellerbroek and G. Cochran. Wave optics propagation code for multiconjugate adaptive optics. In R. K. Tyson, D. Bonaccini, and M. C. Roggemann, editors, *Proc. SPIE*, volume 4494 of *Society of Photo-Optical Instrumentation Engineers (SPIE) Conference Series*, pages 104–120, Feb. 2002. doi: 10.1117/12.454784.

O. J. D. Farley, J. Osborn, T. Morris, M. Sarazin, T. Butterley, M. J. Townson, P. Jia, and R. W. Wilson. Representative optical turbulence profiles for ESO Paranal by hierarchical clustering. *Monthly Notices of the Royal Astronomical Society*, 481(3):4030–4037, 09 2018. ISSN 0035-8711. doi: 10.1093/mnras/sty2536. URL `https://doi.org/10.1093/mnras/sty2536`.

O. J. D. Farley, J. Osborn, T. Morris, T. Fusco, B. Neichel, C. Correia, and R. W. Wilson. Limitations imposed by optical turbulence profile structure and evolution on tomographic reconstruction for the ELT. *Monthly Notices of the Royal Astronomical Society*, 494(2):2773–2784, 04 2020. ISSN 0035-8711. doi: 10.1093/mnras/staa795. URL https://doi.org/10.1093/mnras/staa795.

D. Fohring et al. Ultracam z-band detection of the secondary eclipse of wasp-12b. *Volume 435, Issue 3, 1 November 2013*, page 12268–2273, 2013.

D. Foreman-Mackey, D. W. Hogg, D. Lang, and J. Goodman. emcee: The MCMC hammer. *Publications of the Astronomical Society of the Pacific*, 125(925): 306–312, mar 2013. doi: 10.1086/670067. URL https://doi.org/10.1086%2F670067.

R. Foy and A. Labeyrie. Feasibility of adaptive telescope with laser probe. *Astronomy and Astrophysics*, 152(2):L29–L31, Nov. 1985.

D. L. Fried. Optical resolution through a randomly inhomogeneous medium for very long and very short exposures. *J. Opt. Soc. Am.*, 56(10):1372–1379, Oct 1966. doi: 10.1364/JOSA.56.001372. URL https://opg.optica.org/abstract.cfm?URI=josa-56-10-1372.

T. Fusco, J.-M. Conan, V. Michau, L. M. Mugnier, and G. Rousset. Phase estimation for large field of view: application to multiconjugate adaptive optics. In M. C. Roggemann and L. R. Bissonnette, editors, *Propagation and Imaging through the Atmosphere III*, volume 3763, pages 125 – 133. International Society for Optics and Photonics, SPIE, 1999. doi: 10.1117/12.363606. URL https://doi.org/10.1117/12.363606.

T. Fusco, J.-M. Conan, G. Rousset, L. M. Mugnier, and V. Michau. Optimal wave-front reconstruction strategies for multiconjugate adaptive optics. *J. Opt. Soc. Am. A*, 18(10):2527–2538, Oct 2001. doi: 10.1364/JOSAA.18.002527. URL http://josaa.osa.org/abstract.cfm?URI=josaa-18-10-2527.

T. Fusco, S. Meimon, Y. Clenet, M. Cohen, H. Schnetler, J. Paufique, V. Michau, J.-P. Amans, D. Gratadour, C. Petit, C. Robert, P. Jagourel, E. Gendron, G. Rousset, J.-M. Conan, and N. Hubin. ATLAS: the E-ELT laser tomographic adaptive optics system. In B. L. Ellerbroek, M. Hart, N. Hubin, and P. L. Wizinowich, editors, *Adaptive Optics Systems II*, volume 7736, pages 151 – 162. International Society for Optics and Photonics, SPIE, 2010. doi: 10.1117/12.857468. URL https://doi.org/10.1117/12.857468.

D. Föhring, R. Wilson, J. Osborn, and V. Dhillon. Scintillation noise in exoplanet transit photometry. *Journal of Physics: Conference Series*, 595:012010, apr 2015. doi: 10.1088/1742-6596/595/1/012010. URL https://doi.org/10.1088/1742-6596/595/1/012010.

D. Föhring, R. W. Wilson, J. Osborn, and V. S. Dhillon. Atmospheric scintillation noise in ground-based exoplanet photometry. *Monthly Notices of the Royal Astronomical Society*, 489(4):5098–5108, sep 2019. doi: 10.1093/mnras/stz2444. URL https://doi.org/10.1093%2Fmnras%2Fstz2444.

E. Gendron, F. Assémat, F. Hammer, P. Jagourel, F. Chemla, P. Laporte, M. Puech, M. Marteaud, F. Zamkotsian, A. Liotard, J.-M. Conan, T. Fusco, and N. Hubin. Falcon: multi-object ao. *Comptes Rendus Physique*, 6(10): 1110 – 1117, 2005. ISSN 1631-0705. doi: https://doi.org/10.1016/j.crhy.2005.10.012. URL http://www.sciencedirect.com/science/article/pii/S1631070505001660. Multi-Conjugate Adaptive Optics for very large telescopes.

E. Giannini et al. MiNDSTEp differential photometry of the gravitationally lensed quasars WFI 2033-4723 and HE 0047-1756: microlensing and a new time delay. *Astron. Astrophys.*, 597:A49, 2017. doi: 10.1051/0004-6361/201527422.

B. P. Gompertz, R. Cutter, D. Steeghs, D. K. Galloway, J. Lyman, K. Ulaczyk, M. J. Dyer, K. Ackley, V. S. Dhillon, P. T. O'Brien, G. Ramsay, S. Poshyachinda, R. Kotak, L. Nuttall, R. P. Breton, E. Pallé, D. Pollacco, E. Thrane, S. Aukkaravittayapun, S. Awiphan, M. J. I. Brown, U. Burhanudin, P. Chote,

A. A. Chrimes, E. Daw, C. Duffy, R. A. J. Eyles-Ferris, T. Heikkilä, P. Irawati, M. R. Kennedy, T. Killestein, A. J. Levan, S. Littlefair, L. Makrygianni, T. Marsh, D. Mata Sánchez, S. Mattila, J. Maund, J. McCormac, D. Mkrtichian, Y. L. Mong, J. Mullaney, B. Müller, A. Obradovic, E. Rol, U. Sawangwit, E. R. Stanway, R. L. C. Starling, P. A. Strøm, S. Tooke, R. West, and K. Wiersema. Searching for electromagnetic counterparts to gravitational-wave merger events with the prototype Gravitational-Wave Optical Transient Observer (GOTO-4). *Monthly Notices of the Royal Astronomical Society*, 497 (1):726–738, 07 2020. ISSN 0035-8711. doi: 10.1093/mnras/staa1845. URL `https://doi.org/10.1093/mnras/staa1845`.

J. R. Graham, B. Macintosh, R. Doyon, D. Gavel, J. Larkin, M. Levine, B. Oppenheimer, D. Palmer, L. Saddlemyer, A. Sivaramakrishnan, J.-P. Veran, and K. Wallace. Ground-based direct detection of exoplanets with the gemini planet imager (gpi), 2007.

L. K. Hardy, T. Butterley, V. S. Dhillon, S. P. Littlefair, and R. W. Wilson. pt5m– a 0.5 m robotic telescope on la palma. *Monthly Notices of the Royal Astronomical Society*, 454(4):4316–4325, Oct 2015. ISSN 1365-2966. doi: 10.1093/mnras/stv2279. URL `http://dx.doi.org/10.1093/mnras/stv2279`.

K. E. Hartley and R. W. Wilson. Optimised temporal binning of com- parison star measurements for differential photometry. *Monthly Notices of the Royal Astronomical Society*, Accepted September 2023. doi: 10.1093/mnras/stad2964. URL `https://doi.org/10.1093/mnras/stad2964`.

K. E. Hartley, O. J. D. Farley, M. J. Townson, J. Osborn, and R. W. Wilson. Correction of photometric scintillation noise via tomographic wavefront sensing: simulation and on-sky demonstration. In L. Schreiber, D. Schmidt, and E. Vernet, editors, *Adaptive Optics Systems VIII*, volume 12185, page 121858J. International Society for Optics and Photonics, SPIE, 2022. doi: 10.1117/12.2628703. URL `https://doi.org/10.1117/12.2628703`.

K. E. Hartley, O. J. D. Farley, M. J. Townson, J. Osborn, and R. W. Wilson. First on-sky demonstration of a scintillation correction technique using tomographic wavefront sensing. *Monthly Notices of the Royal Astronomical Society*, 520(3):4134–4146, 02 2023a. ISSN 0035-8711. doi: 10.1093/mnras/stad420. URL `https://doi.org/10.1093/mnras/stad420`.

K. E. Hartley, O. J. D. Farley, M. J. Townson, J. Osborn, and R. W. Wilson. Optical sparse telescope arrays and scintillation noise. *Monthly Notices of the Royal Astronomical Society*, 526(1):1235–1245, 09 2023b. ISSN 0035-8711. doi: 10.1093/mnras/stad2835. URL `https://doi.org/10.1093/mnras/stad2835`.

S. W. Hasinoff. Photon, poisson noise. *Computer Vision, A Reference Guide*, 4, 2014.

F. Hawthorn, D. Bayliss, T. G. Wilson, A. Bonfanti, V. Adibekyan, Y. Alibert, S. G. Sousa, K. A. Collins, E. M. Bryant, A. Osborn, D. J. Armstrong, L. Abe, J. S. Acton, B. C. Addison, K. Agabi, R. Alonso, D. R. Alves, G. Angladа-Escudé, T. Bárczy, T. Barclay, D. Barrado, S. C. C. Barros, W. Baumjohann, P. Bendjoya, W. Benz, A. Bieryla, X. Bonfils, F. Bouchy, A. Brandeker, C. Broeg, D. J. A. Brown, M. R. Burleigh, M. Buttu, J. Cabrera, D. A. Caldwell, S. L. Casewell, D. Charbonneau, S. Charnoz, R. Cloutier, A. C. Cameron, K. I. Collins, D. M. Conti, N. Crouzet, S. Czismadia, M. B. Davies, M. Deleuil, E. Delgado-Mena, L. Delrez, O. D. S. Demangeon, B.-O. Demory, G. Dransfield, X. Dumusque, J. A. Egger, D. Ehrenreich, P. Eigmüller, A. Erickson, Z. Essack, A. Fortier, L. Fossati, M. Fridlund, M. N. Günther, M. Güdel, D. Gandolfi, H. Gillard, M. Gillon, C. Gnilka, M. R. Goad, R. F. Goeke, T. Guillot, A. Hadjigeorghiou, C. Hellier, B. A. Henderson, K. Heng, M. J. Hooton, K. Horne, S. B. Howell, S. Hoyer, J. M. Irwin, J. S. Jenkins, J. M. Jenkins, E. L. N. Jensen, S. R. Kane, A. Kendall, J. F. Kielkopf, L. L. Kiss, G. Lacedelli, J. Laskar, D. W. Latham, A. L. d. Etangs, A. Leleu, M. Lendl, J. Lillo-Box, C. Lovis, D. Mékarnia, B. Massey, T. Masters, P. F. L. Maxted, V. Nascimbeni, L. D. Nielsen, S. M.

O'Brien, G. Olofsson, H. P. Osborn, I. Pagano, E. Pallé, C. M. Persson, G. Piotto, P. Plavchan, D. Pollacco, D. Queloz, R. Ragazzoni, H. Rauer, I. Ribas, G. Ricker, D. Ségransan, S. Salmon, A. Santerne, N. C. Santos, G. Scandariato, F.-X. Schmider, R. P. Schwarz, S. Seager, A. Shporer, A. E. Simon, A. M. S. Smith, G. Srdoc, M. Steller, O. Suarez, G. M. Szabó, J. Teske, N. Thomas, R. H. Tilbrook, A. H. M. J. Triaud, S. Udry, V. Van Grootel, N. Walton, S. X. Wang, P. J. Wheatley, J. N. Winn, R. A. Wittenmyer, and H. Zhang. TOI-836: A super-Earth and mini-Neptune transiting a nearby K-dwarf. *Monthly Notices of the Royal Astronomical Society*, 520(3):3649–3668, Apr. 2023. doi: 10.1093/mnras/stad306.

F. Hill, G. Fischer, S. Forgach, J. Grier, J. Leibacher, H. Jones, P. Jones, R. Kupke, R. Stebbins, and D. Clay. The global oscillation network group site survey, 2: Results. *Solar Physics*, 152, 08 1994. doi: 10.1007/BF00680443.

E. Hog, C. Fabricius, V. V. Makarov, S. Urban, T. Corbin, G. Wycoff, U. Bastian, P. Schwekendiek, and A. Wicenec. The tycho-2 catalogue of the 2.5 million brightest stars. Technical report, Naval Observatory Washington DC, 2000.

S. B. Howell. Two-dimensional aperture photometry: Signal-to-noise ratio of point-source observations and optimal data-extraction techniques. *Publications of the Astronomical Society of the Pacific*, 101(640):616, jun 1989. doi: 10.1086/132477. URL `https://dx.doi.org/10.1086/132477`.

S. B. Howell. Introduction to differential time-series astronomical photometry using charged-coupled devices. In *Astronomical CCD observing and reduction techniques*, volume 23, page 105, 1992.

S. B. Howell. *Handbook of CCD Astronomy*. Cambridge Observing Handbooks for Research Astronomers. Cambridge University Press, 2 edition, 2006. doi: 10.1017/CBO9780511807909.

S. B. Howell and G. H. Jacoby. Time-resolved photometry using a CCD. *Publications of the Astronomical Society of the Pacific*, 98:802, aug 1986. doi: 10.1086/131828. URL https://doi.org/10.1086/131828.

I. Hughes and T. Hase. *Measurements and Their Uncertainties: A Practical Guide to Modern Error Analysis*. OUP Oxford, 2010. ISBN 9780199566327. URL https://books.google.co.uk/books?id=AbEVDAAAQBAJ.

J. F. Kasting. Habitable zones around low mass stars and the search for extraterrestrial life. *Origins of life and evolution of the biosphere*, 27:291–307, June 1997. doi: 10.1023/A:1006586517202. URL https://doi.org/10.1023/A:1006586517202.

E. Kerr, G. Falco, N. Maric, D. Petit, P. Talon, E. G. Petersen, C. Dorn, S. Eves, N. Sánchez-Ortiz, R. D. Gonzalez, et al. Light curves for geo object characterisation. In *8th European Conference on Space Debris*, pages 9–20, 2021.

G. Knoechel and K. von der Heide. Statistically rigorous reduction of optical lunar occultation measurements. *Astronomy and Astrophysics*, 67(2):209–220, July 1978.

A. N. Kolmogorov. The local structure of turbulence in incompressible viscous fluid for very large reynolds numbers. *Proceedings: Mathematical and Physical Sciences*, 434(1890):9–13, 1991. ISSN 09628444. URL http://www.jstor.org/stable/51980.

M. Koppelman. Uncertainty Analysis in Photometric Observations. *Society for Astronomical Sciences Annual Symposium*, 24:107, May 2005.

V. Kornilov. How achromatic is the stellar scintillation on large telescopes? *Monthly Notices of the Royal Astronomical Society*, 417(2):1105–1113, 10 2011. ISSN 0035-8711. doi: 10.1111/j.1365-2966.2011.19329.x. URL https://doi.org/10.1111/j.1365-2966.2011.19329.x.

V. Kornilov. Stellar scintillation on large and extremely large telescopes. *Monthly Notices of the Royal Astronomical Society*, 426(1):647–655, 10 2012. ISSN 0035-8711. doi: 10.1111/j.1365-2966.2012.21653.x. URL https://doi.org/10.1111/j.1365-2966.2012.21653.x.

L. Kreidberg. batman: BAsic transit model cAlculatioN in python. *Publications of the Astronomical Society of the Pacific*, 127(957):1161–1165, nov 2015. doi: 10.1086/683602. URL https://doi.org/10.1086%2F683602.

A. L. Lesage, J. F. P. Spronck, R. Stuik, F. Bettonvil, D. Pollaco, and I. A. G. Snellen. MASCARA: the multi-site all-sky CAameRA: concept and first results. In L. M. Stepp, R. Gilmozzi, and H. J. Hall, editors, *Ground-based and Airborne Telescopes V*, volume 9145 of *Society of Photo-Optical Instrumentation Engineers (SPIE) Conference Series*, page 914514, July 2014. doi: 10.1117/12.2055997.

V. Linnick. On the principal possibility of the reduction of the influence of the atmosphere on the image of a star. *Opt. Spectrosc. 3*, page 401–2, 1957.

J. P. Lloyd. Optical turbulence in the Antarctic atmosphere. In W. A. Traub, editor, *New Frontiers in Stellar Interferometry*, volume 5491, pages 190 – 198. International Society for Optics and Photonics, SPIE, 2004. doi: 10.1117/12.552226. URL https://doi.org/10.1117/12.552226.

G. D. Love and J. Gourlay. Intensity-only modulation for atmospheric scintillation correction by liquid-crystal spatial light modulators. *Opt. Lett.*, 21(18):1496–1498, Sep 1996. doi: 10.1364/OL.21.001496. URL http://ol.osa.org/abstract.cfm?URI=ol-21-18-1496.

J. L. Lumley and H. A. Panofsky. The structure of atmospheric turbulence. *Quarterly Journal of the Royal Meteorological Society*, 91(389):400–400, 1965. doi: 10.1002/qj.49709138926. URL https://rmets.onlinelibrary.wiley.com/doi/abs/10.1002/qj.49709138926.

N. Madhusudhan, H. Knutson, J. J. Fortney, and T. Barman. Exoplanetary atmospheres. In *Protostars and Planets VI*. University of Arizona Press, 2014. doi: 10.2458/azu_uapress_9780816531240-ch032. URL https://doi.org/10.2458%2Fazu_uapress_9780816531240-ch032.

A. W. Mann, E. Gaidos, and G. Aldering. Ground-based submillimagnitude ccd photometry of bright stars using snapshot observations. *Publications of the Astronomical Society of the Pacific*, 123(909):1273–1289, Nov 2011. ISSN 1538-3873. doi: 10.1086/662640. URL http://dx.doi.org/10.1086/662640.

E. Marchetti, R. Brast, B. Delabre, R. Donaldson, E. Fedrigo, C. Frank, N. Hubin, J. Kolb, J.-L. Lizon, M. Marchesi, S. Oberti, R. Reiss, J. Santos, C. Soenke, S. Tordo, A. Baruffolo, P. Bagnara, and CAMCAO Consortium. On-sky Testing of the Multi-Conjugate Adaptive Optics Demonstrator. *The Messenger*, 129: 8–13, Sept. 2007.

E. Marin, V. Garrel, G. Sivo, V. Montes, C. Trujillo, W. Rambold, P. Gigoux, C. Moreno, R. Galvez, G. Gausachs, and M. Barreau. A new slow focus sensor for gems. *Adaptive Optics for Extremely Large Telescopes 4 – Conference Proceedings*, 05 2015. doi: 10.20353/K3T4CP1131578.

Mary, D. L. A statistical analysis of the detection limits of fast photometry. *Astronomy and Astrophysics*, 452(2):715–726, 2006. doi: 10.1051/0004-6361:20054425. URL https://doi.org/10.1051/0004-6361:20054425.

A. H. Mikesell. The scintillation of starlight. *Publications of the U.S. Naval Observatory Second Series*, 17:139–191, Jan. 1955.

E. Milone and C. Sterken. *Astronomical Photometry: Past, Present, and Future*. Astrophysics and Space Science Library. Springer New York, 2011. ISBN 9781441980502. URL https://books.google.co.uk/books?id=Ps_6zjUCR3wC.

G. ming Dai. Modal wave-front reconstruction with zernike polynomials and karhunen–loève functions. *J. Opt. Soc. Am. A*, 13(6):1218–1225, Jun 1996. doi:

10.1364/JOSAA.13.001218. URL http://josaa.osa.org/abstract.cfm?URI=josaa-13-6-1218.

B. Neichel, C. D'Orgeville, J. Callingham, F. Rigaut, C. Winge, and G. Trancho. Characterization of the sodium layer at Cerro Pachón, and impact on laser guide star performance. *Monthly Notices of the Royal Astronomical Society*, 429(4): 3522–3532, 01 2013. ISSN 0035-8711. doi: 10.1093/mnras/sts631. URL https://doi.org/10.1093/mnras/sts631.

N. Nightingale and D. Buscher. Interferometric seeing measurements at the la palma observatory. *Monthly Notices of the Royal Astronomical Society*, 251: 155–166, July 1991. doi: 10.1093/mnras/251.1.155.

R. J. Noll. Zernike polynomials and atmospheric turbulence∗. *J. Opt. Soc. Am.*, 66(3):207–211, Mar 1976. doi: 10.1364/JOSA.66.000207. URL http://www.osapublishing.org/abstract.cfm?URI=josa-66-3-207.

J. Osborn. Scintillation correction for astronomical photometry on large and extremely large telescopes with tomographic atmospheric reconstruction. *Monthly Notices of the Royal Astronomical Society*, 446(2):1305–1311, 11 2014. ISSN 0035-8711. doi: 10.1093/mnras/stu2175. URL https://doi.org/10.1093/mnras/stu2175.

J. Osborn, R. Wilson, T. Butterley, H. Shepherd, and M. Sarazin. Profiling the surface layer of optical turbulence with SLODAR. *Monthly Notices of the Royal Astronomical Society*, 406(2):1405–1408, 07 2010. ISSN 0035-8711. doi: 10.1111/j.1365-2966.2010.16795.x. URL https://doi.org/10.1111/j.1365-2966.2010.16795.x.

J. Osborn, R. W. Wilson, V. S. Dhillon, R. Avila, and G. D. Love. Conjugate-plane photometry: reducing scintillation in ground-based photometry. *Monthly Notices of the Royal Astronomical Society*, 411(2):1223–1230, 02 2011. ISSN

0035-8711. doi: 10.1111/j.1365-2966.2010.17759.x. URL https://doi.org/10.1111/j.1365-2966.2010.17759.x.

J. Osborn, D. Föhring, V. S. Dhillon, and R. W. Wilson. Atmospheric scintillation in astronomical photometry. *Monthly Notices of the Royal Astronomical Society*, 452(2):1707–1716, Jul 2015. ISSN 1365-2966. doi: 10.1093/mnras/stv1400. URL http://dx.doi.org/10.1093/mnras/stv1400.

J. Osborn, R. W. Wilson, M. Sarazin, T. Butterley, A. Chacón, F. Derie, O. J. D. Farley, X. Haubois, D. Laidlaw, M. LeLouarn, and et al. Optical turbulence profiling with stereo-scidar for vlt and elt. *Monthly Notices of the Royal Astronomical Society*, 478(1):825–834, Apr 2018. ISSN 1365-2966. doi: 10.1093/mnras/sty1070. URL http://dx.doi.org/10.1093/mnras/sty1070.

E. A. Petigura and G. W. Marcy. Identification and removal of noise modes in kepler photometry. *Publications of the Astronomical Society of the Pacific*, 124 (920):1073, oct 2012. doi: 10.1086/668291. URL https://dx.doi.org/10.1086/668291.

B. C. Platt and R. Shack. History and principles of shack-hartmann wavefront sensing, 2001.

Pluzhnik, E. A. Differential photometry of speckle-interferometric binary and multiple stars. *A&A*, 431(2):587–596, 2005. doi: 10.1051/0004-6361:20041158. URL https://doi.org/10.1051/0004-6361:20041158.

S. Poddaný, L. Brát, and O. Pejcha. Exoplanet transit database. reduction and processing of the photometric data of exoplanet transits. *New Astronomy*, 15(3): 297–301, mar 2010. doi: 10.1016/j.newast.2009.09.001. URL https://doi.org/10.1016%2Fj.newast.2009.09.001.

D. L. Pollacco, I. Skillen, A. Collier Cameron, D. J. Christian, C. Hellier, J. Irwin, T. A. Lister, R. A. Street, R. G. West, D. R. Anderson, W. I. Clarkson, H. Deeg, B. Enoch, A. Evans, A. Fitzsimmons, C. A. Haswell, S. Hodgkin, K. Horne, S. R.

Kane, F. P. Keenan, P. F. L. Maxted, A. J. Norton, J. Osborne, N. R. Parley, R. S. I. Ryans, B. Smalley, P. J. Wheatley, and D. M. Wilson. The WASP Project and the SuperWASP Cameras. *Publications of the Astronomical Society of the Pacific*, 118(848):1407–1418, Oct. 2006. doi: 10.1086/508556.

F. Pont, S. Zucker, and D. Queloz. The effect of red noise on planetary transit detection. *Monthly Notices of the Royal Astronomical Society*, 373(1):231–242, 10 2006. ISSN 0035-8711. doi: 10.1111/j.1365-2966.2006.11012.x. URL `https://doi.org/10.1111/j.1365-2966.2006.11012.x`.

R. Ragazzoni, E. Marchetti, and F. Rigaut. Modal tomography for adaptive optics. *Astronomy and Astrophysics*, 342:L53–L56, 01 1999.

A. Reeves. Soapy: an adaptive optics simulation written purely in Python for rapid concept development. In E. Marchetti, L. M. Close, and J.-P. Véran, editors, *Adaptive Optics Systems V*, volume 9909, pages 2173 – 2183. International Society for Optics and Photonics, SPIE, 2016. doi: 10.1117/12.2232438. URL `https://doi.org/10.1117/12.2232438`.

F. Rigaut and E. Gendron. Laser guide star in adaptive optics - the tilt determination problem. *åp*, 261:677–684, 01 1992.

F. Rigaut and B. Neichel. Multiconjugate adaptive optics for astronomy. *Annual Review of Astronomy and Astrophysics*, 56(1):277–314, 2018. doi: 10.1146/annurev-astro-091916-055320. URL `https://doi.org/10.1146/annurev-astro-091916-055320`.

F. Roddier. V the effects of atmospheric turbulence in optical astronomy. volume 19 of *Progress in Optics*, pages 281–376. Elsevier, 1981. doi: https://doi.org/10.1016/S0079-6638(08)70204-X. URL `http://www.sciencedirect.com/science/article/pii/S007966380870204X`.

F. Roddier. *Adaptive optics in astronomy*. Cambridge university press, 1999. ISBN 9780521612142.

M. Rosensteiner and R. Ramlau. Kaczmarz algorithm for multiconjugated adaptive optics with laser guide stars. *J. Opt. Soc. Am. A*, 30(8):1680–1686, Aug 2013. doi: 10.1364/JOSAA.30.001680. URL `http://josaa.osa.org/abstract.cfm?URI=josaa-30-8-1680`.

G. Rousset, J. C. Fontanella, P. Kern, P. Gigan, and F. Rigaut. First diffraction-limited astronomical images with adaptive optics. *Astronomy and Astrophysics*, 230(2):L29–L32, Apr. 1990.

P. Ryan and D. Sandler. Scintillation reduction method for photometric measurements. *Publications of the Astronomical Society of the Pacific*, 110(752):1235–1248, 1998. ISSN 00046280, 15383873. URL `http://www.jstor.org/stable/10.1086/316248`.

R. J. Sasiela. *Electromagnetic wave propagation in turbulence: evaluation and application of Mellin transforms*, volume 18 of *Springer Series on Wave Phenomena*. Springer, 2012. doi: 10.1007/978-3-642-85070-7.

D. Saxenhuber, G. Auzinger, M. L. Louarn, and T. Helin. Comparison of methods for the reduction of reconstructed layers in atmospheric tomography. *Appl. Opt.*, 56(10):2621–2629, Apr 2017. doi: 10.1364/AO.56.002621. URL `http://ao.osa.org/abstract.cfm?URI=ao-56-10-2621`.

J. Schmidt. *Numerical Simulation of Optical Wave Propagation with examples in MATLAB*. SPIE, Bellingham, WA, 2010. ISBN 978-0-8194-8326-3.

S. Serjeant, M. Elvis, and G. Tinetti. The future of astronomy with small satellites. *Nature Astronomy*, 4(11):1031–1038, 2020.

H. W. Shepherd, J. Osborn, R. W. Wilson, T. Butterley, R. Avila, V. S. Dhillon, and T. J. Morris. Stereo-SCIDAR: optical turbulence profiling with high sensitivity using a modified SCIDAR instrument. *Monthly Notices of the Royal Astronomical Society*, 437(4):3568–3577, 11 2013. ISSN 0035-8711. doi: 10.1093/mnras/stt2150. URL `https://doi.org/10.1093/mnras/stt2150`.

SIMBAD. "bw vul", simbad, centre de données astronomiques de strasbourg. https://simbad.cds.unistra.fr/simbad/sim-id?Ident=BW+Vul, June 2021.

V. F. Sofieva, F. Dalaudier, and J. Vernin. Using stellar scintillation for studies of turbulence in the earth's atmosphere. *Philosophical Transactions of the Royal Society A: Mathematical, Physical and Engineering Sciences*, 371(1982):20120174, 2013. doi: 10.1098/rsta.2012.0174. URL `https://royalsocietypublishing.org/doi/abs/10.1098/rsta.2012.0174`.

J. Southworth, T. C. Hinse, U. G. Jørgensen, M. Dominik, D. Ricci, M. J. Burgdorf, A. Hornstrup, P. J. Wheatley, T. Anguita, V. Bozza, S. C. Novati, K. Harpsøe, P. Kjærgaard, C. Liebig, L. Mancini, G. Masi, M. Mathiasen, S. Rahvar, G. Scarpetta, C. Snodgrass, J. Surdej, C. C. Thöne, and M. Zub. High-precision photometry by telescope defocusing - I. The transiting planetary system WASP-5. *Monthly Notices of the Royal Astronomical Society*, 396(2):1023–1031, June 2009. doi: 10.1111/j.1365-2966.2009.14767.x.

J. Stebbins. The measurement of the light of stars with a selenium photometer, with an application to the variations of algol. *The Astrophysical Journal*, 32, 1910.

G. Stefansson, S. Mahadevan, L. Hebb, J. Wisniewski, J. Huehnerhoff, B. Morris, S. Halverson, M. Zhao, J. Wright, J. O'rourke, H. Knutson, S. Hawley, S. Kanodia, Y. Li, L. M. Z. Hagen, L. J. Liu, T. Beatty, C. Bender, P. Robertson, J. Dembicky, C. Gray, W. Ketzeback, R. McMillan, and T. Rudyk. Toward space-like photometric precision from the ground with beam-shaping diffusers. *The Astrophysical Journal*, 848(1):9, oct 2017. doi: 10.3847/1538-4357/aa88aa. URL `https://dx.doi.org/10.3847/1538-4357/aa88aa`.

M. Tallon and R. Foy. Adaptive telescope with laser probe: isoplanatism and cone effect. *Astronomy and Astrophysics*, 235:549–557, Aug. 1990.

O. Tamuz, T. Mazeh, and S. Zucker. Correcting systematic effects in a large set of photometric light curves. *Monthly Notices of the Royal Astronomical Society*, 356 (4):1466–1470, feb 2005. doi: 10.1111/j.1365-2966.2004.08585.x. URL `https://doi.org/10.1111%2Fj.1365-2966.2004.08585.x`.

V. I. Tatarski. *Wave propagation in a turbulent medium / V. I. Tatarski; translated from the Russian by R. A. Silverman.* Dover, New York, 1967.

G. I. Taylor. The Spectrum of Turbulence. *Proceedings of the Royal Society of London Series A*, 164(919):476–490, Feb. 1938. doi: 10.1098/rspa.1938.0032.

N. Thatte, M. Tecza, F. Clarke, R. L. Davies, A. Remillieux, R. Bacon, D. Lunney, S. Arribas, E. Mediavilla, F. Gago, N. Bezawada, P. Ferruit, A. Fragoso, D. Freeman, J. Fuentes, T. Fusco, A. Gallie, A. Garcia, T. Goodsall, F. Gracia, A. Jarno, J. Kosmalski, J. Lynn, S. McLay, D. Montgomery, A. Pecontal, H. Schnetler, H. Smith, D. Sosa, G. Battaglia, N. Bowles, L. Colina, E. Emsellem, A. Garcia-Perez, S. Gladysz, I. Hook, P. Irwin, M. Jarvis, R. Kennicutt, A. Levan, A. Longmore, J. Magorrian, M. McCaughrean, L. Origlia, R. Rebolo, D. Rigopoulou, S. Ryan, M. Swinbank, N. Tanvir, E. Tolstoy, and A. Verma. HARMONI: a single-field wide-band integral-field spectrograph for the European ELT. In I. S. McLean, S. K. Ramsay, and H. Takami, editors, *Ground-based and Airborne Instrumentation for Astronomy III*, volume 7735 of *Society of Photo-Optical Instrumentation Engineers (SPIE) Conference Series*, page 77352I, jul 2010. doi: 10.1117/12.857445.

A. Tokovinin. Measurement of seeing and the atmospheric time constant by differential scintillations. *Appl. Opt.*, 41(6):957–964, Feb 2002. doi: 10.1364/AO.41.000957. URL `https://opg.optica.org/ao/abstract.cfm?URI=ao-41-6-957`.

M. J. Townson, O. J. D. Farley, G. O. de Xivry, J. Osborn, and A. P. Reeves. Aotools: a python package for adaptive optics modelling and analysis. *Opt. Express*, 27(22):31316–31329, Oct 2019. doi: 10.1364/OE.27.031316. URL `http://www.opticsexpress.org/abstract.cfm?URI=oe-27-22-31316`.

J. Tregloan-Reed and J. Southworth. An extremely high photometric precision in ground-based observations of two transits in the wasp-50 planetary system. *Monthly Notices of the Royal Astronomical Society*, 431:966, 02 2013. doi: 10.1093/mnras/stt227.

G. T. van Belle, A. B. Meinel, and M. P. Meinel. The scaling relationship between telescope cost and aperture size for very large telescopes. In J. M. O. Jr., editor, *Ground-based Telescopes*, volume 5489, pages 563 – 570. International Society for Optics and Photonics, SPIE, 2004. doi: 10.1117/12.552181. URL `https://doi.org/10.1117/12.552181`.

J. Vernin and F. Roddier. Experimental determination of two-dimensional spatiotemporal power spectra of stellar light scintillation evidence for a multilayer structure of the air turbulence in the upper troposphere. *J. Opt. Soc. Am.*, 63(3): 270–273, Mar 1973. doi: 10.1364/JOSA.63.000270. URL `https://opg.optica.org/abstract.cfm?URI=josa-63-3-270`.

J. Villanueva, Steven, D. Dragomir, and B. S. Gaudi. An Estimate of the Yield of Single-transit Planetary Events from the Transiting Exoplanet Survey Satellite. *The Astronomical Journal*, 157(2):84, Feb. 2019. doi: 10.3847/1538-3881/aaf85e.

von F. Zernike. Beugungstheorie des schneidenver-fahrens und seiner verbesserten form, der phasenkontrastmethode. *Physica*, 1(7):689–704, 1934. ISSN 0031-8914. doi: https://doi.org/10.1016/S0031-8914(34)80259-5. URL `https://www.sciencedirect.com/science/article/pii/S0031891434802595`.

R. Wilson. Results of the jose site evaluation project for adaptive optics at the william herschel telescope. *New Astronomy Reviews*, 42(6):465 – 469, 1998. ISSN 1387-6473. doi: https://doi.org/10.1016/S1387-6473(98)00054-2. URL `http://www.sciencedirect.com/science/article/pii/S1387647398000542`.

J. N. Winn. Transits and occultations. *arXiv preprint arXiv:1001.2010*, 2010.

A. Wolszczan and D. A. Frail. A planetary system around the millisecond pulsar PSR1257 + 12. *Nature*, 355(6356):145–147, Jan. 1992. doi: 10.1038/355145a0.

A. T. Young. Photometric error analysis. viii. the temporal power spectrum of scintillation. *Appl. Opt.*, 8(5):869–885, May 1969. doi: 10.1364/AO.8.000869. URL `http://ao.osa.org/abstract.cfm?URI=ao-8-5-869`.

A. T. Young, R. M. GENET, L. J. BOYD, W. J. BORUCKI, G. W. LOCKWOOD, G. W. HENRY, D. S. HALL, D. P. SMITH, S. L. BALIUNAS, R. DONAHUE, and D. H. EPAND. Precise automatic differential stellar photometry. *Publications of the Astronomical Society of the Pacific*, 103(660):221–242, 1991. ISSN 00046280, 15383873. URL `http://www.jstor.org/stable/40679676`.

H. Zou, X. Zhou, Z. Jiang, M. Ashley, X. Cui, L. Feng, X. Gong, J. Hu, C. A. Kulesa, J. S. Lawrence, et al. Sky brightness and transparency in the i-band at dome a, antarctica. *The Astronomical Journal*, 140(2):602, 2010.